



Analysis and Modelling of induced-turbulence in two-phase flows

Alessio Innocenti

► To cite this version:

Alessio Innocenti. Analysis and Modelling of induced-turbulence in two-phase flows. Fluid mechanics [physics.class-ph]. Sorbonne Université; Università degli studi (Pise, Italie), 2018. English. NNT : 2018SORUS339 . tel-02864786

HAL Id: tel-02864786

<https://theses.hal.science/tel-02864786>

Submitted on 11 Jun 2020

HAL is a multi-disciplinary open access archive for the deposit and dissemination of scientific research documents, whether they are published or not. The documents may come from teaching and research institutions in France or abroad, or from public or private research centers.

L'archive ouverte pluridisciplinaire **HAL**, est destinée au dépôt et à la diffusion de documents scientifiques de niveau recherche, publiés ou non, émanant des établissements d'enseignement et de recherche français ou étrangers, des laboratoires publics ou privés.



UNIVERSITÀ DI PISA

UNIVERSITÉ
**FRANCO
ITALIENNE**

UNIVERSITÀ
**ITALO
FRANCESE**

THÈSE DE DOCTORAT DE L'UNIVERSITÉ
PIERRE ET MARIE CURIE

Ecole doctorale de Sciences Mécaniques,
Acoustique, Électronique et Robotique de Paris

Presentée par

TESI DI DOTTORATO UNIVERSITÀ DI
PISA

Scuola di dottorato in Ingegneria Industriale

Presentata da

ALESSIO INNOCENTI

pour obtenir le grade de Docteur de l'Université
Pierre et Marie Curie

per conseguire il titolo di Dottore di ricerca
dell'Università di Pisa

Analysis and modelling of induced-turbulence in two-phase flows

dirigée par diretta da
SERGIO CHIBBARO, MARIA VITTORIA SALVETTI

à l'Institut Jean Le Rond d'Alembert

al Dipartimento di Ingegneria Civile e
Industriale

Soutenue le 14 Décembre 2018 devant le jury composé de:
Discussa il 14 Dicembre 2018 in presenza della commissione composta da:

M CHIBBARO Sergio	Directeur de Thèse
Mme SALVETTI Maria Vittoria	Directrice de Thèse
M CASCIOLA Carlo Massimo	Rapporteur
M LEGENDRE Dominique	Rapporteur
M GUALTIERI Paolo	Examineur
M MAGNAUDET Jacques	Examineur
M MARIOTTI Alessandro	Examineur
M POPINET Stéphane	Examineur

Résumé: La présente thèse porte sur l'étude et la modélisation des écoulements turbulents diphasiques avec un intérêt particulier pour les mécanismes de turbulence induite par une phase dispersée. L'objectif est de proposer des modèles réduits d'intérêt pour les applications et de comprendre la physique à la base du problème à travers de simulations numériques directes (DNS). Ce travail se compose de deux parties.

Dans la première partie l'attention est portée sur les écoulements gaz-particules solides de petite taille en suivant une approche eulérienne (pour le fluide) - lagrangienne (pour les particules). Nous avons proposé un modèle lagrangien stochastique pour le suivi des particules dans un champ de vitesse à grandes échelles (Large-Eddy-Simulation) dans le cas d'écoulements dilués, c'est à dire où la concentration des particules est petite et on peut négliger l'effet des particules sur le fluide. Le modèle a été testé pour un canal plan turbulent avec des résultats très proches de la DNS.

Ensuite nous avons proposé un modèle pour les écoulements denses (fraction de masse de la phase solide dispersée élevée), avec un couplage de type "two-way", avec la prise en compte des collisions d'un point de vue statistique. Dans le modèle, nous avons choisi de séparer la vitesse des particules dans une composante spatialement corrélée et un résidu décorrélé, et cela nous a permis de considérer correctement l'effet des collisions et de définir différents temps caractéristiques, essentiels pour modéliser les deux différentes parties. Ce modèle a été testé et validé dans plusieurs cas homogènes et non-homogènes, avec un intérêt particulier pour la turbulence induite par les particules (Cluster-Induced-Turbulence).

La deuxième partie est consacrée à l'étude du mouvement de remontée des bulles gazeuses dans un liquide. Tel problème a été traité avec un code numérique (Basilisk) qui résout les deux fluides ainsi que l'interface avec une méthode "Volume-Of-Fluid". En utilisant une configuration périodique avec une seule bulle, afin de valider le code numérique, différents cas de la littérature ont été analysés. L'attention a été consacrée d'abord sur plusieurs problèmes techniques, comme les critères pour le raffinement local du maillage adaptatif et le rapport entre les densités des deux fluides. Ensuite nous avons étudié une configuration de colonne de bulles, caractérisée par une couche avec une fraction volumique élevée de bulles, posés initialement sur le fond d'un réservoir et qui, grâce à la force de flottabilité, remontent dans le fluide. Avec une étude des spectres et des PDFs nous avons caractérisé les fluctuations induites par les bulles dans le fluide.

Sommario: La presente tesi concerne lo studio e la modellizzazione di flussi turbolenti bifase, con particolare interesse ai meccanismi di turbolenza indotta dalla fase dispersa. L'obiettivo è di proporre modelli ridotti di interesse applicativo e di comprendere la fisica alla base del problema attraverso delle simulazioni numeriche dirette (DNS). Il lavoro si articola in due parti.

Nella prima parte l'attenzione è stata posta su flussi gas-particelle solide di piccola taglia seguendo un approccio Euleriano (per il fluido) - Lagrangiano (per le particelle). È stato proposto un modello stocastico Lagrangiano per il tracciamento di particelle all'interno di un campo di velocità a grandi scale (Large-Eddy-Simulation) nel caso di flussi diluiti, ovvero laddove la concentrazione di particelle è bassa e può quindi essere trascurato l'effetto delle particelle sui fluidi. Tale modello è stato testato in un canale piano turbolento con risultati molto vicini a quelli della DNS.

Successivamente è stato proposto un modello per flussi densi (elevata frazione di massa della fase solida dispersa), con accoppiamento di tipo "two-way", considerando da un punto di vista statistico anche le collisioni tra particelle. In tale modello è stata introdotta la novità di separare la velocità delle particelle in una componente spazialmente correlata e un residuo scorrelato, che ha permesso di considerare correttamente l'effetto delle collisioni e di definire diversi tempi caratteristici, fondamentali per modellizzare i due diversi contributi. Tale modello è stato testato e validato in diversi casi omogenei e non-omogenei, con particolare interesse per il problema di turbolenza indotta dalle particelle (Cluster-Induced-Turbulence).

La seconda parte è incentrata sullo studio del moto di risalita di bolle gassose all'interno di un liquido. Tale problema è stato affrontato con un codice numerico (Basilisk) che risolve i due fluidi e l'interfaccia con un metodo "Volume-Of-Fluid". Utilizzando una configurazione periodica con una singola bolla, al fine di validare il codice numerico, sono stati analizzati diversi casi di riferimento della letteratura. È stata posta l'attenzione su alcuni problemi tecnici, quali i criteri per il raffinamento locale della griglia adattiva e il rapporto delle densità dei due fluidi. Infine è stata studiata la configurazione della colonna di bolle caratterizzata da uno strato ad alta concentrazione volumica di bolle posto inizialmente sul fondo di un recipiente e che per effetto della forza di galleggiamento risale all'interno del liquido. Particolare enfasi è stata posta nello studio delle fluttuazioni indotte dalle bolle nel liquido, analizzando spettri e PDFs.

Contents

Preface	1
I Overview of the Thesis	5
1 Background concepts	7
1.1 Turbulent flows	7
1.1.1 A statistical description of turbulent flows	8
1.2 Multiphase flows	9
1.2.1 Particle-laden flows	10
1.2.2 Bubbly flows	13
2 Methodology	17
2.1 Eulerian-Lagrangian DNS of turbulent particle-laden flows	18
2.2 LES of turbulent particle-laden flows	18
2.3 RANS of turbulent particle-laden flows	20
2.4 PDF methods	21
2.5 DNS of bubbly flows	24
2.5.1 Basilisk code	25
II Particle-laden flows	29
3 Lagrangian filtered density function for LES-based stochastic modelling of turbulent particle-laden flows	31
3.1 Introduction	33
3.2 Problem Formulation	35
3.3 Definition of the Filtered Density Function	36
3.3.1 Particle phase	36
3.3.2 LFMDf transport equation	37
3.3.3 Modeled LFMDf transport equation	38
3.3.4 Equivalent Stochastic System	39
3.4 Numerical method	39
3.5 Results	42
3.5.1 Assessment of consistency and convergence	43
3.5.2 Model assessment with inertial particles	46
3.6 Discussion and conclusions	53
3.A Weak first-order Numerical scheme	55

4	A Lagrangian probability-density-function model for collisional turbulent fluid-particle flows	59
4.1	Introduction	61
4.2	Rationale for the model construction	64
4.3	Lagrangian pdf model for the particle phase	66
4.3.1	Modelled equations	67
4.4	Lagrangian pdf model for the fluid seen by particles	69
4.4.1	Closure of the diffusion coefficient	70
4.5	Eulerian pdf model for the fluid phase	72
4.6	RA equations	74
4.7	Statistically homogeneous equations	77
4.7.1	Particle phase	77
4.7.2	Simplified model for particle phase	78
4.7.3	Fluid phase	79
4.8	Numerical results	80
4.8.1	Homogeneous isotropic turbulence	80
4.8.2	Decaying and homogeneous-shear flow	82
4.8.3	Cluster-induced turbulence	88
4.9	Discussion and conclusions	95
4.A	Exact Reynolds-average equations	97
4.A.1	Particle phase	97
4.A.2	Fluid phase	97
4.B	Simulation of a Gaussian vector: the Choleski decomposition	98
4.C	Fokker–Planck equation	98
4.D	Fluid–particle limit	99
4.5	Supplementary material: a detailed description of the coarse-graining steps .	101
5	A Lagrangian probability-density-function model for collisional turbulent fluid-particle flows. Part II: a channel-flow application.	105
5.1	Introduction	106
5.2	The Eulerian-Lagrangian description for particle-laden flows	107
5.2.1	Fluid phase	107
5.2.2	Particle phase	108
5.2.3	Phase average	108
5.3	Lagrangian pdf model for vertical channel flow	109
5.3.1	Stochastic model for particle phase	109
5.3.2	Fluid phase model	112
5.4	Channel flow configuration	114
5.5	Numerical approach	116
5.5.1	Fluid phase	117
5.5.2	Particle phase	117
5.6	Results	119
5.6.1	Test of consistency with tracer particles	119
5.6.2	Inertial particles with two-way coupling	120
5.7	Conclusions	124

5.A Numerical scheme	127
III Bubbly flows	131
6 Bubbly flows: phenomenology of free rise and bubble-induced turbulence at high Reynolds numbers.	133
6.1 Introduction	134
6.2 Mathematical formulation	136
6.2.1 Problem statement	136
6.2.2 Governing equations	137
6.3 Numerical method	138
6.4 Arrays of bubbles	138
6.4.1 Validation tests	138
6.4.2 3-D oblique rise of bubbles	140
6.5 Technical issues	142
6.5.1 Coalescence	143
6.5.2 Grid refinement effect	145
6.6 Bubble column configuration	149
6.7 Conclusions	157
7 Conclusions	161
A Collaboration	165
Bibliography	173

Preface

With multiphase flows we intend those flows where at least two separate phases coexist at the same time in different region of the space and interact reciprocally. Their study has a long history in the scientific literature and their interest is constantly increasing, since they are present in a number of applications and can be encountered in everyday life very frequently. To cite some examples, just think to the drops of rain falling through the air, or to the ashes blown from a vulcan and dispersed at great distances by the wind, or again to a boiler where air bubbles may nucleate and rise inside a liquid. This is to convince who is not familiar with the subject that their understanding is crucial and that numerical and physical experiments can give an important contribution to strengthen the actual knowledge of the topic and to ameliorate existing models for the prediction of these flows.

A key point is the mutual interaction between the two phases, and in particular the continuous exchange of momentum and energy. When one of the two phases is dispersed in the form of inclusions in a continuum (e.g. solid particles in air, air bubbles in a liquid), a possible approach, is to consider the integral effect of the forces exerted by the continuous phase onto the surface of the dispersed one. If the dispersed phase is sufficiently small compared to the smallest fluid scales, like for instance for particles with a diameter of the order of the micrometer up to tenths of millimeter, the particle can safely be considered as a material point, whose acceleration depends on the force exerted by the fluid. Otherwise, if this separation of scales is not marked, the size of the particle should not be neglected. This is particularly important for drops and bubbles, whose size can be likely of the order of the millimeter, and where shape deformations can also be relevant and enhance non-trivial dynamics.

An interesting mechanism that can occur in presence of two-phase flows is the agitation induced in the carrier phase by the dispersed one. From the third principle of mechanics it is clear that if one phase (the carrier) exerts a force on the other phase (the dispersed), which is the sum of several contribution like drag, lift and added mass, then a reaction, of the latter on the former, of equal magnitude but opposite sign occurs. Now, if the dispersed phase consists in a small number of particles/bubbles and we are interested in large scale dynamics, this effect can be safely neglected, otherwise it might have an important impact. More specifically what matters is the portion of volume occupied by one phase with respect to the other, called volume fraction, α . For values of $\alpha > 10^{-3}$, the coupling between the phases starts to be important. There are two concurrent effects that might modify the continuum velocity field of the carrier phase: the first one is inherently due to the fact that a secondary phase is present and occupy a certain region of the space that cannot thus be occupied by the first one; the second one is related to the force that the dispersed phase exerts on the continuum. When the volume fraction is high enough (of the order of few percent) the back-reaction might enhance significative fluctuations in the principal phase, and when the latter becomes the main mechanism of disturbances generation within the flow, it is also referred as cluster/bubble induced turbulence. Indeed, this agitation shares several similarities with classical single-phase turbulence like the highly unsteady motion, the difficult predictability and the power-law scaling of energy, for instance. In

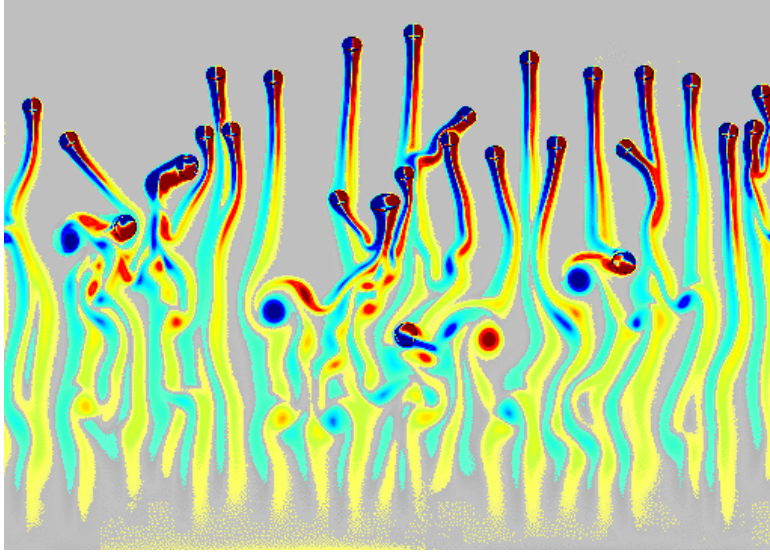


Figure 1: Instantaneous snapshot of the vorticity in the wakes of a swarm of rising bubbles.

bubbly flows those situations are also called bubble-induced agitation [Riboux 2010], or pseudo-turbulence to highlight the different nature with respect to classical turbulence. In figure 1 we show an example of the agitation induced by rising bubbles.

The objective of this thesis is, thus, to analyze the mechanisms of this phenomenon in those cases where it is still not completely clear, and to elaborate and test multiphase models that can accurately predict and describe the physics of the observed problem. To reach this goal we have made use of several instruments that are commonly adopted in the multiphase community and we have followed different numerical approaches depending on the specific case. When available, we have compared our results with experiments performed by other authors, like for instance the homogeneous fully developed cluster-induced-turbulence numerical simulation of [Capecelatro 2015], or the bubble-induced turbulence experiment of [Riboux 2010].

The work has been focused on two different parts, respectively particle-laden and bubbly flows, which have been faced with different approaches and perspectives. Because of the advancement in the study of particle-laden flows, which are more mature and which offer a wide range of numerical and physical experiments, in this part it has been possible to be somehow more technical, answering to specific modelling questions. On the contrary, the part on bubbly flows has been more exploratory and fundamental, in order to provide a further analysis of some mechanisms that are still not completely clear. Indeed, the study of turbulent bubbly flows is more recent, and even if experiments are rather advanced, the numerical approach is still in development, and is progressing at great steps.

The manuscript is therefore divided in three parts and is organised as follows: the first part recalls some concepts of turbulent and multiphase flows, focusing on the main physical features of those flows and drawing a picture of the actual state-of-the-art. Then, the methodologies that have been adopted within the course of our work have been described putting forward the key-points and the drawbacks of each one.

In part II the problem of describing inertial particles in turbulence has been addressed.

We have considered point-particles, because of their negligible size with respect to turbulence scales and we have considered several regimes of particle concentration. Firstly, in the dilute regime (low particle concentration) we have focused on the mechanism of particle preferential concentration, which is the key feature for those flows and that have a great impact in practical applications (e.g. particle accumulations near to the wall). Using direct numerical simulation (DNS) data for the assessment, we have proposed a Lagrangian stochastic model for tracking particles in dilute turbulent flows in the framework of a Large-Eddy-Simulation (LES) where only a filtered fluid velocity field is available, resulting in the loss of the small scale fluid fluctuations. The stochastic particle model has given excellent results in the estimation of the particle near-wall concentration, which is usually underestimated in LES without particle models, and this result has been confirmed by the good reconstruction of the fluid-phase statistics.

Secondly, we have investigated the dense regime (high particle concentration), where turbulence can be modulated by the particle phase and the mechanism of energy generation by the secondary phase can become predominant. For this case, because of the increased complexity (e.g. the back-reaction of the particle on the fluid might easily give rise to numerical instabilities), we have proposed a particle stochastic model to be coupled with the Reynolds-Averaged (RA) fluid-phase equations. This choice has been motivated also by the fact that no Lagrangian particle model for dense flows was present for high volume fraction regime, i.e. CIT. Therefore we have proposed a new stochastic model that can take into account also particle collisions and we have tested it in several homogeneous applications of increasing complexities up to the CIT, obtaining excellent results. Finally, we have tested it also in a non-homogeneous application, which has results particularly challenging. Indeed, the increased complexity due to spatial fluxes and boundary layers makes the resolution of the problem with two-way coupling particularly difficult, with possible numerical instabilities triggered by the back-reaction of particles. For this non-homogeneous application it has been necessary to develop and validate a new numerical scheme for the solution of coupled stochastic differential equations. Even though results are yet less conclusive, we have found consistent results with literature studies.

In part III, we have studied the problem of bubbly flows at moderate to high Reynolds number. The objective was still to investigate the mechanisms of turbulence (agitation) generation by the dispersed phase. However in this case, in the perspective of reaching a good knowledge of the subject to support lower-order models, we needed to start from performing numerical experiments (DNS), because of the need to further analyze several situations of interest. Indeed, albeit some experiments have been done, providing interesting ideas, there are several questions that still remain open related to the bubble agitation mechanism. To follow a rigorous path, we have tested a numerical code capable of describing two-phase interfacial flows (Basilisk), in several rising bubbles configuration, reproducing literature results. Finally, we have performed several 2-dimensional and the first well resolved 3-dimensional DNS of a bubble column to study more in detail the bubble-induced turbulence. Results, show the presence of a typical marker for this situation, identified in the presence of a slope close to -3 in velocity spectra and in asymmetric probability distributions of the velocity fluctuations, which were evidenced also in experimental results. Results seem to suggest many cascade dynamics in different regimes, and work to better understand it appears necessary.

A work resulting from a collaboration with colleagues of Grenoble University about stochastic modelling of the fluid acceleration in a wall-bounded flow is then presented in appendix [A](#)

As it can be seen, the work has been strongly transversal, touching different problematic but with the same common thread of the turbulence induced by a secondary phase. Hence, the methodologies adopted to accomplish this survey have been several. Each chapter of the thesis has been conceived as self-contained and it corresponds to a dedicated paper published, submitted or in preparation to an international scientific journal. Therefore, even if there might be some repetition in the introductory parts of some chapter, the structure and the contents should remain clear, and will facilitate the reader who is interested only in some specific case.

Part I

Overview of the Thesis

Background concepts

1.1 Turbulent flows

Turbulent flows can be observed frequently in our everyday surroundings, ranging from large-scale flows, as ocean and atmosphere circulation, to small-scale ones, as the water flowing in a river or in a waterfall, the smoke from a chimney and the wind on a car. Their range is thus large and the variety of flow scales to be considered is related to the problem size. Nonetheless, the equations describing the motion of Newtonian incompressible fluids are apparently simple. Indeed, the conservation of mass is given by

$$\frac{\partial U_i}{\partial x_i} = 0, \quad (1.1)$$

and momentum by

$$\frac{\partial U_i}{\partial t} + U_j \frac{\partial U_i}{\partial x_j} = -\frac{1}{\rho} \frac{\partial p}{\partial x_i} + \nu \frac{\partial^2 U_i}{\partial x_j \partial x_j} + f_i \quad (1.2)$$

where ρ and ν are the fluid density and kinematic viscosity, U is the velocity field, p is the related pressure field, and f is an eventual external acceleration field, like for instance gravity.

It has long been observed that fluid flows can be calm, moving on parallel paths, or energetic and chaotic. In a classic experiment [Reynolds 1883] O. Reynolds found that these two states of the flow, called laminar and turbulent, could be seen in water flowing through a glass pipe by changing what became known as the Reynolds number. The Reynolds number is the non-dimensional number that controls the transition between a laminar flow and a turbulent flow, and is written

$$Re = \frac{\text{inertial terms}}{\text{viscous terms}} = \frac{UL}{\nu} \quad (1.3)$$

where U and L are some characteristic velocity and length of the flow. The Reynolds number compares the viscous terms, which tend to dampen motion, with the inertial terms that tend to amplify it. In the experiments Reynolds found that for low Reynolds number conditions the dye injected in the flow did not mix, implying that all streamlines remained parallel to the direction of the flow, while for larger Reynolds number the system exhibited a turbulent state, characterized by a time dependent velocity profile and mixing of the injected dye. Therefore it is commonly stated that if $Re \gg 1$ the flow can become turbulent, i.e. infinitesimal disturbances grow indefinitely in time and make the flow chaotic. In the years many researchers have found common characteristics to a wide variety of turbulent flows and, even if a shared formal definition is not always agreed by everybody, the main features of turbulent flows are: (i) the velocity field, as well as other observables, varies significantly and irregularly over time and space. In particular, due to the nature of the system of equations, instantaneous turbulent quantities are not predictable: even if they can be described deterministically by Navier-Stokes equations (NS, eqs. (1.1)-(1.2)), they

experience a high sensitivity to initial conditions and therefore different realizations can differ significantly. (ii) A statistical description, however, is meaningful and can provide a quantitative analysis, i.e. while the instantaneous velocity $U_i(x, t)$ is not predictable, the average velocity at that position and time $\langle U_i(x, t) \rangle$ is stable and can be predicted. This is the reason why a statistical approach is suitable for turbulence. (iii) From a physical point of view the main features of turbulent flows are their large variety of scales, from large ones where energy is injected from the extern, to small ones where it is dissipated, and their highly diffusive behaviour. Because of the latter, turbulence is very efficient at mixing, a quality often appreciated for engineering purposes. The transfer of energy from large to small scales is referred as energy cascade and is one of the key features of turbulence. In particular it is nowadays well known that the spectral energy density evolves as the power of $-5/3$ of the wavenumber in the inertial range of scales, which is the intermediate part between energy injection and energy dissipation.

Different theory of turbulence has been given by many authors over years, starting from the precursor works of [Richardson 1922, Kolmogorov 1941a, Kolmogorov 1941b], and a clear and exhaustive description can be found in different text books [Hinze 1975, Frisch 1995, Pope 2000]. In this work we will concentrate mainly in the statistical description of turbulence, therefore in the following we will briefly recall the main key concepts useful for such approach.

1.1.1 A statistical description of turbulent flows

Since the fluid velocity U of a turbulent flow is a random variable, its instantaneous value at a certain position and time is not meaningful for a quantitative characterisation of the flow. We should rather look at the probability of the velocity to be in a certain range of values at a certain position and time, i.e. at its *probability density function* (PDF), $f(\mathbf{V}; \mathbf{x}, t)$. In terms of this PDF, the mean velocity field can be computed as a statistical moment:

$$\langle \mathbf{U}(\mathbf{x}, t) \rangle = \int \int \int_{-\infty}^{\infty} \mathbf{V} f(\mathbf{V}; \mathbf{x}, t) d\mathbf{V}. \quad (1.4)$$

Using this definition the instantaneous velocity field can be decomposed in a mean part and a fluctuation (which by definition has zero mean):

$$\mathbf{U}(\mathbf{x}, t) = \langle \mathbf{U}(\mathbf{x}, t) \rangle + \mathbf{u}(\mathbf{x}, t) \quad (1.5)$$

which is known as Reynolds decomposition. If the average operator is applied to the NS equations, and using its properties of commutation with the differentiation, the following Reynolds-Averaged NS equation can be obtained for the transport of mean momentum

$$\frac{\partial \langle U_i \rangle}{\partial t} + \langle U_j \rangle \frac{\partial \langle U_i \rangle}{\partial x_j} + \frac{\partial \langle u_i u_j \rangle}{\partial x_j} = -\frac{1}{\rho} \frac{\partial \langle p \rangle}{\partial x_i} + \nu \frac{\partial^2 \langle U_i \rangle}{\partial x_j \partial x_j} + \langle f_i \rangle. \quad (1.6)$$

This equation looks very similar to the NS equation (1.2), with the exception of the term containing the mean of the product of the fluctuating velocities, $\langle u_i u_j \rangle$, which is called Reynolds-stress tensor. This term is of fundamental importance in the statistical description of turbulence and has a direct effect on the mean velocity. For this reason, if we are

seeking for a numerical solution of equation (1.6), we need either to model it or to add a transport equation for it. Still starting from equation (1.2), after some manipulation, a set of transport equations for the Reynolds-stresses (or alternatively for the turbulent kinetic energy $k = \langle u_i u_i \rangle / 2$) can be found:

$$\frac{\partial \langle u_i u_j \rangle}{\partial t} + \langle U_j \rangle \frac{\partial \langle u_i u_j \rangle}{\partial x_j} + \frac{\partial}{\partial x_k} T_{kij} = \mathcal{P}_{ij} + \mathcal{R}_{ij} - \varepsilon_{ij} \quad (1.7)$$

where T , \mathcal{P} , \mathcal{R} and ε_{ij} represent respectively the transport, production, pressure-rate-of-strain and dissipation tensors. Qualitatively, the interaction between the Reynolds-stress and the mean-flow gradient transfers energy from the mean flow to turbulence scales, where then is dissipated by viscous friction. A detailed description of all terms can be found in turbulence textbooks [Pope 2000], but even at first sight it is clear that a "closure" problem arises. In fact in the transport equation of a turbulent statistical quantity, it will always appear at least some higher order moment responsible for the turbulent transport, i.e. the Reynolds-stress tensor $\langle u_i u_j \rangle$ in the momentum equation, the third order tensor T_{kij} , the redistribution \mathcal{R}_{ij} and the dissipation ε_{ij} in the Reynolds-stress equation, and so on. This is to say that when dealing with a statistical equation, a closure, and therefore a model, is needed at some level of the description, since the equations for a statistical moment of order n will always involve some quantity of the order $n + 1$.

1.2 Multiphase flows

When more than a phase is present at the same time we speak of multiphase flows. These flows play a significant role in nature and in man-made systems [Crowe 2011]. We encounter two-phase flows in liquid at a free surface, such as when drinking, washing and cooking, as well as in flows laden with solid particles such as rivers transporting sediments or in volcanic plinian eruptions. Similarly, such flows are in abundance also in industrial applications: heat-transfer by boiling, steel making and nuclear plants just to cite a few examples. These type of flows can be classified into five categories: (i) gas-liquid, (ii) liquid-liquid, (iii) gas-solid, (iv) liquid-solid and (v) three-phase flows. From a physical point of view categories (i) and (ii) deal both with two fluids and therefore they could be grouped together. Another possible criterion for the classification could be that of the relative density between the phases, which may introduce a relative drift in dispersed flows. Concerning gas-liquid and liquid-liquid flows, depending on the form of the interface between the two media and on their material properties, different regimes can be found [McQuillan 1985]. This is illustrated in Figure 1.1 which shows a range of regimes for the case of a boiling liquid (for example water) in a classical vertical heat exchanger. At the bottom of the tube, the liquid has not yet started to boil and we have a single-phase turbulent flow. When nucleation starts at the walls, bubbles can be found as separate inclusions within the liquid (bubbly flows). Then, as more vapour is created we go through the so-called slug and plug regimes where vapour occupies a more important volumetric fraction. As the liquid continues to boil, we find the annular regime with a thin liquid layer at the walls and a central vapour flow with small droplets carried by the vapour. Thus, the scenario ranges from a dispersed two-phase flow, where one phase is a continuum (liquid) and the other phase appears as separate inclusions dispersed within the continuous one,

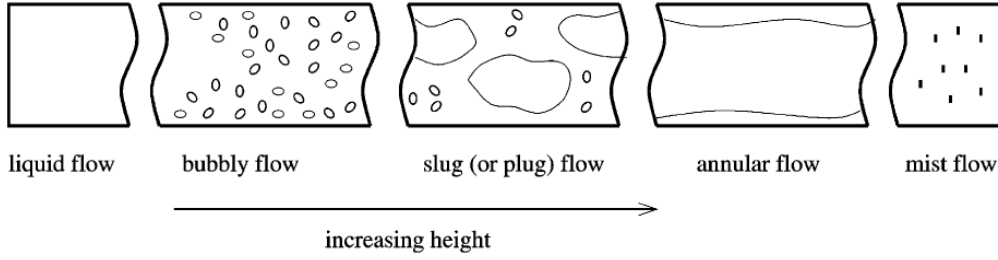


Figure 1.1: Two phase flow regimes on heat exchanger pipes.

to interfacial two-phase flows where large coherent regions of the two different phases coexist, separated by an interface which can deform. For gas-solid flows the situation is more straightforward, since solid particles cannot coalesce and change shape. However, many different regimes are still possible, depending on particle size, mass loading and flow configuration: we speak of particle-laden flows when we have discrete particles within a continuous flow of gas, or of fluidized beds when a gas is introduced into a vessel containing particles which, depending on the gas flow rate, can be suspended by the gas rising through the bed assuming different patterns. In this work we have studied particle-laden flows and bubbly-flows, which belong both to the category of dispersed flows. However, the approach can be completely different, depending mainly on the typical size of the dispersed phase. Namely a point-particle approximation can be possible for both cases if the diameter of the particle (bubble) is small, but even in this case the forces exerted by the continuous fluid on the dispersed phase are of different nature. Moreover, if a finite-size approach is adopted, secondary effects like shape deformation have to be accounted for in bubbly flows.

1.2.1 Particle-laden flows

In particle-laden flows a point-particle approximation can be done if the particle diameter is small compared to the smallest flow scale, i.e. the Kolmogorov scale η in turbulent flows. In this framework a Lagrangian description is more natural than an Eulerian one, and particles can be tracked according to the equations of particle motion derived by [Maxey 1983, Gatignol 1983] where the fluid forces on the sphere were calculated from the results of an unsteady Stokes flow:

$$\frac{d\mathbf{x}_p}{dt} = \mathbf{U}_p, \quad (1.8)$$

$$\begin{aligned}
\frac{d\mathbf{U}_p}{dt} = & \left(1 - \frac{\rho_f}{\rho_p}\right) \mathbf{g} + \frac{\mathbf{U}_s - \mathbf{U}_p}{\tau_p} (1 + 0.15 Re_p^{0.687}) \\
& + \frac{\rho_f}{\rho_p} \frac{D\mathbf{U}_p}{Dt} + C_L \frac{\rho_f}{\rho_p} [(\mathbf{U}_s - \mathbf{U}_p) \times \boldsymbol{\omega}] \\
& + \frac{9\mu}{d_p \rho_p \sqrt{\pi\nu}} \int_0^t \left(\frac{d\mathbf{U}_s}{dt} - \frac{d\mathbf{U}_p}{dt} \right) \frac{d\tau}{(t - \tau)^{0.5}} \\
& + \frac{\rho_f}{2\rho_p} \left(\frac{D\mathbf{U}_s}{Dt} - \frac{d\mathbf{U}_p}{dt} \right)
\end{aligned} \tag{1.9}$$

where \mathbf{U}_p is the particle velocity and \mathbf{U}_s is the fluid velocity at the particle position, namely the fluid velocity "seen" by the particle. Then ρ_f and ρ_p are the fluid and particle densities, d_p is the particle diameter, ν and μ are the kinematic and dynamic viscosities of the fluid, C_L is the lift coefficient and $\boldsymbol{\omega}$ is the vorticity of the fluid. Finally Re_p is the particle Reynolds number defined with the particle diameter as length scale and a characteristic velocity of the particle depending on the flow configuration, and τ_p is the characteristic time of the particle, defined by:

$$\tau_p = \frac{\rho_p d_p^2}{18\rho_f \nu}. \tag{1.10}$$

The first two terms on the right hand side of equation (1.9) are the Archimede force and the drag, while the other terms are in order the effect of the pressure gradient, the lift, the Basset term and the added mass term. The Archimede force accounts for the compensation of gravity by the particle's buoyancy. The Stokes drag force is due to the relative velocities between the particle and the fluid. The pressure gradient term is equivalent to the fluid particle acceleration at the center of mass, the lift is the transverse force present in a rotational fluid; the Basset term takes into account the history of particle motion, i.e. the interaction of a particle with its own wake, and finally the added mass is due to the displaced fluid caused by particle motion. As we will consider the case of heavy particles, so that the fluid density is order of magnitude lower than the particle density, the equation of the particle motion can be simplified further. It has been shown that with the assumption of $\rho_p/\rho_f \gg 1$ drag is the only significant force acting on the particle, so that the simplified equation that will be treated in this work is:

$$\frac{d\mathbf{U}_p}{dt} = \frac{\mathbf{U}_s - \mathbf{U}_p}{\tau_p} + \mathbf{g}. \tag{1.11}$$

One of the key features of particle-laden flows is the tendency of particles to concentrate non-uniformly in turbulent flows, with local regions of anomalously high or low concentrations [Eaton 1994, Balachandar 2010]. Figure 1.2, taken from [Pozorski 2009], shows the preferential concentration of particles in homogeneous isotropic turbulence (HIT) for different particle Stokes number, which is a non-dimensional number that compares the particle time-scale to a fluid time-scale (in this case the Kolmogorov time-scale, i.e. $St = \tau_p/\tau_\eta$). Particles sample different flow regions being captured or repulsed by turbulence structures depending on their inertia. In fact the dense particles cannot follow the instantaneous fluid flow streamlines so an individual particle does not necessarily remain with a given fluid element: if we imagine a heavy particle interacting with a vortex, we can expect the

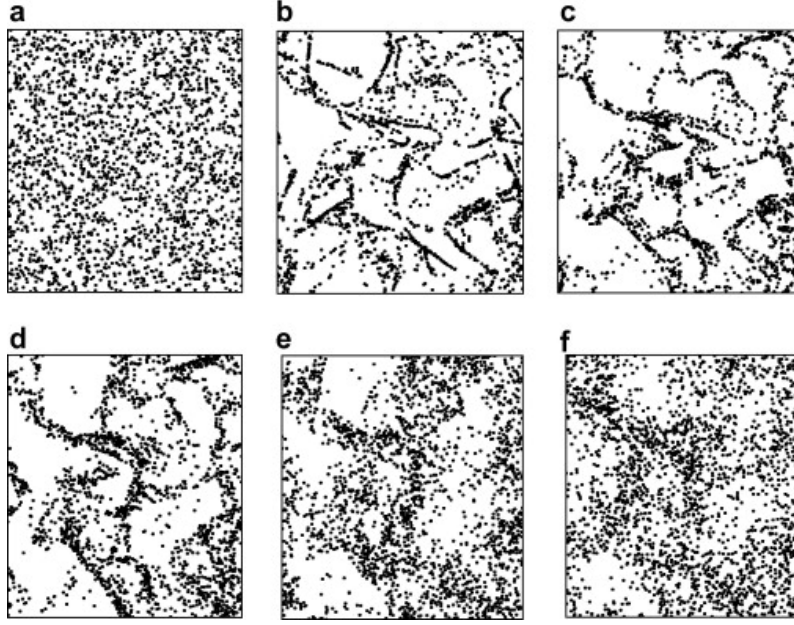


Figure 1.2: Particle preferential concentration: instantaneous particle positions obtained from particle tracking in a DNS for different Stokes number, based on the Kolmogorov time scale. (a) $St = 0.01$; (b) $St = 0.2$; (c) $St = 0.7$; (d) $St = 1$; (e) $St = 2$; (f) $St = 4$. Reprinted from [Pozorski 2009]

particle being thrown away by centrifugal forces, therefore accumulating in the surrounding regions of vortices, and in-between them. On the contrary, particles lighter than the fluid (gas bubbles in liquids) tend to remain trapped in the core low-pressure region of vortices. This physical mechanisms of preferential concentration is nowadays well understood in dilute flows, nevertheless it remains challenging to properly capture it with modeled equations, such as Reynolds-Average turbulence models or Large-Eddy simulations, where not all turbulence scales are resolved [Marchioli 2008b, Pozorski 2009].

It is worth remarking that equations (1.2),(1.11) are valid for dilute flows, i.e. when the volume fraction of the particle phase α_p is small, implying a mass loading $\varphi = (\alpha_p \rho_p)/(\alpha_f \rho_f) < 0.1$. Beyond this limit other effects need to be considered for both phases. In "moderately dense" suspensions two-way coupling between the phases starts to play a role, i.e. particles are felt by the fluid and the back-reaction should be taken into account in the NS equations (1.2). Experiments [Kulick 1994], Eulerian-Lagrangian [Sundaram 1999] and fully resolved calculations [Garcia-Villalba 2012] have shown that wakes generated by small and large particles could have a direct contribution to the turbulent kinetic energy production and dissipation even at low mass loading. For mass-loading of order one or larger the interphase coupling can modify the energy spectrum, leading to a scaling law $E(k) \propto k^{-4}$, that emerges at small scales where the particle forcing balances the viscous dissipation [Gualtieri 2017]. Going further into the "dense" regime, particle-particle collisions become crucial and should therefore be explicitly considered in equation (1.11). Vreman *et al.* [Vreman 2009] showed through simulations at high-mass loading, that particle collisions can deeply modify mean velocity and energy of both phases. Fi-

nally, at sufficiently high mass loading, particle clusters may spontaneously arise due to momentum coupling between the phases and generate and sustain turbulence in the fluid phase, referring to it as cluster-induced-turbulence (CIT) [Capecelatro 2015]. In this particular case, it has been also shown that separating the particle velocity in a correlated and an uncorrelated in space component can be crucial in turbulence modelling, allowing for instance to identify a different time-scale for collisions, which depend only on uncorrelated motion (granular temperature).

1.2.2 Bubbly flows

In bubbly flows the same Lagrangian point-particle approach described above is still possible, but usually consists in a bigger approximation with respect to solid particles. When such approach is adopted we should rather talk of light particles. In numerical simulations however this is still the only viable approach if we want to simulate a huge number of bubbles, in order to assess phenomena like preferential concentration [Spelt 1997, Tagawa 2012]. Not only bubble size, which is usually comparable or larger of the smallest fluid scales, but also their deformability and their complex dynamics cannot be described with such approach. Moreover, bubbles can coalesce and breakup, therefore changing not only their shape but also the size. In this work we do not consider the phases of nucleation, growth and collapse of bubbles [Blander 1975, Atchley 1989], but we will deal only with already formed bubbles which can only coalesce with other bubbles or breakup. In particular we consider gas bubbles dispersed in a liquid, rising under the effect of buoyancy.

In two fluids flows, therefore, the governing equations are the Navier-Stokes equations (1.1)-(1.2) in both fluids with different density and viscosity in the gas and in the liquid phase. A sharp interface separates the two fluids and determines a sudden change in their properties. For continuum scales we can safely assume that interfaces have vanishing thickness. Intermolecular forces, such as van der Waals forces that play an important role in interface physics are modelled by retaining the effect of surface tension. From a molecular point of view, surface tension arises because the interface is not an optimal region thermodynamically. From a mechanical point of view surface tension is simply a force per unit length acting parallel to the surface. It is then straightforward to show that in the Navier-Stokes equation of momentum a term must be added only where the interface is present, resulting in [Tryggvason 2011]:

$$\rho \frac{\partial U_i}{\partial t} + \rho U_j \frac{\partial U_i}{\partial x_j} = -\frac{\partial p}{\partial x_i} + \frac{\partial}{\partial x_j} (2\mu D_{ij}) + \rho f_i + \rho f_{\sigma i} \delta_s, \quad (1.12)$$

where $\delta_s = \delta_s(\mathbf{x} - \mathbf{x}_s)$ is a dirac delta function that identify the presence of the surface, $D_{ij} = (\partial U_i / \partial x_j + \partial U_j / \partial x_i) / 2$, and

$$\mathbf{f}_\sigma = \sigma \kappa \mathbf{n} + \nabla_s \sigma \quad (1.13)$$

is the surface force. The first term is the constant part, depending on the surface tension (a material property), the local curvature $\kappa = \nabla \cdot \mathbf{n}$ and the surface normal, while the last term is different from zero only if a non-constant surface tension is present. In practice the surface tension balance the jump in pressure across the interface and jump relations can

be derived analogously to shock waves. It is worth remarking that since the surface force acts in the plane of the surface, if we integrate it over the whole closed surface, it gives a null contribution.

Many physical parameters may characterise the problem, as the gas volume fraction, the size of bubbles, viscosities and densities of the two fluids, and so on. However, generally this kind of problems are described in terms of non-dimensional numbers. The rise of buoyant bubbles is governed by four non-dimensional groups. Two are the density and viscosity ratio of the two fluids, respectively ρ_b/ρ_l and μ_b/μ_l , where the subscript b indicates the bubble phase and l the continuum phase (liquid). For air bubbles in water, their values are of the order $\rho_b/\rho_l \simeq 10^{-3}$ and $\mu_b/\mu_l \simeq 10^{-2}$. The other two groups can be chosen among different possibilities, but usually in buoyancy driven bubbly flows the Galileo number Ga (or equivalently the Archimede number $Ar = \sqrt{Ga}$) and the Bond (or Eotvos) number are used, defined as:

$$Ga \equiv \frac{\rho_l |\rho_b - \rho_l| g d_b^3}{\mu_l^2}, \quad (1.14)$$

and

$$Bo \equiv \frac{|\rho_b - \rho_l| g d_b^2}{\sigma}. \quad (1.15)$$

Sometimes, especially in the chemical engineering literature, the Archimede number is replaced by the Morton number. The Archimede number is a Reynolds number defined *a priori* by using a velocity scale $\mathcal{U} = \sqrt{g d_b}$ based on the gravity acceleration and the bubble diameter, without the knowledge of the bubble velocity. The Bond number compares gravity with capillary forces.

The rise of a single buoyant bubble, as a function of Ar and Bo , is nowadays well understood [Clift 1978, Cano-Lozano 2016]. When Bo is low, meaning high surface tension or small bubble diameter, the bubble remain spherical as it rises. Increasing Bo the bubble can still remain spherical, in the case of low Ar (high viscosity), or change shape becoming first ellipsoidal and then skirted, but still with a straight path, for higher Ar . Increasing further Ar the wake of the deformed bubble may become unstable, determining a spiral, a planar zig-zag or a chaotic path, depending on the respective values of the non-dimensional groups. A summary of all possible bubble shapes [Clift 1978] and paths [Cano-Lozano 2016] are reported in Figures 1.3 - 1.4 obtained respectively from experiments and numerical simulations. In Figure 1.3 it is also given a graphical correlation between the Reynolds number, the Bond number and the Morton number, $Mo = Bo^3/Ar$. It has been shown that the departure of the bubble trajectory from a straight line is associated with the occurrence of a pair of counterrotating streamwise vortices for the case of a planar zig-zag path, and of a pair of intertwined counterrotating vortices for the case of an helical path. Despite this, the boundaries delimiting the different path regimes are not always in a perfect agreement between experiments and numerical simulations also because of the presence of surfactants in experiments that may alter the boundary conditions at the interface.

Swarms of buoyant rising bubbles have equally been studied in literature, both via experiments [Lance 1991, Riboux 2010, Alm  ras 2017] and numerical simulations [Esmaeeli 1999, Loisy 2017]. Firstly it has been pointed out that the mean bubble velocity is lower with respect to a single bubble, scaling with some exponential law of the

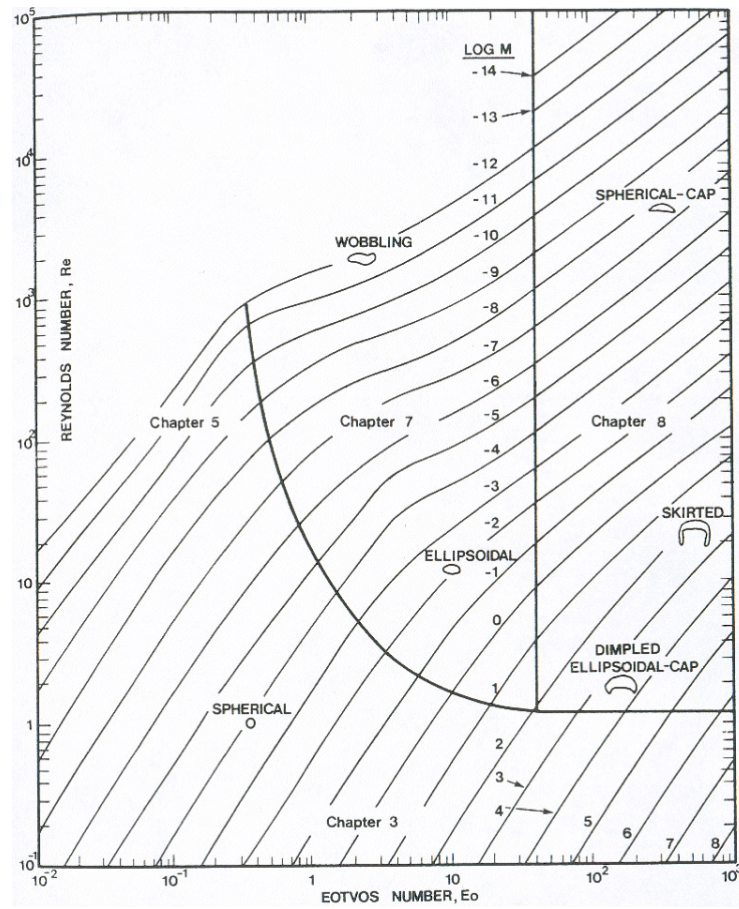


Figure 1.3: Phase diagram summarizing the different shapes of bubbles in experiments. Reprinted from [Clift 1978].

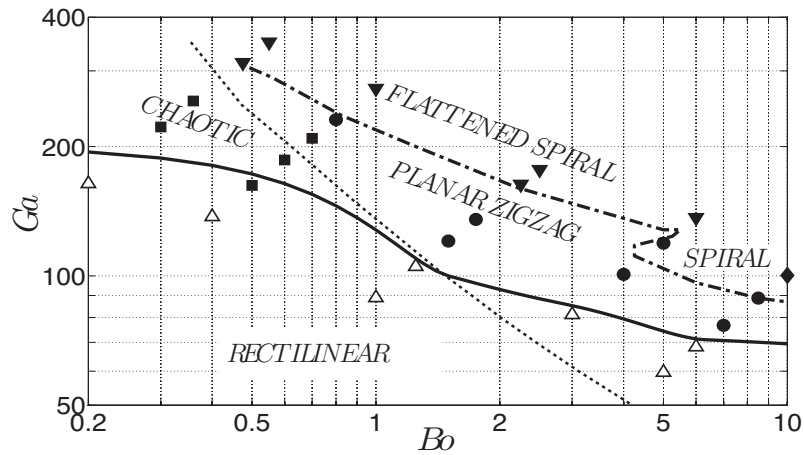


Figure 1.4: Phase diagram summarizing the different styles of path observed in numerical simulations (rectilinear, \triangle ; planar zigzag, \bullet ; flattened spiral, \blacktriangledown ; spiral (helical), \blacklozenge ; and chaotic, \blacksquare) Reprinted from [Cano-Lozano 2016].

volume fraction. Then the interaction with turbulence as well as the agitation generated in the wakes when rising in a quiescent liquid are just two examples of the variety of issues arising in those flows. In particular there is some evidence [Riboux 2010] that the spectral energy density evolves as the power of -3 of the wavenumber, recovering at small scales the classic $-5/3$ characterising turbulence.

To conclude this introductory part, let us say a word about models in multiphase flows. In numerical simulations, with the described continuum Eulerian formulation, only a few number of bubbles can be resolved at limited rising Reynolds number. Industrial-size multiphase flows must by necessity rely on statistical models, based on average equations. With an approach analogous to single-phase turbulent flows, average equations can be derived resulting in a two-fluid description: multiplying equation (1.12) by the bubble and the liquid volume fractions, respectively, give rise to separate average transport equations for the two fluids [Drew 1983, Ishii 1987, Zhang 1994]. As in the turbulence problem, the averaged equations have several unclosed terms which need to be modeled.

Methodology

In this section, a brief overview of all the methodologies used in this thesis is presented. Every problem that is addressed in this work is resolved through a numerical approach, therefore we will talk about the numerical methods to solve the equations of motions in each particular case, being them exact or modeled. First of all we summarise the methods and the approach used. The first part of the thesis on particle-laden flows is focused on modelling through a point-particle Lagrangian approach for the particle-phase and Eulerian Reynolds-Average Navier Stokes (RANS) / Large-Eddy simulations (LES) models for the fluid phase. In particular in dilute flows we have used a Lagrangian stochastic model for the particle phase, coupled with Large-Eddy models for the fluid phase. Moreover a comparison with direct-numerical simulations (DNS) data of Eulerian-Lagrangian simulations carried out in [Marchioli 2008b] has been done, post-processing already available data. In dense particle laden flows we have used a similar approach, coupling a Lagrangian stochastic model for particles, to Eulerian RANS equations for the fluid. However, albeit similar at a first glance, the stochastic models for the dilute and the dense case are rather different. In fact, the model used with LES is a model for the filtered density function of the velocity (FDF), while the one used with RANS is for the probability density function of the velocity (PDF). Hence, the first is related with filtered quantities, while the second with averaged ones. In the following we will talk mainly of the more "classical" PDF methods, since the formalism and the reasoning driving the FDF methods is analogous. By the way, more details on the filtered-density-function model we have used, can be found in chapter 3. Finally, bubbly flows have been investigated by means of direct numerical simulations, solving both the liquid and the gas separated by the bubble interface, using the Basilisk solver. Figure 2.1 shows a scheme of the various methodologies used in this thesis to emphasize the different levels of description that have been used. It should be clear how in the first part it has been possible to cover different techniques and methods, from the numerical experiment (DNS) to large-scale and statistical models, while in the second part, being the topic less advanced, we have focused on DNS to provide useful informations for future modelling works.

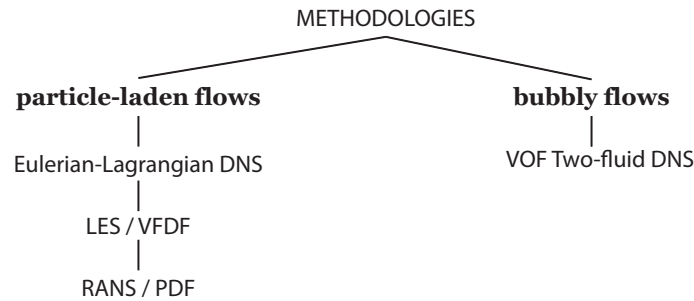


Figure 2.1: Summary of the methodologies used in the thesis.

2.1 Eulerian-Lagrangian DNS of turbulent particle-laden flows

This methodology refers to solving the Navier-Stokes equations for the fluid-phase and then using the fluid velocity field to evaluate the forces on the point-particle and track them according to equation (1.11). In particular we refer to direct-numerical simulation (DNS) when all the scales of the fluid are solved up to the Kolmogorov dissipative scale η . This is a huge problem when we consider turbulent flows at high Reynolds number since the dimension of the dissipative scales (η) and its characteristic time (τ_η) are related with Reynolds number by the Kolmogorov relations:

$$\eta/l_0 \sim Re_l^{-\frac{3}{4}} \quad (2.1)$$

$$\tau_\eta/\tau_0 \sim Re_l^{-\frac{1}{2}}, \quad (2.2)$$

where l_0 and τ_0 are the reference length- and time-scale of the problem. These relationships yields that the requirements on the grid spacing and on the computational time-step are roughly

$$\Delta_x, \Delta_y, \Delta_z \leq \eta \approx l_0 Re_l^{-\frac{3}{4}} \quad (2.3)$$

$$\frac{1}{\Delta_t} \geq f_k \approx \nu l_0^{-2} Re_l^{\frac{3}{2}} \quad (2.4)$$

Thus, because of the high number of scales to be solved, DNS of high Reynolds turbulent flows implies high computational costs and in many practical engineering cases is not possible. Moreover the computational requirements are also increased by the presence of the dispersed phase which is usually represented by a huge number of point particles ($\mathcal{O}(10^5)$) in order to have accurate statistics. Fortunately, in dilute flows (see chapter 3), two-way coupling between the phases is weak and can be neglected, hence, the two-phases can be simulated separately.

In the present work EL-DNS data have been used in the context of particle-laden dilute flows. Simulations were performed in [Marchioli 2008b], therefore we will say just a few words on the numerical code used. The fluid-phase is solved transforming field variables into wavenumber space through a pseudo-spectral incompressible flow solver that uses a Fourier-Galerkin method in the homogeneous directions and a Chebyshev-collocation method in the non-homogeneous direction. A two-level, explicit Adams-Bashfort scheme for the non-linear terms, and an implicit Crank-Nicholson scheme for the viscous terms are employed for time advancement. On the other hand the time advancement of the equations of particle motion is done through a Runge-Kutta fourth order scheme and the fluid velocity is evaluated at the particle position through a second-order interpolation for the estimation of the drag force. More details can be found in [Marchioli 2002].

2.2 LES of turbulent particle-laden flows

A less accurate approach, for the solution of Navier-Stokes equations is the so called Large Eddy Simulation or LES. In large-eddy simulation, the larger three-dimensional unsteady

turbulent motions are directly represented, whereas the effects of the smaller scale motions are modeled. Nearly all of the computational effort in DNS is expended on the smallest, dissipative motions, whereas the energy and anisotropy are contained predominantly in the larger scales.

In LES, the dynamics of large scales (which are affected by the flow geometry and are not universal) are computed explicitly, the influence of the smaller scales (which have, to some extent, a universal character) being represented by simple models. Thus, compared with DNS, the vast computational cost of explicitly representing the small fluctuations is avoided.

If we introduce a filtering operator, [Pope 2000]

$$\tilde{U}(\mathbf{x}, t) = \int_{\Omega} G(\mathbf{r}, \mathbf{x}) U(\mathbf{x} - \mathbf{r}, t) d\mathbf{r}, \quad (2.5)$$

where Ω is the flow domain, $G(\mathbf{r}, \mathbf{x})$ the filter function and $U(\mathbf{x}, t)$ the quantity that has to be filtered, we can decompose the velocity $\mathbf{U}(\mathbf{x}, t)$ into the sum of a filtered (or resolved) component $\tilde{\mathbf{U}}(\mathbf{x}, t)$ and a residual (or subgrid-scale) component $\mathbf{u}'(\mathbf{x}, t)$. In this case $\tilde{\mathbf{U}}(\mathbf{x}, t)$ (three dimensional and time dependent) represent the motion of the large eddies.

If we consider a filter operator $\tilde{\cdot}$ that decompose a generic quantity in filtered and residual, the filtered continuity and Navier-Stokes equations can be rewritten as follows:

$$\frac{\partial \tilde{U}_j}{\partial x_j} = 0, \quad (2.6)$$

$$\frac{\partial \tilde{U}_i}{\partial t} + \tilde{U}_j \frac{\partial \tilde{U}_i}{\partial x_j} = -\frac{1}{\rho} \frac{\partial \tilde{p}}{\partial x_i} + \nu \frac{\partial^2 \tilde{U}_i}{\partial x_j \partial x_j} - \frac{\partial \tau_{ij}}{\partial x_j}. \quad (2.7)$$

where $\tau_{ij} = \widetilde{U_i U_j} - \tilde{U}_i \tilde{U}_j$ is the SGS stress term that must be modeled to close the equation. The closure problem is one of the central problems in LES. The most commonly used SGS models are the Smagorinsky model and its variants. They model the unresolved turbulent scales, in analogy with the Bousinnesq hypothesis, through the addition of an eddy viscosity into the governing equations. The basic formulation of the Smagorinsky model [Smagorinsky 1963] is:

$$\tau_{ij} - \frac{\delta_{ij}}{3} \tau_{kk} = -2\nu_T \tilde{S}_{ij} \quad (2.8)$$

where:

$$\tilde{S}_{ij} = \frac{1}{2} \left(\frac{\partial \tilde{U}_i}{\partial x_j} + \frac{\partial \tilde{U}_j}{\partial x_i} \right) \quad (2.9)$$

is an entry of the strain rate tensor and the eddy viscosity ν_t is calculated as:

$$\nu_T = (C_s \Delta_g)^2 \sqrt{2 \tilde{S}_{ij} \tilde{S}_{ij}} \quad (2.10)$$

where Δ_g is the grid size and C_s is a constant. Many techniques have been developed to calculate C_s . Some models use a static value for C_s , often calculated from experiments of similar flows to those being modeled. Other models dynamically calculate C_s (dynamic Germano model [Germano 1992]) as a function of space and time. In some cases, as

usually happen in two-phase flow LES, the SGS term is completely neglected with the assumption that the long term behaviour of heavy particles is merely affected by the large scale structures.

Most commonly the filter used is defined in the spectral space as in the case of spectral or pseudo-spectral codes, so that it operate a cut-off of the highest wave numbers as follows:

$$\hat{G}_\alpha(k) = \begin{cases} 1 & \text{if } -\pi/\Delta_\alpha \leq k \leq \pi/\Delta_\alpha \\ 0 & \text{otherwise} \end{cases} \quad (2.11)$$

In the present work the numerical scheme used for LES simulations is the same as the one used in DNS, being an adaptation of the same numerical code. Particles are tracked again with a Runge-Kutta fourth order scheme and using the filtered fluid velocity at the particle position for the estimation of the drag force. It is worth remarking that if no subgrid model is used for the particle phase, this approach will result in wrong estimation of particle trajectories due to several sources of error: among them, the most important are the error in the estimation of the drag due to the fact that only the filtered velocity is available (differently to DNS), and the error in the estimation of the filtered velocity itself due to the model used for the closure. More details on this approach will be given in chapter 3.

2.3 RANS of turbulent particle-laden flows

RANS models are the lower order models in terms of computational costs and accuracy in the hierarchy DNS - LES - RANS, yet the most widely used in practical applications. As outlined in section 1.1.1 a statistical description of turbulent flows is straightforward due to their chaotic nature. Introducing a probability density function of the velocity field let us separate the velocity field in an average part and a fluctuation, for every position and time. Moreover the averaging concept can be applied directly to the transport equations of mass and momentum resulting in a set of Reynolds-averaged unclosed equations. In this thesis we have used Reynolds-stress models, i.e. a model has been introduced in the Reynolds-stress equations. This means that in the most general situation we have to solve a set of ten equations: the conservation of mass, the three component of the mean momentum equations, and six equations for the Reynolds-stress transport. An additional scalar equation for the transport of the dissipation ε has also to be introduced to close completely the system. In literature there are several RANS models for single-phase flows of different accuracy and complexity [Pope 2000]. In order of increasing complexity, the most widely used are the Rotta model, the Launder-Reece-Rodi for isotropisation of production (LRR-IP) model [Launder 1975] and elliptic relaxation models [Durbin 1991]. All models are constructed starting from the exact averaged transport equations already introduced in section 1.1.1. The transport of mean momentum, eq. (1.6) does not raise any problem, since the only unknowns it contains are the mean velocity, the given mean pressure and the Reynolds stresses. On the other hand, the exact transport equation of the Reynolds stresses, eq. (1.7), need to be modeled. Namely, the Rotta model, based on experimental evidence, consists in a redistribution term in place of the pressure-rate-of strain term, of the form:

$$\mathcal{R}_{ij} = -C_R \frac{\varepsilon}{k} (\langle u_i u_j \rangle - \frac{3}{2} k \delta_{ij}), \quad (2.12)$$

where C_R is the Rotta constant. Analogously the LRR-IP model consists in the same term with the addition of a redistribution of production. The transport term \mathcal{T} is treated in the same way in the different models, through the decomposition:

$$\mathcal{T}_{kij} = -\nu \frac{\partial \langle u_i u_j \rangle}{\partial x_k} + \frac{2}{3} \delta_{ij} \frac{\langle u_k p' \rangle}{\rho} + \langle u_i u_j u_k \rangle = \mathcal{T}_{kij}^{(v)} + \mathcal{T}_{kij}^{(p')} + \mathcal{T}_{kij}^{(u)}. \quad (2.13)$$

The viscous transport is already in closed form, while the pressure transport and turbulent convection are usually closed through gradient-diffusion models. For instance, we have adopted the model of Daly and Harlow [Daly 1970] which uses the Reynolds-stress tensor to define an anisotropic diffusion coefficient:

$$\mathcal{T}'_{kij} = -C_S \frac{k}{\varepsilon} \langle u_k u_l \rangle \frac{\partial \langle u_i u_j \rangle}{\partial x_l} \quad (2.14)$$

where C_S is a model constant. Finally, the dissipation tensor, at high Reynolds number and away from the walls, is taken to be isotropic:

$$\varepsilon_{ij} = \frac{2}{3} \varepsilon \delta_{ij}. \quad (2.15)$$

It is worth adding that in presence of walls that limit the flow, the basic Reynolds-stress turbulence models need to be modified using damping functions and anisotropic dissipation tensors [Pope 2000].

The standard model equation for the dissipation ε used in Reynolds-stress models is that proposed by Hanjalic and Launder [Hanjalić 1972]:

$$\frac{D\varepsilon}{Dt} = \frac{\partial}{\partial x_i} \left(C_\varepsilon \frac{k}{\varepsilon} \langle u_i u_j \rangle \frac{\partial \varepsilon}{\partial x_j} \right) + C_{\varepsilon 1} \frac{\mathcal{P}\varepsilon}{k} - C_{\varepsilon 2} \frac{\varepsilon^2}{k}, \quad (2.16)$$

with $C_\varepsilon = 0.15$, $C_{\varepsilon 1} = 1.44$ and $C_{\varepsilon 2} = 1.92$.

In this section we have briefly given an overview of standard RANS models used in single phase flows to give the main tools to understand following sections. In particular, in chapter 4, these models will be used as basis to build Reynolds-averaged models for dense two-phase flows, i.e. where the dispersed particles have an effect on the fluid phase (and therefore on its transport equations).

2.4 PDF methods

This class of methods provide an alternative approach to turbulence, yet still in the context of statistical methods. Instead of modelling directly the fluid-phase averaged equations, one can work on the PDF which is used for the evaluation of means as statistical moments. This results in mesoscopic models which lie between the DNS/LES and RANS.

As every statistical system, the dynamics of the PDF of a turbulent flow can be described by a proper transport equation. In general terms one can always state a duality between the deterministic description of the chaotic system and its PDF, namely, if we consider as observable the velocity of a fluid particle, its dynamics will be given by:

$$\frac{D\mathbf{U}}{Dt} = \mathbf{A}(\mathbf{x}, \mathbf{U}) \quad (2.17)$$

and the respective PDF $f(\mathbf{V}; \mathbf{x}, t)$ will be described by:

$$\frac{\partial f}{\partial t} + V_i \frac{\partial f}{\partial x_i} = - \frac{\partial}{\partial V_i} \left(f \langle \mathbf{A} | \mathbf{V} \rangle \right), \quad (2.18)$$

which is called Liouville equation. The same problem of the other modelling approaches to turbulence arises, i.e. an higher order term (the acceleration, \mathbf{A}) is involved and equation (2.18) is unclosed. Usually the Lagrangian approach is preferred because is more straightforward to understand and to be solved numerically. In fact the outcome is the same, we solve the Eulerian transport equation of a PDF or the Lagrangian stochastic equations of the statistical particles related to it through a Monte-Carlo simulation. The average quantities of interest can then be obtained by means of statistical moments or ensemble averages, respectively. The simpler possible model is the Langevin equation, which is a stochastic differential equation of the form:

$$dU(t) = \gamma U(t) + K(t) \quad (2.19)$$

where $K(t)$ is a Gaussian stochastic process ($\langle K(t) \rangle = 0$, $\langle K(t)^2 \rangle = \Gamma$) which is decorrelated at different times ($\langle K(t)K(t') \rangle = 0$ for $t \neq t'$). Equation (2.19) can be solved as an initial value problem:

$$U(t) = U_0 \exp(-\gamma t) + \exp(-\gamma t) \int_0^t \exp(\gamma s) K(s) ds. \quad (2.20)$$

Using the properties of the stochastic process $K(t)$ the mean autocovariance is found to be

$$R(\tau) \equiv \langle U(t)U(t+\tau) \rangle = \frac{\Gamma}{2\gamma} \exp(-\gamma\tau) \quad \text{in the limit of } t \rightarrow \infty. \quad (2.21)$$

The Lagrangian integral time-scale is defined with the autocorrelation function $\rho(\tau) = R(\tau)/\langle U(t)^2 \rangle$, as

$$T_L \equiv \int_0^\infty \rho(\tau) d\tau = -\frac{1}{\gamma}. \quad (2.22)$$

In homogeneous isotropic turbulence (HIT), in order to have a constant turbulent kinetic energy, it must be

$$\Gamma = \frac{2\sigma^2}{T_L} \quad (2.23)$$

with $\sigma^2 = 2/3k$. Therefore the Langevin equation (2.19) can be recast in the form

$$dU(t) = -\frac{U(t)}{T_L} dt + \left(\frac{2\sigma^2}{T_L} \right)^{(1/2)} dW(t), \quad (2.24)$$

where $W(t)$ is a normalised Gaussian process (zero mean, unit variance) called a Wiener process.

The scaling of Kolmogorov theory can be applied to this model by considering the second order Lagrangian structure function $S_2^L(\tau) = \langle [U(t+\tau) - U(t)]^2 \rangle$ in the inertial-range timescales:

$$S_2^L(\tau) = C_0 \varepsilon \tau \quad \text{for } \tau_\eta \ll \tau \ll T_L, \quad (2.25)$$

where \mathcal{C}_0 is a universal constant; whereas the Langevin model gives

$$S_2^L(\tau) = \frac{2\sigma^2}{T_L} \tau. \quad (2.26)$$

Therefore the Langevin equation is consistent with the Kolmogorov hypothesis of a linear dependence of $S_2^L(\tau)$ on τ , and the inverse of the Lagrangian time-scale can be expressed as

$$T_L^{-1} = \frac{3}{4} C_0 \frac{\varepsilon}{k}, \quad (2.27)$$

where C_0 is a model constant not necessarily equal to \mathcal{C}_0 . The final form of the Langevin model in HIT will be:

$$dU(t) = -\frac{3}{4} C_0 \frac{\varepsilon}{k} U(t) dt + (C_0 \varepsilon)^{(1/2)} dW(t). \quad (2.28)$$

This form of the Langevin equation has been the foundation of the Lagrangian stochastic modelling of turbulence. This model has several important limitations, which have been addressed with a wide variety of approaches. The nature of these approaches depends on the model application and the specific statistical results sought, e.g. models used to predict pollution in the atmospheric boundary layer have different requirements than the models used to predict mixing of chemical species in an engineering application. The literature regarding Lagrangian stochastic models in turbulence is vast [Pope 2000], and a complete summary is not attempted here. It is worth remarking that each stochastic Lagrangian model has as counterpart a corresponding PDF equation, e.g. the Fokker-Planck equation for the Langevin model, and consequently corresponds to a precise Reynolds-stress model [Pope 1994b].

This brief description of PDF methods and of the derivation of the basic Langevin equation for turbulent flows, was aimed just introducing those concepts for those who are not familiar with. In this work this approach has been used to model particle-laden flows in those cases where the fluid-phase is not resolved through a DNS but with some modeled equations, e.g. RANS or LES (see chapters 3-4). Indeed a stochastic model can be sought to reintroduce the correct amount of fluctuations that have been lost with the averaging or filtering of the fluid velocity.

In literature different models have been proposed for this purpose [Minier 2001, Pozorski 2009] conceived for dilute flows. For our work focused on particles, a starting point was the model proposed for dilute flows which consisted in adding a stochastic equation that describe the fluid velocity seen by the particle, U_s , to equation 1.11, as follows:

$$dU_{p,i} = \frac{U_{s,i} - U_{p,i}}{\tau_p} dt + g_i dt \quad (2.29)$$

$$\begin{aligned} dU_{s,i} = & -\frac{1}{\rho_f} \frac{\partial \langle p_f \rangle}{\partial x_i} dt + (\langle U_{p,j} \rangle - \langle U_{f,j} \rangle) \frac{\partial \langle U_{f,i} \rangle}{\partial x_j} dt + \frac{1}{T_{L,i}^*} (U_{s,i} - \langle U_{f,i} \rangle) dt \\ & + g_i dt + \left[\varepsilon_f \left(C_0 b_i \frac{\tilde{k}_f}{k_f} + \frac{2}{3} \left(b_i \frac{\tilde{k}_f}{k_f} - 1 \right) \right) \right]^{1/2} dW_{s,i}. \end{aligned} \quad (2.30)$$

where $\langle U_f \rangle$, $\langle p_f \rangle$, k_f and ε_f are respectively the mean velocity, pressure, turbulent kinetic energy and dissipation obtained from the resolved fluid-phase RANS equations. T_L^* and

\tilde{k}_f are a modified time-scale and kinetic energy to take into account particle inertia. For more details on all terms see [Minier 2001]. It is clear how the model is an extension of the Generalised-Langevin-Model (GLM) [Pope 2000] for single-phase flows, with a different Lagrangian time-scale, which appears in the drift term (third term on r.h.s in eq. (2.30)) and indirectly in the diffusion coefficient (last term on r.h.s in eq. (2.30)), and an additional term to model the crossing trajectory effect between fluid and inertial particles. Indeed, the fact that an element ideally attached to an inertial particle has a different dynamics with respect to a fluid particle is modeled in two different steps. Firstly, the inertia of the particle, namely τ_p , is taken into account in the Lagrangian time-scale, varying the fluid time-scale T_L by a coefficient which depends on particle inertia: in the limit of vanishing inertia it will give $T_L^* \rightarrow T_L$ since particles behave like tracers, whereas in the limit of high inertia it will tend to the fluid Eulerian time-scale $T_L^* \rightarrow T_E$ since particles are nearly at a stand-still with respect to fluid elements. Secondly, it is taken into account the possible mean drift between fluid and particles due to external forces, e.g. gravity.

Taking this model as a reference, we have extended it to dense flows in chapter 4, and we have derived a new model for the filtered-density-function (to be used with LES in dilute flows) in chapter 3. It is worth mentioning that numerical schemes for stochastic equations are not trivial and classical schemes for ordinary differential equations cannot be used because of the presence of noise terms. A detailed description of the numerical schemes used is given in each chapter.

2.5 DNS of bubbly flows

As outlined in section 1.2.2 the approach we have adopted for the solution of bubbly flows is to consider the two fluids as continuum with different density and viscosity, separated by a sharp interface which results in a sudden change of the fluid characteristics. With this type of approach the two fluid have to be solved up to the smallest scales, i.e. the Kolmogorov scale if turbulence is present. In any case, even if turbulence is not present, the requirements on the grid spacing might be very strict, dictated by the necessity to reconstruct accurately the geometry of the bubble surface. The key point with respect to standard single-phase DNS is the reconstruction and the advection of the interface. The two fluids are generally identified using a marker function that takes different values in the different fluids. As the fluids move, and the interface change location, the marker function must be updated. Different methods have been proposed in literature, which include the Volume-of-fluid (VOF) method, the level-set, the phase-field and the CIP. An alternative approach can be that of tracking directly the boundary between the different fluids using marker points, and reconstructing the marker function from the location of the interface. These methods are usually referred as front-tracking methods. In this thesis we have make use of the Basilisk code which relies on the VOF method constructed on regular or adaptive Eulerian grids. It is worth remarking that VOF methods have some advantages with respect to the others and in particular to the front-tracking ones: (i) they preserve mass in a natural way; (ii) changes of topology as breakups or coalescences are implicit in the algorithm.

In the following we will present briefly the numerical schemes of which we have make use within the Basilisk solver.

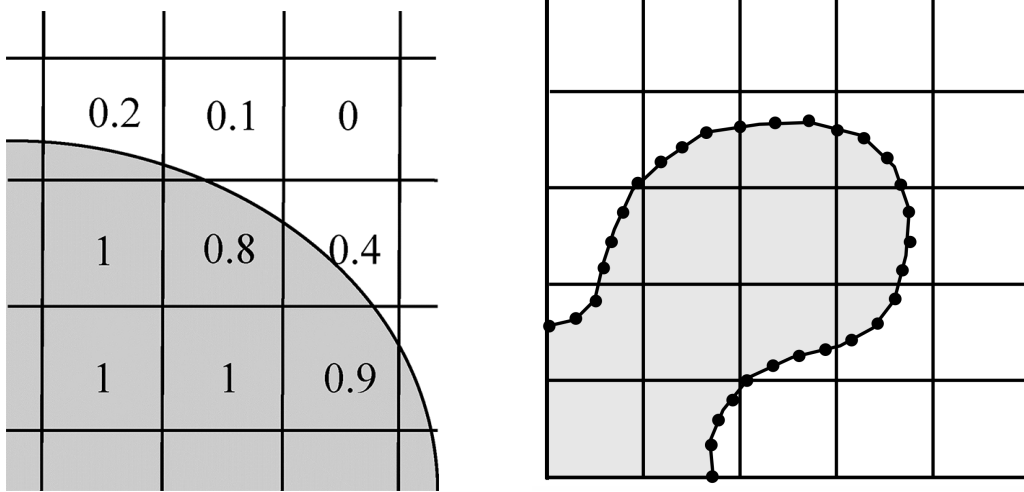


Figure 2.2: A sketch of the VOF function representation in Eulerian method and of the front-tracking Lagrangian markers for the interface advection

2.5.1 Basilisk code

Basilisk (<http://basilisk.fr>) is an ensemble of solver-blocks written using an extension to the C programming language, called Basilisk C, useful to write discretisation schemes in Cartesian grids. Instead of writing an entirely new code, existing blocks of code were combined to solve Navier-Stokes equations with two fluids. As anticipated in section 1.2.2, the incompressible, variable-density, Navier-Stokes equations with surface-tension are

$$\rho \left(\frac{\partial U_i}{\partial t} + U_j \frac{\partial U_i}{\partial x_j} \right) = - \frac{\partial p}{\partial x_i} + \frac{\partial 2\mu D_{ij}}{\partial x_j} + f_i + \sigma \kappa \delta_s n_i, \quad (2.31)$$

$$\frac{\partial \rho}{\partial t} + \frac{\partial \rho U_i}{\partial x_i} = 0, \quad (2.32)$$

$$\frac{\partial U_i}{\partial x_i} = 0, \quad (2.33)$$

where $D_{ij} = (\partial_j U_i + \partial_i U_j)/2$. For two-phase flows we can introduce the volume fraction f of the first fluid and define the two densities and viscosities as

$$\rho(f) = f\rho_1 + (1-f)\rho_2, \quad (2.34)$$

$$\mu(f) = f\mu_1 + (1-f)\mu_2, \quad (2.35)$$

where ρ_1, ρ_2 and μ_1, μ_2 are the densities and viscosities of the first and second fluid. The time discretisation is staggered in time for the volume fraction/density and pressure, reult-

ing in a second-order accurate time scheme:

$$\rho^{n+\frac{1}{2}} \left[\frac{U_i^{n+1} - U_i^n}{\Delta t} + U_j^{n+\frac{1}{2}} \frac{\partial U_i^{n+\frac{1}{2}}}{\partial x_j} \right] = -\frac{\partial p^{n+\frac{1}{2}}}{\partial x_i} + \frac{\partial}{\partial x_j} [\mu^{n+\frac{1}{2}} (D_{ij}^n + D_{ij}^{n+1})] + (\sigma \kappa \delta_s n_i)^{n+\frac{1}{2}}, \quad (2.36)$$

$$\frac{c^{n+\frac{1}{2}} - c^{n-\frac{1}{2}}}{\Delta t} + \frac{\partial}{\partial x_i} (c^n U_i^n) = 0, \quad (2.37)$$

$$\frac{\partial}{\partial x_i} U_i^n = 0. \quad (2.38)$$

The system is then further simplified using a time-splitting projection method

$$\rho^{n+\frac{1}{2}} \left[\frac{U_i^* - U_i^n}{\Delta t} + U_j^{n+\frac{1}{2}} \frac{\partial U_i^{n+\frac{1}{2}}}{\partial x_j} \right] = -\frac{\partial p^{n+\frac{1}{2}}}{\partial x_i} + \frac{\partial}{\partial x_j} [\mu^{n+\frac{1}{2}} (D_{ij}^n + D_{ij}^*)] + (\sigma \kappa \delta_s n_i)^{n+\frac{1}{2}}, \quad (2.39)$$

$$U_i^{n+1} = U_i^* - \frac{\Delta t}{\rho^{n+\frac{1}{2}}} \frac{\partial p^{n+\frac{1}{2}}}{\partial x_i}, \quad (2.40)$$

$$\frac{\partial}{\partial x_i} U_i^{n+1} = 0, \quad (2.41)$$

which requires the solution of the Poisson equation

$$\frac{\partial}{\partial x_i} \left[\frac{\Delta t}{\rho^{n+\frac{1}{2}}} \frac{\partial p^{n+\frac{1}{2}}}{\partial x_i} \right] = \frac{\partial U_i^*}{\partial x_i} \quad (2.42)$$

in order to verify the incompressibility relation

$$\frac{\partial}{\partial x_i} U_i^{n+1} = 0. \quad (2.43)$$

This problem is solved using the multi-level Poisson-Helmholtz solver, once the advection term is provided. The spatial discretisation is done with a finite volume centered method and the advection term $U_i^{n+\frac{1}{2}} \partial(U_i^{n+\frac{1}{2}})/\partial x_j$ is estimated using the Bell-Colella-Glaz second-order unsplit upwind scheme. A regular cartesian multilevel grid can be used as well as an adaptive quadtree/octree grid [Popinet 2009], see figure 2.3.

2.5.1.1 Volume-of-fluid advection scheme

To solve the advection equation (2.37) for the volume fraction Basilisk uses a piecewise-linear geometrical Volume-Of-Fluid (VOF) scheme [Scardovelli 1999] generalised for the quad/octree spatial discretisation. The two steps of the geometrical VOF schemes are (i) the interface reconstruction, and (ii) the geometrical flux computation and interface advection.

In piecewise-linear interface construction (PLIC) methods the interface is approximated by a local segment of equation

$$\mathbf{m} \cdot \mathbf{x} = m_x x + m_y y = \alpha, \quad (2.44)$$

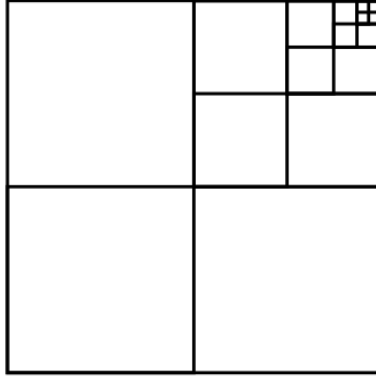


Figure 2.3: A sketch of the quadtree grid structure with adaptive refinement.

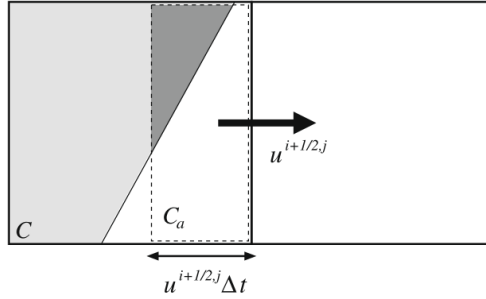


Figure 2.4: Geometrical flux estimation.

where x and y are the local axis of the cell under consideration. Firstly the normal \mathbf{m} is determined with the volume fraction in the cell and in the neighbouring ones using the Mixed-Youngs-Centered scheme [Aulisa 2007], which chose the best approximation between the Central and the Young schemes. Then, the interface line (2.44) is moved along the normal by changing α to obtain the desired volume fraction. Using geometrical arguments, e.g. the symmetry of a Cartesian cell, it is possible to find α without the need of an iterative procedure [Tryggvason 2011].

For the advection of the interface the geometrical flux is evaluated through an Eulerian-split method that evaluates the upwind flux of volume leaving the cell for the solution of equation (2.37). The principle of geometrical flux estimation is illustrated in figure 2.4.

2.5.1.2 Surface tension

The surface tension term in (2.39) is approximated with the continuum-surface-force (CSF) approach of Brackbill [Brackbill 1992] as follows:

$$\sigma \kappa \delta_s \mathbf{n} \approx \sigma \kappa \nabla f, \quad (2.45)$$

This approach is known to suffer from problematic parasitic currents when applied to the case of a stationary droplet in theoretical equilibrium with certain implementations of

the CSF scheme, e.g. with staggered discretisations (velocity and pressure field on shifted grids). This inconvenience has been avoided in Basilisk with the use of a collocated scheme to ensure a correct force-surface tension balance.

Estimating curvature has traditionally been the major challenge for Volume-Of-Fluid schemes. For this reason many recommend level-set, coupled VOF/level-set or front-tracking schemes as alternatives. In Basilisk a height function curvature calculation is used, which has been shown to give practical estimates of the curvature which are comparable in accuracy to estimates obtained using the differentiation of exact level-set functions. The algorithm consists in: (i) evaluating the best alignment of the stencil (horizontal or vertical) based on the direction of the normal to the interface; (ii) building a discrete approximation of the interface height $y = h(x)$ (resp. $x = h(y)$) by summing the volume fractions in each columns (resp. line); (iii) using finite-difference approximations of the derivatives of the discretised height-function to compute the curvature:

$$\kappa = \frac{h''}{(1 + h'^2)^{3/2}} \Big|_{x=0} . \quad (2.46)$$

All the algorithms that have been presented, have been generalised for a use with quad/octree grids. For more details on the numerical schemes see [Popinet 2009] and <http://basilisk.fr>.

Part II

Particle-laden flows

Lagrangian filtered density function for LES-based stochastic modelling of turbulent particle-laden flows

A. Innocenti^{1,2}, C. Marchioli³, S. Chibbaro¹

¹ Sorbonne Université, CNRS, Institut Jean Le Rond d'Alembert, F-75005 Paris, France

² Dipartimento di Ingegneria Civile e Industriale, Università di Pisa, Via G. Caruso 8,
56122 Pisa, Italia

³ Dipartimento Politecnico di Ingegneria e Architettura, Università di Udine, 33100
Udine, Italy

Published on *Physics of Fluids* 28.11 (2016): 115106.

This chapter is the result of a joint work with the University of Udine and is reported here as it appears in the journal *Physics of Fluids*. We tackle here the problem of particle dispersion in dilute flows before moving to dense flows in next chapters. The motion of inertial particle in turbulence is well understood nowadays and in literature there are many works on the subject. The point-particle approach is the most regularly used, but fluid models like LES or RANS still lack in the predictions of relevant quantities. Therefore we have proposed and assessed a stochastic model for particle-laden flows in a Large-Eddy Simulation (LES) context in a non-homogeneous application. In the framework of the thesis the objective was to see if in Eulerian-Lagrangian simulations, stochastic models can constitute a viable approach for the reconstruction of the lost fluid-phase fluctuations after averaging or filtering. We have put particular emphasis on the phenomenon of particle preferential concentration, which generates clustering and accumulation in the near wall region of a turbulent channel flow, and that can be crucial in many practical applications. Indeed, it is well known that when inertial particles are tracked within a LES flow field, the phenomenon of particle accumulation near to the wall is very often underestimated. With the present model, that aim at reconstructing the fluid-phase fluctuations, we show that we are able to recover in most cases DNS accuracy for the velocity statistics and particle concentration.

We think that a complete comprehension of the physics behind particle dispersion in turbulence is fundamental before moving to more complex regimes where the turbulence is modified by the presence of particles and collisions might be present. For this reason,

this first part of the thesis has constituted an important step in view of the following developments.

Abstract: The Eulerian-Lagrangian approach based on Large-Eddy Simulation (LES) is one of the most promising and viable numerical tools to study particle-laden turbulent flows when the computational cost of Direct Numerical Simulation (DNS) becomes too expensive. The applicability of this approach is however limited if the effects of the Sub-Grid Scales (SGS) of the flow on particle dynamics are neglected. In this paper, we propose to take these effects into account by means of a Lagrangian stochastic SGS model for the equations of particle motion. The model extends to particle-laden flows the velocity-filtered density function method originally developed for reactive flows. The underlying filtered density function is simulated through a Lagrangian Monte Carlo procedure that solves a set of Stochastic Differential Equations (SDEs) along individual particle trajectories. The resulting model is tested for the reference case of turbulent channel flow, using a hybrid algorithm in which the fluid velocity field is provided by LES and then used to advance the SDEs in time. The model consistency is assessed in the limit of particles with zero inertia, when “duplicate fields” are available from both the Eulerian LES and the Lagrangian tracking. Tests with inertial particles were performed to examine the capability of the model to capture particle preferential concentration and near-wall segregation. Upon comparison with DNS-based statistics, our results show improved accuracy and considerably reduced errors with respect to the case in which no SGS model is used in the equations of particle motion.

3.1 Introduction

Over the past decades major modelling efforts have been devoted to the prediction of single-phase turbulent flows by means of Large Eddy Simulation (LES) [Rogallo 1984, Sagaut 2006, Lesieur 2005]. The pioneering model was developed by Smagorinsky [Smagorinsky 1963], based on an eddy viscosity closure that relates the unknown Sub-Grid Scale (SGS) stresses to the strain rate of the large flow scales to mimic the dissipative behavior of the unresolved flow scales. Subsequent extensions to dynamic [Germano 1991, Germano 1992] or stochastic models [Zamansky 2013] have improved the quality and reliability of LES, especially for cases where mass, heat and momentum transfer are controlled by the large scales of the flow. Much work has been done also to improve the applicability of LES to chemically-reacting turbulent flows [Fox 2003, Pope 2013] and, more recently, to dispersed turbulent flows [Fox 2012]. The first LES of particle-laden flow, in particular, was performed under the assumption of negligible contribution of the SGS fluctuations to the filtered fluid velocity seen by inertial particles [Armenio 1999]: The choice was justified considering that inertial particles act as low-pass filters that respond selectively to removal of SGS flow scales according to a characteristic frequency proportional to $1/\tau_p$, where τ_p is the particle relaxation time (a measure of particle inertia). The same assumption has been used in other studies [Yamamoto 2001, Vance 2006, Dritselis 2011, Afkhami 2015] in which the filtering due to particle inertia and the moderate Reynolds number of the flow had a relatively weak effect on the (one-particle, two-particles) dispersion statistics examined. However, several studies [Kuerten 2006, Marchioli 2008b, Calzavarini 2011] have demonstrated that neglecting the effect of SGS velocity fluctuations on particle motion leads to significant errors in the quantification of large-scale clustering and preferential concentration, two macroscopic

phenomena that result from particle preferential distribution at the periphery of strong vortical regions into low-strain regions [Fessler 1994, Wang 1993b, Rouson 2001]. It is now well known that LES without SGS modelling for the dispersed phase is bound to underestimate preferential concentration and, in turn, deposition fluxes and near-wall accumulation [Soldati 2012, Soldati 2009, Picciotto 2005]. These flaws have obvious consequences on the applicability of LES to industrial processes and environmental phenomena such as mixing, combustion, depulveration, spray dynamics, pollutant dispersion, or cloud dynamics [Balachandar 2010]. Recent analyses based on Direct Numerical Simulation (DNS) of turbulence have also shown that neither deterministic models nor stochastic homogeneous models have the capability to correct fully the inaccuracy of the LES approach due to SGS filtering [Marchioli 2008a, Bianco 2012, Geurts 2012, Chibbaro 2014]. Prompted by the above-mentioned findings, some attempts have been made on a heuristic ground, both for isotropic [Pozorski 2009, Gobert 2010, Shotorban 2005, Cernick 2015] and wall-bounded flows [Michalek 2013, Jin 2015].

An interesting and viable modelling alternative is represented by the Probability Density Function (PDF) approach, which has proven useful for LES of turbulent reactive flows [Colucci 1998, Jaber 1999, Gicquel 2002, Sheikhi 2003, Sheikhi 2007, Sheikhi 2009]. The LES formalism is based on the concept of Filtered Density Function (FDF), which is essentially the filtered fine-grained PDF of the transport quantities that characterize the flow. In this framework, the SGS effect is included in a set of suitably-defined Stochastic Differential Equations (SDEs), where the effects of advection, drag non-linearity and poly-dispersity appear in a closed form. This constitutes the primary advantage of the PDF/FDF approach with respect to other statistical procedures, in which these effects require additional modelling [Pope 2000].

The objective of the present work is to apply the FDF-based LES formalism for particle-laden turbulent flows. To this aim, several issues must be addressed with respect to the FDF approach already available for turbulent reactive flows. First, the FDF must be Lagrangian since particle dynamics are addressed naturally from the Lagrangian viewpoint. In addition, inertial particles behave like a compressible phase and therefore the mass density function should be considered. This leads to the definition of a joint Lagrangian Filtered Mass Density Function (LFMDF), which represents the mathematical framework required to implement the FDF approach in LES [Minier 2015b]. In particular, a suitable transport equation must be developed for the LFMDF such that the effects of SGS convection appear in closed form (the unclosed terms in the transport equation can be modelled following a procedure similar to Reynolds averaging). In this paper, the numerical solution of the LFMDF transport equation is achieved by means of a Lagrangian Monte Carlo procedure. The consistency of this procedure is assessed by comparing the first two moments of the LFMDF with those obtained from the Eulerian LES of the flow. The results provided by the LFMDF simulations are compared with those predicted by the original Smagorinsky closure, as well as those of the “dynamic” Smagorinsky model, for the reference case of turbulent channel flow. The LFMDF performance is further assessed upon direct comparison with a DNS dataset, paying particular attention to the results for particle preferential concentration.

3.2 Problem Formulation

In the mathematical description of turbulent dispersed flows, the relevant transport variables are the fluid velocity $U_i(\mathbf{x}, t)$, the pressure P , the particle position $\mathbf{x}_p(t)$, and the particle velocity $\mathbf{U}_p(\mathbf{x}_p(t), t)$. In this work, we consider heavy particles carried by an incompressible Newtonian fluid. The equations of motion for the fluid are, in scalar form:

$$\frac{\partial U_i}{\partial x_i} = 0, \quad (3.1)$$

$$\frac{\partial U_i}{\partial t} + U_j \frac{\partial U_i}{\partial x_j} = -\frac{1}{\rho_f} \frac{\partial P}{\partial x_i} + \nu_f \frac{\partial^2 U_i}{\partial x_j^2}, \quad (3.2)$$

where ρ_f and ν_f are the density and the kinematic viscosity of the fluid, respectively. LES of turbulence involves the use of a spatial filter [Germano 1992]:

$$\tilde{f}(\mathbf{x}, t) = \int_{-\infty}^{\infty} f(\mathbf{y}, t) G(\mathbf{y}, \mathbf{x}) d\mathbf{y}, \quad (3.3)$$

where G is the filter function, \tilde{f} represents the filtered value of the transport variable f , and $f' = f - \tilde{f}$ denotes the fluctuation of f with respect to the filtered value. We consider spatially- and temporally-invariant, localized filter functions, thus $G(y, x) \equiv G(x - y)$ with the properties, $G(x) = G(-x)$, and $\int G(x) dx = 1$. Starting from Eqns. (3.1) and (3.2), application of the filtering operator (3.3) yields:

$$\frac{\partial \tilde{U}_j}{\partial x_j} = 0, \quad (3.4)$$

$$\frac{\partial \tilde{U}_i}{\partial t} + \tilde{U}_j \frac{\partial \tilde{U}_i}{\partial x_j} = -\frac{1}{\rho_f} \frac{\partial \tilde{P}}{\partial x_i} + \nu_f \frac{\partial^2 \tilde{U}_i}{\partial x_j^2} - \frac{\partial \tilde{\tau}_{ij}}{\partial x_j}, \quad (3.5)$$

where $\tilde{\tau}_{ij} = \widetilde{U_i U_j} - \tilde{U}_i \tilde{U}_j$ is the SGS tensor component [Germano 1992]. To close the SGS stress tensor, three different cases have been considered in order to compare the differences produced on particle tracking: (1) no SGS model, (2) Smagorinsky SGS model [Smagorinsky 1963] and (3) Germano (dynamic Smagorinsky) SGS model [Germano 1991, Germano 1992, Lilly 1992]. In the case without SGS model, the contribution of the SGS is completely ignored and $\tilde{\tau}_{i,j} = 0$. The Smagorinsky model reads [Smagorinsky 1963]:

$$\tilde{\tau}_{i,j} - \frac{2}{3} k \delta_{i,j} = -2\nu_t \tilde{S}_{i,j}, \quad (3.6)$$

$$\tilde{S}_{i,j} = \frac{1}{2} \left(\frac{\partial \tilde{U}_i}{\partial x_j} + \frac{\partial \tilde{U}_j}{\partial x_i} \right), \quad (3.7)$$

$$\nu_t = (C_S \Delta)^2 \mathcal{S}, \quad (3.8)$$

with $C_S = 0.065$ [Moin 1982], $\mathcal{S} = \sqrt{\tilde{S}_{i,j} \tilde{S}_{i,j}}$ and Δ the characteristic length of the filter. The dynamic version of the Smagorinsky model provides a means of approximating C_S (the reader is referred to [Germano 1992] for further details on the model).

For the case of heavy particles (with density $\rho_p \gg \rho_f$), drag is the dominant force. Neglecting gravity to focus on turbulence effects on particles [Marchioli 2002, Picciotto 2005,

[Soldati 2009] the equations of particle motion in the Lagrangian framework, and in vector form, read as [Clift 1978]:

$$\frac{d\mathbf{x}_p}{dt} = \mathbf{U}_p , \quad (3.9)$$

$$\frac{d\mathbf{U}_p}{dt} = \frac{1}{\tau_p}(\mathbf{U}_s - \mathbf{U}_p) , \quad (3.10)$$

where $\mathbf{U}_s = \mathbf{U}(\mathbf{x}_p, t)$ is the fluid velocity seen by a particle along its trajectory, and:

$$\tau_p = \frac{\rho_p}{\rho_f} \frac{4 d_p}{3 C_D |\mathbf{U}_r|} , \quad (3.11)$$

is the particle relaxation time, with d_p the particle diameter, $C_D = \frac{24}{Re_p}(1 + 0.15 Re_p^{0.687})$ the drag coefficient and $\mathbf{U}_r = \mathbf{U}_p - \mathbf{U}_s$ the particle-to-fluid relative velocity at the particle position. Similarly to what already done for the fluid phase, it is possible to derive the filtered version of Eqns. (3.9) and (3.10). The Lagrangian nature of these equations, however, does not allow a straightforward derivation unless the SGS effects on particle motion are disregarded. In this case one can write:

$$\frac{d\tilde{\mathbf{x}}_p}{dt} = \tilde{\mathbf{U}}_p , \quad (3.12)$$

$$\frac{d\tilde{\mathbf{U}}_p}{dt} = \frac{\tilde{\mathbf{U}}_s - \tilde{\mathbf{U}}_p}{\tilde{\tau}_p} , \quad (3.13)$$

where $\tilde{\tau}_p$ is the particle relaxation timescale expressed in terms of the filtered relative velocity $\tilde{\mathbf{U}}_r$. A more precise definition of the filtering procedure for the particle-phase quantities is given in the following section.

3.3 Definition of the Filtered Density Function

3.3.1 Particle phase

In two-phase flows the exact governing equations are Lagrangian. Accordingly, we introduce a *Lagrangian Filtered Mass Density Function* (LFMDF) formally defined for N individual particles in the domain at the time t as [Minier 2015b]:

$$\begin{aligned} \tilde{F}_L^p(t; \mathbf{y}_p, \mathbf{V}_p, \mathbf{V}_s) &= \int \sum_{i=1}^N m_{p,i} G(\mathbf{y} - \mathbf{y}'_p) \delta(\mathbf{y}'_p - \mathbf{x}_{p,i}(t)) \otimes \delta(\mathbf{V}_p - \mathbf{U}_{p,i}(t)) \otimes \delta(\mathbf{V}_s - \mathbf{U}_{s,i}(t)) d\mathbf{y}' \\ &= \sum_{i=1}^N m_{p,i} G(\mathbf{y} - \mathbf{x}_{p,i}(t)) \otimes \delta(\mathbf{V}_p - \mathbf{U}_{p,i}(t)) \otimes \delta(\mathbf{V}_s - \mathbf{U}_{s,i}(t)) , \end{aligned} \quad (3.14)$$

where $m_{p,i}$ is the mass of the i -th particle. From the LFMDF, it is possible to derive formally the corresponding Eulerian Filtered Mass Density Function (EFMDF):

$$\begin{aligned} \tilde{F}_E^p(t, \mathbf{x}; \mathbf{V}_p, \mathbf{V}_s) &\equiv \tilde{F}_L^p(t; \mathbf{y}_p = \mathbf{x}, \mathbf{V}_p, \mathbf{V}_s) = \\ &= \sum_{i=1}^N m_{p,i} G(\mathbf{x} - \mathbf{x}_{p,i}(t)) \otimes \delta(\mathbf{V}_p - \mathbf{U}_{p,i}(t)) \otimes \delta(\mathbf{V}_s - \mathbf{U}_{s,i}(t)) . \end{aligned} \quad (3.15)$$

Let us now consider the conditional filtered value of a variable $Q(t)$, which is defined as follows:

$$\langle \tilde{Q}(t) | \mathbf{y}_p, \mathbf{V}_p, \mathbf{V}_s \rangle = \frac{\sum_{i=1}^N Q_i m_{p,i} G(\mathbf{y}_p - \mathbf{x}_{p,i}) \otimes \delta(\mathbf{V}_p - \mathbf{U}_{p,i}(t)) \otimes \delta(\mathbf{V}_s - \mathbf{U}_{s,i}(t))}{\tilde{F}_L^p(t; \mathbf{y}, \mathbf{V}_p, \mathbf{V}_s)}. \quad (3.16)$$

Equations (3.15) and (3.16) imply that:

- (i) if $Q(t) = \text{const.}$ then $\langle \tilde{Q}(t) | \mathbf{y}, \mathbf{V}_p, \mathbf{V}_s \rangle = \text{const.}$
- (ii) if $Q(t) \equiv \hat{Q}(\mathbf{x}(t), \mathbf{U}_p(t), \mathbf{U}_s(t))$, where the hat symbol indicates that the variable Q is completely defined by the variables $\mathbf{x}(t)$, $\mathbf{U}_p(t)$, and $\mathbf{U}_s(t)$, then $\langle \tilde{Q}(t) | \mathbf{y}, \mathbf{V}_p, \mathbf{V}_s \rangle = \hat{Q}(\mathbf{y}, \mathbf{V}_p, \mathbf{V}_s)$
- (iii) the following integral property for any variable $Q(t, \mathbf{x})$ holds:

$$\alpha_p(t, \mathbf{x}) \langle \rho \rangle_p \tilde{Q}(t, \mathbf{x}) = \int \int \langle \tilde{Q} | \mathbf{y} = \mathbf{x}, \mathbf{V}_p, \mathbf{V}_s \rangle \tilde{F}_E^p(t, \mathbf{x}; \mathbf{V}_p, \mathbf{V}_s) d\mathbf{V} d\mathbf{U}_s, \quad (3.17)$$

where $\alpha_p(t, \mathbf{x}) \langle \rho \rangle_p = \int \tilde{F}_E^p(t, \mathbf{x}; \mathbf{V}_p, \mathbf{V}_s) d\mathbf{V}_p d\mathbf{V}_s$ is the filtered local value of the particle mass fraction at time t and position \mathbf{x} . From these equations, it follows that the filtered value of any function of the variables in the state-vector is obtained by integration in the sample space:

$$\alpha_p(t, \mathbf{x}) \langle \rho \rangle_p \tilde{Q}(t, \mathbf{x}) = \int \int \hat{Q}(\mathbf{V}_p, \mathbf{V}_s) \tilde{F}_E^p(t, \mathbf{x}; \mathbf{V}, \mathbf{U}_s) d\mathbf{V} d\mathbf{U}_s. \quad (3.18)$$

3.3.2 LFMDf transport equation

To derive the LFMDf transport equation, the time derivative of the fine-grained density function given by Eq. (3.14) is considered. In the present study we are interested in the case on mono-disperse flow, so we assume that all particles have the same mass (namely $m_{p,i}$ is the same for $i = 1, \dots, N$). We can thus derive:

$$\begin{aligned} \frac{\partial \tilde{F}_L^p}{\partial t} &= \sum_{i=1}^N \left(m_{p,i} \frac{\partial G}{\partial t} \delta_{V_p V_s} + m_{p,i} G \frac{\partial \delta_{V_p}}{\partial t} \delta_{V_s} + m_{p,i} G \frac{\partial \delta_{V_s}}{\partial t} \delta_{V_p} \right) \\ &= \sum_{i=1}^N \left(m_{p,i} \frac{\partial G}{\partial \mathbf{x}} \frac{d\mathbf{x}_i}{dt} \delta_{V_p U_s} - m_{p,i} G \frac{d\mathbf{U}_{p,i}}{dt} \frac{\partial \delta_{V_p}}{\partial \mathbf{V}_p} \delta_{U_s} - m_{p,i} G \frac{d\mathbf{U}_{s,i}}{dt} \frac{\partial \delta_{V_s}}{\partial \mathbf{V}_s} \delta_{V_p} \right) \\ &= \sum_{i=1}^N \left(-m_{p,i} \frac{\partial G}{\partial \mathbf{y}} \frac{d\mathbf{x}_i}{dt} \delta_{V_p U_s} - m_{p,i} G \frac{d\mathbf{U}_{p,i}}{dt} \frac{\partial \delta_{V_p}}{\partial \mathbf{V}_p} \delta_{U_s} - m_{p,i} G \frac{d\mathbf{U}_{s,i}}{dt} \frac{\partial \delta_{V_s}}{\partial \mathbf{V}_s} \delta_{V_p} \right) \\ &= \sum_{i=1}^N \left(-\frac{\partial}{\partial \mathbf{y}} (m_{p,i} G \frac{d\mathbf{x}_i}{dt} \delta_{V_p U_s}) - \frac{\partial}{\partial \mathbf{V}_p} (m_{p,i} G \frac{d\mathbf{U}_{p,i}}{dt} \delta_{V_p} \delta_{U_s}) - \frac{\partial}{\partial \mathbf{V}_s} (m_{p,i} G \frac{d\mathbf{U}_{s,i}}{dt} \delta_{V_p} \delta_{V_s}) \right) \\ &= -\frac{\partial}{\partial \mathbf{y}} \left[\left\langle \frac{d\mathbf{x}}{dt} | \mathbf{y}, \mathbf{V}_p, \mathbf{U}_s \right\rangle \tilde{F}_L^p \right] - \frac{\partial}{\partial \mathbf{V}_p} \left[\left\langle \frac{d\mathbf{U}_p}{dt} | \mathbf{y}, \mathbf{V}_p, \mathbf{U}_s \right\rangle \tilde{F}_L^p \right] - \frac{\partial}{\partial \mathbf{V}_s} \left[\left\langle \frac{d\mathbf{U}_s}{dt} | \mathbf{y}, \mathbf{V}_p, \mathbf{V}_s \right\rangle \tilde{F}_L^p \right] \\ &= -\frac{\partial [\mathbf{V}_p \tilde{F}_L^p]}{\partial \mathbf{y}} - \frac{\partial}{\partial \mathbf{V}_p} \left[-\frac{\mathbf{V}_p - \mathbf{V}_s}{\tau_p} \tilde{F}_L^p \right] - \frac{\partial}{\partial \mathbf{V}_s} \left[\left\langle \tilde{\mathbf{A}}_{U_s} | \mathbf{y}, \mathbf{V}_p, \mathbf{U}_s \right\rangle \tilde{F}_L^p \right]. \end{aligned} \quad (3.19)$$

The LFMDf transport equation can be also written separating the filtered and unresolved parts as follows:

$$\begin{aligned} \frac{\partial \tilde{F}_L^p}{\partial t} + \frac{\partial (\tilde{\mathbf{U}}_p \tilde{F}_L^p)}{\partial \mathbf{y}} = & - \frac{\partial}{\partial \mathbf{V}_p} [\tilde{\mathbf{A}}_{U_p} \tilde{F}_L^p] - \frac{\partial}{\partial \mathbf{V}_s} [\tilde{\mathbf{A}}_{U_s} \tilde{F}_L^p] \\ & - \frac{\partial}{\partial \mathbf{y}} [(\mathbf{V}_p - \tilde{\mathbf{U}}_p) \tilde{F}_L^p] \\ & - \frac{\partial}{\partial \mathbf{V}_p} \left\{ \left[\langle \tilde{\mathbf{A}}_{U_p} | \mathbf{y}, \mathbf{V}_p, \mathbf{V}_s \rangle - \tilde{\mathbf{A}}_{U_p} \right] \tilde{F}_L^p \right\} \\ & - \frac{\partial}{\partial \mathbf{V}_s} \left\{ \left[\langle \tilde{\mathbf{A}}_{U_s} | \mathbf{y}, \mathbf{V}_p, \mathbf{V}_s \rangle - \tilde{\mathbf{A}}_{U_s} \right] \tilde{F}_L^p \right\}, \end{aligned} \quad (3.20)$$

where the first term on the right-end side corresponds to the effects of resolved scales whereas the last three terms take into account the effects of the unresolved scales. The EFMDf \tilde{F}_E^p follows by definition the same transport equation.

3.3.3 Modeled LFMDf transport equation

The Langevin model previously developed for turbulent polydispersed flows [Minier 2001, Minier 2004, Minier 2015b] is employed here to close the LFMDf transport equation. The modeled LFMDf equation reads as:

$$\begin{aligned} & - \frac{\partial}{\partial \mathbf{V}_s} \left[\langle \tilde{\mathbf{A}}_{U_s} | \mathbf{y}, \mathbf{V}_p, \mathbf{U}_s \rangle \tilde{F}_L^p \right] \\ \approx & - \frac{\partial}{\partial V_{s,i}} \left\{ \left[-\frac{1}{\rho_f} \frac{\partial \tilde{P}}{\partial x_i} + \nu_f \Delta \tilde{U}_i + (\tilde{U}_{p,j} - \tilde{U}_j) \frac{\partial \tilde{U}_i}{\partial x_j} - \frac{V_{s,i} - \tilde{U}_i}{T_{L,i}^*} \right] \tilde{F}_L^p \right\} \\ & + \frac{1}{2} \frac{\partial^2}{\partial V_{s,i}^2} \left\{ \tilde{\varepsilon} \left[C_0 b_i \frac{\hat{k}_{SGS}}{k_{SGS}} + \frac{2}{3} (b_i \frac{\hat{k}_{SGS}}{k_{SGS}} - 1) \right] \tilde{F}_L^p \right\}, \end{aligned} \quad (3.21)$$

where we have defined the Lagrangian timescale in the longitudinal direction ($i = 1$), and in the transversal directions ($i = 2$ and $i = 3$ respectively) as:

$$T_{L,1}^* = \frac{T_{SGS}}{\sqrt{1 + \beta^2 \frac{|\tilde{\mathbf{U}}_r|^2}{2k_{SGS}/3}}}, \quad T_{L,2}^* = T_{L,3}^* = \frac{T_{SGS}}{\sqrt{1 + 4\beta^2 \frac{|\tilde{\mathbf{U}}_r|^2}{2k_{SGS}/3}}}, \quad (3.22)$$

with $\beta = T_L/T_E$ [Wang 1993a], and:

$$\tilde{\varepsilon} = (C_S \Delta)^2 \mathcal{S}, \quad k_{SGS} = C_\varepsilon (\Delta \tilde{\varepsilon})^{2/3}, \quad T_{SGS} = \frac{k_{SGS}}{\tilde{\varepsilon}} \left(\frac{1}{2} + \frac{3}{4} C_0 \right)^{-1}, \quad (3.23)$$

where $\tilde{\varepsilon}$ is the SGS dissipation rate, Δ is the filter width, k_{SGS} is the SGS kinetic energy, and T_{SGS} is the SGS time-scale. This model is consistent with the Generalised Langevin Model [Pope 2000]. The auxiliary subgrid turbulent kinetic energy is defined as follows:

$$\hat{k}_{SGS} = \frac{3}{2} \frac{\sum_{i=1}^3 b_i [\widetilde{U_{s,i}^2} - \widetilde{U_{s,i}} \tilde{U}_{s,i}]}{\sum_{i=1}^3 b_i}, \quad (3.24)$$

with $b_i = T_{SGS}/T_{L,i}^*$.

3.3.4 Equivalent Stochastic System

The LFMDf transport equation is of the Fokker-Planck kind and provides all the statistical information of the state-vector. However, the most convenient way to solve this equation is through a Lagrangian Monte Carlo method, since the LFMDf equation is equivalent to a system of SDEs in a weak sense [Gardiner 1990]. This approach applies naturally to the dispersed phase since its evolution equations are Lagrangian. The system of SDEs corresponding to Eq. (3.21) reads as:

$$dx_{p,i} = U_{p,i} dt , \quad (3.25)$$

$$dU_{p,i} = \frac{U_{s,i} - U_{p,i}}{\tau_p} dt , \quad (3.26)$$

$$dU_{s,i} = -\frac{1}{\rho_f} \frac{\partial \tilde{P}}{\partial x_i} dt + \nu_f \Delta \tilde{U}_i + \left(\tilde{U}_{p,j} - \tilde{U}_j \right) \frac{\partial \tilde{U}_i}{\partial x_j} dt - \frac{U_{s,i} - \tilde{U}_i}{T_{L,i}^*} dt + B_{s,ij} dW_i , \quad (3.27)$$

where the term dW_i denotes a Wiener process [Gardiner 1990]. In the following we discuss the results obtained with two choices for the diffusion matrix $B_{s,ij} = \sqrt{C_i^* \tilde{\varepsilon}} \delta_{ij}$:

1. a simplified model $C_i^* \approx C_0 b_i + \frac{2}{3}(b_i - 1)$, referred to as *LFMDf1* hereinafter.
2. the complete model $C_i^* = \left[C_0 b_i \frac{\hat{k}_{SGS}}{\bar{k}_{SGS}} + \frac{2}{3} \left(b_i \frac{\hat{k}_{SGS}}{\bar{k}_{SGS}} - 1 \right) \right]$, referred to as *LFMDf2* hereinafter;

It is worth noting that the diffusion matrix, $B_{s,ij}$, is diagonal but not isotropic. This is crucial to reproduce a correct energy flux from the resolved scales to the unresolved ones, and represents a necessary requirement to consider the model acceptable [Minier 2014]. Using the same closure as that of single-phase flows, namely $B_{s,ij} = \sqrt{C_0 \tilde{\varepsilon}} \delta_{ij}$, is inconsistent with the modeled SGS dissipation rate $\tilde{\varepsilon}$.

When dealing with dispersed flows, a limit case of particular importance to assess the capability of a SGS particle model is that of inertia-free particles. These particles behave like fluid tracers and are characterized by $\tau_p \rightarrow 0$: The particle model must be consistent with a correct model in this limit [Minier 2014]. When $\tau_p \rightarrow 0$, our model reduces to:

$$dx_{p,i} = U_{p,i} dt , \quad (3.28)$$

$$U_{p,i} = U_{s,i} , \quad (3.29)$$

$$dU_{s,i} = -\frac{1}{\rho_f} \frac{\partial \tilde{P}}{\partial x_i} dt + \nu_f \Delta \tilde{U}_i - \frac{U_{s,i} - \tilde{U}_i}{T_{L,i}} dt + \sqrt{C_0 \tilde{\varepsilon}} dW_i , \quad (3.30)$$

which is the stochastic system equivalent to the Velocity Filtered Density Function (VFDF) model proposed by Gicquel et al. for the fluid [Gicquel 2002]. This model is consistent with the exact zero-th and first moment equations; but more complete models for the second central moment are also available [Gicquel 2002, Dreeben 1998, Waławczyk 2004].

3.4 Numerical method

The numerical solution of the LES/LFMDf model is obtained using a hybrid Eulerian mean-field LES/Lagrangian Monte Carlo procedure, where the filtered fluid properties

are computed on a mesh while the statistics of the dispersed phase are calculated from particles moving in the computational domain. This procedure has been used previously in the context of RANS [Peirano 2006]. Specifically, let $\{\mathbf{Y}^{[x]}\}$ be the set of filtered fluid flow fields at the different mesh points and let $\{\mathbf{Y}^{(N)}\}$ be the set of filtered fluid flow fields interpolated at particle locations. Let $\{\mathbf{Z}^{(N)}\}$ be the set of variables “attached” to the particles and let $\{\mathbf{Z}^{[x]}\}$ be the set of statistics (defined at cell centres) extracted from $\{\mathbf{Z}^{(N)}\}$. The first step (operator F) is to solve the PDEs for the fluid:

$$\{\mathbf{Y}^{[x]}\}(t_n) \xrightarrow{F} \{\mathbf{Y}^{[x]}\}(t_{n+1}) . \quad (3.31)$$

The second step (projection, operator P) consists of calculating the filtered fluid properties and the filtered particle properties at particle locations:

$$\{\mathbf{Y}^{[x]}\}(t_n) \text{ and } \{\mathbf{Z}^{[x]}\}(t_n) \xrightarrow{P} \{\mathbf{Y}^{(N)}\}(t_n) \text{ and } \{\mathbf{Z}^{(N)}\}(t_n) . \quad (3.32)$$

Then, the stochastic differential system can be integrated in time (operator T):

$$\{\mathbf{Z}^{(N)}\}(t_n) \xrightarrow{T} \{\mathbf{Z}^{(N)}\}(t_{n+1}) . \quad (3.33)$$

Finally, from the newly computed (at particle locations) set of variables, new statistical moments are evaluated at cell centres (operator A):

$$\{\mathbf{Z}^{(N)}\}(t_{n+1}) \xrightarrow{A} \{\mathbf{Z}^{[x]}\}(t_{n+1}) . \quad (3.34)$$

The operator F is a pseudo-spectral method based on transforming the field variables into wavenumber space, using Fourier representations for the periodic streamwise and spanwise (homogeneous) directions and a Chebyshev representation for the wall-normal (non-homogeneous) direction. The projection step, required to evaluate fluid and particle quantities at particle positions, is achieved with three different techniques:

- *no-interpolation* (zero-th order, not symmetric in the wall normal direction): The values of the filtered quantities at the upstream neighbour node of the cell containing the particle are used.
- *NGP* (Nearest Grid Point, symmetric in the wall-normal direction): The average values of the filtered quantities at each node of the cell containing the particle are used.
- *interpolation*: A second-order interpolation of the Eulerian quantities at grid nodes is performed to obtain quantities at the particle position.

Previous studies have shown that no improvement is obtained using higher-order interpolation schemes [Peirano 2006]. In fact, higher-order schemes may even lead to larger errors in hybrid formulations like the one considered here.

The local instantaneous properties of the dispersed phase are obtained by solving the set of SDEs via the operator T . In particular, the numerical solution of the modelled stochastic equations is obtained representing the modelled LFMDf through an ensemble of N statistically identical Monte Carlo particles. Each of these particles carries information pertaining to the fluid velocity seen by the particle, $\mathbf{U}_s^{(n)}(t)$, to the particle velocity, $\mathbf{U}_p^{(n)}(t)$,

and to the particle position, $\mathbf{x}_p^{(n)}(t)$, where $n = 1, 2, \dots, N$. This information is updated upon time-integration of Eqns. (3.25)-(3.27). This system of SDEs has multiple scales and may become stiff, in particular for particles with very small inertia. Moreover, in wall-bounded flows the characteristic fluid time scales become smaller in the near-wall region, thus complicating the integration. For these reasons, an ad-hoc unconditionally-stable, second-order accurate numerical scheme has been developed and implemented here. The scheme is based on that put forward in the RANS context [Peirano 2006]: It adopts the Itô's convention and is developed starting from the analytical solution of Eqns. (3.25)-(3.27) with constant coefficients. Such a scheme ensures stability and consistency with all limit cases. The first-order scheme is the following Euler-Maruyama:

$$x_{p,i}^{n+1} = x_{p,i}^n + A_1 U_{p,i}^n + B_1 U_{s,i}^n + C_1 [T_i^n C_i^n] + \Omega_i^n, \quad (3.35)$$

$$U_{p,i}^{n+1} = U_{p,i}^n \exp(-\Delta t/\tau_p^n) + D_1 U_{s,i}^n + [T_i^n C_i^n](E_1 - D_1) + \Gamma_i^n, \quad (3.36)$$

$$U_{s,i}^{n+1} = U_{s,i}^n \exp(-\Delta t/T_i^n) + [T_i^n C_i^n][1 - \exp(-\Delta t/T_i^n)] + \gamma_i^n, \quad (3.37)$$

where the coefficients are given by the following relations:

$$\begin{aligned} A_1 &= \tau_p^n [1 - \exp(-\Delta t/\tau_p^n)], \\ B_1 &= \theta_i^n [T_i^n (1 - \exp(-\Delta t/T_i^n) - A_1)] \quad \text{with} \quad \theta_i^n = T_i^n / (T_i^n - \tau_p^n), \\ C_1 &= \Delta t - A_1 - B_1, \\ D_1 &= \theta_i^n [\exp(-\Delta t/T_i^n) - \exp(-\Delta t/\tau_p^n)], \\ E_1 &= 1 - \exp(-\Delta t/\tau_p^n). \end{aligned}$$

and $\gamma_i^n, \Gamma_i^n, \Omega_i^n$ are stochastic integrals. The details of the scheme as well as the analytical solutions are given in Appendix 3.A. The second-order scheme is derived using a predictor-corrector technique, in which the prediction step is the first-order scheme given by Eqns. (3.35)-(3.37) [Peirano 2006].

Particle statistics are evaluated by considering the ensemble of particles N_E located within a small volume of fluid δV (a box of size $\Delta_{E,1} \times \Delta_{E,2} \times \Delta_{E,3}$) centered around a given point \mathbf{x} . This ensemble provides one-time one-point statistics. For reliable statistics with minimal numerical dispersion, it is desirable to minimize the size of the averaging domain, namely $\Delta_E = \sqrt[3]{\Delta_{E,1}\Delta_{E,2}\Delta_{E,3}} \rightarrow 0$, and maximize the number of Monte Carlo particles, namely $N_E \rightarrow \infty$. By doing so, the ensemble statistics tend to the desired filtered values:

$$\tilde{a}_E = \frac{1}{N_E} \sum_{n \in \Delta_E} a^{(n)} \xrightarrow[N_E \rightarrow 0]{N_E \rightarrow \infty} \tilde{a} \quad (3.38)$$

$$\tau_E(a, b) = \frac{1}{N_E} \sum_{n \in \Delta_E} (a^{(n)} - \tilde{a}_E)(b^{(n)} - \tilde{b}_E) \xrightarrow[N_E \rightarrow 0]{N_E \rightarrow \infty} \tau(a, b) \quad (3.39)$$

where $a^{(n)}$ and $b^{(n)}$ denote typical information carried by the n -th particle, for instance its velocity components, and the arrows indicate the limit operator. Since we are adopting a Monte Carlo procedure in a LES/LFMDf approach, the quantities obtained following Eqn. (3.39) are filtered Eulerian quantities, \tilde{a} , and subgrid quantities, $\tau(a, b)$, respectively. For example, one can evaluate the particle filtered velocity as:

$$\tilde{U}_{p,i}(\mathbf{x}) \simeq \frac{1}{N_x} \sum_{n=1}^{N_x} U_{p,i}^{(n)}. \quad (3.40)$$

Analogous expressions can be written for all other filtered quantities.

The mean-field LES solver also computes the filtered fluid velocity field so that there is a “redundancy” of the first filtered moments in the $\tau_p \rightarrow 0$ limit. In this case, both the spectral method and the Monte Carlo procedure yield the solution for the particle number density and velocity fields. These fields are referred to as “duplicate fields” hereinafter, and can be exploited to assess the accuracy of the model [Muradoglu 1999, Jenny 2001]. The characteristics of our scheme are summarized in Table 3.1.

3.5 Results

In the present study, the LES/LMFDF approach is applied to track inertial particles in gas-solid turbulent channel flow. The fluid considered is air (assumed to be incompressible and Newtonian) with density $\rho_f = 1.3 \text{ kg/m}^3$ and kinematic viscosity $\nu_f = 1.57 \cdot 10^{-5} \text{ m}^2/\text{s}$. The reference geometry consists of two infinite flat parallel walls: the origin of the coordinate system is located at the center of the channel, with the x -, y - and z - axes pointing in the streamwise, spanwise and wall-normal directions, respectively. Periodic boundary conditions are imposed on the fluid velocity field in x and y , and no-slip boundary conditions are imposed at the walls. Calculations were performed on a computational domain of size $4\pi h \times 2\pi h \times 2h$ in x , y and z , respectively [Soldati 2009]. The domain was discretised using a $32 \times 32 \times 33$ grid with uniform cell spacing in the homogeneous directions and non-uniform cell distribution in the wall-normal direction (Chebyshev collocation points) [Marchioli 2008c]. Simulations were performed with a coarsening factor $CF = 8$ with respect to the reference DNS, at a shear Reynolds number $Re_\tau = 300$ based on the half width h of the channel, and using a fixed time step (see Table 3.2). DNS is based on a pseudo-spectral incompressible flow solver that uses a Fourier-Galerkin method in x and y , and a Chebyshev-collocation method in z . A two-level, explicit Adams-Bashforth scheme for the nonlinear terms, and an implicit Crank-Nicolson scheme for the viscous terms are employed for time advancement. More details can be found in [Marchioli 2002, Marchioli 2008c]. Particles with density $\rho_p = 10^3 \text{ kg/m}^3$ and Stokes numbers as given in Table 3.3, were injected in the flow at randomly-chosen locations under fully-developed flow conditions. Since we are concerned with a Monte-Carlo simulation, a large number of particles is required to minimize statistical errors. In the consistency assessments (see Section 3.5.1), the number of particles per cell was varied selecting $N_{pc} = 20, 40$, and 80 , while simulations with inertial particles were performed imposing $N_{pc} = 40$: This latter value corresponds to a total number of particles $N \simeq 1.31 \cdot 10^6$ in the domain. Particles rebound elastically upon

spectral LES variables	Particle solver variables	mean-field variables	duplicate fields (fluid limit)
\tilde{U}_i	$X_{p,i}$	$\tilde{U}_i, \frac{\partial \tilde{P}}{\partial x_i}$	ρ_f
\tilde{P}	$U_{p,i}, U_{s,i}$	$\frac{\partial \tilde{U}_i}{\partial x_j}, \Delta \tilde{U}_i$	\tilde{U}_i

Table 3.1: Summary of the LES/LFMDf solution procedure.

Time step	Δt	$4.2 \cdot 10^{-5}$	[s]
	$\Delta t^+ = \Delta t u_\tau^2 / \nu_f$	0.15	[w.u.]
DNS grid size	$N_x \times N_y \times N_z$	$256 \times 256 \times 257$	
LES grid size	$N_x \times N_y \times N_z$	$32 \times 32 \times 33$	

Table 3.2: Simulation parameters for the fluid. Superscript + represents variables in wall units, obtained using the shear velocity and the fluid kinematic viscosity.

impact with the wall when their center is less than a diameter away from the wall itself.

In the following, both instantaneous and time-averaged results are discussed. In particular, we examine Reynolds averaged statistics, denoted by an overbar and obtained upon averaging the filtered velocity over the homogeneous flow directions and in time.

3.5.1 Assessment of consistency and convergence

The purpose of this section is to demonstrate the consistency of the LFMDf formulation in the $\tau_p \rightarrow 0$ limit, and to show its convergence. To these objectives, the results obtained via the LES/mean-field are compared against those provided by the LFMDf approach. Given the accuracy of the spectral method, such a comparative validation represents a robust way to assess the performance of the LFMDf solution provided by the Monte Carlo simulation. We are particularly interested in examining the particle velocity statistics, but also the particle number density distribution, which is the macroscopic result of turbophoresis [Marchioli 2002, Soldati 2009] and should remain uniform in the whole domain when $\tau_p \rightarrow 0$. For these observables, we compare the statistics obtained from the Monte Carlo simulation, namely from the solution of Eqns. (3.25)-(3.27), with those of the Eulerian pseudo-spectral simulation, which solves for Eqns. (3.1)-(3.2). As mentioned, in the fluid limit this is equivalent to solving Eq. (3.30), and the resulting duplicate fields (indicated in Table 3.1) should be consistent. The values suggested in the literature for the model parameters are chosen here: $C_0 = 2.1$, $C_\varepsilon = 1$, $\beta = 0.8$ [Minier 2001]. We have also checked the convergence with respect to N_{pc} , which is achieved for $N_{pc} \geq 40$.

Figure 3.1 shows the Reynolds-averaged particle number density, C/C_{in} (with C_{in} the number density at the time of particle injection), and particle streamwise velocity, \overline{U}_x along the wall-normal coordinate. The different profiles correspond to different interpolation techniques. To avoid cross-effects, no subgrid model is used in the Eulerian simulation. While velocity appears unaffected by the particular interpolation technique employed (results are perfectly consistent), particle number density is sensitive. In particular significant errors in the near-wall region are found when no interpolation is performed or when the

St	τ_p [s]	d_p^+ [w.u.]	d_p [μm]
1	$0.283 \cdot 10^{-3}$	0.153	10.2
5	$1.415 \cdot 10^{-3}$	0.342	22.8
25	$7.077 \cdot 10^{-3}$	0.763	50.9

Table 3.3: Simulation parameters for the particles.

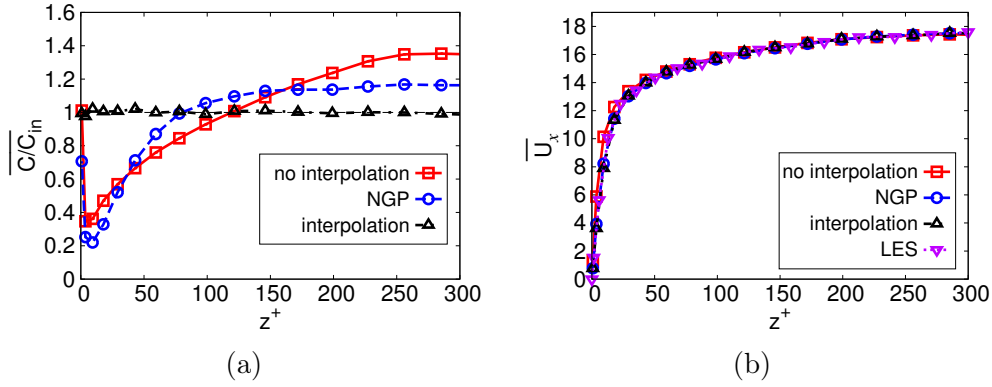


Figure 3.1: Reynolds-averaged particle number density (a) and filtered streamwise velocity (b), obtained with different SGS particle models: no-interpolation of LES and particle quantities (\square), NGP interpolation (\circ) and second-order interpolation (\triangle). Downward triangles (∇) in panel (b) refer to the filtered streamwise velocity provided by LES. The time window for averaging is $\Delta t^+ = 3000$, in wall units.

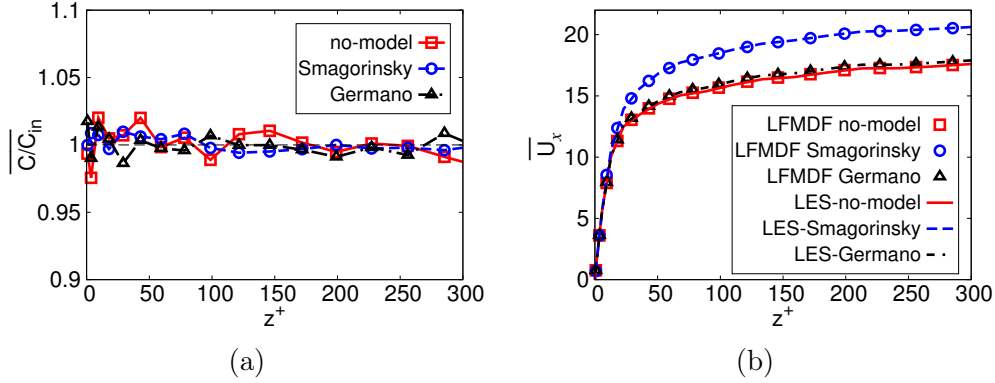


Figure 3.2: Reynolds-averaged particle number density (a) and filtered streamwise velocity (b), obtained with different SGS models for the fluid: No-model (\square , $-$), Smagorinsky model (\circ , $--$) and Germano dynamic model (\triangle , $-.$). The time window for averaging is $\Delta t^+ = 3000$, in wall units.

nearest-grid-point technique is used. A second-order interpolation, however, is sufficient to recover the expected behaviour and ensure $\overline{C/C_{in}} \simeq 1$ everywhere (as expected for tracer particles). In figure 3.2, the averaged number density profile and the averaged velocity provided by the different SGS models for the fluid are shown. The LFMDF model appears to be consistent with all models tested, since the $\overline{C/C_{in}}$ profile remains uniform once the stationary state is reached and the velocity is (again) perfectly consistent. It is also observed that, in the $\tau_p \rightarrow 0$ limit, the first moments of the Germano model are nearly the same as those obtained without SGS model. Therefore results discussed hereinafter refer to simulations performed using the Germano model for the fluid phase, unless otherwise stated. A further proof of consistency is provided by figure 4.9, which shows the scatter plots of the streamwise and wall-normal velocity components, indicated as \tilde{U}_x and \tilde{U}_z respectively. Velocities in the Eulerian simulations were evaluated at the center of the computational cells. The velocity correlation is quite satisfactory, except perhaps for very

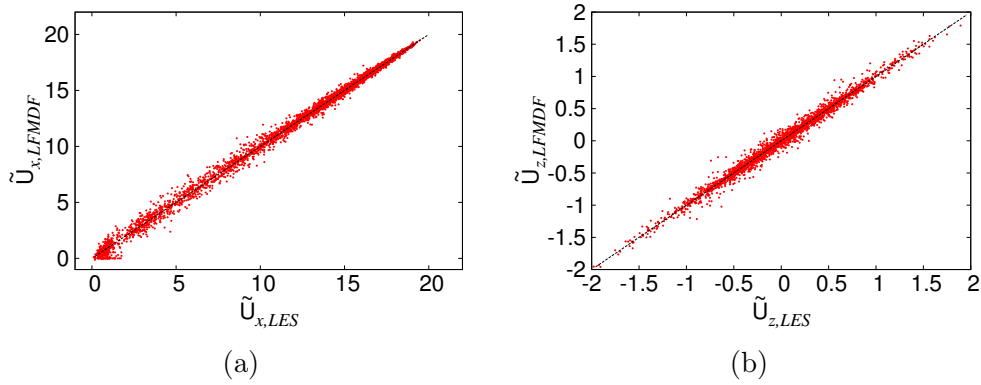


Figure 3.3: Scatter plot correlating particle velocity components evaluated from LES and from LFMDf: (a) streamwise component, (b) wall-normal component.

small values of \tilde{U}_x .

To assess the consistency of the LFMDf formulation from a physical (and more intuitive) point of view, in Fig. 3.4, we compare the near-wall fluid streaks that can be rendered from the Eulerian LES (panel a) and from the Monte Carlo LFMDf simulation (panel b). Streaks are known to play a crucial role in determining the transport mechanisms in turbulent boundary layers [Picciotto 2005, Marchioli 2002], and are visualised here by instantaneous contour plots of the fluctuating streamwise velocity on a x - y plane located at a distance $z^+ = 10$ from the wall. Visual inspection shows only small differences in the color map, indicating that the streaks, and indirectly the near-wall turbulent coherent structures that generate it, are indeed recovered by the LFMDf simulation in the fluid limit.

To complete the model assessment, we have also checked the sensitivity of Reynolds averaging to the size of the reference volume δV (introduced in Section IV) over which averaging is performed. To this aim, we considered different grids made of cubic volumes centered around the LES (Eulerian) nodes. The size of each volume, Δ_E , was varied to be either smaller or larger than the cell size Δ in the reference 32^3 LES grid. Figure 3.5 shows the averaged filtered streamwise velocity at varying Δ_E (with a fixed number of particles per cell, $N_{pc} = 40$). It can be seen that all profiles overlap even for large Δ_E ($\Delta_E = 2\Delta$) indicating that the mean filtered velocity is not sensitive to the size of the averaging volume, at least in the range of Δ_E analysed. For this reason we have chosen $\Delta_E = \Delta$ for all simulations. To test this choice we have also considered higher-order moments, namely the root mean square (rms) of filtered velocity, and we have analysed the convergence in relation to the DNS results. In figure 3.6 we show the rms of the filtered velocity, defined as $rms(\tilde{U}) = \sqrt{\overline{(\tilde{U} - \bar{\tilde{U}})^2}}$. The different profiles do not collapse and the LFMDf is in better agreement than LES with DNS, when the volume size is $\Delta_E = \Delta$, confirming the validity of the overall method in the fluid limit. It is worth noting that the discrepancy between Eulerian LES and LFMDf is not related to some incongruity, since these two models are not fully consistent at the Reynolds-stress level. As suggested in previous studies [Gicquel 2002], an even better convergence to DNS would be probably possible with smaller Δ_E and much higher N . However, this choice would increase the

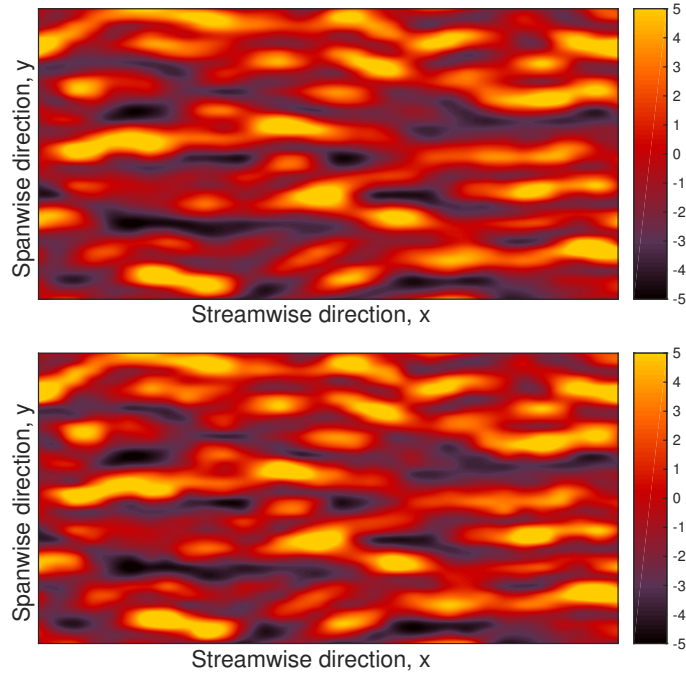


Figure 3.4: Near-wall fluid velocity streaks. Low-speed (high-speed) streaks are rendered using colored contours of negative (positive) streamwise fluctuating velocity on a horizontal plane at $z^+ = 10$ from the wall. Top panel refers to the Eulerian LES, performed with no SGS model for the particles and with $N_{pc} = 40$; bottom panel refers to the LFMDf simulation.

computational cost considerably thus making the model not relevant application-wise.

3.5.2 Model assessment with inertial particles

In this section we validate the LFMDf approach for the case of inertial particles via comparative assessment against DNS data. In particular, first we exploit DNS to determine the range of empirical constants appearing in the LFMDf sub-model (*a priori* assessment). Second, we compare the predictions of the LFMDf-based simulations with the statistics provided by DNS, which is regarded here as the reference numerical experiment (*a posteriori* assessment). In the latter case, comparison is also made with the statistics provided by LES when no particle SGS model is used, in order to point out the impact of the proposed stochastic model on statistics. As mentioned, one of the main difficulties of modelling inertial particle dynamics in LES is to capture preferential concentration [Marchioli 2008a, Marchioli 2008b]. Hence, the primary observable considered for comparative assessment is the *instantaneous* particle number density distribution along the wall-normal direction, which is a macroscopic manifestation of preferential concentration. Such comparison is particularly severe since any error associated with the proposed particle SGS model will inevitably sum up over time and may thus lead to significant deviations in the final density distribution (we remark here that all LES/LFMDf simulations are

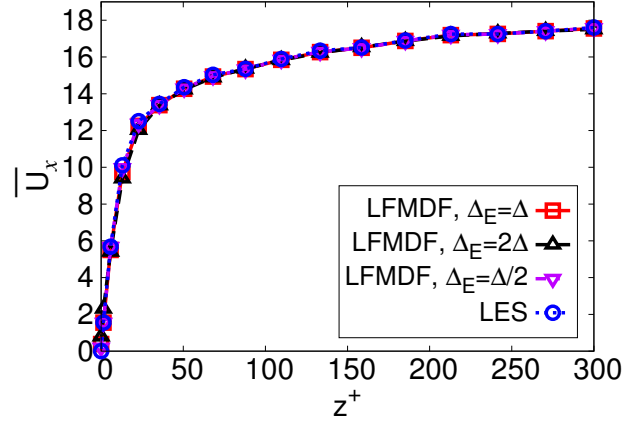


Figure 3.5: Mean velocity of the filtered streamwise velocity at varying Δ_E . Time window for averaging is $\Delta t^+ = 3000$ with $N_{pc} = 40$ particle per cell.

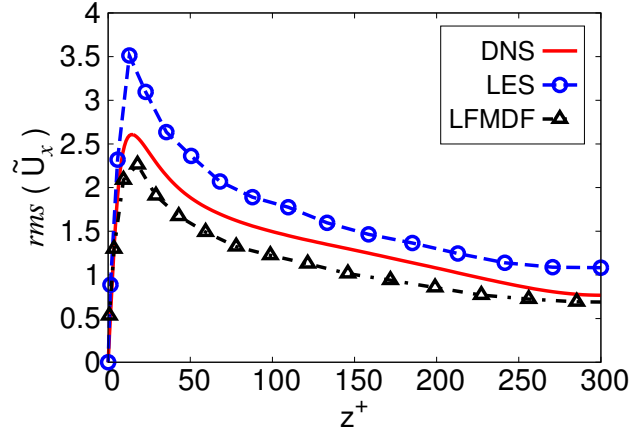


Figure 3.6: Root mean square of the filtered streamwise velocity.

carried out with a rather large coarsening factor, $CF = 8$ with respect to DNS).

Figure 3.7 shows the particle number density profiles along the wall-normal coordinate for different Stokes numbers. Two different formulations of the proposed LFMDf model are tested: The simplified *LFMDf1* formulation, and the complete *LFMDf2* formulation (see Sec. 3.3.4). In both formulations we use $C_0 = 2.1$, $C_\varepsilon = 1$, $\beta = 0.8$. The *LFMDf1* predictions (dark magenta profiles) deviate substantially from the reference DNS results (red profiles) for all Stokes numbers: This is due, of course, to the assumption of isotropic velocity fluctuations on which the *LFMDf1* formulation is based. On the other hand, the *LFMDf2* formulation, which has a more complete diffusion term, leads to improved predictions (black profiles), especially for the two larger Stokes numbers: $St = 5$, panel (b); and $St = 25$, panel (c). Discrepancies, however, are still evident and lead to a significant over-estimation (under-estimation) of particle accumulation in the viscous sub-layer for the smaller $St = 1$ (large $St = 25$) particles, as shown in Fig. 3.7(a) and in Fig. 3.7(c) respectively. The main reasons are that the present model does not have all the necessary viscous terms needed to capture properly the flow dynamics in the viscous sublayer [Colucci 1998,

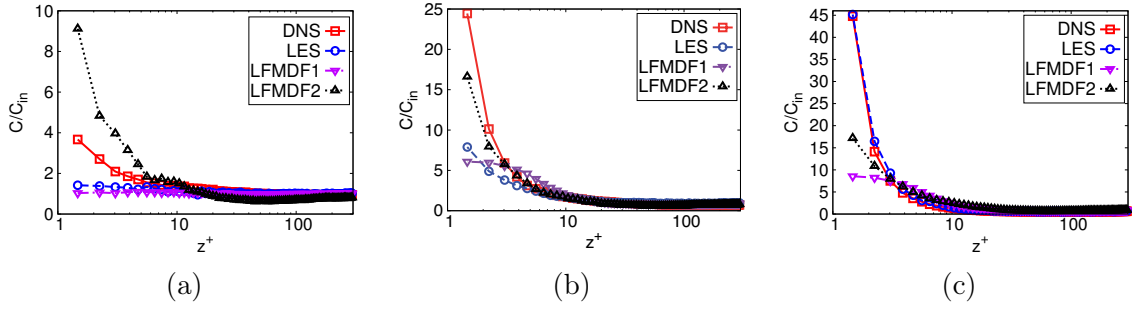


Figure 3.7: Comparison of particle number density distributions predicted by two different particle SGS model formulations: Simplified stochastic model (*LFMDF1*, ∇) and complete stochastic model (*LFMDF2*, \triangle). See also Sec. 3.3.4. Other symbols: \square DNS, \circ LES without particle SGS model. Panels: (a) $St = 1$ particles, (b) $St = 5$ particles, (c) $St = 25$ particles. Profiles are computed at $t^+ = 2130$ after particle injection into the flow.

Jaberi 1999, Gicquel 2002, Sheikhi 2003, Sheikhi 2007, Sheikhi 2009, Waćławczyk 2004], and also that the closure of the LFMDF2 formulation involves two parameters, C_0 and C_ε , which are known to be quite sensitive to the characteristic features of both the turbulent flow and the numerical approach. For instance, turbulent theory gives the value $C_0 = 2.1$ for stochastic models in homogeneous flows [Pope 2000], whereas numerical simulations of wall-bounded flows in the RANS framework suggest to set $C_0 = 3.5$ [Minier 1999]. Since we are mostly interested in the near-wall statistics, in the following we shall limit ourselves to the complete model LFMDF2, and neglect the isotropic LFMDF1 formulation, which underestimates particle number density in the wall-normal direction and is not sensitive to the Stokes number (hence it cannot take into account inertial effects on particle dispersion [Zhao 2012]). Nevertheless, we remark here that the LFMDF1 formulation is much simpler than the complete model and appears to work reasonably well outside of the viscous sub-layer in the case of small Stokes numbers. Therefore its use could be considered to study particle dynamics far from the wall or in unbounded flows (e.g. jets and mixing layers).

In this study, we exploit DNS to obtain *a priori* estimates of the two model constants. We remark that our purpose is not to find optimal values for C_0 and C_ε , but rather to quantify the sensitivity of the model to a change in the value of these constants. Figure 3.8 shows the number density profiles obtained at varying C_0 (while keeping C_ε constant and equal to 1). This figure shows that C_0 has a significant influence on particle wall-normal accumulation only for large-inertia particles (high Stokes numbers), and suggests that $C_0 = 3.5$ provides the best predictions over the range of Stokes numbers considered here. This result is in agreement with [Dreeben 1998, Minier 1999]. We performed a similar analysis to estimate C_ε while keeping C_0 constant (and equal to 3.5). Results are shown in Fig. 3.9 and demonstrate that C_ε affects particle spatial distribution at all Stokes numbers. In particular, we observe higher accumulation of particles at the wall for smaller values of C_ε . This finding indicates that the diffusion term is at least as important as the drift term in the present flow configuration. Based on this comparison, we select $C_\varepsilon = 0.1$ to calibrate the LFMDF model.

A combined analysis of Figs. 3.8 and 3.9 indicates that, regardless of the value considered for C_0 and C_ε , the near-wall volume concentration of small inertia particles (rep-

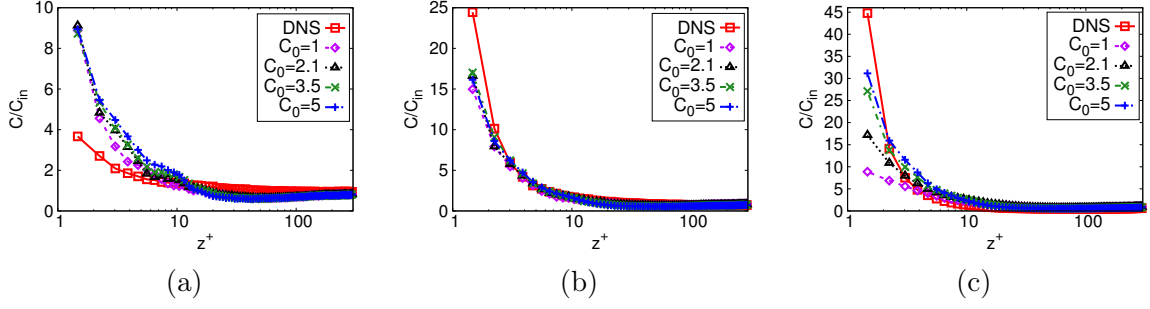


Figure 3.8: Effect of parameter C_0 on particle number density along the wall-normal coordinate (*a-priori* estimate). Red symbols (\square) refer to the DNS result, all other symbols refer to LES results obtained with the LFMDf2 model. Panels: (a) $St = 1$, (b) $St = 5$, (c) $St = 25$. Profiles are computed at $t^+ = 2130$ after particle injection.

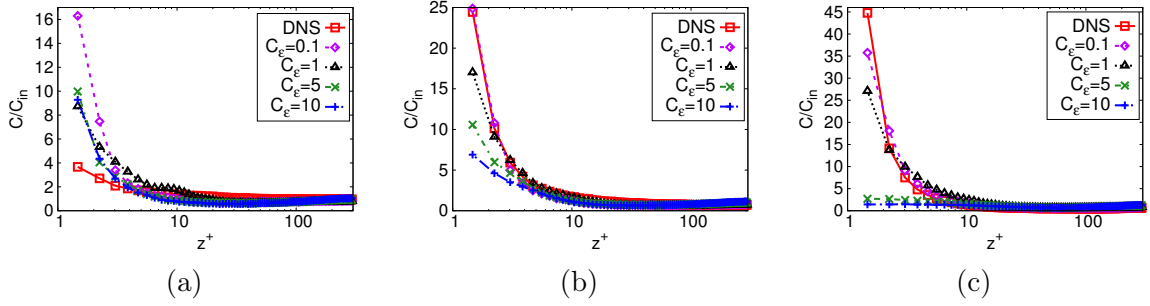


Figure 3.9: Effect of parameter C_ϵ on particle number density along the wall-normal coordinate (*a-priori* estimate). Red symbols (\square) refer to the DNS result, all other symbols refer to LES results obtained with the LFMDf2 model. Panels: (a) $St = 1$, (b) $St = 5$, (c) $St = 25$. Profiles are computed at $t^+ = 2130$ after particle injection.

resented by the $St = 1$ particles in this study) is always overestimated by the LFMDf2 model, whereas the opposite occurred with the LFMDf1 model (see Fig. 3.7a). For such particles, therefore, the critical modelling issue in order to retrieve the correct physical behaviour seems to be the closure of the diffusion term. We remark here that particles with small inertia are subject to a weaker turbophoretic wallward drift and tend to remain more homogeneously distributed within the flow domain [Soldati 2009, Marchioli 2002]. As a consequence, the instantaneous Eulerian statistics that can be extracted from local particle ensemble averages may exhibit significant statistical errors in the near-wall region, where the control volumes to which averaging is applied become smaller and smaller. This source of error becomes less important as particle inertia increases, namely as particle accumulation in the near-wall region increases with St .

The key quantity for a correct evaluation of the diffusion term is the kinetic energy ratio $\widehat{k}_{SGS}/k_{SGS}$. If \widehat{k}_{SGS} is computed from Eq. (3.24), which implies Lagrangian ensemble averaging, then it will be affected by the resulting statistical error. To improve the model,

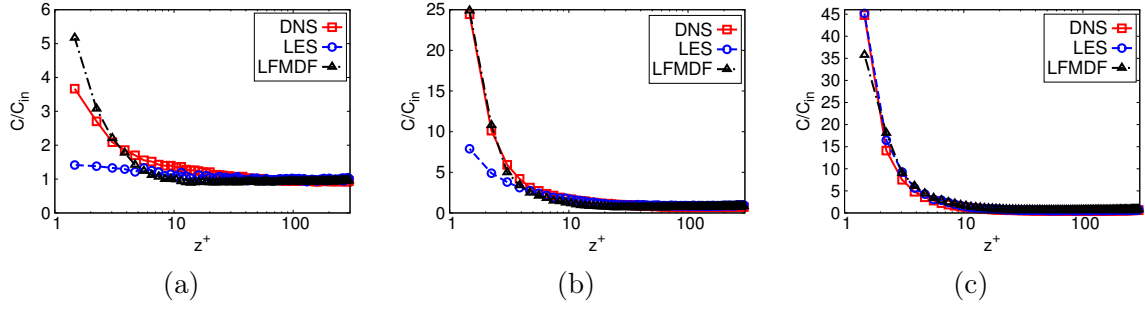


Figure 3.10: Comparative assessment of the LFMDf2 model with Eq. (3.41): Predictions of the instantaneous particle number density at varying Stokes numbers (Δ) are compared with DNS results (\square) and with LES results with no particle SGS model (\circ). Panels: (a) $St = 1$, (b) $St = 5$, (c) $St = 25$. Profiles are computed at $t^+ = 2130$ after particle injection.

we propose a new formulation to evaluate k_{SGS} , which is slightly different from Eq. (3.23):

$$k_{SGS} = \tau(U_{s,i}, U_{s,i}) = \frac{1}{2} \sum_{i=1}^3 \left[\widetilde{U_{s,i}^2} - (\widetilde{U_{s,i}})^2 \right]. \quad (3.41)$$

In the limit of $N_{pc} \rightarrow \infty$, Eq. (3.41) is equivalent to Eq. (3.24), but is expected to decrease the variance of the model estimations for finite values of N_{pc} at small Stokes numbers. In the following, results for the $St = 1$ particles refer to calculations performed using this new formulation, unless otherwise stated. In particular, Fig. 3.10 shows the comparison of the LFMDf results for particle number density. For completeness, also the LES results without particle SGS model are included. The overshoot of particle accumulation at the wall for $St = 1$ is strongly reduced with respect to the predictions reported in Figs. 3.8 and 3.9, and there is a nearly perfect match with the DNS profile for the intermediate-inertia particles ($St = 5$, Fig. 3.10b). As expected, wall accumulation at large Stokes numbers is unaffected. We remark that the values of particle number density within a distance of few wall units from the wall are very noisy even in DNS [Prevel 2013]: This implies that the only relevant information one can extract from the viscous sublayer portion of the profiles shown in Fig. 3.10 is just the trend in model performance at varying particle inertia.

To provide a phenomenological perspective to our discussion, we complement the statistical description of particle wall-normal distribution with the analysis of particle clustering in the near-wall region. As demonstrated in previous studies (see [Marchioli 2002, Picciotto 2005, Soldati 2009] and references therein, for a review), the tendency that inertial particles have to form clusters is crucial to develop peaks of particle concentration within the flow. Therefore, a reliable particle SGS model should be able to capture (in a statistical sense) also these phenomena. To perform this analysis, we quantify particle clusters by means of Voronoï diagrams, which represent an efficient and robust tool to diagnose and quantify clustering [Monchaux 2010]. One Voronoï cell is defined as the ensemble of points that are closer to a given particle than to any other particle in the flow: The area of a Voronoï cell is therefore the inverse of the local particle number density. In addition Voronoï areas are naturally evaluated around each particle and, differently from standard box counting methods, provide a direct measure of particle preferential concentration at inter-particle length scale [Monchaux 2010].

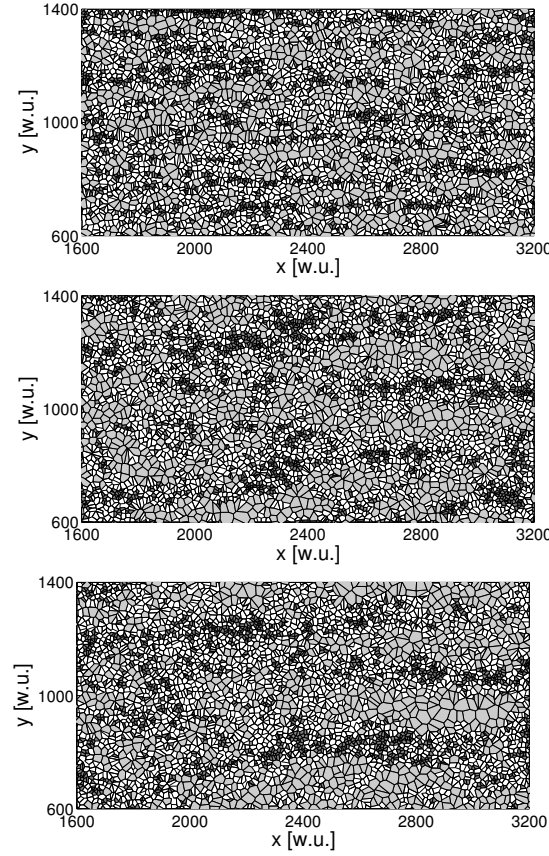


Figure 3.11: Voronoï tessellation for the $St = 5$ particles on a wall-parallel fluid slab ($1 \leq z^+ \leq 5$) at time $t^+ = 2130$ after particle injection. Particle clusters are in dark gray, voids are in light gray. Panels: (top) DNS, (middle) LES with no particle SGS model, (bottom) LES with the calibrated LMFDF2 model.

An example of Voronoï diagram for the present channel flow configuration is shown in Fig. 3.11, which focuses on the instantaneous distribution of the $St = 5$ particles within a wall-parallel fluid slab of thickness $1 \leq z^+ \leq 5$. Only a portion of the $x - y$ plane is shown to highlight the presence of the well-known particle streaks. Compared to the visualisation provided by DNS (Fig. 3.11a), both LES results (with no particle SGS model in Fig. 3.11(b); with the LMFDF model in Fig. 3.11(c), respectively) show broader particle streaks and wider inter-cluster spacing. Clusters and voids are identified by comparing the PDF of Voronoï areas obtained from the simulations to that of a synthetic random Poisson process, whose shape is well approximated by a Gamma distribution [Monchaux 2010]. This comparison is shown in Fig. 3.12, where the Voronoï areas are normalized using the average Voronoï area, \bar{A} (equivalent to the inverse of the mean particle number density), independent of the spatial organization of the particles.

As found previously [Monchaux 2010], in the case of heavy particles, the PDFs clearly depart from the Poisson distribution, with higher probability of finding depleted regions (large Voronoï areas) and concentrated regions (small Voronoï areas), a typical signature of preferential concentration. In the present study, the inclusion of the LMFDF model into

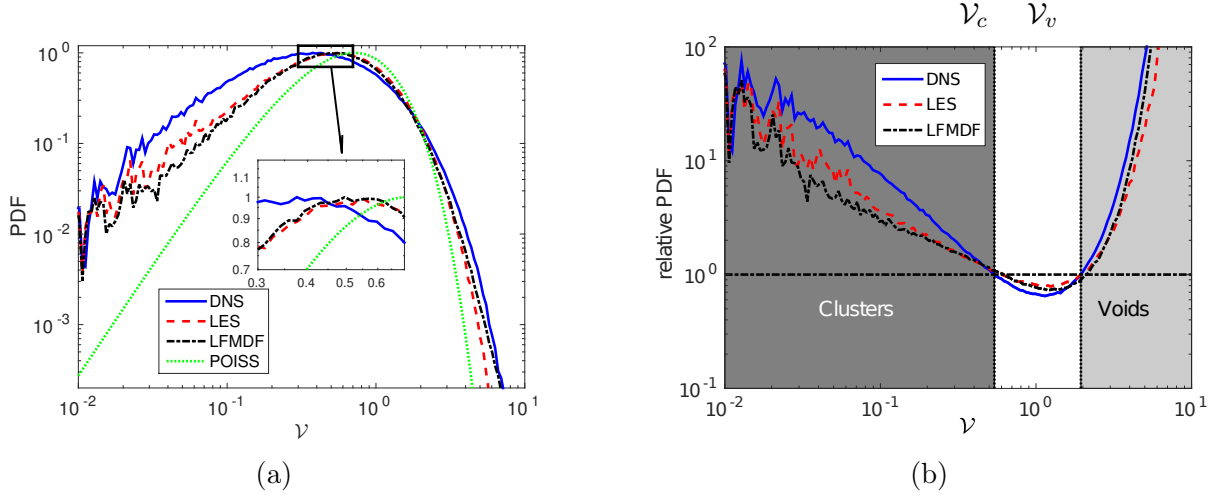


Figure 3.12: PDF of normalized Voronoï areas ($\mathcal{V} = A/\bar{A}$) of $St = 5$ particles on a wall-parallel fluid slab located at distance $1 \leq z^+ \leq 5$ from the wall.

the LES has little effect on the prediction of concentrated regions, and the first cross-over point, \mathcal{V}_c , representing the threshold value below which Voronoï areas are considered to belong to a cluster, occurs at slightly larger values than in DNS. The model improves prediction of depleted regions even if the second cross-over point, \mathcal{V}_v , representing the threshold value above which Voronoï areas are considered to belong to a void, is always well predicted.

To complete the LFMDf model assessment, in Fig. 3.13 we show the statistics of the root mean square of particle velocity. In particular, we focus on the streamwise and wall-normal components, which are the most interesting as far as particle wall transport is concerned. It can be seen that the calibrated LFMDf improves the LES prediction for all Stokes numbers, with just small (yet persistent) discrepancies for the wall-normal rms of the $St = 1$ particles (Fig. 3.13d). This explains the peak of concentration observed for these particles in the number density statistics.

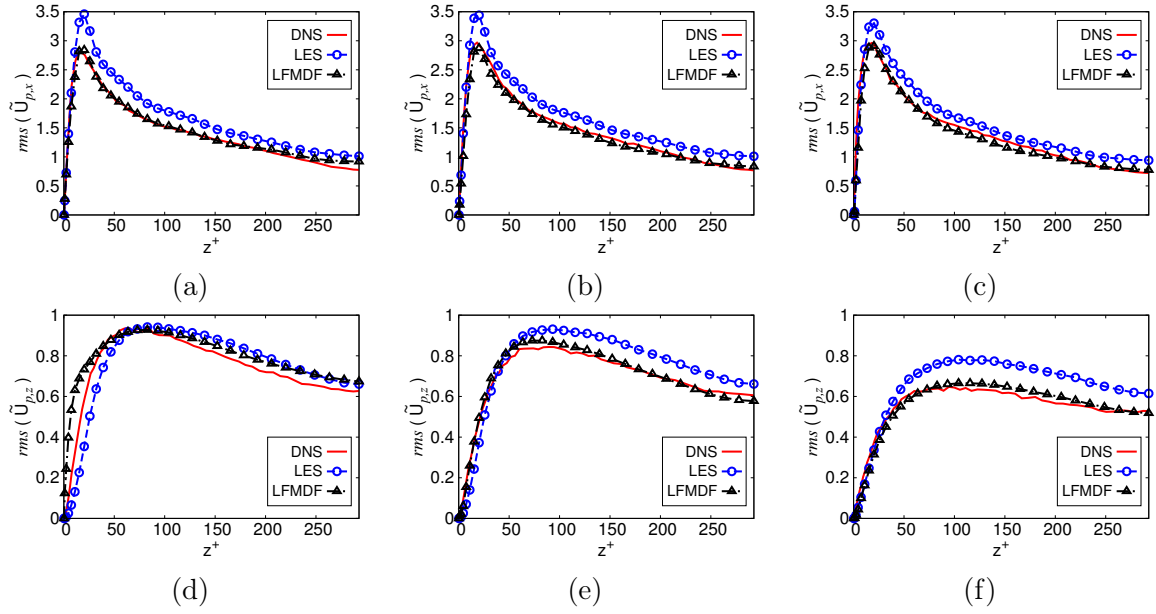


Figure 3.13: Comparative assessment of the LFMDf2 model: Prediction of the particle velocity rms at varying Stokes number (Δ) are compared with DNS results (—) and with LES results with no particle SGS model (\circ). Panels: (a),(d) $St = 1$, (b),(e) $St = 5$, (c)-(f) $St = 25$; (a)-(c) streamwise component, (d)-(f) wall-normal component. Statistics are obtained averaging over a time window $\Delta t^+ = 1800$.

3.6 Discussion and conclusions

In this work, we have assessed the performance of a new FDF approach to the simulation of turbulent dispersed flows. The approach is derived from RANS-based models that have been successfully applied to the simulation of reactive and polydispersed flows [Pope 2000, Fox 2012, Peirano 2006, Minier 2015b]. We have adopted a Lagrangian Filtered Mass Density Function (LFMDf) model that provides the Lagrangian probability density function of the SGS particle variables and of the fluid velocity seen by the particles. Important features of the proposed method are that (1) at variance with reactive flows, the approach is Lagrangian and (2) a mass density function is considered, as done in compressible flows. The exact transport equation for the LFMDf has been presented, and a modeled transport equation for the filtered density function has been considered using a closure strategy inspired by PDF methods. Specifically, two different formulations have been proposed, which differ in the treatment of the SGS scales. The simpler formulation, which assumes isotropic flow conditions, appears to work reasonably well away from the wall and for small-Stokes-number particles. The complete formulation, which accounts for flow anisotropy, works better close to the wall and with intermediate- to large-Stokes-number particles.

The modeled LFMDf transport equation has been solved numerically using a Lagrangian Monte Carlo scheme and considering a set of equivalent stochastic differential equations. These equations have been discretized with an unconditionally-stable numerical scheme based on the analytical solution that the equations admit with constant coefficients.

This scheme is the natural extension of the one developed in the context of RANS simulations and is the key ingredient for the treatment of multi-scale problems. A turbulent channel flow at shear Reynolds number $Re_\tau = 300$ based on the channel half height has been simulated and the results yield by the LFMDf method in conjunction with LES have been compared with those provided by large-eddy simulations in which no SGS model is included in the particle equations. To provide a numerical experiment as reference, results from DNS of the same flow configuration have been considered as well. It is important to remark here that Reynolds number effects on the considered statistics are expected to be marginal up to $Re_\tau \simeq 900$ [Geurts 2012], so that present results can be considered reliable below such threshold value.

The convergence of the Monte Carlo simulations and the consistency of the LFMDf formulation in the fluid-tracer limit have been assessed by comparing particle number density and low-order velocity moments with those obtained from in the purely Eulerian framework. The good agreement of duplicate (Eulerian and Lagrangian) fields demonstrates that the model can safely be applied in the case of particles with small or negligible inertia. We were also able to quantify the effect that the number of particles needed to compute the statistical observables of interest (especially the number density distribution) may have.

The *a priori* assessment made against DNS allowed us to calibrate the values of the model coefficients for the specific channel flow parameters considered in the present study. Even without dynamic calibration of the coefficients, the *a posteriori* assessment made against DNS and no-model LES show improved predictions of particle statistics (e.g. particle number density along the wall-normal coordinate and particle velocity fluctuations), especially at intermediate Stokes numbers. In spite of this, however, it should be noted that the LFMDf is a purely statistical method, and therefore can not recover much as far as turbulent coherent structures are concerned.

In our opinion, the LFMDf formulation considered in this paper provides a rigorous and physically-sound approach to the large-eddy simulation of turbulent dispersed flows. Compared to the existing stochastic models, it offers a sound theoretical framework in which the basic exact equations for the particle phase are approximated by Lagrangian closures without requiring ad-hoc term. In particular, the approach ensures consistency (up to second-order) among the moments extracted from the stochastic particle system in the tracer-particle limit, a property that not all stochastic models and heuristic approaches possess. Moments consistency in the tracer limit is one of the requirements set forth in the recent analysis of the formulation of stochastic models for single- and two-phase flows [Minier 2014]. Compared to structural subgrid scale models for particles, the main advantage of the LFMDf approach is its ability to provide reasonably accurate predictions regardless of the grid coarseness and of the flow Reynolds number: approximate deconvolution is known to worsen its performance on coarse grids at high Reynolds numbers, when the range of unresolved scales that cannot be reconstructed by deconvolution widens [Gobert 2010]; fractal interpolation is inaccurate at low Reynolds numbers, when the fluid velocity changes relatively smoothly in the domain and therefore interpolation becomes inefficient since there is no fractal form to be copied [Marchioli 2008a]. The discretized equations of the LFMDf model are also very easy to code and require incremental computational costs compared to LES with no SGS model. While we believe it should be used

as the natural framework to develop Lagrangian sub-grid models for the dispersed phase, we are also aware that there is room for further improving the quality and predictive capabilities of the model. A first step would be the development of a dynamic procedure to determine the optimal values of the model coefficients, possibly as a function of the particle Stokes number. Another improvement could be represented by the implementation of higher order closures in the Langevin equation for the fluid velocity seen by the particles. Finally, it would be very useful to implement low- Re corrections to better capture the near-wall behaviour of the statistics: This should improve the model predictions at relatively low particle inertia (e.g. $St = 1$ in the present study).

Acknowledgments

The Authors warmly thank J.-P. Minier for the contribution in the development of the formalism, and Alfredo Soldati and Maria Vittoria Salvetti for the useful discussions.

3.A Weak first-order Numerical scheme

The analytical solution to the Eqns. (3.25)-(3.27) can be obtained with constant coefficients, resorting to Itô's calculus in combination with the method of the variation of constants. Let us consider the fluid velocity seen by the particles, for instance. One seeks a solution of the form $U_{s,i}(t) = H_i(t) \exp(-t/T_i)$, where $H_i(t)$ is a stochastic process defined by (indicating $T_{L,i}^*$ with T_i for ease of notation):

$$dH_i(t) = \exp(t/T_i)[C_i dt + \check{B}_i dW_i(t)], \quad (3.42)$$

that is, by integration on a time interval $[t_0, t]$ ($\Delta t = t - t_0$),

$$U_{s,i}(t) = U_{s,i}(t_0) \exp(-\Delta t/T_i) + C_i T_i [1 - \exp(-\Delta t/T_i)] \quad (3.43)$$

$$+ \check{B}_i \exp(-t/T_i) \int_{t_0}^t \exp(s/T_i) dW_i(s), \quad (3.44)$$

where $\check{B}_i = B_{ii}$ since B_{ij} is a diagonal matrix. The derivation of the weak first-order scheme is now rather straightforward since the analytical solutions to Eqns. (3.25)-(3.27) with constant coefficients have been already calculated. Indeed, the Euler scheme (which is a weak scheme of order 1) is simply obtained by freezing the coefficients at the beginning of the time interval $\Delta t = [t_n, t_{n+1}]$. Let Z_i^n and Z_i^{n+1} be the approximated values of $Z_i(t)$ at time t_n and t_{n+1} , respectively. The Euler scheme is then simply written by using the expression reported in Table 5.3 and expressing the stochastic integrals through the Choleski algorithm, as reported in Table 3.5. The second-order scheme is based on a prediction-correction algorithm, in which the prediction step is the first-order scheme of equations (3.35)-(3.37) and the corrector step is generated by a Taylor expansion under the assumption that the acceleration terms vary linearly with time [Peirano 2006].

Table 3.4: Analytical solutions to system (3.27) for time-independent coefficients.

$$\begin{aligned}
x_{p,i}(t) &= x_{p,i}(t_0) + U_{p,i}(t_0)\tau_p[1 - \exp(-\Delta t/\tau_p)] + U_{s,i}(t_0)\theta_i\{T_i[1 - \exp(-\Delta t/T_i)] \\
&\quad + \tau_p[\exp(-\Delta t/\tau_p) - 1]\} + [C_i T_i]\{\Delta t - \tau_p[1 - \exp(-\Delta t/\tau_p)] - \theta_i(T_i[1 - \exp(-\Delta t/T_i)] \\
&\quad + \tau_p[\exp(-\Delta t/\tau_p) - 1])\} + \Omega_i(t) \\
&\quad \text{with } \theta_i = T_i/(T_i - \tau_p)
\end{aligned} \tag{3.45}$$

$$\begin{aligned}
U_{p,i}(t) &= U_{p,i}(t_0)\exp(-\Delta t/\tau_p) + U_{s,i}(t_0)\theta_i[\exp(-\Delta t/T_i) - \exp(-\Delta t/\tau_p)] \\
&\quad + [C_i T_i]\{[1 - \exp(-\Delta t/\tau_p)] - \theta_i[\exp(-\Delta t/T_i) - \exp(-\Delta t/\tau_p)]\} + \Gamma_i(t)
\end{aligned} \tag{3.46}$$

$$U_{s,i}(t) = U_{s,i}(t_0)\exp(-\Delta t/T_i) + C_i T_i[1 - \exp(-\Delta t/T_i)] + \gamma_i(t) \tag{3.47}$$

The stochastic integrals $\gamma_i(t)$, $\Gamma_i(t)$, $\Omega_i(t)$ are given by:

$$\gamma_i(t) = \check{B}_i \exp(-t/T_i) \int_{t_0}^t \exp(s/T_i) dW_i(s), \tag{3.48}$$

$$\Gamma_i(t) = \frac{1}{\tau_p} \exp(-t/\tau_p) \int_{t_0}^t \exp(s/\tau_p) \gamma_i(s) ds, \tag{3.49}$$

$$\Omega_i(t) = \int_{t_0}^t \Gamma_i(s) ds. \tag{3.50}$$

By resorting to stochastic integration by parts, $\gamma_i(t)$, $\Gamma_i(t)$, $\Omega_i(t)$ can be written:

$$\gamma_i(t) = \check{B}_i \exp(-t/T_i) I_{1,i}, \tag{3.51}$$

$$\Gamma_i(t) = \theta_i \check{B}_i [\exp(-t/T_i) I_{1,i} - \exp(-t/\tau_p) I_{2,i}], \tag{3.52}$$

$$\Omega_i(t) = \theta_i \check{B}_i \{(T_i - \tau_p) I_{3,i} - [T_i \exp(-t/T_i) I_{1,i} - \tau_p \exp(-t/\tau_p) I_{2,i}]\}, \tag{3.53}$$

$$\text{with } I_{1,i} = \int_{t_0}^t \exp(s/T_i) dW_i(s), \quad I_{2,i} = \int_{t_0}^t \exp(s/\tau_p) dW_i(s), \quad I_{3,i} = \int_{t_0}^t dW_i(s).$$

Table 3.5: Derivation of the covariance matrix for constant coefficients.

$$\langle \gamma_i^2(t) \rangle = \check{B}_i^2 \frac{T_i}{2} [1 - \exp(-2\Delta t/T_i)] \quad \text{where} \quad \check{B}_i^2 = B_{ii}^2 \quad (3.54)$$

$$\begin{aligned} \langle \Gamma_i^2(t) \rangle = \check{B}_i^2 \theta_i^2 \left\{ \frac{T_i}{2} [1 - \exp(-2\Delta t/T_i)] - \frac{2\tau_p T_i}{T_i + \tau_p} [1 - \exp(-\Delta t/T_i) \exp(-\Delta t/\tau_p)] \right. \\ \left. + \frac{\tau_p}{2} [1 - \exp(-2\Delta t/\tau_p)] \right\} \end{aligned} \quad (3.55)$$

$$\begin{aligned} \frac{1}{\check{B}_i^2 \theta_i^2} \langle \Omega_i^2(t) \rangle = (T_i - \tau_p)^2 \Delta t + \frac{T_i^3}{2} [1 - \exp(-2\Delta t/T_i)] + \frac{\tau_p^3}{2} [1 - \exp(-2\Delta t/\tau_p)] \\ - 2T_i^2 (T_i - \tau_p) [1 - \exp(-\Delta t/T_i)] + 2\tau_p^2 (T_i - \tau_p) [1 - \exp(-\Delta t/\tau_p)] \\ - 2 \frac{T_i^2 \tau_p^2}{T_i + \tau_p} [1 - \exp(-\Delta t/T_i) \exp(-\Delta t/\tau_p)] \end{aligned} \quad (3.56)$$

$$\begin{aligned} \langle \gamma_i(t) \Gamma_i(t) \rangle = \check{B}_i^2 \theta_i T_i \left\{ \frac{1}{2} [1 - \exp(-2\Delta t/T_i)] - \frac{\tau_p}{T_i + \tau_p} [1 - \exp(-\Delta t/T_i) \exp(-\Delta t/\tau_p)] \right\} \\ \langle \gamma_i(t) \Omega_i(t) \rangle = \check{B}_i^2 \theta_i T_i \left\{ (T_i - \tau_p) [1 - \exp(-\Delta t/T_i)] - \frac{T_i}{2} [1 - \exp(-2\Delta t/T_i)] \right. \\ \left. + \frac{\tau_p^2}{T_i + \tau_p} [1 - \exp(-\Delta t/T_i) \exp(-\Delta t/\tau_p)] \right\} \end{aligned} \quad (3.57)$$

$$\begin{aligned} \frac{1}{\check{B}_i^2 \theta_i^2} \langle \Gamma_i(t) \Omega_i(t) \rangle = (T_i - \tau_p) \{ T_i [1 - \exp(-\Delta t/T_i)] - \tau_p [1 - \exp(-\Delta t/\tau_p)] \} \\ - \frac{T_i^2}{2} [1 - \exp(-2\Delta t/T_i)] - \frac{\tau_p^2}{2} [1 - \exp(-2\Delta t/\tau_p)] \\ + T_i \tau_p [1 - \exp(-\Delta t/T_i) \exp(-\Delta t/\tau_p)] \end{aligned} \quad (3.58)$$

The stochastic integrals γ_i^n , Ω_i^n , Γ_i^n are simulated by:

$$\gamma_i^n = P_{11}^i \mathcal{G}_{1,i},$$

$$\Omega_i^n = P_{21}^i \mathcal{G}_{1,i} + P_{22}^i \mathcal{G}_{2,i}$$

$$\Gamma_i^n = P_{31}^i \mathcal{G}_{1,i} + P_{32}^i \mathcal{G}_{2,i} + P_{33}^i \mathcal{G}_{3,i},$$

where $\mathcal{G}_{1,i}$, $\mathcal{G}_{2,i}$, $\mathcal{G}_{3,i}$ are independent $\mathcal{N}(0, 1)$ random variables.

The coefficients P_{11}^i , P_{21}^i , P_{22}^i , P_{31}^i , P_{32}^i , P_{33}^i are defined as:

$$P_{11}^i = \sqrt{\langle (\gamma_i^n)^2 \rangle},$$

$$P_{21}^i = \frac{\langle \Omega_i^n \gamma_i^n \rangle}{\sqrt{\langle (\gamma_i^n)^2 \rangle}}, \quad P_{22}^i = \sqrt{\langle (\Omega_i^n)^2 \rangle - \frac{\langle \Omega_i^n \gamma_i^n \rangle^2}{\langle (\gamma_i^n)^2 \rangle}},$$

$$P_{31}^i = \frac{\langle \Gamma_i^n \gamma_i^n \rangle}{\sqrt{\langle (\gamma_i^n)^2 \rangle}}, \quad P_{32}^i = \frac{1}{P_{22}^i} (\langle \Omega_i^n \Gamma_i^n \rangle - P_{21}^i P_{31}^i), \quad P_{33}^i = \sqrt{\langle (\Gamma_i^n)^2 \rangle - (P_{31}^i)^2 - (P_{32}^i)^2}.$$

A Lagrangian probability-density-function model for collisional turbulent fluid-particle flows

A. Innocenti^{1,2}, R. O. Fox³, M. V. Salvetti², S. Chibbaro¹

¹ Sorbonne Université, CNRS, Institut Jean Le Rond d'Alembert, F-75005 Paris, France

² Dipartimento di Ingegneria Civile e Industriale, Università di Pisa, Via G. Caruso 8,
56122 Pisa, Italia

³ Department of Chemical and Biological Engineering, 618 Bissell Road, Iowa State
University, Ames, IA 50011-1098, USA

Paper under revision for *Journal of Fluid Mechanics*.

In this chapter we have faced the problem of dense fluid-particle flows in homogeneous flow conditions. The work is under revision for publication on the *Journal of Fluid Mechanics*. Initially it was conceived in two parts: part (i) was about the model derivation ([arXiv:1803.00251](#)), while part (ii) proposed several homogenous applications ([arXiv:1803.00318](#)). Under the review process it has been merged in a single paper, shortening some parts to make it more readable. Therefore we propose here the work as-is in the actual revised form, and we will add more details on the part of model derivations at the end of the chapter.

As it was shown in the previous chapter particles tend to cluster when they are immersed in a turbulent flow and thus regions with high concentrations, where two-way coupling becomes important, might arise. More simply, in some cases, the coupling can be important just because the initial particle concentration is high, yet uniform. To address the coupling regime we have proposed a stochastic particle model based on the RANS/PDF formalism.

The objective was to try to recreate a homogeneous cluster-induced-turbulence, where, starting from rest, particles start to fall under the effect of gravity and induce turbulence in the carrier phase. This effect however can be seen only if the particle mass loading is high enough, resulting in a moderately dense regime, where also inter-particle collisions might play an important role.

Hence, we have proposed a stochastic model that separate the particle velocity into a correlated and an uncorrelated in space component, which are treated as two separate processes. In this way collisions can be correctly taken into account in the non correlated part

and it is also possible to identify different Lagrangian time scales for the two components, which are important to identify the correct rate of energy transfer from the correlated to the uncorrelated part, and to couple the fluid and particle phases. Moreover, we have shown that the model is fully consistent, in a statistical sense, to the hydrodynamic description proposed by [Capecelatro 2015]. Overall the model has provided excellent results in the CIT case, compared to DNS, and has proved to be consistent also at lower mass loadings, below the collisional regime but where particle-turbulence modulation is still present.

Beside this, we have also proposed a compact form of the model without the velocity decomposition but still with two-way coupling, and we have shown that, thanks to some improvements with respect to existing models, it is able to trigger the instability which leads to the generation of turbulence. However only a qualitative agreement with the DNS can be reached. This has proven the idea behind this part of work, that was to see if a simple stochastic model for particle-laden flows with two-way coupling, was or not a good candidate to reproduce the phenomenon of turbulence generation by a dispersed phase.

A key point in both models, that was not present in stochastic models for dilute flows, is the possibility to predict a drift velocity $u_d = \langle U_s \rangle - \langle U_f \rangle$, (where U_s is the fluid velocity seen by the particles) which is necessary in order to have a production of energy in the fluid due to the particle-phase, and which is therefore fundamental to reproduce CIT.

Abstract: Inertial particles in turbulent flows are characterised by preferential concentration and segregation and, at sufficient mass loading, dense particle clusters may spontaneously arise due to momentum coupling between the phases. These clusters, in turn, can generate and sustain turbulence in the fluid phase, which we refer to as cluster-induced turbulence (CIT). In the present work, we tackle the problem of developing a framework for the stochastic modelling of moderately dense particle-laden flows, based on a Lagrangian probability-density-function formalism. This framework includes the Eulerian approach, and hence can be useful also for the development of two-fluid models. A rigorous formalism and a general model have been put forward focusing, in particular, on the two ingredients that are key in moderately dense flows, namely, two-way coupling in the carrier phase, and the decomposition of the particle-phase velocity into its spatially correlated and uncorrelated components. Specifically, this last contribution allows to identify in the stochastic model the contributions due to the correlated fluctuating energy and to the granular temperature of the particle phase, which determines the time scale for particle–particle collisions. The model is then validated and assessed against direct-numerical-simulation data for homogeneous configurations of increasing difficulty: (i) homogeneous isotropic turbulence, (ii) decaying and shear turbulence, and (iii) CIT.

4.1 Introduction

Particle-laden flows represent an important class of natural and industrial flows [Crowe 2011]. In many applications, these flows are heavily loaded with particles [Stickel 2005, Forterre 2008, Guazzelli 2011] and are often turbulent [Balachandar 2010]. Given the complexity of the physical phenomena involved in such flows, they remain relatively poorly understood and, notably, the formulation of physically sound reduced models is mandatory for practical purposes. To guide this development it is very useful to disentangle the different physical mechanisms at play, and in particular to understand how to cope with the effect of increasing the particle mass loading and the consequent growing importance of collisions and two-way coupling. Indeed, the back reaction exerted by the particles on the fluid gives rise to an extra complexity in modelling [Elghobashi 1994]. The understanding of the mechanisms at play, even at a purely qualitative level, is an important subject of research for developing efficient models of relevance to applications [Post 2002, Jenny 2012, Gualtieri 2017]. Unfortunately, it is hard to find clear-cut frontiers between the different regimes [Elghobashi 1992], and thus some heuristic considerations are always needed.

Generally speaking, two classes of probability-density-function (pdf) modelling approaches can be chosen for turbulent flows, namely, Eulerian and Lagrangian [Pope 2000]. When the flow is dilute or moderately dense, the Lagrangian pdf approach is mature [Minier 2014] and has the desirable features detailed below [Peirano 2006]. On the other hand, when the volume occupied by the particles is relatively large, collisions are completely dominant, the matter becomes granular, turbulence is absent (or has no effect on the particles) and a hydrodynamic approach is often natural [Puglisi 2014]. We consider in this work the intermediate regime of moderately dense turbulent flows, which is less clear.

From a historical perspective, turbulence models for dense flows have been developed in an Eulerian pdf framework on a purely heuristic grounds in analogy with single-phase

models [Elghobashi 1983, Viollet 1994]. Only recently, it has been shown that most of those models suffer from some drawbacks and a more rigorous approach has been followed to formulate a complete Reynolds-stress model [Fox 2014]. From a modelling point of view, the key, but often overlooked, point for the modelling of turbulent dense flows seems to be the separation between the spatially correlated part, contributing to the turbulent kinetic energy, and the uncorrelated part, responsible for the granular temperature [Dasgupta 1994, Février 2005]. This decomposition is motivated by several works in the literature [Capecelatro 2015, Capecelatro 2016b] which pointed out that it leads to a clear distinction between the particle turbulent kinetic energy, related to the spatially correlated part, and the granular temperature due to the uncorrelated part. These two quantities are driven by different mechanisms and therefore need to be modelled separately in moderately dense flows [Capecelatro 2015]. In particular, owing to the fact that particle–particle collisions are driven by the spatially uncorrelated velocity component, this decomposition is thought to be crucial for collisional flows. Based upon this decomposition, we have developed in the present work a Lagrangian pdf approach, which leads to a stochastic model for the particle phase, that has to be coupled with a consistent Reynolds-stress model for the fluid.

There were several motivations for choosing a Lagrangian pdf approach: (i) it is more intuitive for particle-laden flows and therefore relevant; (ii) some specific issues are particularly arduous to tackle in the Eulerian pdf approach, requiring the Lagrangian one, namely, local but nonlinear phenomenon like polydispersity and chemical reactions [Pope 2000, Fox 2003]; (iii) the Lagrangian pdf approach provides more detailed information, in particular the velocity of the fluid seen by particles is available whereas it is not in Eulerian pdf models; moreover, it is possible to capture the crossing-trajectory effect due to the mean drift of particles due to the spatial variation of fluid velocity [Minier 2001]; (iv) the possibility to test different models will provide insights into the role of each term, notably the granular energy, in the development of the particle and fluid turbulence; (v) it is quite difficult to propose sound and realisable Eulerian moment equations for the particle phase, wherein many terms appear unclosed. The development of the Lagrangian pdf approach also helps to derive consistent Eulerian pdf models, which cannot be derived in other ways.

More specifically, in this work, we test two Lagrangian pdf models describing the particle phase, coupled with Reynolds-average Eulerian equations for the fluid phase. The first model is based on the velocity partitioning between correlated and uncorrelated components. The second one is a simplified version, where only the total particle velocity, derived as the sum of the two components, is resolved, leading to the lack of distinction between the particle turbulent kinetic energy and the granular temperature. We focus here on statistically homogeneous turbulence. In particular, the goal of the paper is to understand if the pdf models are able to deal with the momentum and energy exchange between phases, and the particle concentration fluctuations. These ingredients are essential in all moderately dense particle-laden flows, and therefore it is important to use the homogeneous cases in order to isolate their modelling from other complex features present in inhomogeneous configurations (e.g. spatial fluxes). In particular, we are interested in cluster-induced turbulence (CIT), which occurs in fluid–particle flows when (i) the mean mass loading φ , defined by the ratio of the specific masses of the particle and fluid phases, is of order one or

larger; and (ii) the difference between the mean phase velocities is non-zero. Interestingly, in statistically stationary flows, fluctuations in particle concentration can generate and sustain fluid-phase turbulence, which we refer to as fully developed CIT. Given that the density ratio $\frac{\rho_p}{\rho_f}$ is very large in gas–particle flows, CIT is ubiquitous in practical engineering and environmental flows when body forces or inlet conditions generate a mean velocity difference, such as the gravity-driven flows studied herein. Some fundamental properties of such flows has been recently studied via Eulerian–Lagrangian numerical simulations [Capecelatro 2014, Capecelatro 2015], which will be used for comparison. Notably, the use of models can be relevant to emphasise the mechanisms underlying the volume-fraction fluctuations.

From a physical point of view, we want to assess the pdf models with respect to their ability to reproduce the statistical features of both the particle and fluid phases at high mass loading. It is well known that turbulent particle-laden flows in the dilute limit, where the fluid-phase turbulence interacts with inertial particles without significant feedback from the particles, display a preferential concentration of particles in certain regions [Balkovsky 2001, Balachandar 2010]. In particular, it is well established that dilute suspensions of heavy particles in isotropic turbulence will preferentially concentrate in regions of high strain rate and low vorticity [Eaton 1994]. When two-way coupling between the phases is non-negligible, additional effects may be responsible for enhancing the settling rate and spatial segregation of the particles. Among the possible effects, it is worth mentioning the enhancement of particle settling velocity with increasing volume fraction [Bosse 2006], and the creation of strong anisotropy due to the crossing-trajectory effect [Ferrante 2003] causing also a drag reduction. However, even more impressive is the situation at higher mass loading, where the fluctuating segregation of particles, together with collisions, have been found to create large clusters that induce turbulence in a fluid otherwise at rest [Glasser 1998, Capecelatro 2015], giving rise to CIT. Notably, in gravity-driven CIT, particles accumulate in regions of low vorticity, as is seen in classical preferential concentration of low-mass-loading suspensions. However, in CIT the vorticity is generated in shear layers between clusters, unlike in classical preferential concentration, where vorticity would exist even in the absence of the disperse phase.

The goal of the present work is precisely to understand whether the proposed pdf models are capable of reproducing quantitatively the phenomena observed in homogeneous particle-laden flows, and also to determine which elements are necessary to trigger the instability leading to CIT.

The paper is organised as follows. In §4.2 we derive the exact Lagrangian pdf equations, which are the starting point to build the pdf model. In §4.3 the Lagrangian pdf model for the particle phase is presented, followed in §4.4 by the one for the fluid velocity seen by particles, and in §4.5 the Eulerian Reynolds-average (RA) model for the fluid phase. Then, in §4.6 RA equations corresponding to the Lagrangian pdf model and in §4.7 the complete set of fluid- and particle-phase RA equations are specified for the statistically homogeneous case. In §4.8, the models are applied to increasingly more complex particle-laden flows and the results compared to data from the literature, and finally in §4.9, conclusions are drawn concerning the relative merits of the proposed pdf models, along with a discussion of future challenges to be faced with applying them to spatially inhomogeneous flows.

4.2 Rationale for the model construction

When dealing with fluid–particle flows, several levels of description are possible, depending on the amount of information we retain and on the accuracy we are willing to accept. A direct-numerical simulation (DNS) of the Navier–Stokes (NS) equations where the fluid phase is completely resolved around particles, along with the application of no-slip boundary conditions on the particle surface, is what we refer to as the microscopic description [Ten Cate 2004, Chouippe 2015, Picano 2015, Tanaka 2017]. It implies a large amount of information to be handled, since we need a sufficient number of points per particle diameter to describe accurately particle geometry and fluid–particle interactions. Therefore the number of resolved particles is generally limited because of the high computational demand, and this level of description is often unnecessary since particles are small enough to justify a point-wise approximation [Gatignol 1983, Maxey 1983], even though finite-size effects are important for small systems [Pedley 1992], and larger particles [Picano 2013, Mehrabadi 2018].

Adopting a Lagrangian point of view, small particles with a high particle–fluid density ratio, $\rho_p/\rho_f \gg 1$, can be treated as point particles, where the equation of motion for a particle (k) reduces to:

$$\frac{d\mathbf{V}_p^{(k)}}{dt} = \frac{\mathbf{U}_f(\mathbf{x}_p) - \mathbf{V}_p^{(k)}}{\tau_p} + \mathbf{g} + \mathbf{A}_c^{(k)} \quad (4.1)$$

where $\mathbf{U}_f(\mathbf{x}_p)$ is the fluid velocity at the particle position, \mathbf{g} is gravity acceleration, \mathbf{A}_c is the acceleration term due to collisions, and τ_p is the particle relaxation time

$$\tau_p = \frac{\rho_p d_p^2}{18\rho_f \nu_f}. \quad (4.2)$$

Instead of building a pdf model directly on (4.1), we propose to do an intermediate step where we apply a Lagrangian coarse-graining operator, $f^L(\mathbf{x}^{(k)}(t), \mathbf{V}_p, t)$, to (4.1). This function is the Lagrangian pdf counterpart of the kinetic approach developed for rapid granular flows animated by elastic or inelastic collisions [Jenkins 1983, Brey 1998, Brilliantov 2010], and used in the Eulerian pdf description of turbulent flows [Capece de Almeida 2015]. Therefore, this procedure allows to find a Lagrangian pdf level of description. In particular, this operator is a local average and yields a decomposition of the particle velocity into a spatially correlated component and an uncorrelated one, as initially introduced by [F  vrier 2005] in the dilute case. Moreover the coarse-graining operator has the following properties: (i) the residual part has zero mean; (ii) the residual part is uncorrelated with the filtered part. With this definition, we have that the hydrodynamic or correlated component is

$$\tilde{\mathbf{V}}_p(\mathbf{x}^{(k)}(t), t) = \int \mathbf{V}_p f^L(\mathbf{x}^{(k)}(t), \mathbf{V}_p, t) d\mathbf{V}_p, \quad (4.3)$$

and the complete velocity is given by

$$\mathbf{V}_p^{(k)} = \tilde{\mathbf{V}}_p(\mathbf{x}^{(k)}(t), t) + \delta\mathbf{V}_p^{(k)} \quad (4.4)$$

where we have indicated the coarse-grained quantities with the tilde symbol \sim . It is interesting to remark that this coarse graining shares some similarity with a recent

Lagrangian pdf large-eddy simulation filtering formalism applied to particle-laden flows [Innocenti 2016].

We can now apply the coarse-graining operator to (4.1), neglecting for the moment the effect of collisions:

$$\frac{d\widetilde{V}_{p,i}}{dt} = \frac{\partial \widetilde{V}_{p,i}}{\partial t} + \widetilde{V}_{p,j} \frac{\partial \widetilde{V}_{p,i}}{\partial x_j} + \frac{\partial \delta \widetilde{V}_{p,i} \delta \widetilde{V}_{p,j}}{\partial x_j} = \frac{\widetilde{U}_{f,i} - \widetilde{V}_{p,i}}{\tau_p} + g_i. \quad (4.5)$$

The Lagrangian transport equation of $\widetilde{V}_{p,i}$ can therefore be expressed as

$$\begin{aligned} \frac{d\widetilde{V}_{p,i}}{dt} &= \frac{\partial \widetilde{V}_{p,i}}{\partial t} + V_{p,j} \frac{\partial \widetilde{V}_{p,i}}{\partial x_j} \\ &= \frac{\partial \widetilde{V}_{p,i}}{\partial t} + \widetilde{V}_{p,j} \frac{\partial \widetilde{V}_{p,i}}{\partial x_j} + \delta V_{p,j} \frac{\partial \widetilde{V}_{p,i}}{\partial x_j} \\ &= \frac{\widetilde{U}_{f,i} - \widetilde{V}_{p,i}}{\tau_p} + g_i - \frac{\partial \delta \widetilde{V}_{p,i} \delta \widetilde{V}_{p,j}}{\partial x_j} + \delta V_{p,j} \frac{\partial \widetilde{V}_{p,i}}{\partial x_j}. \end{aligned} \quad (4.6)$$

On the other hand, it is also possible to explicitly express the residual part, since its material derivative is given by

$$\begin{aligned} \frac{d\delta V_{p,i}}{dt} &= \frac{d(V_{p,i} - \widetilde{V}_{p,i})}{dt} \\ &= \frac{\widetilde{U}_{f,i} - V_{p,i}}{\tau_p} + g_i - \frac{\widetilde{U}_{f,i} - \widetilde{V}_{p,i}}{\tau_p} - g_i + \frac{\partial \delta \widetilde{V}_{p,i} \delta \widetilde{V}_{p,j}}{\partial x_j} - \delta V_{p,j} \frac{\partial \widetilde{V}_{p,i}}{\partial x_j} \\ &= -\frac{\delta V_{p,i}}{\tau_p} + \frac{\partial \delta \widetilde{V}_{p,i} \delta \widetilde{V}_{p,j}}{\partial x_j} - \delta V_{p,j} \frac{\partial \widetilde{V}_{p,i}}{\partial x_j}. \end{aligned} \quad (4.7)$$

Multiplying (4.7) by $\delta V_{p,j}$ and summing with its transpose term, the Lagrangian transport equation for the uncorrelated energy tensor, i.e. the particle-phase pressure tensor, can be obtained:

$$\begin{aligned} d(\delta V_{p,i} \delta V_{p,j}) &= -2 \frac{\delta V_{p,i} \delta V_{p,j}}{\tau_p} dt - \delta V_{p,i} \delta V_{p,k} \frac{\partial \widetilde{V}_{p,j}}{\partial x_k} dt - \delta V_{p,j} \delta V_{p,k} \frac{\partial \widetilde{V}_{p,i}}{\partial x_k} dt \\ &\quad + \delta V_{p,i} \frac{\partial \delta \widetilde{V}_{p,j} \delta \widetilde{V}_{p,k}}{\partial x_k} dt + \delta V_{p,j} \frac{\partial \delta \widetilde{V}_{p,i} \delta \widetilde{V}_{p,k}}{\partial x_k} dt. \end{aligned} \quad (4.8)$$

Following this decomposition, we can thus define two different Lagrangian stochastic processes, one for the coarse-grained particle velocity and one for the residual component:

$$\begin{cases} d\widetilde{V}_{p,i} = \frac{\widetilde{U}_{f,i} - \widetilde{V}_{p,i}}{\tau_p} dt + g_i dt - \frac{\partial \delta \widetilde{V}_{p,i} \delta \widetilde{V}_{p,k}}{\partial x_k} dt + \delta V_{p,k} \frac{\partial \widetilde{V}_{p,i}}{\partial x_k} dt \\ d\delta V_{p,i} = -\frac{\delta V_{p,i}}{\tau_p} dt + \frac{\partial \delta \widetilde{V}_{p,i} \delta \widetilde{V}_{p,k}}{\partial x_k} dt - \delta V_{p,k} \frac{\partial \widetilde{V}_{p,i}}{\partial x_k} dt \end{cases} \quad (4.9)$$

These equations are the Lagrangian pdf counterpart of the *Eulerian equations* of [Jenkins 1983] and [Capecelatro 2015] and we will refer to them as *Lagrangian pdf equations*.

It is important to underline that this picture is valid for a given fluid realisation. For laminar flows, which are not sensitive to initial and boundary conditions, the flow is always the same, independent from the realisation, given the geometry and the initial state. For turbulent flows, the situation is more complicated and, because of the inevitable presence of small perturbations, the instantaneous field changes at each realisation. Therefore if one performs averages of the relevant observables over different realisations, the statistical quantities obtained are the Reynolds-averaged (RA) ones. In particular, the RA transport equations obtained from (4.9) (reported in appendix 4.A), are not closed and cannot be used without a modelling step. Instead of modelling directly the RA equations, as done for instance by [Capecelatro 2016b], we model here the Lagrangian pdf equations through a stochastic approach in order to retrieve the correct terms in an average sense.

4.3 Lagrangian pdf model for the particle phase

To clearly explain the derivation of the pdf model, we need to introduce some concepts related to the averaging procedure. Keeping in mind the definition of a phase-average (PA) [Capecelatro 2015], where a quantity is weighted with the volume fraction when averaging, we recall that the RA of a Lagrangian quantity is also a PA, since we are implicitly weighting with the phase volume fraction. In particular, if we indicate the average with brackets $\langle \cdot \rangle$, we will have for the fluid phase $\langle (\cdot) \rangle_f = \langle \alpha_f (\cdot) \rangle / \langle \alpha_f \rangle$ and for the particle phase $\langle (\cdot) \rangle_p = \langle \alpha_p (\cdot) \rangle / \langle \alpha_p \rangle$, where $\langle \alpha_p \rangle$ and $\langle \alpha_f \rangle = 1 - \langle \alpha_p \rangle$ are respectively the particle-phase and the fluid-phase volume fractions. To simplify the notation we will drop the subscript indicating the phase, except when doing cross averages, as for instance a fluid quantity weighted with the particle volume fraction.

From the definition of the coarse-graining operator given in §4.2, we have that

$$\langle \tilde{\mathbf{V}}_p \rangle = \langle \mathbf{V}_p \rangle, \quad \langle \delta \mathbf{V}_p \rangle = 0. \quad (4.10)$$

The total particle-phase fluctuating energy is defined by

$$\kappa_p = \frac{1}{2} \langle \mathbf{v}_p \cdot \mathbf{v}_p \rangle \quad (4.11)$$

where $\mathbf{v}_p = \mathbf{V}_p - \langle \mathbf{V}_p \rangle$ is the total fluctuation in the particle velocity, which can also be expressed as the sum of two contributions: the fluctuation of the coarse-grained, correlated part, $\tilde{\mathbf{v}}_p = \tilde{\mathbf{V}}_p - \langle \tilde{\mathbf{V}}_p \rangle$, and the uncorrelated part, $\delta \mathbf{V}_p$. By means of this decomposition, the total particle-phase fluctuating energy can, in turn, be split in two contributions, the turbulent particle-phase kinetic energy and the granular temperature:

$$\kappa_p = k_p + \frac{3}{2} \langle \Theta_p \rangle \quad (4.12)$$

where

$$k_p = \frac{1}{2} \langle \tilde{\mathbf{v}}_p \cdot \tilde{\mathbf{v}}_p \rangle \quad \langle \Theta \rangle_p = \frac{1}{3} \langle \widetilde{\delta \mathbf{V}_p \cdot \delta \mathbf{V}_p} \rangle. \quad (4.13)$$

The granular temperature can equally be found from the trace of the particle-phase pressure tensor

$$\langle \mathbf{P} \rangle = \langle \widetilde{\delta \mathbf{V}_p \otimes \delta \mathbf{V}_p} \rangle. \quad (4.14)$$

The distinction between k_p and $\langle\Theta_p\rangle$, as already said, is crucial in turbulence modelling of multiphase flows because, for example, they have different boundary conditions and the particle–particle collision frequency depends on Θ_p [Capecelatro 2016b].

4.3.1 Modelled equations

To distinguish modelled terms from exact ones, we will call \mathbf{U}_p the model for $\tilde{\mathbf{V}}_p$, and $\delta\mathbf{v}_p$ the model for $\delta\mathbf{V}_p$. It is worth recalling that \mathbf{U}_p and $\delta\mathbf{v}_p$ are two stochastic processes modelling the particle total velocity, and therefore they are both advected by it, i.e., by $\mathbf{V}_p = \mathbf{U}_p + \delta\mathbf{v}_p$.

Keeping in mind (4.9), the principle that drives the modelling is to retain the closed terms (drag force), which can be expressed exactly, while the transport terms, which involve spatial gradients (last two terms in (4.9)) are split in a mean part and a fluctuation. The mean part, being available from Lagrangian averages, is plugged in the model, while fluctuations are modelled through white noises and drift terms. Those terms have been constructed in order to give the correct RA equations when compared to the exact ones in appendix 4.A. We recall that RA quantities can be found as statistical moments of the underlying pdf.

The proposed stochastic model for the particle phase reads

$$dx_{p,i} = V_{p,i} dt = (U_{p,i} + \delta v_{p,i}) dt, \quad (4.15)$$

$$\begin{aligned} dU_{p,i} = & \frac{U_{s,i} - U_{p,i}}{\tau_p} dt + g_i dt - \frac{1}{\langle\alpha_p\rangle\rho_p} \frac{\partial\langle\alpha_p\rangle\rho_p\langle P_{ij}\rangle}{\partial x_j} + \delta v_{p,j} \frac{\partial\langle U_{p,i}\rangle}{\partial x_j} dt \\ & - \frac{1}{T_{Lp}} (U_{p,i} - \langle U_{p,i}\rangle) dt + \sqrt{C_p\varepsilon_p} dW_{p,i}, \end{aligned} \quad (4.16)$$

$$\begin{aligned} d\delta v_{p,i} = & -\frac{\delta v_{p,i}}{\tau_p} dt + \frac{1}{\langle\alpha_p\rangle\rho_p} \frac{\partial\langle\alpha_p\rangle\rho_p\langle P_{ij}\rangle}{\partial x_j} - \delta v_{p,j} \frac{\partial\langle U_{p,i}\rangle}{\partial x_j} dt + B_{\delta,ij} dW_{\delta,j} \\ & - \frac{(1+e)(3-e)}{4\tau_c} \delta v_{p,i} dt + \sqrt{\frac{1}{2\tau_c}(1+e)^2\langle\Theta_p\rangle} dW_{c,i}. \end{aligned} \quad (4.17)$$

The first term of the RHS of (4.16) is the drag force related to the correlated part of the particle velocity, in which \mathbf{U}_s stands for the model for $\tilde{\mathbf{U}}_f$, the fluid velocity seen by the particle (whose expression will be given in the following) and τ_p the particle relaxation time. The second term is the effect of gravity, \mathbf{g} , while the third is a pressure term, in which ρ_p is the particle density, α_p the particle-phase volume fraction and $\langle P_{ij}\rangle = \langle\delta v_{p,i}\delta v_{p,j}\rangle$ is the particle-phase pressure tensor. The fourth and fifth terms are production and relaxation, respectively, in which T_{Lp} is the particle Lagrangian time scale defined by:

$$T_{Lp} = \left(\frac{1}{2} + \frac{3}{4}C_{0p} + \frac{f_s}{2} \right)^{-1} \frac{k_p}{\varepsilon_p}, \quad (4.18)$$

where $k_p = \frac{1}{2}\langle\mathbf{u}_p \cdot \mathbf{u}_p\rangle$ is the particle-phase turbulent kinetic energy with $\mathbf{u}_p = \mathbf{U}_p - \langle\mathbf{U}_p\rangle$, ε_p represents the particle-phase dissipation, to be specified shortly, and C_{0p} is a free parameter equivalent to C_0 for the fluid Lagrangian time [Pope 2000]. Finally, the last contribution is a diffusion term, in which C_p is a model constant to be a priori assigned and $dW_{p,i}$ is a Wiener stochastic process [Gardiner 1990]. The constant C_p in the diffusion coefficient

of (4.16) is related to the Lagrangian timescale to obtain a redistribution tensor and a dissipation tensor, by the relation

$$C_p = C_{0p} + \frac{2}{3}f_s. \quad (4.19)$$

The parameter f_s is introduced to account for anisotropy in the particle-phase dissipation tensor [Capecelatro 2016b], which is needed to predict the anisotropy of the particle-phase pressure tensor $\langle \mathbf{P} \rangle$. The last two terms in (4.16) in particular, are those used to model unclosed fluctuations in (4.9) and they give at the RA level a redistribution and a dissipation term (ε_p) in the equation of the particle Reynolds-stresses.

The first four terms in the RHS of (4.17) are analogous to the ones in (4.16). However, in order to obtain the correct averaged equations, we have had to break the original symmetry of the two parts. In particular, while the averaged terms are the same for the correlated and uncorrelated parts, the fluctuating ones cannot be. In the model for the fluctuations, dW_δ is a Wiener process and B_δ is a diffusion matrix, whose expression is given in the following. The last two terms take into account collisions; e is a restitution coefficient, to be a priori specified, $dW_{c,i}$ is another Wiener process uncorrelated with $dW_{\delta,i}$, since they represent different physics, and $\langle \Theta_p \rangle$ is the granular temperature, defined as $\langle \Theta_p \rangle = \frac{1}{3} \langle \delta \mathbf{v}_p \cdot \delta \mathbf{v}_p \rangle$. Finally, τ_c is a characteristic time for collisions, having the following expression:

$$\tau_c = \frac{\sqrt{\pi}d_p}{6C_c\langle \alpha_p \rangle \langle \Theta_p \rangle^{1/2}}, \quad (4.20)$$

d_p being the particle diameter and C_c a model parameter [Capecelatro 2016b]. This Lagrangian model for collisions gives, at the RA level, the same model as in [Capecelatro 2016b]. This collision model is applicable to rapid granular flows that can be modelled by the Boltzmann equation with inelastic hard-sphere collisions, i.e., the collisional and frictional contributions are not accounted for in the particle-phase pressure tensor.

When the correlation $\langle \delta v_{p,i} \delta v_{p,j} \rangle$ is evaluated, the diffusion matrix B_δ must give the particle-phase Reynolds-stress multiplied by the proper coefficient added to a diagonal isotropic part. Using the Choleski decomposition (see appendix 4.B) we obtain:

$$\begin{aligned} B_{\delta,11} &= \left(f_s \frac{\varepsilon_p}{k_p} \langle u_{p,1} u_{p,1} \rangle + (1 - f_s) \frac{2}{3} \varepsilon_p \right)^{1/2}, \\ B_{\delta,i1} &= \frac{1}{B_{\delta,11}} \left(f_s \frac{\varepsilon_p}{k_p} \langle u_{p,i} u_{p,1} \rangle \right), \quad 1 < i \leq 3 \\ B_{\delta,ii} &= \left(f_s \frac{\varepsilon_p}{k_p} \langle u_{p,i} u_{p,i} \rangle + (1 - f_s) \frac{2}{3} \varepsilon_p - \sum_{j=1}^{i-1} B_{\delta,ij}^2 \right)^{1/2}, \quad 1 < i \leq 3 \\ B_{\delta,ij} &= \frac{1}{B_{\delta,jj}} \left(f_s \frac{\varepsilon_p}{k_p} \langle u_{p,i} u_{p,j} \rangle - \sum_{k=1}^{j-1} B_{\delta,ik} B_{\delta,jk} \right), \quad 1 < j < i \leq 3 \\ B_{\delta,ij} &= 0, \quad i < j \leq 3 \end{aligned} \quad (4.21)$$

where repeated indices do not imply summation.

As in Lagrangian pdf methods for single-phase flows [Pope 2000], it should be borne in mind that such a model is intended to represent the pdf, or the statistical moments, associated with the particle phase, and not the instantaneous particle dynamics, which is “fictitious”.

4.4 Lagrangian pdf model for the fluid seen by particles

The equation for the particle velocity (4.16) contains the velocity of the fluid at the position of the particle, or the fluid seen by particles. Since in RANS simulations we have no access to this quantity, nor to its average, a model for it has to be specified. Furthermore, given that we are considering flow with two-way coupling, this effect has to be included also in the fluid-phase equation. We develop in this section a new stochastic model for \mathbf{U}_s , which will be a Langevin equation of the type

$$dU_{s,i} = [A_{s,i} + A_{p \rightarrow s,i}] dt + B_{s,ij} dW_{s,j} \quad (4.22)$$

where $A_{p \rightarrow s,i}$ represents explicitly the effect of the particles on the fluid, and $dW_{s,j}$ is a different Wiener process from those present in (4.16) and (4.17). The drift term, \mathbf{A}_s , is modelled following the path pointed out for dilute flows [Minier 2001, Minier 2004, Peirano 2006]:

$$A_{s,i} = -\frac{\langle \alpha_f \rangle}{\rho_f} \frac{\partial \langle p_f \rangle}{\partial x_i} + (\langle U_{p,j} \rangle - \langle U_{f,j} \rangle) \frac{\partial \langle U_{f,i} \rangle}{\partial x_j} + G_{ij} (U_{s,j} - \langle U_{f,j} \rangle) + g_i. \quad (4.23)$$

The first term of the RHS is the pressure-gradient term, where ρ_f is the fluid density and p_f the fluid pressure, which models the fluid pressure gradient seen by particles. In general, the subscript f denotes a flow variable in the fluid phase. This pressure term has been weighted by the local averaged fluid volume fraction in order to model the possible presence of a drift velocity even in homogeneous flows. The second term models the crossing-trajectory effect (CTE), while the third term is a relaxation term, where

$$G_{ij} = -\frac{1}{T_{L,i}^*} \delta_{ij} + G_{ij}^a \quad (4.24)$$

is the matrix defining the corresponding Reynolds stress model. The first part is the simplified Langevin model (SLM) adapted to the inertial particles, while \mathbf{G}^a is a traceless matrix to be added to generalise the model. For instance, the Launder–Reece–Rodi model [Launder 1975] (LRR-IP) model reads

$$G_{ij}^a = C_{2f} \frac{\partial \langle U_{f,i} \rangle}{\partial x_j} \quad (4.25)$$

and C_{2f} is the isotropisation-of-production (IP) constant, usually taken $C_{2f} = \frac{3}{5}$ consistent with rapid-distortion theory.

$T_{L,i}^*$ is a modified time scale that take into account particle inertia according to Csanady’s analysis:

$$T_{L,i}^* = \frac{T_{Lf}}{\sqrt{1 + \zeta_i \beta^2 \frac{3|\langle \mathbf{U}_r \rangle|^2}{2k_f}}} \quad (4.26)$$

where

$$T_{Lf} = \frac{1}{\left(\frac{1}{2} + \frac{3}{4}C_{0f}\right)} \frac{k_f}{\varepsilon_f} \quad (4.27)$$

is the Lagrangian time scale, C_{0f} being linked to the Rotta constant by the relation

$$C_{0f} = \frac{2}{3}(C_R - 1), \quad (4.28)$$

and the relative velocity is defined by

$$\mathbf{U}_r = \mathbf{U}_p - \mathbf{U}_s. \quad (4.29)$$

Moreover, $\zeta_1 = 1$ in the mean drift direction and $\zeta_{2,3} = 4$ in the cross directions, $\beta = T_{Lf}/T_{Ef}$ is the ratio of the Lagrangian and Eulerian timescales [Wang 1993a].

The modelling of the two-way coupling term instead is as follows. The exact expression for the two-way coupling term, $\mathbf{A}_{p \rightarrow s}$, which is induced by the presence of the discrete particles, is not *a priori* known. The underlying force corresponds to the exchange of momentum between the fluid and particles, but should not be confused with the total force acting on particles since the latter includes external forces such as gravity. The effect of particles on fluid properties is expressed directly in the model for \mathbf{U}_s through a simple stochastic equation. The force exerted by one particle on the fluid corresponds to the drag force written here as

$$\mathbf{F}_{p \rightarrow f} = -m_p \frac{\mathbf{U}_s - \mathbf{U}_p}{\tau_p} \quad (4.30)$$

where m_p is the mass of a particle. The total force acting on the fluid element surrounding a discrete particle is then obtained as the sum of all elementary forces, $\mathbf{F}_{p \rightarrow f}$, and the resulting acceleration is modelled here as [Peirano 2002]

$$A_{p \rightarrow s, i} = -\varphi \frac{U_{s, i} - U_{p, i}}{\tau_p} \quad (4.31)$$

where φ is the mean mass loading, $\varphi = \frac{\langle \alpha_p \rangle \rho_p}{\langle \alpha_f \rangle \rho_f}$.

4.4.1 Closure of the diffusion coefficient

The drift terms are given by (4.23) and (4.31), but the diffusion coefficient needs to be specified in order to obtain a complete closure. Analogously to dilute flows, we look for a diffusion matrix in a diagonal, but anisotropic form. To close this term, we consider the decay of the turbulent kinetic energy in the homogeneous case, in absence of mean shear, and we make the following assumption

$$\frac{dk_f}{dt} \simeq \frac{dk_{f@p}}{dt} \quad (4.32)$$

where $k_f = \frac{1}{2} \langle \mathbf{u}_f \cdot \mathbf{u}_f \rangle$ is the turbulent kinetic energy of the fluid phase, with $\mathbf{u}_f = \mathbf{U}_f - \langle \mathbf{U}_f \rangle$ the fluid fluctuation, and $k_{f@p} = \frac{1}{2} \langle \mathbf{u}_f \cdot \mathbf{u}_f \rangle_p$ is the turbulent kinetic energy of the fluid phase seen by the particles. It is worth recalling that fluid-phase RA terms such as k_f and $\langle U_{f, i} \rangle$ are known from the RA transport equation, which will be presented in §4.5. A

possible alternative could be to impose an analogous relation, but for all the Reynolds-stress components, which would lead to a much more complex model.

Recalling the phase averaging introduced in §4.3, we can obtain the following equality for the fluid velocity fluctuations:

$$\langle \mathbf{u}_f \rangle_p = \langle \mathbf{U}_f - \langle \mathbf{U}_f \rangle_f \rangle_p = \langle \mathbf{U}_s \rangle - \langle \mathbf{U}_f \rangle. \quad (4.33)$$

Thus, (4.32) can be rewritten as

$$\frac{dk_f}{dt} = \frac{1}{2} \frac{d}{dt} \sum_{i=1}^3 [\langle U_{s,i}^2 \rangle + \langle U_{f,i}^2 \rangle - 2\langle U_{s,i} \rangle \langle U_{f,i} \rangle] \quad (4.34)$$

where time variations of the fluid velocity and the fluid velocity seen by particles in the homogeneous case are expressed by

$$\frac{d\langle U_{f,i} \rangle}{dt} = f_i + g_i + \varphi \frac{\langle U_{p,i} - U_{s,i} \rangle}{\tau_p}, \quad (4.35)$$

$$dU_{s,i} = \langle \alpha_f \rangle f_i dt - \frac{1}{T_{L,i}^*} (U_{s,i} - \langle U_{f,i} \rangle) dt + g_i dt + \varphi \frac{U_{p,i} - U_{s,i}}{\tau_p} dt + B_{s,ii} dW_{s,i}, \quad (4.36)$$

$$\begin{aligned} \frac{d\langle U_{s,i}^2 \rangle}{dt} &= 2\langle \alpha_f \rangle f_i \langle U_{s,i} \rangle - \frac{2}{T_{L,i}^*} \langle U_{s,i}^2 \rangle + \frac{2}{T_{L,i}^*} \langle U_{s,i} \rangle \langle U_{f,i} \rangle + 2g_i \langle U_{s,i} \rangle \\ &\quad + 2\varphi \frac{\langle U_{p,i} U_{s,i} \rangle - \langle U_{s,i}^2 \rangle}{\tau_p} + B_{s,ii}^2, \end{aligned} \quad (4.37)$$

$$\frac{d\langle U_{f,i}^2 \rangle}{dt} = 2\langle U_{f,i} \rangle \frac{d\langle U_{f,i} \rangle}{dt} = 2f_i \langle U_{f,i} \rangle + 2g_i \langle U_{f,i} \rangle + 2\varphi \langle U_{f,i} \rangle \frac{\langle U_{p,i} - U_{s,i} \rangle}{\tau_p}, \quad (4.38)$$

$$\begin{aligned} \frac{d\langle U_{s,i} \rangle \langle U_{f,i} \rangle}{dt} &= -\frac{1}{T_{L,i}^*} (\langle U_{f,i} \rangle \langle U_{s,i} \rangle - \langle U_{f,i} \rangle^2) + f_i (\langle \alpha_f \rangle \langle U_{f,i} \rangle + \langle U_{s,i} \rangle) \\ &\quad + g_i (\langle U_{f,i} \rangle + \langle U_{s,i} \rangle) + \varphi \langle U_{f,i} \rangle \frac{\langle U_{p,i} - U_{s,i} \rangle}{\tau_p} + \varphi \langle U_{s,i} \rangle \frac{\langle U_{p,i} - U_{s,i} \rangle}{\tau_p} \end{aligned} \quad (4.39)$$

with $f_i = -(1/\rho_f) \partial \langle p_f \rangle / \partial x_i$. Now, if we substitute (4.37)–(4.39) into (4.34), the following relation is obtained:

$$\begin{aligned} \frac{dk_f}{dt} &= -\varepsilon_f + \sum_{i=1}^3 \left[\varphi \frac{\langle U_{p,i} U_{s,i} \rangle - \langle U_{s,i}^2 \rangle}{\tau_p} - \varphi \langle U_{f,i} \rangle \frac{\langle U_{p,i} - U_{s,i} \rangle}{\tau_p} \right] \\ &= \sum_{i=1}^3 \left[-\frac{1}{T_{L,i}^*} (\langle U_{s,i} - \langle U_{f,i} \rangle \rangle^2) - \langle \alpha_p \rangle f_i (\langle U_{s,i} \rangle - \langle U_{f,i} \rangle) + \frac{B_{s,ii}^2}{2} + \varphi \frac{\langle u_{p,i} u_{s,i} \rangle - \langle u_{s,i}^2 \rangle}{\tau_p} \right]. \end{aligned} \quad (4.40)$$

The terms $(1/T_{L,i}^*) \langle (U_{s,i} - \langle U_{f,i} \rangle)^2 \rangle$ and ε_f can be rearranged together, whereas the other terms are redistributed on each corresponding component shown above. The result is

$$\begin{aligned} B_{s,ii}^2 &= 2\varphi \frac{\langle U_{p,i} - U_{s,i} \rangle}{\tau_p} (\langle U_{s,i} \rangle - \langle U_{f,i} \rangle) + 2\langle \alpha_p \rangle f_i (\langle U_{s,i} \rangle - \langle U_{f,i} \rangle) \\ &\quad + \varepsilon_f \left[C_0 b_i \frac{\tilde{k}_f}{k_f} + \frac{2}{3} \left(b_i \frac{\tilde{k}_f}{k_f} - 1 \right) \right] \end{aligned} \quad (4.41)$$

with $b_i = T_L/T_{L,i}^*$ and

$$\tilde{k}_f = \frac{3}{2} \frac{\sum_{i=1}^3 b_i \langle (U_{s,i} - \langle U_{f,i} \rangle)^2 \rangle}{\sum_{i=1}^3 b_i}. \quad (4.42)$$

Therefore the final form of the Lagrangian pdf equation for the fluid velocity seen by particles, to be coupled with (4.15)–(4.17) for the particle position and velocity, is

$$\begin{aligned} dU_{s,i}(t) = & -\frac{\langle \alpha_f \rangle}{\rho_f} \frac{\partial \langle p_f \rangle}{\partial x_i} dt + (\langle U_{p,j} \rangle - \langle U_{f,j} \rangle) \frac{\partial \langle U_{f,i} \rangle}{\partial x_j} dt \\ & + G_{ij}(U_{s,j} - \langle U_{f,j} \rangle) dt - \varphi \left(\frac{U_{s,i} - U_{p,i}}{\tau_p} \right) dt + g_i dt \\ & + \left[\varepsilon_f \left(C_0 b_i \frac{\tilde{k}_f}{k_f} + \frac{2}{3} \left(b_i \frac{\tilde{k}_f}{k_f} - 1 \right) \right) + 2\varphi \frac{\langle U_{p,i} - U_{s,i} \rangle}{\tau_p} (\langle U_{s,i} \rangle - \langle U_{f,i} \rangle) \right. \\ & \left. - 2 \frac{\langle \alpha_p \rangle}{\rho_f} \frac{\partial \langle p_f \rangle}{\partial x_i} (\langle U_{s,i} \rangle - \langle U_{f,i} \rangle) \right]^{1/2} dW_{s,i}. \end{aligned} \quad (4.43)$$

It is worth remarking that in the presence of a mean shear, the anisotropic term G_{ij}^a should also be considered in the derivation of the diffusion coefficient, which will give rise to an additional term in (4.41) in analogy with single phase flows [Pope 1994a]:

$$\frac{2}{3} C_{2f} \mathcal{P}_{Sfs} \quad (4.44)$$

where \mathcal{P}_{Sfs} is one-half the trace of the tensor

$$\mathcal{P}_{Sfs} = -(\langle (\mathbf{U}_s - \langle \mathbf{U}_f \rangle) \otimes (\mathbf{U}_s - \langle \mathbf{U}_f \rangle) \rangle \cdot \nabla \langle \mathbf{U}_f \rangle)^\dagger. \quad (4.45)$$

The set of equations for the particle and fluid velocities can be recast in vector form as follows:

$$d\mathbf{X} = \mathbf{A} dt + [B] d\mathbf{W} \quad (4.46)$$

where \mathbf{A} is the drift term, and

$$\mathbf{X} = \begin{pmatrix} \mathbf{U}_p \\ \delta \mathbf{v}_p \\ \mathbf{U}_s \end{pmatrix} \quad [B] = \begin{bmatrix} C[I] & 0 & 0 & 0 \\ 0 & [B_\delta] & K[I] & 0 \\ 0 & 0 & 0 & [B_s] \end{bmatrix} \quad d\mathbf{W} = \begin{pmatrix} d\mathbf{W}_p \\ d\mathbf{W}_\delta \\ d\mathbf{W}_c \\ d\mathbf{W}_s \end{pmatrix} \quad (4.47)$$

$C = \sqrt{C_p \varepsilon_p}$ is the diagonal diffusion coefficient in the equation of the correlated velocity and $K = \sqrt{1/(2\tau_c)(1 + e^2)\langle \Theta_p \rangle}$ is the diagonal diffusion coefficient for the collisions in the uncorrelated velocity equation.

4.5 Eulerian pdf model for the fluid phase

The RA fluid-phase equations (4.114)–(4.117) could easily be replaced by a suitable RANS model (k - ε , Reynolds-stress models, see [Pope 2000]); however, single-phase turbulence models typically do not take into account two-way coupling between the phases. Thus, both in the momentum and in the Reynolds-stress equations, we need to formulate the

terms that mimic this effect. We follow here the approach first proposed by [Peirano 2002]. We consider the direct effect of the particles on the fluid through a random force. Since a fluid and a discrete particle will not be present at the same spatial position in the same instant with probability one, we define this random force as

$$\mathbf{A}_{pf} \equiv \frac{\rho_p}{\rho_f} \frac{\mathbf{U}_p - \mathbf{U}_s}{\tau_p} \quad (4.48)$$

with a probability $\langle \alpha_p \rangle(t, \mathbf{x}_f)$, where \mathbf{A}_{pf} is a random variable which is formed from the discrete particles at the location $\mathbf{x}_p = \mathbf{x}$.

In other words, from the stochastic models for the discrete particles, or from the one-point particle pdf value at location $\mathbf{x} = \mathbf{x}_f$, we form the random variables \mathbf{A}_{pf} with the same distribution. This random term mimics the reverse forces due to the discrete particles and is only non-zero where the fluid particle is in the close neighbourhood of a discrete particle. At the location \mathbf{x} considered, \mathbf{A}_{pf} is defined as a random acceleration term in the equation for \mathbf{U}_f , correlated with \mathbf{U}_f , so that we have

$$\langle \mathbf{A}_{pf} \rangle = \frac{\rho_p}{\rho_f} \left\langle \frac{\mathbf{U}_p - \mathbf{U}_s}{\tau_p} \right\rangle = \frac{\rho_p}{\rho_f} \left\langle \frac{\mathbf{U}_p - \mathbf{U}_f}{\tau_p} \right\rangle_p, \quad (4.49a)$$

$$\langle \mathbf{A}_{pf} \otimes \mathbf{U}_f \rangle = \frac{\rho_p}{\rho_f} \left\langle \frac{(\mathbf{U}_p - \mathbf{U}_s) \otimes \mathbf{U}_s}{\tau_p} \right\rangle = \frac{\rho_p}{\rho_f} \left\langle \frac{(\mathbf{U}_p - \mathbf{U}_f) \otimes \mathbf{U}_f}{\tau_p} \right\rangle_p. \quad (4.49b)$$

Thus, the resulting RA equations for the fluid phase will be

$$\frac{\partial}{\partial t} (\langle \alpha_f \rangle \rho_f) + \nabla \cdot (\langle \alpha_f \rangle \rho_f \langle \mathbf{U}_f \rangle) = 0, \quad (4.50)$$

$$\begin{aligned} \frac{\partial \langle \alpha_f \rangle \langle \mathbf{U}_f \rangle}{\partial t} + \nabla \cdot \langle \alpha_f \rangle (\langle \mathbf{U}_f \rangle \otimes \langle \mathbf{U}_f \rangle + \langle \mathbf{u}_f \otimes \mathbf{u}_f \rangle) &= -\frac{\langle \alpha_f \rangle}{\rho_f} \nabla \langle p_f \rangle \\ &+ \langle \alpha_f \rangle \nu \nabla^2 \langle \mathbf{U}_f \rangle + \frac{\langle \alpha_p \rangle \rho_p}{\rho_f} \left\langle \frac{\mathbf{U}_p - \mathbf{U}_s}{\tau_p} \right\rangle + \langle \alpha_f \rangle \mathbf{g}. \end{aligned} \quad (4.51)$$

The resulting Reynolds-stress transport equation is closed here by the LRR-IP model [Pope 2000], and the two-way coupling term of (4.49b):

$$\begin{aligned} \frac{\partial \langle \alpha_f \rangle \langle \mathbf{u}_f \otimes \mathbf{u}_f \rangle}{\partial t} + \nabla \cdot \langle \alpha_f \rangle (\langle \mathbf{U}_f \rangle \otimes \langle \mathbf{u}_f \otimes \mathbf{u}_f \rangle) &= \nabla \cdot (\langle \alpha_f \rangle \nu \nabla \langle \mathbf{u}_f \otimes \mathbf{u}_f \rangle) \\ &+ \mathcal{L} + \langle \alpha_f \rangle \mathcal{P}_f + \langle \alpha_f \rangle \mathcal{R}_f - \frac{2}{3} \langle \alpha_f \rangle \varepsilon_f \mathbf{I} + \langle \alpha_p \rangle [\langle \mathbf{\Pi}_p \otimes \mathbf{U}_f \rangle - \langle \mathbf{U}_f \rangle \otimes \langle \mathbf{\Pi}_p \rangle]^\dagger \end{aligned} \quad (4.52)$$

where the symbol $(\cdot)^\dagger$ implies the summation of a second-order tensor with its transpose. The turbulent mean-gradient production term is defined by

$$\mathcal{P}_f = -(\langle \mathbf{u}_f \otimes \mathbf{u}_f \rangle \cdot \nabla \langle \mathbf{U}_f \rangle)^\dagger \quad (4.53)$$

and the pressure-redistribution term is modeled by

$$\mathcal{R}_f = -C_{Rf} \frac{\varepsilon_f}{k_f} \left(\langle \mathbf{u}_f \otimes \mathbf{u}_f \rangle - \frac{2}{3} k_f \mathbf{I} \right) - C_{2f} \left(\mathcal{P}_f - \frac{2}{3} \mathcal{P}_f \mathbf{I} \right). \quad (4.54)$$

The transport term \mathcal{L} may be modelled with the different standard models present in literature [Pope 2000]. Here we leave it in an unclosed form, since it does not play a role in the homogeneous flows presented hereinafter.

Some remarks are in order concerning the fluid-phase Reynolds-stress model. Following [Capecelatro 2016b], we have chosen the LRR-IP model, which is widely used and give reasonably good results, but any other realisable Reynolds-stress model could be chosen, if needed. The important point is that it has been demonstrated that a realisable Reynolds-stress model exists for every Lagrangian pdf model for the fluid [Pope 1994a]. Furthermore, consistency between Eulerian and Lagrangian models of the fluid should be always assured [Muradoglu 2001, Chibbaro 2011, Minier 2014]. Notably, the Rotta model is consistent with the standard Langevin model (SLM) for the fluid [Pope 2000], and for this reason it is usually chosen as the standard model to be used in hybrid Eulerian/Lagrangian pdf approach [Minier 2014].

4.6 RA equations

The Fokker–Planck (FP) equation corresponding, from the pdf point of view, to the Lagrangian system of stochastic differential equations (4.15)–(4.17), (4.43), is defined in appendix 4.C. It can be used to derive the PA equations for the particle phase by integration of the Eulerian mass density function (mdf), $F_p^E(t, \mathbf{x}; \mathbf{U}_p, \delta \mathbf{v}_p, \mathbf{U}_s)$, over the phase space:

$$\langle \alpha_p \rangle(t, \mathbf{x}) \rho_p \langle \mathbb{O} \rangle_p(t, \mathbf{x}) := \int \mathbb{O}(\mathbf{U}_p, \delta \mathbf{v}_p, \mathbf{U}_s) F_p^E(t, \mathbf{x}; \mathbf{U}_p, \delta \mathbf{v}_p, \mathbf{U}_s) d\mathbf{U}_p d\delta \mathbf{v}_p d\mathbf{U}_s \quad (4.55)$$

where \mathbb{O} is a generic observable attached to a discrete particle.

Closed RA transport equations can now be derived from the FP equation. The so-obtained RA continuity equation is the following

$$\frac{\partial}{\partial t} (\langle \alpha_p \rangle \rho_p) + \nabla \cdot (\langle \alpha_p \rangle \rho_p \langle \mathbf{U}_p \rangle) = 0. \quad (4.56)$$

The momentum equation reads

$$\langle \alpha_p \rangle \rho_p \frac{D}{Dt} \langle \mathbf{U}_p \rangle = -\nabla \cdot \langle \alpha_p \rangle \rho_p (\langle \mathbf{u}_p \otimes \mathbf{u}_p \rangle + \langle \mathbf{P} \rangle) + \langle \alpha_p \rangle \rho_p \left\langle \frac{\mathbf{U}_s - \mathbf{U}_p}{\tau_p} \right\rangle + \langle \alpha_p \rangle \mathbf{g} \quad (4.57)$$

where $D/Dt = \partial/\partial t + \langle \mathbf{U}_p \rangle \cdot \nabla$. Second-order moments, on the other hand, give the following equations for the particle-phase Reynolds stress:

$$\begin{aligned} \langle \alpha_p \rangle \rho_p \frac{D}{Dt} \langle \mathbf{u}_p \otimes \mathbf{u}_p \rangle &= -\nabla \cdot (\langle \alpha_p \rangle \rho_p \langle \mathbf{u}_p \otimes \mathbf{u}_p \otimes \mathbf{u}_p \rangle) - \langle \alpha_p \rangle \rho_p (\langle \mathbf{u}_p \otimes \mathbf{u}_p \rangle \cdot \nabla \langle \mathbf{U}_p \rangle)^\dagger \\ &\quad + \frac{\langle \alpha_p \rangle \rho_p}{\tau_p} (\langle \mathbf{u}_s \otimes \mathbf{u}_p \rangle - \langle \mathbf{u}_p \otimes \mathbf{u}_p \rangle)^\dagger + \langle \alpha_p \rangle \rho_p \mathcal{R}_p - \langle \alpha_p \rangle \rho_p \varepsilon_p \end{aligned} \quad (4.58)$$

where the redistribution is expressed by

$$\mathcal{R}_p = -C_{Rp} \frac{\varepsilon_p}{k_p} \left(\langle \mathbf{u}_p \otimes \mathbf{u}_p \rangle - \frac{2}{3} k_p \mathbf{I} \right) \quad (4.59)$$

with

$$C_{Rp} = 1 + \frac{3}{2} C_{0p}, \quad (4.60)$$

and the dissipation tensor is closed using the Rotta model [Pope 2000]:

$$\varepsilon_p = \varepsilon_p \left[f_s \frac{\langle \mathbf{u}_p \otimes \mathbf{u}_p \rangle}{k_p} + (1 - f_s) \frac{2}{3} \mathbf{I} \right]. \quad (4.61)$$

The transport equation for the particle-phase pressure tensor is

$$\begin{aligned} \langle \alpha_p \rangle \rho_p \frac{D}{Dt} \langle \mathbf{P} \rangle = & - \nabla \cdot [\langle \alpha_p \rangle \rho_p (\langle \mathbf{u}_p \otimes \mathbf{P} \rangle + \langle \mathbf{Q} \rangle)] - \langle \alpha_p \rangle \rho_p (\langle \mathbf{P} \rangle \cdot \nabla \langle \mathbf{U}_p \rangle)^\dagger + \langle \alpha_p \rangle \rho_p \varepsilon_p \\ & - \frac{2}{\tau_p} \langle \alpha_p \rangle \rho_p \langle \mathbf{P} \rangle + \frac{1}{2\tau_c} [(1 + e)^2 \langle \Theta_p \rangle \mathbf{I} - (1 + e)(3 - e) \langle \mathbf{P} \rangle]. \end{aligned} \quad (4.62)$$

Comparing (4.58), (4.62) to (4.112), (4.113), we can see that the closed terms have been reproduced correctly in the Lagrangian pdf model, while the previously unclosed terms such as dissipation are now modelled.

Particular attention should be given to the closure of the term $\varepsilon_p = \langle \mathbf{P} \cdot \nabla \tilde{\mathbf{v}}_p \rangle$, which plays the role of a sink in the equation of the particle-phase turbulent kinetic energy and of a source in the equation of the particle-phase pressure tensor. In analogy to single-phase flow, where dissipation of turbulent kinetic energy leads to viscous heating, it is modelled as a particle-phase anisotropic dissipation tensor ε_p , whose trace divided by two gives the scalar particle-phase dissipation ε_p . As shown in [Capecelatro 2015, Capecelatro 2016a], when the mean mass loading is significant, the particle-phase pressure tensor is highly anisotropic due to the source term ε_p (i.e., $f_s \approx 0.93$ in (4.61)).

The transport equation of the scalar particle-phase dissipation is modelled as follows:

$$\begin{aligned} \frac{\partial \langle \alpha_p \rangle \varepsilon_p}{\partial t} + \nabla \cdot (\langle \alpha_p \rangle \langle \mathbf{U}_p \rangle \varepsilon_p) = & \nabla \cdot \left[\langle \alpha_p \rangle \left(\nu_p + \frac{\nu_{p,t}}{\sigma_{\varepsilon,p}} \right) \nabla \varepsilon_p \right] \\ & - \langle \alpha_p \rangle C_{\varepsilon 1p} \langle \mathbf{u}_p \otimes \mathbf{u}_p \rangle : \nabla \langle \mathbf{U}_p \rangle \frac{\varepsilon_p}{k_p} - \langle \alpha_p \rangle C_{\varepsilon 2p} \frac{\varepsilon_p^2}{k_p} + \langle \alpha_p \rangle \frac{C_{3p}}{\tau_p} \left(\frac{k_{fp}}{k_{f@p}} \varepsilon_f - \beta_p \varepsilon_p \right) \end{aligned} \quad (4.63)$$

where $C_{\varepsilon 1p}$, $C_{\varepsilon 2p}$, C_{3p} and β_p are model parameters. Equation (4.63) differs slightly from the model in [Fox 2014] because k_{fp} is known in the Lagrangian pdf model proposed here. Now that we have modelled the particle-phase dissipation, we can define a timescale for the particle phase $T_p = k_p / \varepsilon_p$ to be used in the model equation for the fluid-phase dissipation.

For the fluid-phase dissipation, we propose the following model, built with the standard single-phase fluid dissipation model equation [Pope 2000] and an additional contribution due to particle–fluid interactions:

$$\begin{aligned} \frac{\partial \langle \alpha_f \rangle \varepsilon_f}{\partial t} + \nabla \cdot (\langle \alpha_f \rangle \langle \mathbf{U}_f \rangle \varepsilon_f) = & \nabla \cdot \left[\langle \alpha_f \rangle \left(\nu + \frac{\nu_t}{\sigma_\varepsilon} \right) \nabla \varepsilon_f \right] \\ & - \langle \alpha_f \rangle C_{\varepsilon 1f} \langle \mathbf{u}_f \otimes \mathbf{u}_f \rangle : (\nabla \langle \mathbf{U}_f \rangle) \frac{\varepsilon_f}{k_f} - \langle \alpha_f \rangle C_{\varepsilon 2f} \frac{\varepsilon_f^2}{k_f} \\ & + \frac{\rho_p \langle \alpha_p \rangle}{\rho_f} \frac{C_{3f}}{\tau_p} \left(\frac{k_{fp}}{k_{f@p}} \varepsilon_p - \beta_f \varepsilon_f \right) + \frac{\rho_p \langle \alpha_p \rangle}{\rho_f} \frac{C_4}{\tau_p} \frac{(\langle \mathbf{U}_p \rangle - \langle \mathbf{U}_f \rangle) \cdot \langle \mathbf{u}_d \rangle}{2} \frac{\varepsilon_p}{k_p} \end{aligned} \quad (4.64)$$

where $C_{\varepsilon 1f}$, $C_{\varepsilon 2f}$, C_{3f} , β_f and C_4 are model constants, and $\langle \mathbf{u}_d \rangle = \langle \mathbf{U}_s \rangle - \langle \mathbf{U}_f \rangle$. Here, we have split the total energy rate dissipation into two contributions, arising from the energy

exchange between phases (fourth term on the r.h.s.), and from the drag production (last term).

The Lagrangian pdf approach is tantamount to computing the entire pdf of the variables considered in the state vector. Compared with an Eulerian moment approach, it means that more information is available. Notably, we wish to derive here the RA equations for the mean fluid velocity seen by the particles $\langle \mathbf{U}_s \rangle$, and for all the second-order velocity moments, $\langle \mathbf{u}_s \otimes \mathbf{u}_s \rangle$, $\langle \mathbf{u}_s \otimes \mathbf{u}_p \rangle$, which cannot be accessed in present two-fluid models. We can obtain the RA equations starting from the transport equation of the Eulerian mdf F_p^E (4.119):

$$\begin{aligned} \langle \alpha_p \rangle \rho_p \frac{D}{Dt} \langle \mathbf{U}_s \rangle = & -\nabla \cdot (\langle \alpha_p \rangle \rho_p \langle \mathbf{u}_s \otimes \mathbf{u}_p \rangle) \\ & + \langle \alpha_p \rangle \rho_p \left[-\frac{\langle \alpha_f \rangle}{\rho_f} \nabla \langle p_f \rangle + (\nabla \langle \mathbf{U}_f \rangle) \cdot (\langle \mathbf{U}_p \rangle - \langle \mathbf{U}_f \rangle) + \mathbf{G} \cdot (\langle \mathbf{U}_s \rangle - \langle \mathbf{U}_f \rangle) + \mathbf{g} \right] \\ & - \langle \alpha_p \rangle \rho_p \varphi \left(\frac{\langle \mathbf{U}_s - \mathbf{U}_p \rangle}{\tau_p} \right) \end{aligned} \quad (4.65)$$

where $D/Dt = \partial/\partial t + \langle \mathbf{U}_p \rangle \cdot \nabla$.

For the second-order moments we obtain

$$\begin{aligned} \langle \alpha_p \rangle \rho_p \frac{D}{Dt} \langle \mathbf{u}_s \otimes \mathbf{u}_p \rangle = & -\nabla \cdot [\langle \alpha_p \rangle \rho_p (\langle \mathbf{u}_s \otimes \mathbf{u}_p \otimes \mathbf{u}_p \rangle + \langle \mathbf{u}_s \otimes \delta \mathbf{v}_p \otimes \delta \mathbf{v}_p \rangle)] \\ & - \langle \alpha_p \rangle \rho_p (\langle \mathbf{u}_s \otimes \mathbf{u}_p \rangle \cdot \nabla \langle \mathbf{U}_p \rangle^T) - \langle \alpha_p \rangle \rho_p [(\langle \mathbf{u}_p \otimes \mathbf{u}_p \rangle + \langle \delta \mathbf{v}_p \otimes \delta \mathbf{v}_p \rangle) \cdot \nabla \langle \mathbf{U}_s \rangle^T] \\ & + \langle \alpha_p \rangle \rho_p \mathbf{G} \cdot \langle \mathbf{u}_s \otimes \mathbf{u}_p \rangle^T + \langle \alpha_p \rangle \rho_p \varphi \frac{\langle \mathbf{u}_p \otimes \mathbf{u}_p \rangle - \langle \mathbf{u}_s \otimes \mathbf{u}_p \rangle}{\tau_p} \\ & - \langle \alpha_p \rangle \rho_p \frac{1}{\mathbf{T}_{Lp}} \circ \langle \mathbf{u}_p \otimes \mathbf{u}_s \rangle + \langle \alpha_p \rangle \rho_p \frac{\langle \mathbf{u}_s \otimes \mathbf{u}_s \rangle - \langle \mathbf{u}_p \otimes \mathbf{u}_s \rangle}{\tau_p} \end{aligned} \quad (4.66)$$

and

$$\begin{aligned} \langle \alpha_p \rangle \rho_p \frac{D}{Dt} \langle \mathbf{u}_s \otimes \mathbf{u}_s \rangle = & -\nabla \cdot (\langle \alpha_p \rangle \rho_p \langle \mathbf{u}_s \otimes \mathbf{u}_s \otimes \mathbf{u}_s \rangle) - \langle \alpha_p \rangle \rho_p (\langle \mathbf{u}_s \otimes \mathbf{u}_s \rangle \cdot \nabla \langle \mathbf{U}_s \rangle)^\dagger \\ & + \langle \alpha_p \rangle \rho_p (\mathbf{G} \cdot \langle \mathbf{u}_s \otimes \mathbf{u}_s \rangle)^\dagger + \langle \alpha_p \rangle \rho_p \varphi \frac{\langle \mathbf{u}_s \otimes \mathbf{u}_p \rangle^\dagger - 2\langle \mathbf{u}_s \otimes \mathbf{u}_s \rangle}{\tau_p} + \langle \alpha_p \rangle \rho_p \langle \mathbf{B}_s \mathbf{B}_s^T \rangle \end{aligned} \quad (4.67)$$

where the \circ symbol denotes an element-by-element product.

Eulerian transport equations for the cross-correlations $\langle \mathbf{u}_p \otimes \delta \mathbf{v}_p \rangle$ and $\langle \mathbf{u}_s \otimes \delta \mathbf{v}_p \rangle$ could also be written to demonstrate that $\delta \mathbf{v}_p$ is uncorrelated with the other variables. Also, it is important to note that these moment equations are, in general, not closed (*e. g.* the turbulent fluxes involve the third-order moments). However, for statistically homogeneous flows such as particle-laden isotropic turbulence [F  vrier 2005, Sundaram 1999, Elghobashi 1994] and CIT [Capecelatro 2015], the spatial gradients (except for fluid pressure, whose gradient is constant) are zero, and a closed set of moment equations results.

4.7 Statistically homogeneous equations

4.7.1 Particle phase

For statistically homogeneous flow, the Eulerian equations corresponding to the stochastic equation system (4.15)–(4.17) and (4.43) are the following:

$$\frac{d\langle \mathbf{U}_p \rangle}{dt} = \frac{1}{\tau_p} \langle \mathbf{U}_s - \mathbf{U}_p \rangle + \mathbf{g}, \quad (4.68)$$

$$\langle \delta \mathbf{v}_p \rangle = 0, \quad (4.69)$$

$$\frac{d\langle \mathbf{U}_s \rangle}{dt} = -\frac{\langle \alpha_f \rangle}{\rho_f} \nabla \langle p_f \rangle + \mathbf{G} \cdot (\langle \mathbf{U}_s \rangle - \langle \mathbf{U}_f \rangle) + \frac{\varphi}{\tau_p} \langle \mathbf{U}_p - \mathbf{U}_s \rangle + \mathbf{g}. \quad (4.70)$$

The particle-phase pressure tensor, $\langle \mathbf{P} \rangle = \langle \delta \mathbf{v}_p \otimes \delta \mathbf{v}_p \rangle$, is found from

$$\frac{d\langle \mathbf{P} \rangle}{dt} = \mathcal{P}_P + \varepsilon_p - \frac{2}{\tau_p} \langle \mathbf{P} \rangle + \frac{1}{2\tau_c} [(1+e)^2 \langle \Theta_p \rangle \mathbf{I} - (1+e)(3-e) \langle \mathbf{P} \rangle] \quad (4.71)$$

where $\langle \Theta_p \rangle = \frac{1}{3} \text{Trace}(\langle \mathbf{P} \rangle)$ and the production term due to mean velocity gradients is

$$\mathcal{P}_P = -(\langle \mathbf{P} \rangle \cdot \nabla \langle \mathbf{U}_p \rangle)^\dagger. \quad (4.72)$$

For the particle-phase Reynolds-stress tensor, we obtain

$$\frac{d\langle \mathbf{u}_p \otimes \mathbf{u}_p \rangle}{dt} = \mathcal{P}_p + \mathcal{R}_p - \varepsilon_p. \quad (4.73)$$

The redistribution term is expressed as

$$\mathcal{R}_p = -C_{Rp} \frac{\varepsilon_p}{k_p} \left(\langle \mathbf{u}_p \otimes \mathbf{u}_p \rangle - \frac{2}{3} k_p \mathbf{I} \right) \quad (4.74)$$

The production term in (4.73) is defined by $\mathcal{P}_p = \mathcal{P}_{Sp} + \mathcal{P}_{Dp}$ where \mathcal{P}_{Sp} is the mean-shear-production term, given by

$$\mathcal{P}_{Sp} = -(\langle \mathbf{u}_p \otimes \mathbf{u}_p \rangle \cdot \nabla \langle \mathbf{U}_p \rangle)^\dagger; \quad (4.75)$$

and \mathcal{P}_{Dp} is the drag-production term, given by

$$\mathcal{P}_{Dp} = \frac{1}{\tau_p} (\langle \mathbf{u}_s \otimes \mathbf{u}_p \rangle^\dagger - 2 \langle \mathbf{u}_p \otimes \mathbf{u}_p \rangle). \quad (4.76)$$

The fluid-seen Reynolds-stress tensor is found from

$$\frac{d\langle \mathbf{u}_s \otimes \mathbf{u}_s \rangle}{dt} = \mathcal{P}_s + (\mathbf{G} \cdot \langle \mathbf{u}_s \otimes \mathbf{u}_s \rangle)^\dagger + \langle \mathbf{B}_s \mathbf{B}_s^T \rangle \quad (4.77)$$

where \mathbf{B}_s is the diffusion matrix in (4.43) and $k_{f@p} = \frac{1}{2} \langle (\mathbf{U}_s - \langle \mathbf{U}_f \rangle) \cdot (\mathbf{U}_s - \langle \mathbf{U}_f \rangle) \rangle$. The production term in (4.77) is defined by $\mathcal{P}_s = \mathcal{P}_{Ss} + \mathcal{P}_{Ds}$ where \mathcal{P}_{Ss} is the mean-shear-production term, given by

$$\mathcal{P}_{Ss} = -(\langle \mathbf{u}_s \otimes \mathbf{u}_s \rangle \cdot \nabla \langle \mathbf{U}_s \rangle)^\dagger; \quad (4.78)$$

and \mathcal{P}_{Ds} is the drag-production term, given by

$$\mathcal{P}_{Ds} = \frac{\varphi}{\tau_p} (\langle \mathbf{u}_s \otimes \mathbf{u}_p \rangle^\dagger - 2\langle \mathbf{u}_s \otimes \mathbf{u}_s \rangle). \quad (4.79)$$

The fluid-particle covariance Reynolds-stress tensor is found from

$$\frac{d\langle \mathbf{u}_s \otimes \mathbf{u}_p \rangle}{dt} = \mathcal{P}_{sp} + \mathbf{G} \cdot \langle \mathbf{u}_s \otimes \mathbf{u}_p \rangle^T - \frac{1}{T_{Lp}} \langle \mathbf{u}_p \otimes \mathbf{u}_s \rangle \quad (4.80)$$

where $k_{fp} = \frac{1}{2} \langle \mathbf{u}_s \cdot \mathbf{u}_p \rangle$. The production term in (4.80) is defined by $\mathcal{P}_{sp} = \mathcal{P}_{Ssp} + \mathcal{P}_{Dsp}$ where \mathcal{P}_{Ssp} is the mean-shear-production term, given by

$$\mathcal{P}_{Ssp} = -\langle \mathbf{u}_s \otimes \mathbf{u}_p \rangle \cdot \nabla \langle \mathbf{U}_p \rangle^T - (\langle \mathbf{u}_p \otimes \mathbf{u}_p \rangle + \langle \mathbf{P} \rangle) \cdot \nabla \langle \mathbf{U}_s \rangle^T; \quad (4.81)$$

and \mathcal{P}_{Dsp} is the drag-production term, given by

$$\mathcal{P}_{Dsp} = \frac{1}{\tau_p} (\langle \mathbf{u}_s \otimes \mathbf{u}_s \rangle - \langle \mathbf{u}_p \otimes \mathbf{u}_s \rangle) + \frac{\varphi}{\tau_p} (\langle \mathbf{u}_p \otimes \mathbf{u}_p \rangle - \langle \mathbf{u}_s \otimes \mathbf{u}_p \rangle). \quad (4.82)$$

The particle-phase dissipation equation becomes

$$\frac{d\varepsilon_p}{dt} = (C_{\varepsilon 1p} \mathcal{P}_{Sp} - C_{\varepsilon 2p} \varepsilon_p) \frac{\varepsilon_p}{k_p} + \frac{C_{3p}}{\tau_p} \left(\frac{k_{fp}}{k_{f@p}} \varepsilon_f - \beta_p \varepsilon_p \right). \quad (4.83)$$

Finally, all the fluid-phase quantities are obtained through the RA equations presented in §4.7.3.

4.7.2 Simplified model for particle phase

We propose here a simplified model for the particle phase, where collisions between particles are neglected and only the total particle velocity is modelled, thus losing information about its decomposition into the correlated and uncorrelated parts. In particular, this corresponds to assuming that the particle velocity coincides with the correlated part, i.e. $\mathbf{V}_p = \mathbf{U}_p$. The resulting set of SDEs for the simplified model is

$$\left\{ \begin{array}{l} dx_{p,i}(t) = V_{p,i} dt, \\ dV_{p,i}(t) = \frac{U_{s,i} - V_{p,i}}{\tau_p} dt + g_i dt, \\ dU_{s,i}(t) = -\frac{\langle \alpha_f \rangle}{\rho_f} \frac{\partial \langle p_f \rangle}{\partial x_i} dt - \frac{1}{T_{L,i}^*} (U_{s,i} - \langle U_{f,i} \rangle) dt - \varphi \left(\frac{U_{s,i} - V_{p,i}}{\tau_p} \right) dt + g_i dt \\ \quad + \left[\varepsilon_f \left(C_{0f} b_i \frac{\tilde{k}_f}{k_f} + \frac{2}{3} \left(b_i \frac{\tilde{k}_f}{k_f} - 1 \right) \right) + 2\varphi \frac{\langle V_{p,i} - U_{s,i} \rangle}{\tau_p} (\langle U_{s,i} \rangle - \langle U_{f,i} \rangle) \right. \\ \quad \left. - 2 \frac{\langle \alpha_p \rangle}{\langle \alpha_f \rangle \rho_f} \frac{\partial \langle p_f \rangle}{\partial x_i} (\langle U_{s,i} \rangle - \langle U_{f,i} \rangle) \right]^{1/2} dW_{s,i} \end{array} \right. \quad (4.84)$$

where all of the parameters were defined in the complete model above.

The corresponding Eulerian RA equations for statistically homogeneous flow are

$$\frac{d\langle \mathbf{V}_p \rangle}{dt} = \frac{1}{\tau_p} \langle \mathbf{U}_s - \mathbf{V}_p \rangle + \mathbf{g}, \quad (4.85)$$

$$\frac{d\langle \mathbf{U}_s \rangle}{dt} = -\frac{\langle \alpha_f \rangle}{\rho_f} \nabla \langle p_f \rangle - \frac{1}{\mathbf{T}_L^*} \circ (\langle \mathbf{U}_s \rangle - \langle \mathbf{U}_f \rangle) + \frac{\varphi}{\tau_p} \langle \mathbf{V}_p - \mathbf{U}_s \rangle + \mathbf{g}. \quad (4.86)$$

For the second-order moments, we obtain

$$\frac{d\langle \mathbf{v}_p \otimes \mathbf{v}_p \rangle}{dt} = \mathcal{P}_{Vp} + \frac{1}{\tau_p} (\langle \mathbf{u}_s \otimes \mathbf{v}_p \rangle^\dagger - 2\langle \mathbf{v}_p \otimes \mathbf{v}_p \rangle), \quad (4.87)$$

$$\begin{aligned} \frac{d\langle \mathbf{u}_s \otimes \mathbf{v}_p \rangle}{dt} = \mathcal{P}_{Vsp} - \frac{1}{\mathbf{T}_L^*} \circ \langle \mathbf{u}_s \otimes \mathbf{v}_p \rangle + \frac{1}{\tau_p} (\langle \mathbf{u}_s \otimes \mathbf{u}_s \rangle - \langle \mathbf{v}_p \otimes \mathbf{u}_s \rangle) \\ + \frac{\varphi}{\tau_p} (\langle \mathbf{v}_p \otimes \mathbf{v}_p \rangle - \langle \mathbf{u}_s \otimes \mathbf{v}_p \rangle), \end{aligned} \quad (4.88)$$

$$\frac{d\langle \mathbf{u}_s \otimes \mathbf{u}_s \rangle}{dt} = \mathcal{P}_{Ss} - \frac{2}{\mathbf{T}_L^*} \circ \langle \mathbf{u}_s \otimes \mathbf{u}_s \rangle + \langle \mathbf{B}_s \mathbf{B}_s^T \rangle + \frac{\varphi}{\tau_p} (\langle \mathbf{u}_s \otimes \mathbf{v}_p \rangle^\dagger - 2\langle \mathbf{u}_s \otimes \mathbf{u}_s \rangle). \quad (4.89)$$

The mean-shear-production terms are

$$\mathcal{P}_{Vp} = -(\langle \mathbf{v}_p \otimes \mathbf{v}_p \rangle \cdot \nabla \langle \mathbf{V}_p \rangle)^\dagger \quad (4.90)$$

and

$$\mathcal{P}_{Vsp} = -\langle \mathbf{u}_s \otimes \mathbf{v}_p \rangle \cdot \nabla \langle \mathbf{V}_p \rangle^T - \langle \mathbf{v}_p \otimes \mathbf{v}_p \rangle \cdot \nabla \langle \mathbf{U}_s \rangle^T. \quad (4.91)$$

This model is similar to the model previously proposed by [Minier 2004, Peirano 2006] for the fluid velocity seen by the particles, but with a modified diffusion term, as discussed in detail in §4.4.1. Furthermore, both models have the same dilute limit ($\langle \alpha_f \rangle = 1$).

4.7.3 Fluid phase

The Eulerian RA equation describing the fluid-phase mass balance for a statistically homogeneous flow reduces to

$$\frac{d\langle \alpha_f \rangle}{dt} = 0 \quad (4.92)$$

i.e., $\langle \alpha_f \rangle$ is constant. The fluid-phase velocity and Reynolds stresses are found from

$$\frac{d\langle \mathbf{U}_f \rangle}{dt} = -\frac{1}{\rho_f} \nabla \langle p_f \rangle + \frac{\varphi}{\tau_p} \langle \mathbf{U}_p - \mathbf{U}_s \rangle + \mathbf{g}, \quad (4.93)$$

and

$$\frac{d\langle \mathbf{u}_f \otimes \mathbf{u}_f \rangle}{dt} = \mathcal{P}_f - C_{Rf} \frac{\varepsilon_f}{k_f} \left(\langle \mathbf{u}_f \otimes \mathbf{u}_f \rangle - \frac{2}{3} k_f \mathbf{I} \right) - C_{2f} \left(\mathcal{P}_{Sf} - \frac{2}{3} \mathcal{P}_{Sf} \mathbf{I} \right) - \frac{2}{3} \varepsilon_f \mathbf{I} \quad (4.94)$$

where $k_f = \frac{1}{2} \langle \mathbf{u}_f \cdot \mathbf{u}_f \rangle$. The production term is $\mathcal{P}_f = \mathcal{P}_{Sf} + \mathcal{P}_{Df}$ where \mathcal{P}_{Sf} is the mean-shear-production term, given by

$$\mathcal{P}_{Sf} = -(\langle \mathbf{u}_f \otimes \mathbf{u}_f \rangle \cdot \nabla \langle \mathbf{U}_f \rangle)^\dagger; \quad (4.95)$$

and \mathcal{P}_{Df} is the drag-production term, given by

$$\mathcal{P}_{Df} = \frac{\varphi}{\tau_p} [\langle \mathbf{u}_s \otimes (\mathbf{u}_p - \mathbf{u}_s) \rangle + \langle \mathbf{U}_s - \mathbf{U}_f \rangle \otimes \langle \mathbf{U}_p - \mathbf{U}_s \rangle]^\dagger. \quad (4.96)$$

In (4.94), C_{Rf} is the Rotta constant for the redistribution [Pope 2000], and $\mathcal{P}_{Sf} = \frac{1}{2}\text{trace}(\mathcal{P}_{Sf})$.

The fluid-phase dissipation equation becomes:

$$\frac{d\varepsilon_f}{dt} = (C_{\varepsilon 1f}\mathcal{P}_{Sf} - C_{\varepsilon 2f}\varepsilon_f) \frac{\varepsilon_f}{k_f} + C_{3f} \frac{\varphi}{\tau_p} \left(\frac{k_{fp}}{k_{f@p}} \varepsilon_p - \beta_f \varepsilon_f \right) + C_4 \frac{\varepsilon_p}{k_p} \mathcal{P}_D \quad (4.97)$$

with

$$\mathcal{P}_D = \frac{\varphi}{\tau_p} \frac{\langle \mathbf{U}_s - \mathbf{U}_f \rangle \cdot \langle \mathbf{U}_p - \mathbf{U}_f \rangle}{2}. \quad (4.98)$$

If the RA equations for the fluid phase are coupled with the simplified model described in §4.7.2, \mathbf{U}_p must be replaced with \mathbf{V}_p . Moreover, the particle-phase Lagrangian time-scale k_p/ε_p is not specified, and it is thus replaced by a fluid time-scale through a proportionality constraint:

$$\frac{\varepsilon_p}{k_p} = \alpha \frac{\varepsilon_f}{k_{f@p}}. \quad (4.99)$$

Now, substituting (4.99) in (5.45) and incorporating α in the model constants, gives the following equation for dissipation:

$$\frac{d\varepsilon_f}{dt} = (C_{\varepsilon 1f}\mathcal{P}_{Sf} - C_{\varepsilon 2f}\varepsilon_f) \frac{\varepsilon_f}{k_f} + C_{3f} \frac{\varphi}{\tau_p} \left(\frac{k_p}{k_{f@p}} k_{fp} - \beta_f k_{f@p} \right) \frac{\varepsilon_f}{k_{f@p}} + C_4 \frac{\varepsilon_f}{k_{f@p}} \mathcal{P}_D \quad (4.100)$$

The values of C_{3f} and C_4 in (4.100) may need to be adjusted as compared to (5.45) to account for the alternative time scale.

4.8 Numerical results

We present three spatially homogeneous examples of increasing complexity: (i) isotropic turbulence with one-way coupling [Février 2005], (ii) isotropic decaying [Sundaram 1999] and sheared turbulence [Ahmed 2000] with two-way coupling, and (iii) gravity-driven CIT [Capece de Almeida 2015]. The first example is aimed at appraising the partitioning of the particle kinetic energy, the second at testing the dynamics in the absence/presence of shear production (i.e., \mathcal{P}_{Sf}) without a mean velocity difference, and the third, and most important one, at validating the model for production due to a mean velocity difference (i.e., (4.98)).

4.8.1 Homogeneous isotropic turbulence

In order to illustrate the effectiveness of the decomposition of the particle velocity, we apply the models developed for the particle phase to the homogeneous isotropic turbulence simulations of [Février 2005] for non-collisional particles. For this example, the mean velocities \mathbf{U}_p , \mathbf{U}_f , \mathbf{U}_s are null, and $\varphi = 0$. At a first glance it may appear odd to compare the results of a model developed for collisional flows to DNS data for non-collisional particles. However, the crucial point for the modelling is the correlation between the fluid and particle velocities as captured by k_f and k_p , respectively. The applicability of the proposed models to non-collisional flows depends on the model used for turbulent dissipation, since the relative balance between k_p and Θ_p is determined by ε_p , for both dilute

and dense flows. The scope of this section is thus to verify if in the dilute case, where collisions do not play any role, energy budgets are well predicted. The point-particle DNS simulations of [F  vrier 2005] use one-way coupling with stationary fluid turbulence, and a particle-Reynolds-number-dependent drag coefficient f_D (instead of a constant τ_p). Therefore, the drag time scale is Stokes-number-dependent, and only qualitative comparisons can be made.

When a cloud of particles is put into a box filled with a homogeneous, isotropic turbulent flow and thus is agitated by the fluid turbulence, after a transient period, the statistics of particle velocities will reach equilibrium values. These limit values are of course functions of the (constant) statistics of the fluid (its mean kinetic energy, the Lagrangian timescale, among others). The relations giving the equilibrium values in terms of the fluid statistics are called the Tchen's relations. They were first obtained by [Tchen 1947] and later reformulated by [Hinze 1975]. In Tchen or Hinze's works, the determination of the equilibrium values was obtained through spectral analysis and manipulation of the fluid and particle energy spectra, where the fluid spectrum is assumed to have an exponential form. This derivation can be cumbersome and the physical meaning of the exponential form is not obvious. On the other hand, the same relations are derived from the Lagrangian pdf model in a straightforward way.

In forced, homogeneous, isotropic turbulence without body forces, all mean velocities are zero and the Reynolds-stress and particle-phase pressure tensors are isotropic. Moreover, $k_{f@p} = k_f$. With one-way coupling and fixed k_f and ε_f , the relevant moment equations from the complete model for the particle phase reduce to

$$\frac{dk_p}{dt} = \frac{2}{\tau_p}(k_{fp} - k_p) - \varepsilon_p, \quad (4.101a)$$

$$\frac{3}{2} \frac{d\langle\Theta_p\rangle}{dt} = -\frac{3\langle\Theta_p\rangle}{\tau_p} + \varepsilon_p, \quad (4.101b)$$

$$\frac{dk_{fp}}{dt} = -\left(\frac{1}{T_{Lf}} + \frac{1}{T_{Lp}}\right)k_{fp} + \frac{1}{\tau_p}(k_f - k_{fp}), \quad (4.101c)$$

$$\frac{d\varepsilon_p}{dt} = -C_{\varepsilon 2p} \frac{\varepsilon_p^2}{k_p} + \frac{C_{3p}}{\tau_p} \left(\frac{k_{fp}}{k_f} \varepsilon_f - \beta_p \varepsilon_p\right) \quad (4.101d)$$

where T_{Lf} is given by (4.27) and T_{Lp} by (4.18). After a transient period, all the statistics reach their steady-state values. This yields

$$2 \frac{k_{fp} - k_p}{\tau_p} - \varepsilon_p = 0, \quad (4.102a)$$

$$-\frac{3\langle\Theta_p\rangle}{\tau_p} + \varepsilon_p = 0, \quad (4.102b)$$

$$\frac{k_f}{\tau_p} - \left(\frac{1}{\tau_p} + \frac{1}{T_{Lf}} + \frac{1}{T_{Lp}}\right)k_{fp} = 0, \quad (4.102c)$$

$$St_p^2 - \frac{C_{3p}}{C_{\varepsilon 2p}} \left(\frac{k_{fp}}{k_p} St_f - \beta_p St_p\right) = 0 \quad (4.102d)$$

where $St_p = \tau_p \varepsilon_p / k_p$ and $St_f = \tau_p \varepsilon_f / k_f$. Summing (4.102a) and (4.102b) then yields

$$k_{fp} = \kappa_p, \quad (4.103)$$

which can be used together with (4.102c) to obtain a Tchen-like relation:

$$\kappa_p = \frac{1}{1 + \tau_p/T'_L} k_f \quad (4.104)$$

with $C_0 = C_{0p} = C_{0f}$ and

$$\frac{1}{T'_L} = \frac{1}{T_{Lf}} + \frac{1}{T_{Lp}} = \left(\frac{1}{2} + \frac{3}{4}C_0 \right) \left(\frac{\varepsilon_f}{k_f} + \frac{\varepsilon_p}{k_p} \right). \quad (4.105)$$

Here, τ_p/T'_L is an effective integral-scale Stokes number for the particles. Furthermore, St_p is constant, and can be related to St_f using (4.102a) and (4.102d). With $\beta_p = 1$, this relation depends only on the parameter ratio $\frac{C_{3p}}{C_{\varepsilon 2p}}$, and thus $St_p = St_f$ when $C_{3p} = 2C_{\varepsilon 2p}$. Note that the value of St_p controls the ratio $k_p/\kappa_p = 2/(2 + St_p)$ and, as expected, all of the particle-phase kinetic energy is spatially correlated when $St_p = 0$.

[F  vrier 2005] presented time-dependent DNS results of particle-laden homogeneous and isotropic turbulence for $St_f = 0.81$ and $\varphi = 0$, for three sets of initial conditions: (i) $\kappa_p = k_{fp} = 1$, $k_p = 1$; (ii) $\kappa_p = k_{fp} = 0$, $k_p = 0$; and (iii) $\kappa_p = 0.83$, $k_p = k_{fp} = 0$. We reproduced the same cases by solving the dimensionless forms of system (4.101) with the following values of the model constants: $C_0 = 1$, $C_{\varepsilon 2p} = 1.92$, $C_{3p} = 3.5$ and $\beta_p = 1$. For consistency with k_p , ε_p is initially set to zero when $k_p = 0$ and for case (i) the initial value of dissipation is $\varepsilon_p = 2$. Figure 4.1(a) shows the time evolution of κ_p , k_p and Θ_p obtained with the full model for the three different sets of considered initial conditions, while the evolution of κ_p obtained with the simplified model for the same cases is reported in figure 4.1(b). Moreover, 4.1(c) shows the same quantities as in figure 4.1(a) obtained with the model proposed in [Fox 2014] and 4.1(d) the results of the DNS of [F  vrier 2005]. In all cases, after a transient a steady state is reached, as expected. It can be seen how in DNS the total particle kinetic energy is distributed in the correlated part and in the uncorrelated granular temperature. This energy partition is satisfactorily captured by our complete model as well as by the model proposed in [Fox 2014]. Clearly, the simplified model can only give the total energy κ_p , which is however in good agreement with that of DNS and of more complete models. The transient behaviour is also in very good qualitative agreement with that obtained in DNS.

4.8.2 Decaying and homogeneous-shear flow

In this section we focus on the particle–turbulence interactions in homogeneous flows, and, in particular, on the cases simulated by DNS in [Sundaram 1999] for decaying turbulence and in [Ahmed 2000] for homogeneous-shear flows. For these examples, the mean velocities \mathbf{U}_p , \mathbf{U}_f , \mathbf{U}_s are null. In both cases the particle-phase volume fraction is such that two-way interactions need to be considered: flow modification by non-collisional point particles reveal a non-trivial dependence on the particle Stokes number and mass loading φ . It is thus interesting to verify if our model is able to reproduce such physics and if the same dependencies on the particle Stokes number are found.

The Eulerian RA equations describing the fluid and particle phases for the considered cases have been shown in §4.7. In particular, in the shear flow case a constant shear is present $\mathcal{S}_f = \partial\langle U_{f,1} \rangle / \partial x_2$, while $\mathcal{S}_f = 0$ in decaying turbulence. Gravity and collisions are not considered in these test cases. Note that when \mathcal{S}_f is null

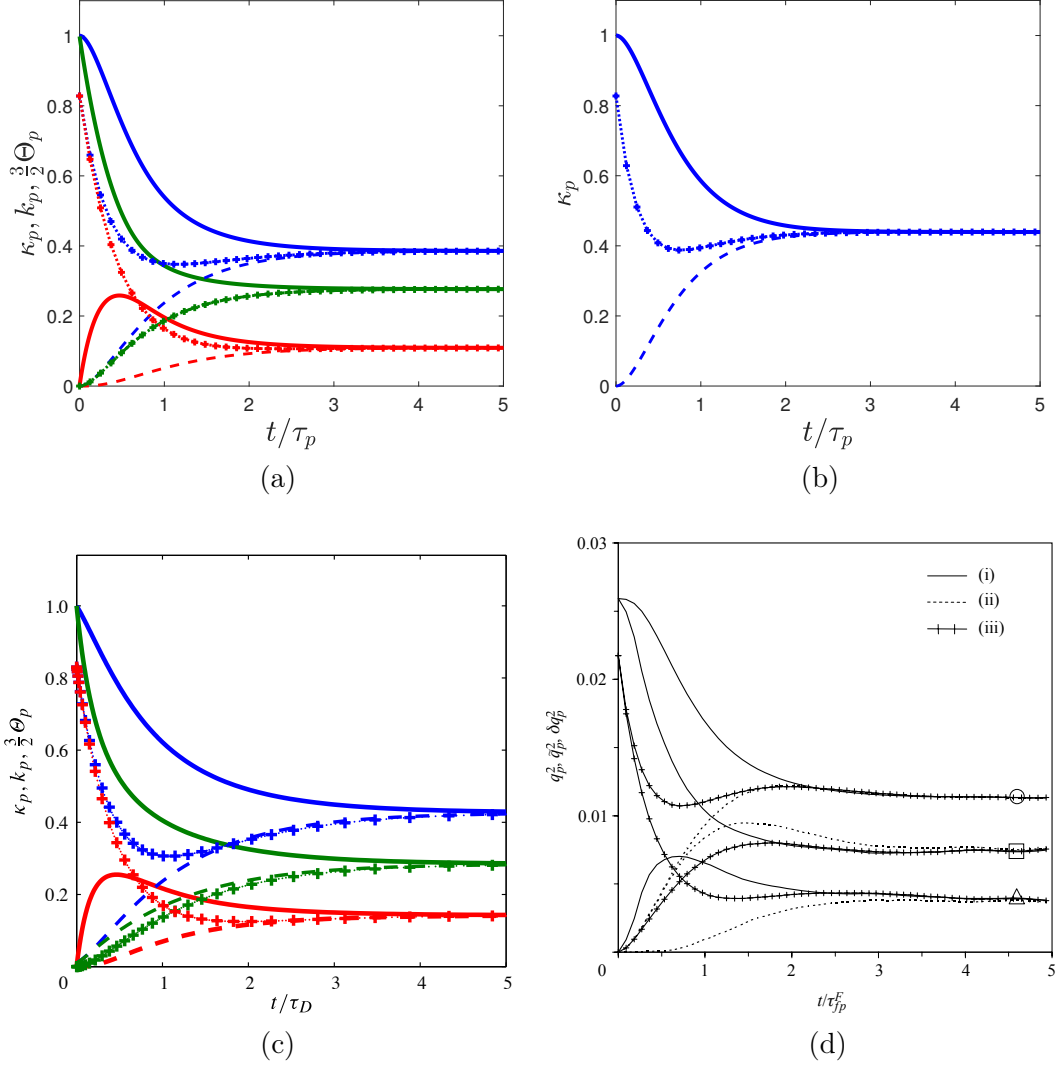


Figure 4.1: Time evolution of the dimensionless particle-phase energy components for $St_f = 0.81$. The curves correspond to the three considered sets of initial conditions: case (i) solid lines; (ii) dashed lines; and (iii) + line. κ_p is plotted in blue, k_p in green and $\frac{3}{2}\Theta_p$ in red. (a) Simulations with the complete particle model (4.101). (b) Simulations carried out with the simplified particle model (4.84) with $C_0 = 2.1$. Only total kinetic energy κ_p is computed. (c) Results from [Fox 2014] with the same initial conditions as in (a). (d) Results of point-particle DNS from figure 8 of [F  vrier 2005], where the results are in dimensional form. The notation in [F  vrier 2005] is $q_p^2 = \kappa_p$, $\tilde{q}_p^2 = k_p$, $\delta q_p^2 = \frac{3}{2}\Theta_p$ and $\tau_{fp}^F \propto \tau_D$.

(i.e., decaying turbulence), all second-order tensors will be isotropic so that only their traces are needed. Otherwise the non-zero components of the second-order moments are $(i, j) = (1, 1), (1, 2), (2, 1), (2, 2), (3, 3)$.

The mean gradients for the particle phase and fluid seen obey

$$\frac{d\mathcal{S}_p}{dt} = \frac{1}{\tau_p}(\mathcal{S}_s - \mathcal{S}_p), \quad (4.106a)$$

$$\frac{d\mathcal{S}_s}{dt} = \frac{1}{\tau_p}(\mathcal{S}_f - \mathcal{S}_s). \quad (4.106b)$$

In the following, the particle-phase velocity is initially the same as the fluid-phase velocity such that $\mathcal{S}_p(t) = \mathcal{S}_s(t) = \mathcal{S}_f$ and thus system (4.106) is not needed.

It is worth noting that, even in these simple flow conditions, the model still retains some of its features, as, for instance, the distinction between the fluid kinetic energy and the fluid-particle velocity correlation, which can be computed from Lagrangian quantities by averaging, i.e. $k_{fp} = \frac{1}{2}\langle u_{p,k}u_{s,k} \rangle$, while in Eulerian models that do not account for the fluid seen by the particles (see [Fox 2014]), it is modeled as $k_{fp} = (k_f k_p)^{1/2}$. Moreover, it should be remarked that only a part of the crossing trajectory effect is taken into account, that is when there is a mean drift, and thus, a mean relative velocity between fluid and particles. This means that in the case that we are testing, the modified Lagrangian timescale equals the fluid Lagrangian timescale, $T_L^* = T_L$, for all Stokes numbers. Conversely, particle inertia should affect the Lagrangian timescale of the fluid velocity seen by the particles. In particular, if we consider the limit cases, we have two situations: particles with very low inertia, i.e. $\tau_p/T_L \ll 1$, follow almost exactly the fluid, yielding $T_L^* = T_L$ for the fluid velocity seen. Particles with high inertia, i.e. $\tau_p/T_L \gg 1$, are nearly at a standstill with respect to the fluid and therefore, the fluid velocity seen time scale is approximately the Eulerian time scale, $T_L^* = T_E$. This inconsistency has already been pointed out by [Pozorski 1998], and, even if it can be neglected in flows where a mean drift drives the particles, becoming secondary, here it is of crucial importance, especially if we are interested in finding the trends of the decay rate with respect to particle inertia. For this reason we propose to add a Stokes dependence in $C_{\varepsilon 2}$ of the kind $C_{\varepsilon 2} = C(1 - \varphi St)$ with $C = 1.92$, in order to retrieve the good trend with St . Note that this simple model, which was also used in [Fox 2014] for the same test case, is just qualitative and valid for the range of conditions considered herein. A more refined analysis may be necessary for general situations.

4.8.2.1 Decaying turbulence

Concerning the values of other model constants, they are the same as in the stationary case, i.e. $C_{\varepsilon 2} = C_{\varepsilon 2p} = C_{\varepsilon 2f}$, $\beta = \beta_f = \beta_p = 1$, $C_3 = C_{3f} = C_{3p} = 3.5$ and $C_0 = C_{0f} = C_{0p} = 1$.

As $\mathcal{S}_f = 0$, the isotropic model equations for k_f , $k_{f@p}$, k_p and k_{fp} are solved directly:

$$\frac{dk_f}{dt} = \frac{2\varphi}{\tau_p}(k_{fp} - k_{f@p}) - \varepsilon_f, \quad (4.107a)$$

$$\frac{dk_{f@p}}{dt} = \frac{2\varphi}{\tau_p}(k_{fp} - k_{f@p}) - \varepsilon_f, \quad (4.107b)$$

$$\frac{dk_p}{dt} = \frac{2}{\tau_p}(k_{fp} - k_p) - \varepsilon_p, \quad (4.107c)$$

$$\frac{dk_{fp}}{dt} = \frac{1}{\tau_p}[k_{f@p} + \varphi k_p - (1 + \varphi)k_{fp}] - \left(\frac{1}{2} + \frac{3}{4}C_0\right)\left(\frac{\varepsilon_f}{k_f} + \frac{\varepsilon_p}{k_p}\right)k_{fp}, \quad (4.107d)$$

$$\frac{d\varepsilon_f}{dt} = -C_{\varepsilon 2}\frac{\varepsilon_f^2}{k_f} + C_3\frac{\varphi}{\tau_p}\left(\frac{k_{fp}}{k_{f@p}}\varepsilon_p - \varepsilon_f\right), \quad (4.107e)$$

$$\frac{d\varepsilon_p}{dt} = -C_{\varepsilon 2}\frac{\varepsilon_p^2}{k_p} + \frac{C_3}{\tau_p}\left(\frac{k_{fp}}{k_{f@p}}\varepsilon_f - \varepsilon_p\right). \quad (4.107f)$$

In the decaying turbulence test, initial conditions for the simulation are $k_f(0) = k_{f@p}(0) = k_p(0) = k_{fp}(0) = 1.314$, in accordance with the DNS by [Sundaram 1999], and $\varepsilon_f(0) = \varepsilon_p(0) = 1.0112$. Moreover, the mass loading is set to $\varphi = 0.162$. Note that because $k_f(0) = k_{f@p}(0)$, the first two equations in system (4.107) will yield $k_f(t) = k_{f@p}(t)$ so that only k_f is required to model decaying turbulence for this case.

Figure 4.2(a) shows the time evolution of the fluid turbulent kinetic energy obtained with the particle models, for particle sets characterized by four different Stokes numbers, namely $St = \tau_p/T_e = 0$ (fluid tracers), $St = 0.17$, $St = 0.35$ and $St = 0.69$ (where $T_e = 1.7328$ is the initial eddy-turnover time in DNS of [Sundaram 1999]). Note that the case at $St = 0$ was obtained from the particle equations as the limit case for $\tau_p/T_L \ll 1$, as described in appendix A. Figures 4.2(b)–2(d) show the same quantities as in figure 4.2(a), obtained by the simplified version of the present model, the Eulerian model by [Fox 2014] and the DNS by [Sundaram 1999] respectively. The same comparisons for the particle-phase turbulent kinetic energy are reported in figure 4.3. It can be seen that the effect of the Stokes number on the decay of the turbulent kinetic energy of both the fluid and the particle phases is qualitatively well captured by the present stochastic model, in its complete version as well as in the simplified one, although the initial stages of the time evolution are quite different from the DNS results.

4.8.2.2 Homogeneous-shear flow

We consider now the case of a homogeneous shear flow with $\mathcal{S}_f = 0.6$ as in [Fox 2014], and solve the anisotropic model equations given in §4.7. The mass loading is $\varphi = 0.162$ and the initial conditions $\varepsilon_f(0) = \varepsilon_p(0) = 0.25$. As in the previous decaying case, simulations have been carried out for the following four Stokes numbers: $St = 0, 0.17, 0.35, 0.69$. The values of the constants in our model are the same as in the previous case of homogeneous decaying turbulence with $C_{\varepsilon 1f} = C_{\varepsilon 1p} = 1.44$, which are standard values for single-phase turbulence models [Pope 2000]. For the simplified model $C_{\varepsilon 1f} = 1.2$. Figure 4.4 shows the time evolution of the fluid turbulent kinetic energy obtained with the particle model, both in its complete and simplified versions, with the same quantity obtained from the Eulerian model in [Fox 2014]. Comparison should also be made with the DNS data of [Ahmed 2000].

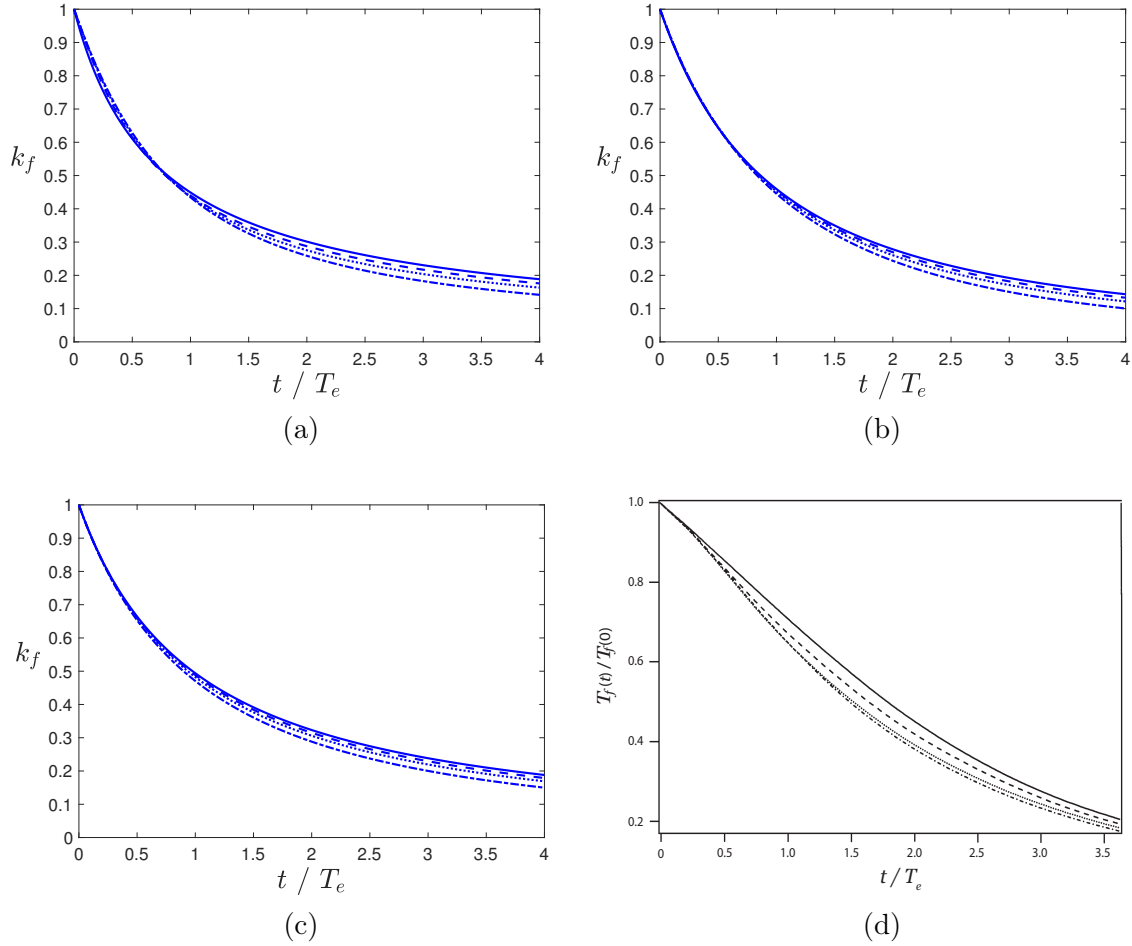


Figure 4.2: Fluid turbulent kinetic energy as a function of the non-dimensional time, t/T_e , in decaying fluid-particle turbulence: (a) complete particle model, (b) simplified particle model, (c) [Fox 2014] Eulerian model and (d) DNS of [Sundaram 1999]. The curves correspond to four different Stokes number: $St = 0$, solid line; $St = 0.17$, dashed lines; $St = 0.35$, dotted lines; $St = 0.69$, dash-dotted lines. In panel (c) the light dotted line is relative to an additional value of the Stokes number, not reported in the other panels; in panel (d) $T_f \propto k_f$.

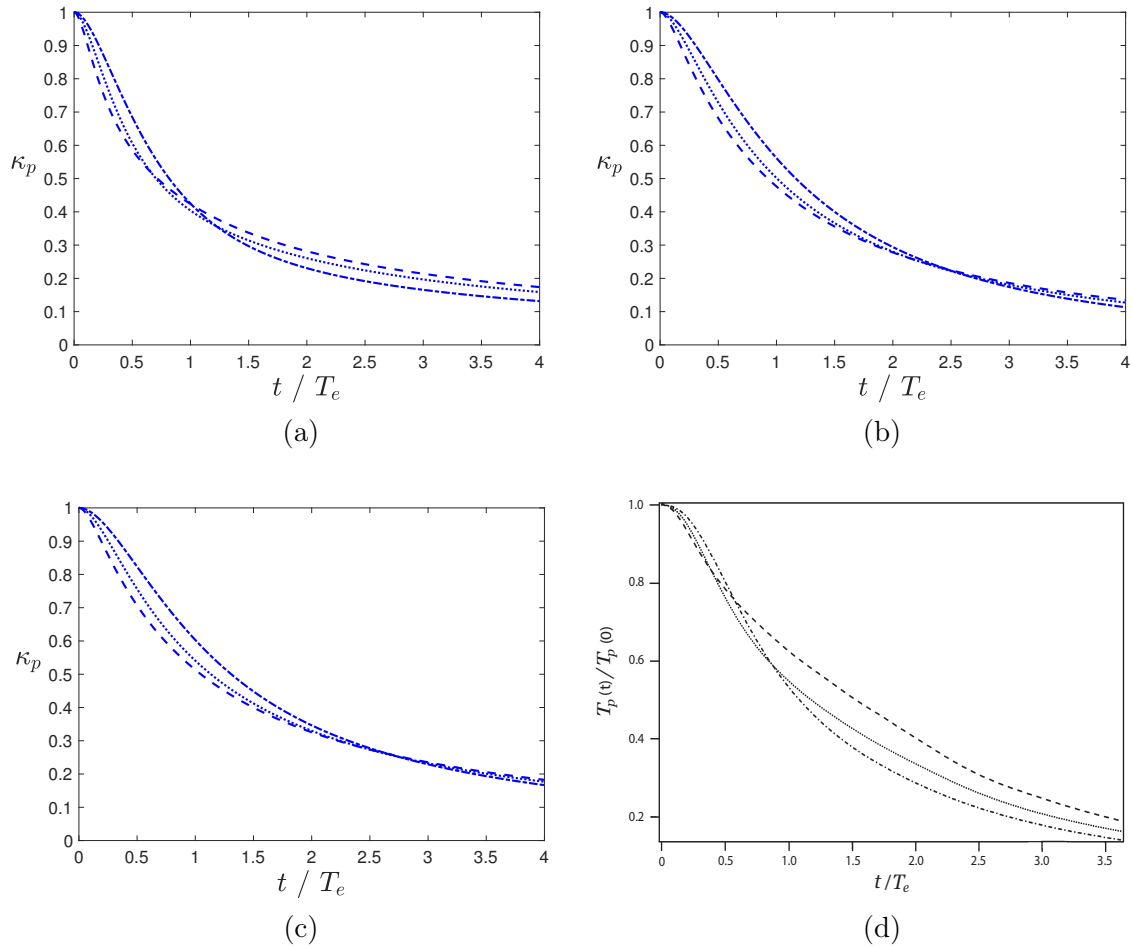


Figure 4.3: Particle-phase fluctuating energy as a function of the non-dimensional time, t/T_e , in decaying fluid–particle turbulence: (a) complete particle model, (b) simplified particle model, (c) Eulerian model of [Fox 2014] and (d) DNS of [Sundaram 1999]. The curves correspond to the following Stokes number: $St = 0.17$, dashed lines; $St = 0.35$, dotted lines; $St = 0.69$, dash-dotted lines. In panel (c) the light dotted line is relative to an additional value of the Stokes number, not reported in the other panels; in panel (d) $T_f \propto k_f$.

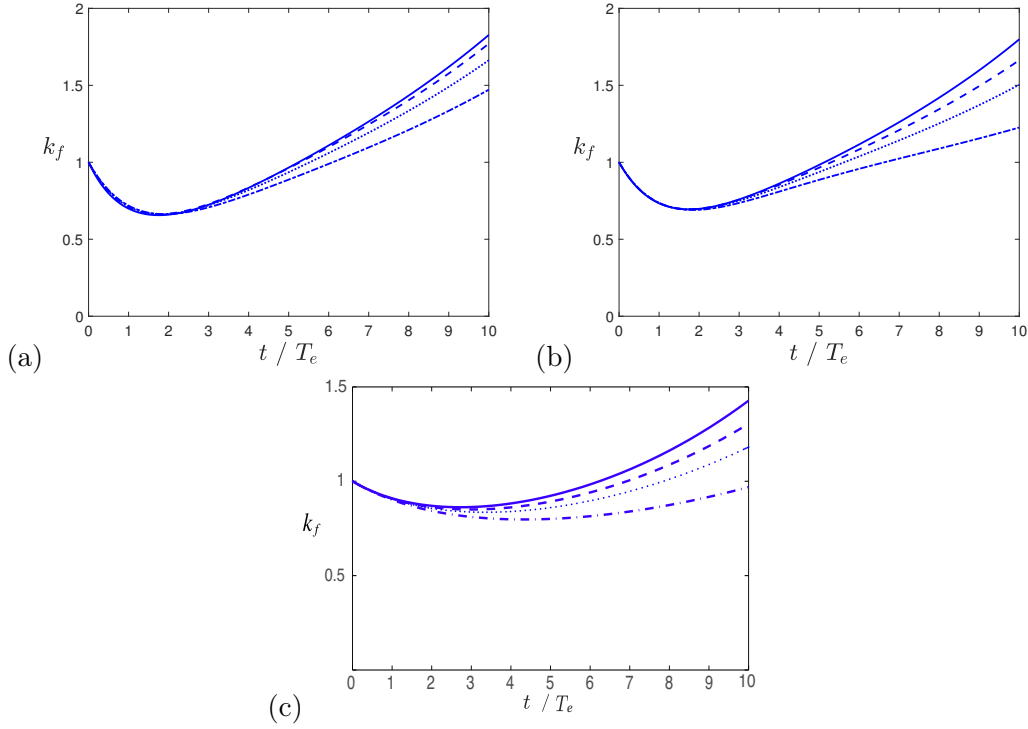


Figure 4.4: Homogeneous shear flow. Fluid turbulent kinetic energy as a function of the non-dimensional time, t/T_e with (a) the complete stochastic model; (b) the simplified stochastic model and (c) the Eulerian model by [Fox 2014]. The curves correspond to four different Stokes numbers: $St = 0$, solid line; $St = 0.17$, dashed lines; $St = 0.35$, dotted lines; $St = 0.69$, dash-dotted lines. In panel (c) the light dotted line is relative to an additional value of the Stokes number, not reported in the other panels.

For all the models, the time behaviour is qualitatively similar to that observed in DNS, with an initial decrease of the fluid turbulent kinetic energy followed by an increase. The value of the minima of k_f given by the complete model are closer to those obtained in DNS. Moreover, the effect of particle inertia on the time evolution of k_f is also correctly captured, i.e., the rate of increase of the fluid turbulent kinetic energy after the minimum is reduced as the inertia of the particles increases. The same effect is found also for the particle-phase fluctuating energy, κ_p , in agreement with [Fox 2014], as it can be seen in figure 4.5. No DNS data are available for this quantity.

4.8.3 Cluster-induced turbulence

To isolate the effect of turbulence generated by particles through two-way coupling, we consider a flow initially at rest laden with a random distribution of finite-size particles of diameter d_p subject to gravity oriented in the downward x_1 direction. The physical parameters are chosen to correspond to the Euler–Lagrange (EL) point-particle simulation of [Capecehatro 2015] as summarized in table 4.1. The dimensionless two-phase parameters that characterize the flow include the particle-to-fluid density ratio $\rho_p/\rho_f = 1000$, the average particle-phase volume fraction $\langle \alpha_p \rangle = 0.01$ and the particle Reynolds numbers $Re_p = \tau_p g d_p / \nu_f = 1$ where $\tau_p = \rho_p d_p^2 / (18 \rho_f \nu_f)$ is the particle relaxation time, ν_f is the

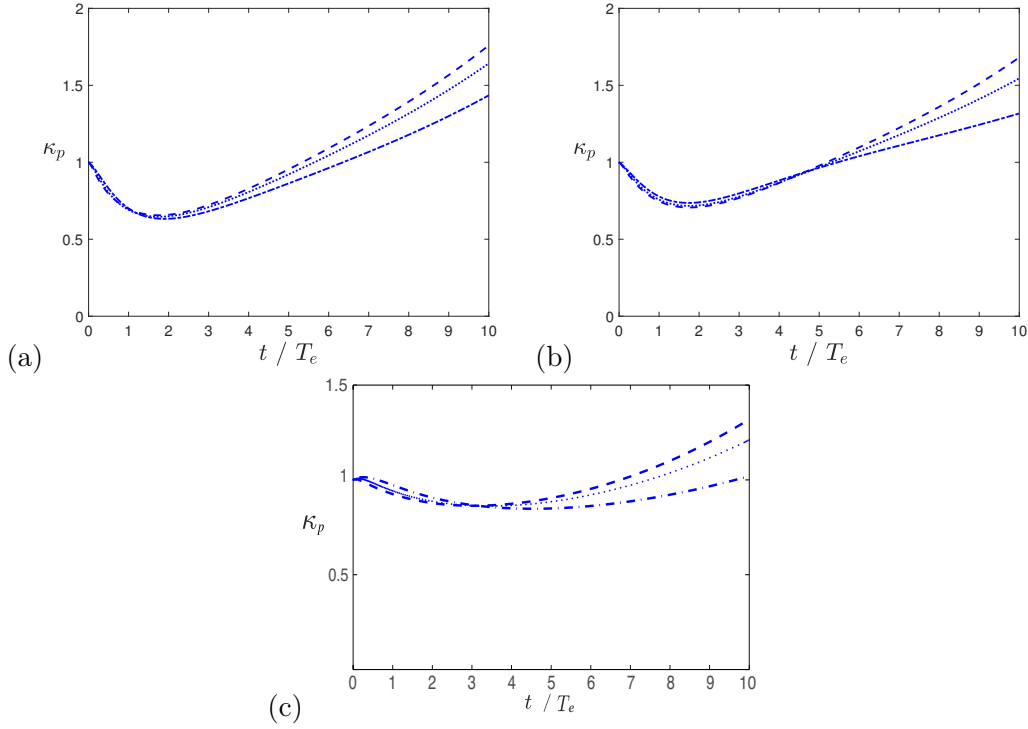


Figure 4.5: Homogeneous shear flow. Particle-phase fluctuating energy as a function of the non-dimensional time, t/T_e with (a) complete particle model; (b) simplified particle model and (c) Eulerian model in [Fox 2014]. The curves correspond to the Stokes numbers: $St = 0.17$, dashed lines; $St = 0.35$, dotted lines; $St = 0.69$, dash-dotted lines. In panel (c) the light dotted line is relative to an additional value of the Stokes number, not reported in the other panels.

fluid-phase kinematic viscosity and g is the magnitude of the gravity vector. Combination of these non-dimensional numbers yields the mass loading $\varphi = \rho_p \langle \alpha_p \rangle / (\rho_f \langle \alpha_f \rangle) = 10.1$, where $\langle \alpha_f \rangle = 1 - \langle \alpha_p \rangle$ is the average fluid-phase volume fraction. Finally, $\mathcal{V} = g\tau_p$ is the settling velocity for a single particle.

The CIT case is statistically homogeneous in all directions with periodic boundary conditions; therefore, in the context of the present formalism, it reduces to a 0-D description, with only the time dependency. Moreover, as in the previous considered cases, since the RA equations obtained from the stochastic ones are in closed form for a homogeneous configuration, we can limit ourselves to solving a system of coupled ODEs, instead of carrying out a Lagrangian Monte-Carlo simulation. The simulation is performed starting from an initial condition where both the particle and fluid phases are at rest and it is evolved in time up to the steady state. The fluid-phase pressure gradient is dynamically adjusted in order to keep the mean fluid velocity $\langle \mathbf{U}_f \rangle$ equal to zero. The model constants have been set in order to obtain a good prediction of the steady-state values for first-order moments. The values, so obtained, are reported in tables 4.2–4.3. A comment is in order concerning the values of C_{0f} and C_{3p} . These values are taken different from those used in the isotropic cases previously analysed. The results obtained in the CIT case with the previous values are in reasonable agreement with the full numerical simulation, but show some discrep-

Physical parameters		
d_p	Particle diameter	0.09 mm
ρ_p	Particle density	1000 kg m ⁻³
ρ_f	Fluid density	1 kg m ⁻³
ν_f	Fluid kinematic viscosity	1.8 · 10 ⁻⁵ m ² s ⁻¹
g	Gravity magnitude	8 m s ⁻²
Non-dimensional parameters		
e	Restitution coefficient	0.90
$\langle\alpha_p\rangle$	Mean particle volume fraction	0.01
φ	Mean mass loading	10.1
Re_p	Particle Reynolds number	1
Dimensional parameters		
τ_p	Drag time	0.025 s
\mathcal{V}	Settling velocity	0.20 m s ⁻¹

Table 4.1: Fluid–particle parameters used in CIT simulations [Capecelatro 2015].

C_{0f}	C_{0p}	$C_{\varepsilon 2}$	C_{3f}	C_{3p}	C_4	f_s	β_f	C_c
3.5	0.18	1.92	3.5	7.0	6.81	0.4	1	1

Table 4.2: Values of the model constants used in CIT simulations for the complete model.

ancy which has been eliminated using the values proposed in table 4.2. In fact, C_{3p} has an insignificant effect on the asymptotic results, but the present higher value smooths the transient dynamics. In contrast, the value of C_{0f} turns out to be key to get the correct level of turbulent kinetic energy.

The steady-state solution of first-order moments equations yields $\langle U_{s,1} - U_{p,1} \rangle = \mathcal{V}$, which agrees with the EL simulations of [Capecelatro 2015], and

$$\langle U_{s,1} \rangle = -\langle\alpha_p\rangle(1 + \varphi)\frac{T_{L,1}^*}{\tau_p}\mathcal{V} \quad (4.108)$$

where, using the definition in §4.4.1,

$$\frac{T_{L,1}^*}{\tau_p} = \left[\left(\frac{1}{2} + \frac{3}{4}C_{0f} \right)^2 \left(1 + \frac{3\beta^2\mathcal{V}^2}{2k_f} \right) \right]^{-1/2} \frac{1}{St_f} \quad (4.109)$$

and $St_f = \frac{\tau_p \varepsilon_f}{k_f}$. $\beta = T_{Lf}/T_{Ef}$ is set equal to 0.8. In fully developed CIT, the turbulence is generated by the clusters and the resulting Stokes number is nearly constant [Capecelatro 2016b]. The complete model therefore predicts that the steady-state value of

C_{0f}	$C_{\varepsilon 2}$	C_{3f}	C_4	β_f
0.8	6	0.02	0.1	0.75

Table 4.3: Values of the model constants used in CIT simulations for the simplified model.

$\langle U_{s,1} \rangle / \mathcal{V}$ depends on the particle volume fraction, the mass loading, and the dimensionless fluid-phase turbulent kinetic energy $2k_f/\mathcal{V}^2$. The prediction of $\langle \mathbf{U}_s \rangle$ is perhaps the most important contribution of the Lagrangian pdf model for CIT because information on the fluid seen by the particles is not available in most multiphase turbulence models for fluid-particle flows [?, see, e.g.,]for details[Fox2014].

The second-order moments have two independent, non-zero components, i.e., the vertical (1, 1) and horizontal (2, 2). For the fluid phase, these are found by solving (4.94). In CIT, the fluid-phase Reynolds stresses are anisotropic because of the mean velocities appearing in $\mathcal{P}_{f,11}$. In general, redistribution is weak so that $\langle u_{f,2}^2 \rangle \ll \langle u_{f,1}^2 \rangle$. In CIT, the anisotropy of the particle-phase pressure tensor arises due to the source terms $\varepsilon_{p,11}$, $\varepsilon_{p,22}$, whose anisotropy is controlled by f_s . For example, if $f_s = 1$ and collisions are negligible, the particle-phase pressure tensor and Reynolds stresses will have the same anisotropy. The value of the free parameter C_c in the collision term, on the other hand, will control the anisotropy of the particle-phase pressure tensor. For the particle phase, the Reynolds stresses are found by solving (4.73). The anisotropy of the particle-phase Reynolds stresses arises due to the production terms, i.e., due to the anisotropy of $\langle u_{s,i} u_{p,j} \rangle$. The latter are found by solving (4.66). Likewise, the Reynolds stresses for the fluid seen by the particles are found from (4.77). As seen for the fluid phase, the anisotropy of fluid seen is mainly due to the production terms, but is also due to the directional dependence of $T_{L,i}^*$. The dissipation rates ε_p and ε_f are found by solving (5.28) and (5.45) with the mean-shear-production terms set to zero.

Figures 4.6–4.8 show the time evolution of some mean velocities and second-order moments of both the fluid and particle phase, obtained with the complete and simplified models. It can be seen that all the quantities, after a transient of about $80\text{--}100\tau_p$ due to the non-trivial coupling between particles and fluid, tend to a steady value. The dashed horizontal line in the figures is the steady-state value obtained in the EL simulation by [Capecelatro 2015]. It can be seen that the mean velocities (figure 4.6) are well captured by both the complete and simplified models. As anticipated, an important feature of the Lagrangian pdf models is to provide a prediction of the fluid velocity seen by the particles, as compared to Eulerian pdf models in which it must be *a priori* specified. As for the second-order moments (figures 4.7 and 4.8), the complete model still gives a good agreement with EL simulations for both the fluid and particle phases, while the simplified version significantly overestimates the steady-state values.

Tables 4.4–4.6, in which the steady-state values of particle and fluid statistics are reported, confirm the previous observations. Table 4.5 also shows the repartition of the particle turbulent kinetic energy, κ_p , into the coherent part, k_p , and granular temperature, Θ_p . For the simplified model, by definition, $\Theta_p = 0$ and $\kappa_p = k_p$. The complete model also underestimates the granular temperature, most likely due to underestimating the value of ε_p through the choice of C_{3p} . Nonetheless, the decomposition of the particle turbulent kinetic energy appears to be essential to well predict second-order statistics, as done by the complete model in contrast to the simplified one. The complete model also well reproduces the fact that for all the quantities, except for the uncorrelated part of the particle velocity, turbulence fluctuations in the vertical direction are much higher than those in the horizontal directions. The complete model is able to correctly reproduce the anisotropy of the second-order tensors while the simplified model only gives a qualitative

	$2k_f/\mathcal{V}^2$	$\langle u_{f,1}^2 \rangle / (2k_f)$	$\langle u_{f,2}^2 \rangle / (2k_f)$
EL simulation	8.04	0.82	0.09
Complete model	8.74	0.93	0.04
Simplified model	16.60	0.98	0.01

Table 4.4: Steady-state values of fluid-phase velocity statistics. EL simulation data are taken from [Capecelatro 2015].

	$\langle U_{p,1} \rangle / \mathcal{V}$		
EL simulation	-2.28		
Complete model	-2.28		
Simplified model	-2.22		

	$2\kappa_p/\mathcal{V}^2$	$\langle v_{p,1}^2 \rangle / (2\kappa_p)$	$\langle v_{p,2}^2 \rangle / (2\kappa_p)$
EL simulation	5.41	0.78	0.11
Complete model	5.13	0.81	0.09
Simplified model	12.71	0.96	0.02

	k_p/κ_p	$\langle u_{p,1}^2 \rangle / (2k_p)$	$\langle u_{p,2}^2 \rangle / (2k_p)$
EL simulation	0.89	0.81	0.09
Complete model	0.99	0.81	0.09

	$3\langle \Theta_p \rangle / (2\kappa_p)$	$\langle P_{11} \rangle / (3\langle \Theta_p \rangle)$	$\langle P_{22} \rangle / (3\langle \Theta_p \rangle)$
EL simulation	0.11	0.51	0.25
Complete model	0.01	0.49	0.25

Table 4.5: CIT - Steady-state values of particle-phase velocity statistics. EL simulation data are taken from [Capecelatro 2015].

agreement.

Finally in figure 4.9 it is shown the time evolution of the correlation coefficient

$$\rho_{fp} = \frac{k_{fp}}{\sqrt{k_{f@p}k_p}}, \quad (4.110)$$

which proves the importance of having a stochastic model that predicts k_{fp} , leading to a correlation coefficient ρ_{fp} that can vary in time, instead of setting it to a constant value. Moreover, we can then use ρ_{fp} in the dissipation-exchange terms in (4.63) and (4.64). For example, similar to the model proposed by [Fox 2014], $\frac{k_{fp}\varepsilon_f}{k_{f@p}}$ and $\frac{k_{fp}\varepsilon_p}{k_{f@p}}$ in (4.63) and (4.64), respectively, could be replaced with $\rho_{fp}\sqrt{\varepsilon_p\varepsilon_f}$, which may help to increase the value of ε_p when applied to CIT.

	$\langle U_{s,1} \rangle / \mathcal{V}$		
EL simulation	-1.25		
Complete model	-1.28		
Simplified model	-1.22		
	$2k_{f@p} / \mathcal{V}^2$	$\langle u_{s,1}^2 \rangle / (2k_{f@p})$	$\langle u_{s,2}^2 \rangle / (2k_{f@p})$
EL simulation	8.32	0.85	0.07
Complete model	8.06	0.88	0.06
Simplified model	15.36	0.96	0.02
	$2k_{fp} / \mathcal{V}^2$	$\langle u_{s,1} u_{p,1} \rangle / (2k_{fp})$	$\langle u_{s,2} u_{p,2} \rangle / (2k_{fp})$
EL simulation	5.45	0.82	0.09
Complete model	5.13	0.82	0.09
Simplified model	12.71	0.96	0.02

Table 4.6: CIT - Steady-state values of fluid-phase turbulence statistics seen by particles. EL simulation data are taken from [Capecelatro 2015].

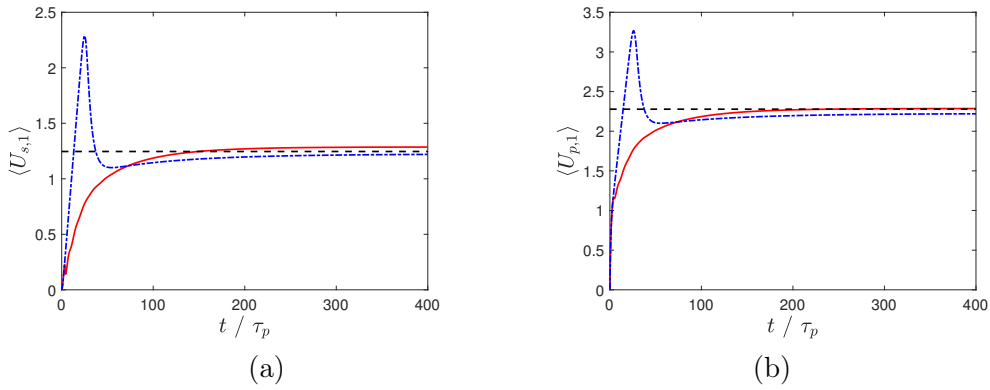


Figure 4.6: Time evolution of the vertical mean fluid velocity seen by the particles (a) and of the vertical mean particle velocity (b) from the complete (red line) and from the simplified (blue dot-dashed line) stochastic model. The horizontal black dashed line represents the steady state mean velocity from the DNS of [Capecelatro 2015].

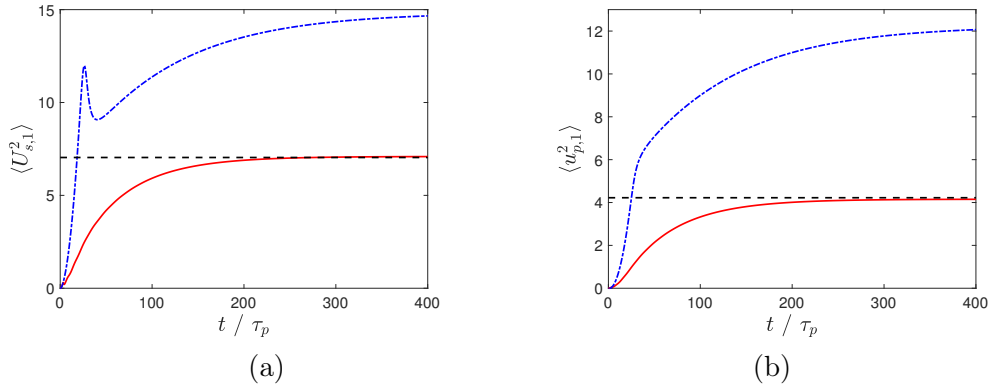


Figure 4.7: Time evolution of second-order moments of the vertical mean fluid velocity seen by the particles (a) and of the vertical mean particle velocity (b) from the complete (red line) and from the simplified (blue dot-dashed line) stochastic model. The horizontal black dashed line represents the steady state mean velocity from the DNS of [Capecelatro 2015].

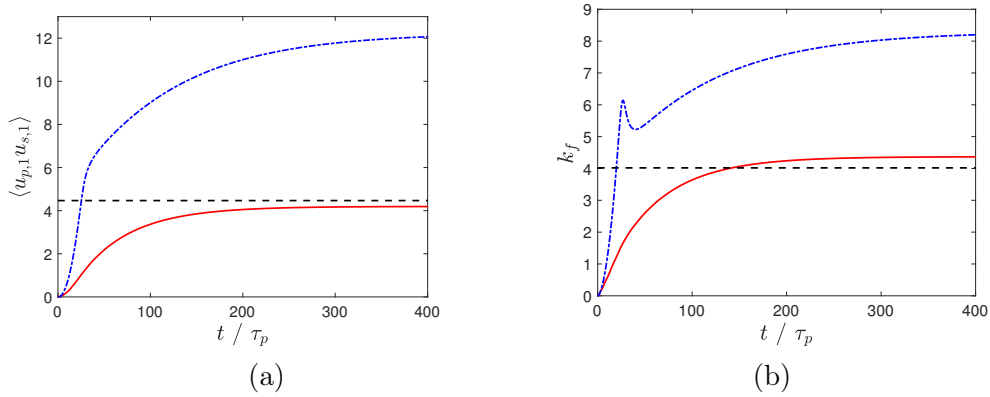


Figure 4.8: Time evolution of $\langle u_{p,1} u_{s,1} \rangle$ (a) and of k_f (b) from the complete (red line) and from the simplified (blue dot-dashed line) stochastic model. The horizontal black dashed line represents the steady state mean velocity from the DNS of [Capecelatro 2015].

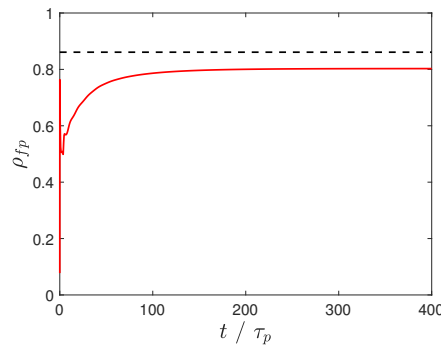


Figure 4.9: Time evolution of $\rho_{fp} = k_{fp}/(k_{f@p}k_p)^{1/2}$ from the complete stochastic model. The horizontal black dashed line represents the steady-state mean value from the DNS of [Capecelatro 2015].

4.9 Discussion and conclusions

The main objective of this work was to develop a novel pdf modelling approach for particle-laden turbulent flows including in a statistical sense particle–particle collisions. The approach is based on the development of a modelled equation for the one-particle Lagrangian pdf. As for the single-phase turbulent pdf approach [Pope 2000, Fox 2003], the corresponding Reynolds-averaged moment equations are taken as a useful guideline for the construction of a sound model. In the present case, the recent Reynolds-averaged framework developed by [Fox 2014] and validated in [Capecelatro 2016b] has been taken as reference. One of the most original points of the present approach consists in developing a Lagrangian pdf model based upon the decomposition of the velocity into two separate particle-phase velocity variables (\mathbf{U}_p and $\delta\mathbf{v}_p$), which are statistically uncorrelated. This decomposition has been found to be key in the correct reproduction of moderately dense particle flows and has been never used before in the framework of Lagrangian pdf modelling, where only the total particle velocity is available.

The new framework put forward is very general, but a precise model has to be proposed to make actual simulations. From a technical point of view, we have proposed a new stochastic model, which represents the joint state variables $(\mathbf{x}_p, \mathbf{V}_p, \delta\mathbf{v}_p, \mathbf{U}_s)$ as a diffusion process, or informally a Langevin equation, that is the corresponding joint pdf is given by a Fokker–Planck equation. The model has been built phenomenologically, and the unclosed terms in the exact Lagrangian equations have been replaced by return-to-equilibrium and fluctuating terms, following fluctuation–dissipation arguments [Marconi 2008]. To highlight the role of the decomposition of the velocity, we have also developed a simplified model that takes into account the two-way coupling between the phases but does not consider the presence of an uncorrelated part of the velocity. This model bears some similarity to a previous proposition [Minier 2001, Peirano 2006], but in fact even this model is new since it differs in the closure of the drift and diffusion coefficients. In particular, it has been built to describe the presence of a drift velocity even in homogeneous cases. The Reynolds-averaged equations derived from the complete pdf model are shown to be consistent with the ones obtained in the Eulerian framework [Fox 2014]. On the other hand, and this is one of the significant advantages of Lagrangian pdf approaches [Pope 2000, Minier 2001], the level of content of the present model is more detailed, notably the fluid velocity seen by the particles \mathbf{U}_s is included and therefore all the related one-point moments can be computed. When the mean mass loading is non-negligible, the dynamics of the fluid velocity seen by the particles is strongly affected by coupling with the particle phase. The Lagrangian pdf model thus provides a closure for the moments of \mathbf{U}_s , which need a closure in the Eulerian framework. It is expected that the present model has the same range of validity as the corresponding Eulerian one, namely it should be valid for moderate mean mass loadings where volume fraction is only a few percent $\alpha_p \leq 0.05$. For higher mass loading, new terms should be added taking into account rheological effects. This is a challenging and interesting perspective.

Once the pdf formalism and the Lagrangian pdf model were defined, we have validated it using the same test cases employed to validate a recently developed Eulerian model [Fox 2014, Capecelatro 2015]. In particular, the Lagrangian pdf model is applied to statistically homogeneous flows of increasing difficulty, namely, (i) particle-laden homogeneous

isotropic turbulence [F  vrier 2005, Sundaram 1999], (ii) homogeneous sheared turbulence [Elghobashi 1994], and (iii) CIT [Capecelatro 2015]. In the first two cases, the mean fluid- and particle-phase velocities are null, and hence the production of fluid-phase turbulence by fluid drag is absent. These cases are useful for validating the coupling terms in the Lagrangian pdf model for the exchange of turbulent kinetic energy between the two phases, and their dependence on the mass loading. In contrast, case (iii) provides a difficult and physically more interesting validation test of the model for $\langle \mathbf{U}_s \rangle$. Indeed it determines the mean slip velocity between the two phases (see (4.57)), and of the exchange/dissipation models, which determine the relative contributions of correlated k_p and uncorrelated Θ_p turbulent kinetic energy. Interestingly, the steady-state model for $\langle \mathbf{U}_s \rangle$ given in (4.108) is relatively simple (compare, for example, the correlation used in [Capecelatro 2016b]), with the Lagrangian time scale $T_{L,1}^*$ playing a prominent role. The complete and simplified models are both qualitatively in agreement with DNS and experiments in the homogeneous isotropic and shear cases, although the simplified model cannot predict the quantities related to the uncorrelated part of the velocity. Instead, important differences are encountered for the CIT case. While the complete pdf model gives satisfactory results for all observables, the simplified model is able to provide good predictions for the first moments but strongly overestimates the energy. This result is important, since it demonstrates that the decomposition of the particle velocity into correlated and uncorrelated parts is necessary to correctly represent the dynamics of moderately dense flows. From a physical point of view, it is interesting to note, however, that even though the agreement is only qualitative, the simple two-way coupling, without collisions, is able to induce CIT.

To conclude, in this work we have developed a general approach, in which we have proposed a specific model validated in some relevant test cases. To assess and improve the model, it would be interesting, in future work, to investigate CIT over a wide range of $\langle \alpha_p \rangle$ and φ values to determine whether the parameters in the model for $T_{L,1}^*$ should depend on these quantities. In fact, it would be useful to develop a model for the fluid pressure gradient seen by particles directly from DNS. More generally, the complete pdf model should be tested for inhomogeneous particle-laden flows wherein the spatial transport terms play an important role. For example, the particle-laden channel flows of [Capecelatro 2016a, ?] would be a challenging test cases. In particular, for channel flows the correlated and uncorrelated particle velocity components generate separate spatial fluxes for all statistics. From the RA model developed in [Capecelatro 2016b], it is known that, depending on the Stokes number, one or the other of these fluxes may be dominant. As a result, the wall-normal distribution of $\langle \alpha_p \rangle$, as well as other statistics, is very sensitive to how the spatial fluxes are modelled. In any case, as shown in this work, it can be expected that by including a stochastic model for \mathbf{U}_s the resulting models for the spatial fluxes will provide more robust closures for inhomogeneous turbulent particle-laden flows.

Acknowledgments

We thank Dr. Alexander Vichansky for his remarks during the revision process. ROF was partially supported by grants from the U.S. National Science Foundation (CBET-1437865 and ACI-1440443).

4.A Exact Reynolds-average equations

4.A.1 Particle phase

We show here the RA form of the Lagrangian pdf transport equations (4.9)–(4.8). It is worth noting that they correspond exactly to the RA transport equations obtained in [Capecelatro 2015] from the corresponding hydrodynamics ones. From the equation for $\tilde{\mathbf{V}}_p$ (4.9), applying a RA (ensemble averaging over a large number of fluid realizations), the exact RA equations can be retrieved for the particle mean velocity $\langle \mathbf{V}_p \rangle = \langle \tilde{\mathbf{V}}_p \rangle$:

$$\frac{\partial \langle \alpha_p \rangle \langle \tilde{\mathbf{V}}_p \rangle}{\partial t} + \nabla \cdot \langle \alpha_p \rangle (\langle \tilde{\mathbf{V}}_p \rangle \otimes \langle \tilde{\mathbf{V}}_p \rangle + \langle \mathcal{P} \rangle) = \langle \alpha_p \rangle \left(\left\langle \frac{\tilde{\mathbf{U}}_f - \tilde{\mathbf{V}}_p}{\tau_p} \right\rangle + \mathbf{g} \right). \quad (4.111)$$

The Reynolds stresses of the correlated part $\langle \tilde{\mathbf{v}}_p \otimes \tilde{\mathbf{v}}_p \rangle$ can be obtained analogously, and it gives the following Eulerian transport equation:

$$\begin{aligned} \frac{\partial \langle \alpha_p \rangle \langle \tilde{\mathbf{v}}_p \otimes \tilde{\mathbf{v}}_p \rangle}{\partial t} + \nabla \cdot \langle \alpha_p \rangle (\langle \tilde{\mathbf{V}}_p \rangle \otimes \langle \tilde{\mathbf{v}}_p \otimes \tilde{\mathbf{v}}_p \rangle) + \nabla \cdot \langle \alpha_p \rangle \langle \tilde{\mathbf{v}}_p \otimes \tilde{\mathbf{v}}_p \otimes \tilde{\mathbf{v}}_p \rangle = \\ - \langle \alpha_p \rangle (\langle \tilde{\mathbf{v}}_p \otimes \tilde{\mathbf{v}}_p \rangle \cdot \nabla \langle \tilde{\mathbf{V}}_p \rangle)^\dagger - \langle \alpha_p \rangle \langle \tilde{\mathbf{v}}_p \otimes \nabla \cdot (\delta \tilde{\mathbf{V}}_p \otimes \delta \tilde{\mathbf{V}}_p) \rangle^\dagger \\ + \langle \alpha_p \rangle \frac{(\langle \tilde{\mathbf{u}}_f \otimes \tilde{\mathbf{v}}_p \rangle - \langle \tilde{\mathbf{v}}_p \otimes \tilde{\mathbf{v}}_p \rangle)^\dagger}{\tau_p}. \end{aligned} \quad (4.112)$$

Finally, applying first the coarse-graining operator and then the RA one to (4.8), we get the equation for the particle-phase pressure tensor:

$$\begin{aligned} \frac{\partial \langle \alpha_p \rangle \langle \mathbf{P} \rangle}{\partial t} + \nabla \cdot \langle \alpha_p \rangle \left(\langle \tilde{\mathbf{V}}_p \rangle \otimes \langle \mathbf{P} \rangle + \langle \delta \tilde{\mathbf{V}}_p \otimes \delta \mathbf{V}_p \otimes \delta \mathbf{V}_p \rangle + \langle \delta \tilde{\mathbf{V}}_p \otimes \delta \mathbf{V}_p \otimes \tilde{\mathbf{v}}_p \rangle \right) = \\ - 2 \langle \alpha_p \rangle \frac{\langle \mathbf{P} \rangle}{\tau_p} - \langle \alpha_p \rangle (\langle \mathbf{P} \rangle \cdot \nabla \langle \tilde{\mathbf{V}}_p \rangle)^\dagger - \langle \alpha_p \rangle \langle \mathbf{P} \cdot \nabla \tilde{\mathbf{v}}_p \rangle^\dagger. \end{aligned} \quad (4.113)$$

4.A.2 Fluid phase

Taking the RA of the hydrodynamic fluid-phase equations, see [Capecelatro 2015], yields the RA fluid-phase transport equation. It gives for the volume fraction:

$$\frac{\partial \langle \alpha_f \rangle}{\partial t} + \nabla \cdot \langle \alpha_f \rangle \langle \mathbf{U}_f \rangle_f = 0. \quad (4.114)$$

For the fluid velocity:

$$\begin{aligned} \frac{\partial \langle \alpha_f \rangle \langle \mathbf{U}_f \rangle_f}{\partial t} + \nabla \cdot \langle \alpha_f \rangle (\langle \mathbf{U}_f \rangle_f \otimes \langle \mathbf{U}_f \rangle_f + \langle \mathbf{u}_f \otimes \mathbf{u}_f \rangle_f) = \\ - \frac{\langle \alpha_f \rangle}{\rho_f} \nabla \langle p_f \rangle + \frac{\langle \alpha_f \rangle}{\rho_f} \nabla \cdot \langle \boldsymbol{\sigma}_f \rangle - \langle \alpha_f \rangle \varphi \left\langle \frac{\mathbf{U}_f - \mathbf{U}_p}{\tau_p} \right\rangle_p + \langle \alpha_f \rangle \mathbf{g} \end{aligned} \quad (4.115)$$

where

$$\varphi = \frac{\rho_p \langle \alpha_p \rangle}{\rho_f \langle \alpha_f \rangle} \quad (4.116)$$

is the mean mass loading, and $\langle \mathbf{u}_f \otimes \mathbf{u}_f \rangle_f$ is the fluid-phase Reynolds stress tensor.

And for the Reynolds-stress tensor we find

$$\begin{aligned}
 & \frac{\partial \langle \alpha_f \rangle \langle \mathbf{u}_f \otimes \mathbf{u}_f \rangle_f}{\partial t} + \nabla \cdot \langle \alpha_f \rangle (\langle \mathbf{U}_f \rangle_f \otimes \langle \mathbf{u}_f \otimes \mathbf{u}_f \rangle_f + \langle \mathbf{u}_f \otimes \mathbf{u}_f \otimes \mathbf{u}_f \rangle_f) = \\
 & - \langle \alpha_f \rangle (\langle \mathbf{u}_f \otimes \mathbf{u}_f \rangle_f \cdot \nabla \langle \mathbf{U}_f \rangle_f)^\dagger + \frac{\langle \alpha_f \rangle}{\rho_f} (\nabla \cdot \langle \boldsymbol{\sigma}_f \otimes \mathbf{u}_f \rangle - \nabla \langle p_f \mathbf{u}_f \rangle)^\dagger \\
 & - \frac{\langle \alpha_f \rangle}{\rho_f} (\langle \boldsymbol{\sigma}_f \cdot \nabla \mathbf{u}_f \rangle - \langle p_f \nabla \mathbf{u}_f \rangle)^\dagger \\
 & + \frac{\langle \alpha_f \rangle \varphi}{\tau_p} [\langle \mathbf{u}_f \otimes \mathbf{u}_p \rangle_p - \langle \mathbf{u}_f \otimes \mathbf{u}_f \rangle_p + \langle \mathbf{u}_f \rangle_p \otimes (\langle \mathbf{U}_p \rangle_p - \langle \mathbf{U}_f \rangle_f)]^\dagger. \tag{4.117}
 \end{aligned}$$

The fluid-phase variables that are averaged with respect to the particle phase, i.e. $\langle \mathbf{u}_f \rangle_p$, appear due to fluid–particle coupling (*e. g.* due to clusters).

4.B Simulation of a Gaussian vector: the Choleski decomposition

Let $\mathbf{X} = (X_1, \dots, X_d)$ be a Gaussian vector defined by a zero mean and a covariance matrix $C_{ij} = \langle X_i X_j \rangle$. For all positive symmetric matrices (such as C_{ij}), there exists a (lower or upper) triangular matrix P_{ij} which satisfies

$$\mathbf{C} = \mathbf{P}\mathbf{P}^t \implies C_{ij} = \sum_{k=1}^d P_{ik} P_{jk}.$$

\mathbf{P} is given by the Choleski algorithm (here for the lower triangular matrix):

$$\begin{aligned}
 P_{i1} &= \frac{C_{i1}}{\sqrt{C_{11}}}, \quad 1 \leq i \leq d \\
 P_{ii} &= \left(C_{ii} - \sum_{j=1}^{i-1} P_{ij}^2 \right)^{1/2}, \quad 1 < i \leq d \\
 P_{ij} &= \frac{1}{P_{jj}} \left(C_{ij} - \sum_{k=1}^{j-1} P_{ik} P_{jk} \right), \quad 1 < j < i \leq d \\
 P_{ij} &= 0, \quad i < j \leq d.
 \end{aligned}$$

Let $\mathbf{G} = (G_1, \dots, G_d)$ be a vector composed of independent $\mathcal{N}(0, 1)$ Gaussian random variables, then it can be shown that the vector $\mathbf{Y} = \mathbf{P}\mathbf{G}$ is a Gaussian vector of zero mean and whose covariance matrix is $\mathbf{C} = \mathbf{P}\mathbf{P}^t$. Therefore, \mathbf{X} and \mathbf{Y} are identical, that is

$$\mathbf{X} = \mathbf{P}\mathbf{G} \implies X_i = \sum_{k=1}^d P_{ik} G_k. \tag{4.118}$$

4.C Fokker–Planck equation

The state vector of the Lagrangian description, given by $\mathbf{Z} = (\mathbf{x}_p, \mathbf{U}_p, \delta \mathbf{v}_p, \mathbf{U}_s)$, is associated with a single particle, while $\langle \mathbf{Z} \rangle$ stands for $\langle \mathbf{Z} \rangle[\mathbf{x}^{(k)}]$. The particle system is thus

represented by this set of Lagrangian pdf equations, where the particle state variables are modelled through a Langevin equation, or to be more rigorous as a diffusion process. This set of Lagrangian pdf equations for the trajectories of the sample particles corresponds, from the pdf point of view, to the following Fokker–Planck (FP) equation for the Eulerian mass density function (mdf) [Pope 1985, Minier 2001, Fox 2003]:

$$\begin{aligned}
& \frac{\partial F_p^E}{\partial t} + U_{p,i} \frac{\partial F_p^E}{\partial x_i} + \delta v_{p,i} \frac{\partial F_p^E}{\partial x_i} = \\
& - \frac{\partial}{\partial U_{p,i}} \left(\left[\frac{(U_{s,i} - U_{p,i})}{\tau_p} - \frac{1}{\langle \alpha_p \rangle \rho_p} \frac{\partial \langle \alpha_p \rangle \rho_p \langle P_{ij} \rangle}{\partial x_j} + \delta v_{p,j} \frac{\partial \langle U_{p,i} \rangle}{\partial x_j} - \frac{1}{T_{Lp}} (U_{p,i} - \langle U_{p,i} \rangle) + g_i \right] F_p^E \right) \\
& + \frac{1}{2} C_p \varepsilon_p \delta_{ij} \frac{\partial^2 F_p^E}{\partial U_{p,i} \partial U_{p,j}} \\
& - \frac{\partial}{\partial \delta v_{p,i}} \left(\left[-\frac{\delta v_{p,i}}{\tau_p} + \frac{1}{\langle \alpha_p \rangle \rho_p} \frac{\partial \langle \alpha_p \rangle \rho_p \langle P_{ij} \rangle}{\partial x_j} - \delta v_{p,j} \frac{\partial \langle U_{p,i} \rangle}{\partial x_j} - \frac{(1+e)(3-e)}{4\tau_c} \delta v_{p,i} \right] F_p^E \right) \\
& + \frac{1}{2} \left[(B_\delta B_\delta^T)_{ij} + \frac{1}{2\tau_c} (1+e)^2 \langle \Theta_p \rangle \delta_{ij} \right] \frac{\partial^2 F_p^E}{\partial \delta v_{p,i} \partial \delta v_{p,j}} \\
& + \left[\frac{\langle \alpha_f \rangle}{\rho_f} \frac{\partial \langle p_f \rangle}{\partial x_i} - (\langle U_{p,j} \rangle - \langle U_{f,j} \rangle) \frac{\partial \langle U_{f,i} \rangle}{\partial x_j} - g_i \right] \frac{\partial F_p^E}{\partial U_{s,i}} \\
& - \frac{\partial}{\partial U_{s,i}} \left[\left(G_{ij} (U_{s,j} - \langle U_{f,j} \rangle) - \varphi \frac{(U_{s,i} - U_{p,i})}{\tau_p} \right) F_p^E \right] + \frac{1}{2} B_{s,ii}^2 \frac{\partial^2 F_p^E}{\partial U_{s,i} \partial U_{s,i}} \quad (4.119)
\end{aligned}$$

where $B_{s,ii}$ is the diffusion matrix given by (4.41), and it is not given here explicitly for the sake of clarity. $F_p^E(t, \mathbf{x}; U_p, \delta \mathbf{v}_p, U_s)$ is the probable mass of discrete particles in an element in the phase-space of volume $dU_p d\delta \mathbf{v}_p dU_s$ at a position \mathbf{x} .

4.D Fluid–particle limit

The limit behaviour of the equations is only shown in homogeneous isotropic conditions for the sake of simplicity. In the limit case of tracer particles, i.e., $\tau_p \rightarrow 0$, we know from the equations for the stochastic model that $U_p \rightarrow U_s$ and $U_s \rightarrow U_f$, but we do not know if the model equation for U_s is exactly the same as U_p . At the same time we have that the particle-phase uncorrelated velocity goes to zero, which is consistent. When the particle inertia becomes very small where $\beta_p = \beta_f \rightarrow 1$ and $k_{fp} = k_{f@p} \rightarrow k_f$, the particle-phase dissipation tends to $\varepsilon_p \rightarrow \varepsilon_f$, as we can see from (4.120) and (4.121):

$$\frac{d\varepsilon_f}{dt} = (C_{\varepsilon 1} \mathcal{P} - C_{\varepsilon 2} \varepsilon_f) \frac{\varepsilon_f}{k_f} + C_3 \frac{\varphi}{\tau_p} \left(\frac{k_{fp}}{k_{f@p}} \varepsilon_p - \beta_f \varepsilon_f \right), \quad (4.120)$$

$$\frac{d\varepsilon_p}{dt} = (C_{\varepsilon 1} \mathcal{P} - C_{\varepsilon 2} \varepsilon_p) \frac{\varepsilon_p}{k_p} + C_3 \frac{1}{\tau_p} \left(\frac{k_{fp}}{k_{f@p}} \varepsilon_f - \beta_p \varepsilon_p \right). \quad (4.121)$$

Now we can check what happens to the stochastic equation for U_s . From the spatially homogeneous Lagrangian model, we can obtain

$$dU_s + \varphi dU_p = -\frac{1}{T_L} U_s dt - \frac{\varphi}{T_{Lp}} U_p dt + \sqrt{C_0 \varepsilon_f} dW_s + \varphi \sqrt{C_{0p} \varepsilon_p} dW_p. \quad (4.122)$$

Now, when $\tau_p \rightarrow 0$, we can use one of the two equations to prove $dU_s = dU_p$, while the other two will give $\delta v_p \rightarrow 0$ and

$$dU_s = -\frac{1}{T_L} U_s dt + \frac{1}{(1+\varphi)} \sqrt{C_0 \varepsilon_f} (dW_s + \varphi dW_p). \quad (4.123)$$

To obtain exactly the same equation as for one-way coupling, the white noise of the particle equation dW_p should be replaced, in this limit, by the one employed in the fluid velocity equation dW_s .¹ If this is not done, when the transport equation of the second-order moments is evaluated, i.e., $d\langle U_s^2 \rangle$, there will be a spurious term $-2\varphi/(\varphi+1)^2 C_0 \varepsilon_f$ due to the fact that the two noises are uncorrelated. In any case, this term goes consistently to zero when the mass fraction φ vanishes.

¹In terms of the distribution function (i.e., weak convergence), the sum of two Wiener processes multiplied by constants is equivalent to a third Wiener process multiplied by the sum of the constants [Kloeden 1992].

4.5 Supplementary material: a detailed description of the coarse-graining steps

We provide here all the coarse-graining steps that have been followed for the derivation of the model and that may help in the collocation of the latter. In particular, we show how the model is conceived to be consistent with the exact hydrodynamic mesoscopic Eulerian description of the particle phase. Since the microscopic particle-resolved level is generally too detailed for realistic applications, it is tempting to search for a kinetic description of the particle phase, in analogy with the Boltzmann treatment of the molecules of a fluid [Cercignani 1988]. If the fluid presence can be neglected (a dense dry suspension), this is the standard problem of granular flows. Grains replace molecules as microscopic constituents and a kinetic equation can be written for a probability density function (pdf) $f(\mathbf{x}, \mathbf{V}_p, t)$, where \mathbf{x}, \mathbf{V}_p represent the possible position and velocity of the grains. In principle, the approach is justified, yet the difficult issue here is to propose a suitable closure for the collision term, since grains are different from molecules and notably collisions are not necessarily elastic. In such a framework, the kinetic approach has been developed for rapid granular flows animated by elastic or inelastic collisions that drive the distribution function towards a local Maxwell–Boltzmann equilibrium [Jenkins 1983, Jenkins 1985, Lun 1986, Brey 1998, Brilliantov 2010].

When the suspension is not dry, the fluid phase has to be added. If we consider that the fluid velocity at the position of each particle is known (from numerical simulations or analytical specification), the generalisation consists in specifying the force exerted by the fluid on particles, which is added as an external term in the kinetic equation, but the distribution function remains well defined as $f(\mathbf{x}, \mathbf{V}_p, t)$. The kinetic equation reads [Jenkins 1983]

$$\frac{\partial f}{\partial t} + \frac{\partial}{\partial \mathbf{x}} \cdot (\mathbf{V}_p f) + \frac{\partial}{\partial \mathbf{V}_p} \cdot [(\mathcal{A}_p + \mathbf{g})f] = \mathcal{C} \quad (4.124)$$

where \mathcal{A}_p is the acceleration due to fluid–particle interactions, \mathbf{g} is the gravity acceleration and \mathcal{C} is the collision operator. It is worth underlining that if the fluid field is not known, the problem is not well posed and the kinetic approach, that is only \mathbf{x} and \mathbf{V}_p are considered as variables, is incomplete [Minier 2015a]. The kinetic level of description can be considered valid in a wide range of situations. In analogy with statistical mechanics terminology, this is the mesoscopic level of description.

From the kinetic equation it is possible to derive corresponding hydrodynamic equations through averaging over the kinetic distribution function [Huang 1963]. These equations are purely formal if a systematic procedure to compute averages is not given and the distribution function is unknown. If one considers local equilibrium, notably the Maxwellian for elastic collisions, it is possible to resort to the Chapman–Enskog asymptotic method, valid for the kinetic theory of dilute gases [Chapman 1970]. First works derived hydrodynamic equations considering Maxwellian equilibrium and in absence of the fluid-phase force, yet small deviations from Maxwellian can be taken into account considering instead the Sonine polynomials [Van Noije 1998, Garzó 2012]. Assuming that particles are frictionless hard spheres of equal density and diameter (i.e. monodisperse) and that collisions are nearly elastic, the conservation of mass and momentum of the hydrodynamic variables (zeroth and first-order moments of the kinetic distribution function), in the presence of a

constant-density fluid, are given by the following equations:

$$\frac{\partial \alpha_p}{\partial t} + \nabla \cdot \alpha_p \mathbf{U}_p = 0, \quad (4.125)$$

$$\frac{\partial \alpha_p \mathbf{U}_p}{\partial t} + \nabla \cdot \alpha_p (\mathbf{U}_p \otimes \mathbf{U}_p + \mathbf{P}) = \alpha_p \left(\frac{\mathbf{U}_f - \mathbf{U}_p}{\tau_p} + \mathbf{g} \right) \quad (4.126)$$

where α_p is the particle-phase volume fraction, \mathbf{U}_p is the particle-phase velocity (it should not be confused with U_p within the paper, which stands for the modelled particle velocity), \mathbf{U}_f is the fluid-phase velocity and \mathbf{P} is the particle-phase pressure tensor, given by the second-order moments of the kinetic distribution function [Jenkins 1983]. From (4.126), the transport equation for the particle-phase velocity tensor product can be obtained as

$$\frac{\partial \alpha_p \mathbf{U}_p \otimes \mathbf{U}_p}{\partial t} + \nabla \cdot (\alpha_p \mathbf{U}_p \otimes \mathbf{U}_p \otimes \mathbf{U}_p) + [\mathbf{U}_p \otimes \nabla \cdot (\alpha_p \mathbf{P})]^\dagger = \alpha_p \left[\mathbf{U}_p \otimes \left(\frac{\mathbf{U}_f - \mathbf{U}_p}{\tau_p} + \mathbf{g} \right) \right]^\dagger \quad (4.127)$$

where the symbol $[\cdot]^\dagger$ implies the summation of a second-order tensor with its transpose. For non-equilibrium flows a transport equation for the pressure tensor is necessary, and can be derived from (4.124) and (4.127):

$$\frac{\partial \alpha_p \mathbf{P}}{\partial t} + \nabla \cdot \alpha_p (\mathbf{U}_p \otimes \mathbf{P} + \mathbf{Q}) = -\alpha_p (\mathbf{P} \cdot \nabla \mathbf{U}_p)^\dagger - \frac{2}{\tau_p} \alpha_p \mathbf{P} + \frac{12}{\sqrt{\pi} d_p} \alpha_p^2 \Theta^{1/2} (\Delta^* - \mathbf{P}). \quad (4.128)$$

In this equation $\Theta (= \frac{1}{3} \text{Tr}(\mathbf{P}))$ is the granular temperature, \mathbf{Q} is a heat-flux tensor that contains the third-order central moments of the velocity distribution function, and the last term on the right-hand side is the particle-particle collision term that has been closed using the Bhatnagar–Gros–Krook (BGK) approximation [Bhatnagar 1954] extended to inelastic collisions [Passalacqua 2011], where $0 \leq e \leq 1$ is the coefficient of restitution, d_p is the particle diameter and Δ^* is the second-order moments of the collisional equilibrium distribution, given by

$$\Delta^* = \frac{1}{4} (1 + e)^2 \Theta \mathbf{I} + \frac{1}{4} (1 - e)^2 \mathbf{P}. \quad (4.129)$$

By taking one-third of the trace of (4.128), the equation for the granular temperature can be found

$$\frac{\partial \alpha_p \Theta}{\partial t} + \nabla \cdot \alpha_p \left(\mathbf{U}_p \Theta + \frac{2}{3} \mathbf{q} \right) = -\frac{2}{3} \alpha_p \mathbf{P} : \nabla \mathbf{U}_p - \frac{2}{\tau_p} \alpha_p \Theta - \frac{6(1 - e^2)}{\sqrt{\pi} d_p} \alpha_p^2 \Theta^{3/2} \quad (4.130)$$

where \mathbf{q} is the granular temperature flux, i.e. the trace of \mathbf{Q} . This is the *hydrodynamic* level of description and is inherently macroscopic.

It can be seen how the set of hydrodynamic mesoscopic equations (4.126)–(4.128) is the Eulerian equivalent of the Lagrangian coarse-grained equation (4.9) derived within the paper. Indeed, the Lagrangian coarse-graining operator defined in section 4.2 is the counterpart of the kinetic distribution function defined in equation (4.124).

The exact RA transport equations may be derived taking the RA of the hydrodynamic equations (4.125)–(4.128) and keeping in mind the PA decomposition defined in section 4.3. Taking the RA of (4.125) yields

$$\frac{\partial \langle \alpha_p \rangle}{\partial t} + \nabla \cdot \langle \alpha_p \rangle \langle \mathbf{U}_p \rangle_p = 0. \quad (4.131)$$

The PA particle-phase momentum equation found from (4.126) is given by

$$\frac{\partial \langle \alpha_p \rangle \langle \mathbf{U}_p \rangle_p}{\partial t} + \nabla \cdot \langle \alpha_p \rangle (\langle \mathbf{U}_p \rangle_p \otimes \langle \mathbf{U}_p \rangle_p + \langle \mathcal{P} \rangle_p) = \langle \alpha_p \rangle \left(\left\langle \frac{\mathbf{U}_f - \mathbf{U}_p}{\tau_p} \right\rangle_p + \mathbf{g} \right) \quad (4.132)$$

where $\langle \mathcal{P} \rangle_p = \langle \mathbf{P} \rangle_p + \langle \mathbf{u}_p \otimes \mathbf{u}_p \rangle_p$ is the sum of the particle-phase stress tensor and the particle-phase Reynolds stress tensor.

The PA particle-phase stress tensor that appears in $\langle \mathcal{P} \rangle_p$ is governed by the following equation found from (4.128):

$$\begin{aligned} \frac{\partial \langle \alpha_p \rangle \langle \mathbf{P} \rangle_p}{\partial t} + \nabla \cdot \langle \alpha_p \rangle (\langle \mathbf{U}_p \rangle_p \otimes \langle \mathbf{P} \rangle_p + \langle \mathbf{u}_p \otimes \mathbf{P} \rangle_p + \langle \mathbf{Q} \rangle_p) = \\ - \langle \alpha_p \rangle (\langle \mathbf{P} \rangle_p \cdot \nabla \langle \mathbf{U}_p \rangle_p + \langle \mathbf{P} \cdot \nabla \mathbf{u}_p \rangle_p)^\dagger - \frac{2}{\tau_p} \langle \alpha_p \rangle \langle \mathbf{P} \rangle_p + \frac{12 \langle \alpha_p \rangle}{\sqrt{\pi} d_p} \langle \alpha_p \Theta^{1/2} (\Delta^* - \mathbf{P}) \rangle_p. \end{aligned} \quad (4.133)$$

Taking the RA of the granular temperature transport equation (4.130) (or one-third the trace of (4.133)) yields

$$\begin{aligned} \frac{\partial \langle \alpha_p \rangle \langle \Theta \rangle_p}{\partial t} + \nabla \cdot \langle \alpha_p \rangle \left(\langle \mathbf{U}_p \rangle_p \langle \Theta \rangle_p + \langle \mathbf{u}_p \Theta \rangle_p + \frac{2}{3} \langle \mathbf{q} \rangle_p \right) \\ = - \frac{2}{3} \langle \alpha_p \rangle (\langle \mathbf{P} \rangle_p : \nabla \langle \mathbf{U}_p \rangle_p + \langle \mathbf{P} : \nabla \mathbf{u}_p \rangle_p) - \frac{2}{\tau_p} \langle \alpha_p \rangle \langle \Theta \rangle_p - \frac{6(1 - e^2)}{\sqrt{\pi} d_p} \langle \alpha_p^2 \Theta^{3/2} \rangle. \end{aligned} \quad (4.134)$$

The transport equation for the particle-phase Reynolds stress tensor is computed by subtracting the transport equation for the particle-phase mean velocity tensor product from the RA of (4.127), yielding

$$\begin{aligned} \frac{\partial \langle \alpha_p \rangle \langle \mathbf{u}_p \otimes \mathbf{u}_p \rangle_p}{\partial t} + \nabla \cdot \langle \alpha_p \rangle (\langle \mathbf{U}_p \rangle_p \otimes \langle \mathbf{u}_p \otimes \mathbf{u}_p \rangle_p + \langle \mathbf{u}_p \otimes \mathbf{u}_p \otimes \mathbf{u}_p \rangle_p + \langle \mathbf{P} \otimes \mathbf{u}_p \rangle_p^\dagger) = \\ - \langle \alpha_p \rangle (\langle \mathbf{u}_p \otimes \mathbf{u}_p \rangle_p \cdot \nabla \langle \mathbf{U}_p \rangle_p)^\dagger + \langle \alpha_p \rangle \langle \mathbf{P} \cdot \nabla \mathbf{u}_p \rangle_p^\dagger + \frac{\langle \alpha_p \rangle}{\tau_p} (\langle \mathbf{u}_f \otimes \mathbf{u}_p \rangle_p - \langle \mathbf{u}_p \otimes \mathbf{u}_p \rangle_p)^\dagger. \end{aligned} \quad (4.135)$$

A Lagrangian probability-density-function model for collisional turbulent fluid-particle flows. Part II: a channel-flow application.

A. Innocenti^{1,2}, R. O. Fox³, M. V. Salvetti², S. Chibbaro¹

¹ Sorbonne Université, CNRS, Institut Jean Le Rond d'Alembert, F-75005 Paris, France

² Dipartimento di Ingegneria Civile e Industriale, Università di Pisa, Via G. Caruso 8, 56122 Pisa, Italia

³ Department of Chemical and Biological Engineering, 618 Bissell Road, Iowa State University, Ames, IA 50011-1098, USA

Technical report. Paper in preparation for *Journal of Fluid Mechanics*.

This chapter shows the application of the model derived in chapter 4 to a non-homogeneous flow. We have addressed the problem of turbulence transition in a particle-laden channel flow, considering the work of [Capecelatro 2018] as reference. In particular, we have tested different mass loadings, from $\varphi = 0$ to $\varphi = 2$ showing a qualitative agreement with DNS in the prediction of the energy decrease from low to intermediate mass loadings. Specifically, these tests were useful to prove the robustness of the model, since we have kept the same constants as in the homogeneous CIT at $\varphi = 10$, addressing a rather different flow condition, where CIT is not yet present.

As for the previous chapters, we propose the work in a self-contained matter, therefore the reader might find some repetitions in the introductory parts, e.g. in section 5.2 where the Eulerian-Lagrangian approach for particle laden flows is explained. In addition to the previous part of model derivation and homogeneous applications, we have rephrased the fluid and particle model equations for the channel flow and we have proposed a numerical scheme for the solution of the Lagrangian stochastic equations with two-way coupling and velocity decomposition. In the previous chapters, where only homogeneous applications were tested, a numerical solution of the Lagrangian particle equations was not needed, but the corresponding Eulerian equations were directly simulated, since if a homogeneous condition holds, they can be recasted in a closed form. Here, on the contrary, the problem dependency on the wall-normal coordinate precludes the direct solution of the Eulerian particle transport equations because of the additional unclosed transport terms. Hence, to avoid additional modelling it is necessary to solve the Lagrangian form of the particle equations through a Monte-Carlo simulation. The numerical scheme has several novelties

compared to existing ones for dilute flows, namely the accounting of two-way coupling and particle velocity decomposition.

5.1 Introduction

Particle-laden turbulent flows are present in a number of industrial and geophysical applications and their study has a long history in the literature. Depending on the volume fraction of the particle phase within the flow, different regimes have been identified with totally different mechanisms of energy production and transfer between the phases [Capecelatro 2018]. Several pioneering works [Wang 1993b, Eaton 1994, Marchioli 2002] have investigated the so called dilute regime, where interphase coupling might be null or weak and the majority of the fluid-phase turbulence is generated by mean-shear production. In this regime particles exhibit several features due to the interaction with turbulent structures, like for instance their tendency to addensate in particular regions of the flow, depending on their inertia, and to form clusters [Balachandar 2010]. At sufficiently high mass loading ($\varphi = (\rho_p \alpha_p)/(\rho_f \alpha_f) \geq 10$), recent works [Capecelatro 2015] have shown that even in homogeneous conditions, spatial fluctuations of particle clusters can generate turbulence even in a resting fluid just under the effect of gravity. Under these conditions turbulence is mainly fed by the interaction with particles instead of the classical mean-shear production and the primary source of turbulence production is a term proportional to the drift velocity and to the mean slip between the phases. At intermediate mass loadings, of order unity, it has been found [Dritselis 2016, Gualtieri 2013, Capecelatro 2018] that particles tend to reduce the turbulent kinetic energy of the carrier phase and relaminarization of the flow is even possible.

The most widely used numerical approach for particle-laden flows is Eulerian-Lagrangian (EL) point-particle simulation, where the continuous fluid phase is described by means of a Direct Numerical Simulation (DNS) or using some turbulence modelling (Reynolds-Averaged equations, Large-Eddy-Simulations), and the dispersed particle phase is tracked from a Lagrangian point of view [Maxey 1983, Gatignol 1983]. This type of approach offers an extremely good approximation whenever particles are very small compared to the smallest turbulence length scales, otherwise particle size should be taken into account explicitly through particle-resolved simulations [Burton 2005, Uhlmann 2008]. The coupling of turbulence fluid models with the Lagrangian equations of particle motion has been shown to suffer from several drawbacks, e.g. a wrong estimation of particle clustering and concentration, because of the lack of informations due to the reduced level of description [Marchioli 2008b, Pozorski 2009]. Several works have shown the possibility of partially reconstructing the fluid-phase fluctuations by means of a stochastic model in the equation of particle motion [Peirano 2006, Minier 2015b, Innocenti 2016] for dilute flows. Our recent work have extended the possibility to use this class of models for cases characterized by high mass loading. Namely it has been developed a stochastic particle model for the case of homogeneous fully developed cluster-induced-turbulence (CIT), based on the exact mesoscopic equations derived from the kinetic-theory of collisional fluid-particle flows. In the present chapter we apply this model to a non-homogeneous flow, i.e. a channel flow, comparing our results with the EL-DNS of [Capecelatro 2018]. The objective is to test the

model to see if it is able to capture the transition of the flow that occurs when increasing the mass loading from zero to values above unity. In section 5.2 we recall the equations describing the fluid-particle flow and some concepts on phase-averaging.

In section 5.3 we summarise the model equation for the channel flow case; in 5.4 the flow and geometric parameters of the flow are described; in section 5.5 a new numerical scheme is derived for the solution of coupled stochastic equations; in section 5.6 we show results for tracer and inertial particles with mass loadings up to $\varphi = 2$.

5.2 The Eulerian-Lagrangian description for particle-laden flows

In this section we present the governing equations describing solid spherical particles in a constant-density gas. Unlike in single-phase flows where the Navier-Stokes equations can be directly averaged to obtain a set of mean-flow equations [Pope 2000], special care needs to be taken for turbulent multiphase flows. The fluid and particle phase equations are presented in the following section, followed by the model equations recasted for the channel flow.

5.2.1 Fluid phase

Hydrodynamic equations for the fluid phase are obtained by applying a volume-filtering operator to the microscale NS equations [Anderson 1967]. This for a constant-density fluid gives:

$$\frac{\partial \alpha_f}{\partial t} + \nabla \cdot \alpha_f \mathbf{U}_f = 0 \quad (5.1)$$

and

$$\frac{\partial \alpha_f \mathbf{U}_f}{\partial t} + \nabla \cdot (\alpha_f \mathbf{U}_f \otimes \mathbf{U}_f) = -\frac{1}{\rho_f} \nabla p_f + \frac{1}{\rho_f} \nabla \cdot \boldsymbol{\sigma}_f - \alpha_f \Phi \frac{\mathbf{U}_f - \mathbf{U}_p}{\tau_p} + \alpha_f \mathbf{g} \quad (5.2)$$

where \mathbf{U}_f and p_f are the instantaneous fluid-phase velocity and pressure, α_f is the fluid-phase volume fraction, ρ_f and ν_f are the fluid-phase density and kinematic viscosity and \mathbf{g} the acceleration due to gravity. The particle characteristic time scale τ_p is defined as

$$\tau_p = \frac{\rho_p d_p^2}{18 \rho_f \nu_f} \quad (5.3)$$

with ρ_p and d_p being, respectively, the particle-phase density and diameter. The (instantaneous) mass loading Φ is defined as

$$\Phi = \frac{\rho_p \alpha_p}{\rho_f \alpha_f}. \quad (5.4)$$

The fluid-phase viscous stress tensor is defined as

$$\boldsymbol{\sigma}_f = \rho_f \nu_f [\nabla \mathbf{U}_f + (\nabla \mathbf{U}_f)^T - \frac{2}{3} \nabla \cdot \mathbf{U}_f \mathbf{I}] \quad (5.5)$$

where \mathbf{I} is the identity tensor. The unclosed terms coming from the volume filtering of the microscopic stress tensor have been neglected here since it has been shown that they do not

influence noticeably the flow physics [Capecelatro 2015]. Moreover, concerning the effects of the particles on the fluid, we have retained only the drag force, since we are considering cases where $\rho_p/\rho_f \gg 1$.

From (5.2) and enforcing (5.1), a transport equation for the fluid-phase velocity tensor product can be found

$$\begin{aligned} \frac{\partial \alpha_f \mathbf{U}_f \otimes \mathbf{U}_f}{\partial t} + \nabla \cdot (\alpha_f \mathbf{U}_f \otimes \mathbf{U}_f \otimes \mathbf{U}_f) = & -\frac{1}{\rho_f} (\mathbf{U}_f \otimes \nabla p_f)^\dagger + \frac{1}{\rho_f} (\mathbf{U}_f \otimes \nabla \cdot \boldsymbol{\sigma}_f)^\dagger \\ & - \alpha_f \Phi \left[\mathbf{U}_f \otimes \left(\frac{\mathbf{U}_f - \mathbf{U}_p}{\tau_p} \right) \right]^\dagger + \alpha_f (\mathbf{U}_f \otimes \mathbf{g})^\dagger. \end{aligned} \quad (5.6)$$

5.2.2 Particle phase

As anticipated in the introduction, we neglect the finite-size effect and hence the displacement of a point-wise particle is described by the following Newton's second law of motion [Gatignol 1983, Maxey 1983]

$$\frac{d\mathbf{V}_p^{(k)}}{dt} = \frac{\mathbf{U}_f[\mathbf{x}_p^{(k)}] - \mathbf{V}_p^{(k)}}{\tau_p} + \mathbf{F}_c^{(k)} + \mathbf{g} \quad (5.7)$$

where $\mathbf{x}_p^{(k)}$ is the position of particle k and \mathbf{F}_c is the collisional acceleration experienced by the particle. Moreover, as previously said, since it is assumed that $\rho_p \gg \rho_f$, only the drag force exerted by the fluid is considered, while all other contributions from the fluid phase (*e. g.* added mass and lift forces) are neglected.

5.2.3 Phase average

Analogous to Favre averaging in variable density flows, the phase average (PA) is useful in multiphase modelling. In particular, if we indicate the average with brackets $\langle \cdot \rangle$, we will have for the fluid phase $\langle (\cdot) \rangle_f = \langle \alpha_f (\cdot) \rangle / \langle \alpha_f \rangle$ and for the particle phase $\langle (\cdot) \rangle_p = \langle \alpha_p (\cdot) \rangle / \langle \alpha_p \rangle$, where $\langle \alpha_p \rangle$ and $\langle \alpha_f \rangle = 1 - \langle \alpha_p \rangle$ are respectively the averaged particle-phase and the fluid-phase volume fractions. Fluctuations about the PA fluid velocity are expressed as

$$\mathbf{u}_f = \mathbf{U}_f - \langle \mathbf{U}_f \rangle_f \quad \text{with} \quad \langle \mathbf{u}_f \rangle_f = 0 \quad (5.8)$$

but in general $\langle \mathbf{u}_f \rangle_p \neq 0$. This gives for the fluid-phase turbulent kinetic energy

$$k_f = \frac{1}{2} \langle \mathbf{u}_f \cdot \mathbf{u}_f \rangle_f \quad (5.9)$$

Similarly, the PA can be applied to the particle-phase component. As described in [Capecelatro 2015] and in chapter 4, in dense fluid-particle flows the particle velocity may be conveniently decomposed into its spatially correlated and uncorrelated components, *i.e.* $\mathbf{V}_p = \mathbf{U}_p + \delta \mathbf{v}_p$. With this definition, when applying the PA to the particle fluctuating energy, this can be decomposed into the granular temperature

$$\langle \Theta \rangle_p = \frac{1}{3} \langle \delta \mathbf{v}_p \cdot \delta \mathbf{v}_p \rangle_p, \quad (5.10)$$

and into the turbulent particle kinetic energy

$$k_p = \frac{1}{2} \langle \mathbf{u}_p \cdot \mathbf{u}_p \rangle_p, \quad (5.11)$$

with the total fluctuating energy being

$$\kappa_p = \frac{1}{2} \langle \mathbf{v}_p \cdot \mathbf{v}_p \rangle_p = k_p + \frac{3}{2} \langle \Theta \rangle_p \quad (5.12)$$

To simplify the notation we will drop the subscript indicating the phase. The distinction between k_p and $\langle \Theta_p \rangle$, as already said, is crucial in turbulence modelling of multiphase flows because, for example, they have different boundary conditions and the particle–particle collision frequency depends on Θ_p [Capecelatro 2016b].

If the PA operator is applied to the NS equations (5.1)–(5.2), (5.6), the exact RA fluid-phase transport equations can be found. Similarly, if the PA operator is applied to the mesoscopic particle-phase equations [Capecelatro 2015], one can find the RA transport equations for the fluid phase. In this work we use the model recently derived in chapter 4, that consists in a set of Eulerian RA equations for the fluid and stochastic Lagrangian equations for the particles. In particular, the fluid RA equations are an extension of the single-phase Reynolds-stress model, where two-way coupling additional terms have been derived consistently with the exact RA transport equations, and the Lagrangian particle stochastic equations are modeled in such a way that the exact RA equations are retrieved in a statistical sense. For more details on the model derivation and term-to-term comparison between modeled and exact RA equations we refer the reader to chapter 4

5.3 Lagrangian pdf model for vertical channel flow

Here we provide an overview of the model equations for dense fluid–particle flows, adapted to a vertical channel flow configuration. We consider a vertical channel flow of width W , with the span-wise direction denoted by x , the wall-normal direction as y ($0 \leq y \leq W$), and the vertical direction as z . All statistical quantities depend only on the wall-normal direction, y . The fluid–particle model consists in a set of Reynolds-Average (RA) equations for the fluid phase and in a set of Lagrangian stochastic equations for the particle phase. In the RA fluid-phase model equations the only relevant quantities for the channel flow application are the following: $\langle U_{f,z} \rangle$ (mean vertical velocity), $\langle u_{f,x} u_{f,x} \rangle$, $\langle u_{f,y} u_{f,y} \rangle$, $\langle u_{f,z} u_{f,z} \rangle$, $\langle u_{f,y} u_{f,z} \rangle$ (Reynolds-stress tensor). In addition, a transport equation for the fluid-phase dissipation ε_f has to be included to close the model. On the other hand, the modeled Lagrangian quantities are y_p (particle wall-normal position), $\delta \mathbf{v}_p$, \mathbf{U}_p and \mathbf{U}_s , which are respectively the uncorrelated, the correlated in space particle velocity and the fluid velocity seen by particles. The stream-wise and span-wise components of the particle position are not relevant since the channel is homogeneous in those directions and particle statistics are evaluated over slabs parallel to the channel walls.

5.3.1 Stochastic model for particle phase

The set of stochastic equations for the particle phase, expressed for a homogeneous flow, is detailed in (5.13)–(5.19) below.

$$dy_p = V_{p,y} dt = (U_{p,y} + \delta v_{p,y}) dt \quad (5.13)$$

where y_p is the particle wall-normal position and \mathbf{V}_p is the particle velocity. As previously explained, following [F  vrier 2005] and [Capecelatro 2015], the particle velocity is decomposed in a spatially correlated part \mathbf{U}_p , and in an uncorrelated residual, $\delta\mathbf{v}_p$. The former is governed by

$$\begin{aligned} dU_{p,i} = & \frac{U_{s,i} - U_{p,i}}{\tau_p} dt + g_i dt - \frac{1}{\langle\alpha_p\rangle\rho_p} \frac{\partial\langle\alpha_p\rangle\rho_p\langle P_{ij}\rangle}{\partial x_j} + \delta v_{p,j} \frac{\partial\langle U_{p,i}\rangle}{\partial x_j} dt \\ & - \frac{1}{T_{Lp}} (U_{p,i} - \langle U_{p,i}\rangle) dt + \sqrt{C_p\varepsilon_p} dW_{p,i}. \end{aligned} \quad (5.14)$$

The first term of the RHS of (5.14) is the drag force related to the correlated part of the particle velocity, in which τ_p is given in (5.3). The second term is the effect of gravity, $\mathbf{g} = [0, 0, g]^T$, while the third is a pressure term, in which $\langle P_{ij}\rangle = \langle\delta v_{p,i}\delta v_{p,j}\rangle$ is the particle-phase pressure tensor. It is worth remarking that in a Lagrangian approach, when doing an ensemble average of particle quantities over a computational cell, we are intrinsically weighting with the volume fraction. The fourth and fifth terms are production and relaxation, respectively, in which T_{Lp} is the particle Lagrangian time scale:

$$T_{Lp} = \frac{2}{(1 + \frac{3}{2}C_{0p} + f_s)} \frac{k_p}{\varepsilon_p}. \quad (5.15)$$

Finally, the last contribution is a diffusion term, in which C_p is a model constant related to C_{0p} by the relation

$$C_p = C_{0p} + \frac{2}{3}f_s, \quad (5.16)$$

where f_s is defined in the following. Finally, ε_p is the particle dissipation and $dW_{p,i}$ is a Wiener stochastic process.

The uncorrelated residual velocity is modelled by

$$\begin{aligned} d\delta v_{p,i} = & -\frac{\delta v_{p,i}}{\tau_p} dt + \frac{1}{\langle\alpha_p\rangle\rho_p} \frac{\partial\langle\alpha_p\rangle\rho_p\langle P_{ij}\rangle}{\partial x_j} - \delta v_{p,j} \frac{\partial\langle U_{p,i}\rangle}{\partial x_j} dt + B_{\delta,ij} dW_{\delta,j} \\ & - \frac{(1+e)(3-e)}{4\tau_c} \delta v_{p,i} dt + \sqrt{\frac{1}{2\tau_c}(1+e)^2\langle\Theta_p\rangle} dW_{c,i}. \end{aligned} \quad (5.17)$$

The first four terms in the RHS of (5.17) are analogous to the ones in (5.14). In particular, dW_δ is a Wiener stochastic process and B_δ is a diffusion matrix, whose expression will be given in the following. The last two terms take into account collisions; e is a restitution coefficient, to be a priori specified, dW_c is another Wiener process and $\langle\Theta_p\rangle$ is the granular temperature, defined in (5.10). Finally, τ_c is a characteristic time for collisions, having the following expression:

$$\tau_c = \frac{\sqrt{\pi}d_p}{6C_c\langle\alpha_p\rangle\langle\Theta_p\rangle^{1/2}}, \quad (5.18)$$

C_c being a model parameter [Capecelatro 2016b].

The model for the fluid velocity seen by the particles is a generalisation of the model for dilute flows proposed by [Minier 2001], in which we use a modified pressure gradient weighted with the fluid-phase volume fraction, and a different diffusion coefficient which

takes into account possible velocity difference between the fluid average velocity, $\langle \mathbf{U}_f \rangle$ and the mean fluid velocity seen by particles, $\langle \mathbf{U}_s \rangle$. This results in the following equation:

$$\begin{aligned} dU_{s,i}(t) = & -\frac{\langle \alpha_f \rangle}{\rho_f} \frac{\partial \langle p_f \rangle}{\partial x_i} dt + G_{i,j}(U_{s,j} - \langle U_{f,j} \rangle) dt - \varphi \left(\frac{U_{s,i} - U_{p,i}}{\tau_p} \right) dt + g_i dt \\ & + \left[\varepsilon_f \left(C_{0f} b_i \frac{\tilde{k}_f}{k_f} + \frac{2}{3} \left(b_i \frac{\tilde{k}_f}{k_f} - 1 \right) \right) + 2\varphi \frac{\langle U_{p,i} - U_{s,i} \rangle}{\tau_p} (\langle U_{s,i} \rangle - \langle U_{f,i} \rangle) \right. \\ & \left. - 2 \frac{\langle \alpha_p \rangle}{\rho_f} \frac{\partial \langle p_f \rangle}{\partial x_i} (\langle U_{s,i} \rangle - \langle U_{f,i} \rangle) + \frac{2}{3} C_{2f} \mathcal{P}_{Sfs} \right]^{1/2} dW_{s,i}. \end{aligned} \quad (5.19)$$

The first term of the RHS is the pressure gradient term. The second term is a relaxation term, where

$$G_{ij} = -\frac{1}{T_{L,i}^*} \delta_{ij} + G_{ij}^a. \quad (5.20)$$

$T_{L,i}^*$ is a modified fluid time-scale, which takes into account the anisotropy of the flow and particle inertia, defined by

$$T_{L,i}^* = \frac{T_{Lf}}{\sqrt{1 + \zeta_i \beta^2 \frac{3|\langle \mathbf{U}_r \rangle|^2}{2k_f}}}, \quad T_{Lf} = \frac{2}{\left(1 + \frac{3}{2} C_{0f}\right)} \frac{k_f}{\varepsilon_f} \quad (5.21)$$

where $\zeta_1 = 1$ in the mean drift direction and $\zeta_{2,3} = 4$ in the cross directions, $\beta = T_{Lf}/T_{Ef}$ is the ratio of the Lagrangian and the Eulerian timescales and $\mathbf{U}_r = \mathbf{U}_p - \mathbf{U}_s$ is the relative velocity. k_f and ε_f are the fluid turbulent kinetic energy and dissipation. \mathbf{G}^a is a traceless matrix added to generalize the model as shown in Part I:

$$G_{ij}^a = C_{2f} \frac{\partial \langle U_{f,i} \rangle}{\partial x_j}. \quad (5.22)$$

It corresponds to the Isotropization-of-production (IP) contribution in the Launder-Reece-Rodi model [Launder 1975] (LRR-IP), with C_{2f} being the IP constant. The value of the model constant C_{0f} is established by the relation, see [Pope 1994b]:

$$C_{0f} = \frac{2}{3} (C_{Rf} - 1). \quad (5.23)$$

where C_{Rf} is the Rotta constant. The third term in (5.19) accounts for two-way coupling. Finally, the last term is a stochastic diffusion process extended to dense flows in which $b_i = T_{Lf}/T_{L,i}^*$,

$$\tilde{k}_f = \frac{3}{2} \frac{\sum_{i=1}^3 b_i \langle (U_{s,i} - \langle U_{f,i} \rangle)^2 \rangle}{\sum_{i=1}^3 b_i} \quad (5.24)$$

and \mathcal{P}_{Sfs} is one-half the trace of the tensor

$$\mathcal{P}_{Sfs} = -(\langle (\mathbf{U}_s - \langle \mathbf{U}_f \rangle) \otimes (\mathbf{U}_s - \langle \mathbf{U}_f \rangle) \rangle \cdot \nabla \langle \mathbf{U}_f \rangle)^\dagger. \quad (5.25)$$

The Wiener process dW_s is uncorrelated with those present in the particle equations.

When the correlation $\langle \delta v_{p,i} \delta v_{p,j} \rangle$ is evaluated, the diffusion matrix B_δ must give the particle-phase Reynolds-stress tensor multiplied by the proper coefficient together with a

diagonal isotropic part. Using a Choleski decomposition we obtain:

$$\begin{aligned}
B_{\delta,11} &= \left[f_s \frac{\varepsilon_p}{k_p} \langle u_{p,1} u_{p,1} \rangle + (1 - f_s) \frac{2}{3} \varepsilon_p \right]^{1/2}, \\
B_{\delta,i1} &= \frac{1}{B_{\delta,11}} f_s \frac{\varepsilon_p}{k_p} \langle u_{p,i} u_{p,1} \rangle, \quad 1 < i \leq 3 \\
B_{\delta,ii} &= \left[f_s \frac{\varepsilon_p}{k_p} \langle u_{p,i} u_{p,i} \rangle + (1 - f_s) \frac{2}{3} \varepsilon_p - \sum_{j=1}^{i-1} B_{\delta,ij}^2 \right]^{1/2}, \quad 1 < i \leq 3 \\
B_{\delta,ij} &= \frac{1}{B_{\delta,jj}} \left(f_s \frac{\varepsilon_p}{k_p} \langle u_{p,i} u_{p,j} \rangle - \sum_{k=1}^{j-1} B_{\delta,ik} B_{\delta,jk} \right), \quad 1 < j < i \leq 3 \\
B_{\delta,ij} &= 0, \quad i < j \leq 3;
\end{aligned} \tag{5.26}$$

where $0 \leq f_s \leq 1$ is a parameter tuning the anisotropy of the particle dissipation tensor. The latter is defined as follows:

$$\boldsymbol{\varepsilon}_p = \varepsilon_p \left[f_s \frac{\langle \mathbf{u}_p \otimes \mathbf{u}_p \rangle}{k_p} + (1 - f_s) \frac{2}{3} \mathbf{I} \right] \tag{5.27}$$

where ε_p is one-half the trace of $\boldsymbol{\varepsilon}_p$.

The particle-phase dissipation is modelled through an Eulerian equation in analogy to single-phase flows [Fox 2014]:

$$\frac{d\varepsilon_p}{dt} = (C_{\varepsilon 1p} \mathcal{P}_{Sp} - C_{\varepsilon 2p} \varepsilon_p) \frac{\varepsilon_p}{k_p} + \frac{C_{3p}}{\tau_p} \left(\frac{k_{fp}}{k_{f@p}} \varepsilon_f - \beta_p \varepsilon_p \right) \tag{5.28}$$

where $C_{\varepsilon 1p}$, $C_{\varepsilon 2p}$, C_{3p} and β_p are model parameters.

To summarize, the particle-phase is described by the following system of stochastic differential equation:

$$d\mathbf{Z}_p = \mathbf{A} dt + [\mathbf{B}] d\mathbf{W}, \tag{5.29}$$

where \mathbf{A} is the drift term, and

$$\mathbf{Z}_p = \begin{pmatrix} \mathbf{U}_p \\ \delta \mathbf{v}_p \\ \mathbf{U}_s \end{pmatrix} \quad [\mathbf{B}] = \begin{bmatrix} C[I] & 0 & 0 & 0 \\ 0 & [B_\delta] & K[I] & 0 \\ 0 & 0 & 0 & [B_s] \end{bmatrix} \quad d\mathbf{W} = \begin{pmatrix} d\mathbf{W}_p \\ d\mathbf{W}_\delta \\ d\mathbf{W}_c \\ d\mathbf{W}_s \end{pmatrix} \tag{5.30}$$

$C = \sqrt{C_p \varepsilon_p}$ is the diagonal diffusion coefficient in the equation of the correlated velocity and $K = \sqrt{1/(2\tau_c)(1 + e^2)\langle \Theta_p \rangle}$ is the diagonal diffusion coefficient for the collisions in the uncorrelated velocity equation.

5.3.2 Fluid phase model

The transport of the RA fluid-phase volume fraction $\langle \alpha_f \rangle$ reduces to the wall-normal component

$$\frac{\partial \langle \alpha_f \rangle \langle U_{f,y} \rangle}{\partial y} = 0. \tag{5.31}$$

Since the wall-normal velocity is null at the walls, this expression yields $\langle U_{f,y} \rangle(y) = 0$.

The only non-zero components of the fluid-phase momentum equation are given by:

$$0 = -\frac{1}{\rho_f} \frac{\partial \langle p_f \rangle}{\partial y} - \frac{1}{\langle \alpha_f \rangle} \frac{\partial \langle \alpha_f \rangle \langle u_{f,y} u_{f,y} \rangle}{\partial y} - \frac{\varphi}{\tau_p} \langle U_{s,y} \rangle, \quad (5.32)$$

$$\frac{\partial \langle U_{f,z} \rangle}{\partial t} = -\frac{1}{\rho_f} \frac{\partial \langle p_f \rangle}{\partial z} - \frac{1}{\langle \alpha_f \rangle} \frac{\partial \langle \alpha_f \rangle \langle u_{f,y} u_{f,z} \rangle}{\partial y} + \nu_f \frac{\partial^2 \langle U_{f,z} \rangle}{\partial y^2} - g + \frac{\varphi}{\tau_p} (\langle U_{p,z} \rangle - \langle U_{s,z} \rangle), \quad (5.33)$$

where the RA mass loading $\varphi(y)$ varies only in the y direction. From equation (5.32) the pressure gradient in the y direction can be determined, and it can be used in the Lagrangian equation of U_s .

There are four non-zero components of the Reynolds-stress tensor; the corresponding governing equations are the following:

$$\frac{\partial \langle u_{f,x} u_{f,x} \rangle}{\partial t} = \mathcal{R}_{f,xx} - \varepsilon_{f,xx} + \mathcal{DE}_{f,xx} + \frac{1}{\langle \alpha_f \rangle} \frac{\partial}{\partial y} \langle \alpha_f \rangle (\nu_{ft} + \nu_f) \frac{\partial \langle u_{f,x} u_{f,x} \rangle}{\partial y}, \quad (5.34)$$

$$\frac{\partial \langle u_{f,y} u_{f,y} \rangle}{\partial t} = \mathcal{R}_{f,yy} - \varepsilon_{f,yy} + \mathcal{DE}_{f,yy} + \frac{1}{\langle \alpha_f \rangle} \frac{\partial}{\partial y} \langle \alpha_f \rangle (\nu_{ft} + \nu_f) \frac{\partial \langle u_{f,y} u_{f,y} \rangle}{\partial y}, \quad (5.35)$$

$$\begin{aligned} \frac{\partial \langle u_{f,z} u_{f,z} \rangle}{\partial t} = & \mathcal{R}_{f,zz} - \varepsilon_{f,zz} - 2 \langle u_{f,y} u_{f,z} \rangle \frac{\partial \langle U_{f,z} \rangle}{\partial y} + \mathcal{DE}_{f,zz} + \mathcal{DP}_{f,zz} \\ & + \frac{1}{\langle \alpha_f \rangle} \frac{\partial}{\partial y} \langle \alpha_f \rangle (\nu_{ft} + \nu_f) \frac{\partial \langle u_{f,z} u_{f,z} \rangle}{\partial y}, \end{aligned} \quad (5.36)$$

$$\frac{\partial \langle u_{f,y} u_{f,z} \rangle}{\partial t} = \mathcal{R}_{f,yz} - \varepsilon_{f,yz} - \langle u_{f,y} u_{f,y} \rangle \frac{\partial \langle U_{f,z} \rangle}{\partial y} + \mathcal{DE}_{f,yz} + \frac{1}{\langle \alpha_f \rangle} \frac{\partial}{\partial y} \langle \alpha_f \rangle (\nu_{ft} + \nu_f) \frac{\partial \langle u_{f,y} u_{f,z} \rangle}{\partial y}. \quad (5.37)$$

$\mathcal{DP}_{f,ij}$ and \mathcal{DE}_{ij} are the drag production and the drag exchange tensors:

$$\mathcal{DP}_{f,ij} = \frac{2\varphi}{\tau_p} (\langle U_{s,z} \rangle - \langle U_{f,z} \rangle) (\langle U_{p,z} \rangle - \langle U_{f,z} \rangle) \delta_{iz} \delta_{jz}, \quad (5.38)$$

$$\mathcal{DE}_{f,ij} = \frac{\varphi}{\tau_p} (\langle u_{s,i} u_{p,j} \rangle + \langle u_{p,i} u_{s,j} \rangle - 2 \langle (U_{s,i} - \langle U_{f,i} \rangle) (U_{s,j} - \langle U_{f,j} \rangle) \rangle). \quad (5.39)$$

$\mathcal{R}_{f,ij}$ is the redistribution tensor for which the LRR-IP model has been used:

$$\mathcal{R}_{f,ij} = -C_R \frac{\varepsilon_f}{k_f} \left(\langle u_{f,i} u_{f,j} \rangle - \frac{2}{3} k_f \delta_{ij} \right) - C_{2f} \left(\mathcal{P}_{Sf,ij} - \frac{2}{3} \mathcal{P}_{Sf} \delta_{ij} \right) \quad (5.40)$$

with

$$\mathcal{P}_{Sf,ij} = -\langle u_{f,i} u_{f,k} \rangle \frac{\partial \langle U_{f,j} \rangle}{\partial x_k} - \langle u_{f,j} u_{f,k} \rangle \frac{\partial \langle U_{f,i} \rangle}{\partial x_k}; \quad (5.41)$$

and $\mathcal{P}_{Sf} = \frac{1}{2}\text{trace}(\mathcal{P}_{Sf})$.

The wall-normal transport terms for the Reynolds-stress tensors are closed using a gradient-diffusion model with the following turbulent viscosity:

$$\nu_{ft} = C_s \frac{k_f}{\varepsilon_f} \langle u_{f,y} u_{f,y} \rangle. \quad (5.42)$$

The standard value for the model constant is $C_s = 0.22$. An anisotropic form of the dissipation tensor has been chosen, including a low-Reynolds model when the wall is approached:

$$\varepsilon_{f,ij} = f_s \frac{\langle u_{f,i} u_{f,j} \rangle}{k_f} + (1 - f_s) \frac{2}{3} \varepsilon_f \delta_{ij} \quad (5.43)$$

with

$$f_s = \exp \left[- \left(\frac{Re_L}{150} \right)^2 \right] \quad (5.44)$$

and $Re_L = k_f^2 / (\nu_f \cdot \varepsilon_f)$.

Quantities involving U_p and U_s are available from the Lagrangian particle solver. To completely close the above set of equations describing the fluid phase we still need a transport equation for the fluid dissipation:

$$\frac{\partial \varepsilon_f}{\partial t} = (C_{\varepsilon 1f} \mathcal{P}_{Sf} - C_{\varepsilon 2f} \varepsilon_f) \frac{\varepsilon_f}{k_f} + C_{3f} \frac{\varphi}{\tau_p} \left(\frac{k_{fp}}{k_{f@p}} \varepsilon_p - \beta_f \varepsilon_f \right) + C_4 \frac{\varepsilon_p}{k_p} \mathcal{DP} + \left(\frac{\nu_{ft}}{\sigma_\varepsilon} + \nu_f \right) \frac{\partial^2 \varepsilon_f}{\partial y^2} \quad (5.45)$$

where $C_{\varepsilon 1f}$, $C_{\varepsilon 2f}$, C_{3f} , β_f and C_4 are model constants, and \mathcal{DP} is one half the trace of $\mathcal{DP}_{f,ij}$. To better capture the near-wall behavior, the fluid-phase turbulence integral time scale is defined as $T_f = \max(k_f/\varepsilon_f, 6\sqrt{\nu_f/\varepsilon_f})$ in the RA equations.

To initially simplify the computations, we have neglected the spatial variations of the volume fraction, leading to replace the correct diffusive terms, in (5.34)-(5.37), with an approximation of them

$$\frac{1}{\langle \alpha_f \rangle} \frac{\partial}{\partial y} \left[\langle \alpha_f \rangle (\nu_{ft} + \nu_f) \frac{\partial}{\partial y} \langle u_{f,i} u_{f,j} \rangle \right] \simeq \frac{\partial}{\partial y} \left[(\nu_{ft} + \nu_f) \frac{\partial}{\partial y} \langle u_{f,i} u_{f,j} \rangle \right] \quad (5.46)$$

It is worth remarking that this fluid model is the same of the one that have been presented in chapter 4, with some minor modifications already present in literature [Pope 2000], to take into account low Reynolds effects near to the wall.

5.4 Channel flow configuration

The present study considers a vertical channel flow of width $2W$, with the span-wise direction denoted by x , the wall-normal direction as y ($0 \leq y \leq 2W$), and the vertical stream-wise direction as z . The same flow parameters as in the DNS of [Capecelatro 2018] have been chosen and are reported in table 5.1. The prescribed friction Reynolds number is $Re_\tau = (u_\tau \cdot W)/\nu_f = 300$, where the channel half-width W is equal to 1.8cm and u_τ is the friction velocity. The numerical discretisation consists in a 1-dimensional grid allocated along the wall-normal direction. Namely a uniform grid spacing is imposed, with a total number of points $N_y = 200$, which leads to a discretisation size $\Delta y^+ = 1.5$. Here

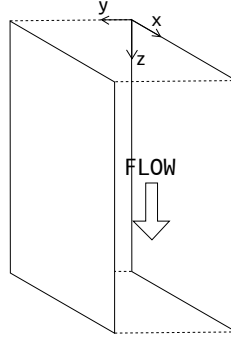


Figure 5.1: channel geometry

the superscript $+$ denotes normalisation with the viscous scales for length ν_f/u_τ and time ν_f/u_τ^2 .

The fluid is subjected to a mean pressure gradient and to the gravity acceleration, both in the vertical direction, the latter being constant, while the pressure gradient being dynamically adjusted in order to keep a constant mass flow rate after the injection of particles. Once a steady state is reached with the desired shear Reynolds number, Re_τ , particles are injected randomly with an initial velocity equal to the mean fluid velocity interpolated at particle position. It is worth remarking that we are dealing with statistical particles which have only the aim of reconstructing the associated statistical quantities, i.e. mean velocity, root mean square, etc. This means also that the particle volume fraction is not directly connected to the total number of particles, i.e. doubling the volume fraction does not require to double the number of particles. Indeed at the beginning of the computation the average volume fraction $\overline{\langle \alpha_p \rangle}$ (where the overbar imply spatial averaging over the wall normal coordinate) is fixed, and then the local mean volume fraction $\langle \alpha_p \rangle$ is scaled to the initial one through a constant. The mean mass loading of the channel is defined by:

$$\Phi = \frac{\rho_p}{\rho_f} \frac{\overline{\langle \alpha_p \rangle}}{\langle \alpha_f \rangle} \quad (5.47)$$

The mass loading ranges from $0 \leq \Phi \leq 2$ corresponding to $0 \leq \overline{\langle \alpha_p \rangle} \leq 0.001$. The density ratio is $\rho_p/\rho_f = 2000$. The particle Stokes number that has been considered corresponds to the smaller case of [Capecelatro 2018], namely $St_\tau = \tau_p u_\tau / W = 0.21$, corresponding to a particle diameter $d_p^+ = 0.74, 2.39$. The particle Reynolds number for this class of particles is $Re_p = d_p \tau_p g / \nu_f = 0.32$. The values used in the simulations are summarised in table 5.1. Each simulation has been performed with the same number of statistical particles $N_p = 5 \cdot 10^4$.

The nominal pressure gradient for the unladen case (which is known once the shear Reynolds is fixed), is dynamically adjusted in the laden cases, in order to maintain a constant bulk fluid velocity in the vertical direction,

$$\overline{U}_{f,z} = \frac{1}{W \overline{\alpha}_f} \int_0^W \langle \alpha_f \rangle(y) \langle U_{f,z} \rangle(y) dy, \quad (5.48)$$

5.5 Numerical approach

The fluid-particle flow is simulated through an hybrid Eulerian/Lagrangian algorithm. Fluid-phase equations are discretised on the Eulerian regular grid, while particle-phase equations are discretised just in time through a numerical scheme suitable for stochastic differential equations, which will be described in the following. The algorithm can be decomposed in different steps:

- Evaluation of RA quantities of the particle phase (i.e. $\langle U_{p,z} \rangle, \langle U_{s,z} \rangle$, etc.): quantities attached to single particles are averaged over computational cells (infinite slices parallel to the wall) by means of an ensemble average and reported on the Eulerian grid nodes. Calling $a^{(n)}$ a quantity attached to the n th particle, the ensemble average will be given by

$$\langle a_E \rangle = \frac{1}{N_E} \sum_{n \in \Delta_E} a^{(n)} \xrightarrow[\Delta_E \rightarrow 0]{N_E \rightarrow \infty} \langle a \rangle \quad (5.49)$$

where N_E is the number of particles in the cell and Δ_E is the cell size. For reliable statistics with minimal numerical dispersion, it is desirable to minimise the size of the averaging domain, namely $\Delta_E \rightarrow 0$, and maximize the number of statistical particles, namely $N_E \rightarrow \infty$. But since the Lagrangian equations are coupled with the Eulerian RA fluid-phase equations, it is not required to use finer discretisation than the Eulerian one because that would not increase the global accuracy, but would probably lead to misleading spurious effects. Thus, for averaging Lagrangian quantities we have used the same Eulerian grid used to discretise the fluid-phase equations.

- Particle and fluid RA quantities, that are needed in the stochastic equations, are interpolated at each particle position with a second order interpolation.
- Equations (5.29) are advanced in time through an Euler first order scheme for stochastic equations, which is inspired by the one proposed by [Peirano 2006], but with the addition of two-way coupling terms. Namely, two-way coupling prevents from solving the three equations of $U_{s,i}$, $U_{p,i}$ and $x_{p,i}$ in cascade as typically done in dilute flows. For this reason an initial diagonalisation of the system of equations is needed to uncouple the variables $U_{p,i}$ and $U_{s,i}$.
- Equations (5.33)-(5.37),(5.45) are advanced in time with a finite difference semi-implicit scheme (viscous terms), including the two-way coupling terms not present in the classical Reynolds-stress models for single-phase flows.
- The mean pressure gradient is updated manually every N_{pres} steps to adjust the mass flow rate. Too rapid changes of this terms may lead to numerical instabilities, therefore it is more suitable to reach the desired mass flow rate by steps where each time a steady state is reached before changing the pressure gradient.

Initial condition for the fluid phase are those obtained at steady state in the dilute case (without two-way coupling).

5.5.1 Fluid phase

The Eulerian equations describing the fluid phase are discretized through a finite difference scheme, both in space and time. For the space discretization we have used a second order semi-implicit centered scheme, where convective non-linear terms are treated explicitly, while diffusive terms are implicit. The discretization of the mean momentum equation in the vertical direction yields:

$$\begin{aligned} \frac{\langle U_{f,z} \rangle_i^{n+1} - \langle U_{f,z} \rangle_i^n}{\Delta t} = & -C_f - \frac{\langle u_{f,y} u_{f,z} \rangle_{i+1}^n - \langle u_{f,y} u_{f,z} \rangle_{i-1}^n}{2\Delta y} \\ & + \frac{\nu_f}{\langle \alpha_f \rangle_i^n} \frac{\langle U_{f,z} \rangle_{i+1}^{n+1} - 2\langle U_{f,z} \rangle_i^{n+1} + \langle U_{f,z} \rangle_{i-1}^{n+1}}{\Delta y^2} - g + \frac{\varphi_i^n}{\tau_p} (\langle U_{p,z} \rangle_i^n - \langle U_{s,z} \rangle_i^n) \end{aligned} \quad (5.50)$$

where C_f stands for the mean pressure gradient.

For the Reynolds stresses and the fluid dissipation we apply the same reasoning and we obtain analogous discretised equations. The 6 fluid variables are then grouped in a single vector

$$X = [\langle U_{f,z} \rangle \langle u_{f,x} u_{f,x} \rangle \langle u_{f,y} u_{f,y} \rangle \langle u_{f,z} u_{f,z} \rangle \langle u_{f,y} u_{f,z} \rangle \varepsilon_f], \quad (5.51)$$

of length $N_y \times 6$, and the matrix associated to the system is built. The equations are, thus, put in the form $[A]X^{n+1} = b$, and the system is solved to find fluid quantities at $n + 1$.

No-slip boundary condition are imposed for the mean velocity and all Reynolds stresses at the wall, while at the channel center we impose a symmetry condition, with the only exception of $\langle u_{f,y} u_{f,z} \rangle$ which must be zero (antisymmetric). The boundary condition on the fluid dissipation ε_f is of zero-flux at the wall and at the channel center.

It is worth remarking that the source terms due to two way coupling with the particle-phase, are obtained by means of ensemble averages of stochastic quantities, therefore can be noisy and be the cause of numerical issues. Two strategies are used to smooth these quantities: using a high number of statistical particles (i.e. $N_p = 5 \cdot 10^4$ particles corresponds to an average number of particles per cell $N_{cell} = 250$), and time-averaging of the ensemble-averaged quantities.

5.5.2 Particle phase

Stochastic differential equations need ad-hoc numerical scheme for a proper discretization. In particular [Peirano 2006] have proposed a first and a second order scheme based on the analytical solution with constant coefficients in time. That scheme cannot be used with the particle model that we have proposed since two-way coupling modifies the nature of the system of SDEs, as a consequence of the appearance of \mathbf{U}_p in the equation of \mathbf{U}_s . This leads to a complete coupling between the two equations of the particle velocity and the fluid velocity seen which prevents us to directly find the analytical solution with constant coefficient of \mathbf{U}_s . The strategy we have adopted has been to put the system of SDEs in diagonal form in order to uncouple \mathbf{U}_s and \mathbf{U}_p .

We start by considering the sub-system composed by the equations of U_p and U_s which can be put in vectorial form as follows (the i index stands for the three spatial dimensions)

$$d\mathbf{X}_i = \mathbf{C}_i dt + [A]_i \mathbf{X}_i dt + [B]_i d\mathbf{W}_i, \quad (5.52)$$

with

$$\mathbf{X}_i = \begin{pmatrix} U_{p,i} \\ U_{s,i} \end{pmatrix} \quad \mathbf{C}_i = \begin{pmatrix} \langle U_{p,i} \rangle / T_{Lp} - \frac{1}{\langle \alpha_p \rangle \rho_p} \frac{\partial \langle \alpha_p \rangle \rho_p \langle P_{ij} \rangle}{\partial x_j} + \delta v_{p,j} \frac{\partial \langle U_{p,i} \rangle}{\partial x_j} + g_i \\ -\frac{1}{\rho_f} \frac{\partial \langle p_f \rangle}{\partial x_i} + \langle U_{f,i} \rangle / T_{L,i}^* + g_i \end{pmatrix} \quad (5.53)$$

$$[A]_i = \begin{bmatrix} -(1/\tau_p + 1/T_{Lp}) & 1/\tau_p \\ \varphi/\tau_p & -(1/T_{L,i}^* + \varphi/\tau_p) \end{bmatrix} \quad [B]_i = \begin{bmatrix} C & 0 \\ 0 & B_{s,i} \end{bmatrix} \quad (5.54)$$

where $B_{s,i}$ is the diffusion coefficient of $U_{s,i}$, C the constant diffusion coefficient of U_p and $d\mathbf{W}_i = (dW_{p,i} \ dW_{s,i})^T$. To simplify the derivation of the numerical scheme we have decided to treat explicitly the production term $\delta v_{p,j} \frac{\partial \langle U_{p,i} \rangle}{\partial x_j}$, otherwise the system would have been fully coupled, not only in the three variables $U_p, U_s, \delta v_p$, but also in the three directional component x, y, z , yielding a system matrix of size 9×9 to be diagonalized for each particle. With the actual explicit treatment, on the contrary, we have to diagonalize three 2×2 more handling matrices. If we diagonalize the system we obtain

$$d\mathbf{Y}_i = [T]_i^{-1} \mathbf{C}_i dt + [D]_i \mathbf{Y}_i dt + [T]_i^{-1} [B]_i d\mathbf{W}_i, \quad (5.55)$$

where $[T]_i$ and $[D]_i$ are the eigenvector matrix and the eigenvalues diagonal matrix relative to $[A]_i$, and the transformation is given by $\mathbf{X}_i = [T]_i \mathbf{Y}_i$. Now we can decouple the two components of \mathbf{Y}_i and write the equations in the following form

$$dY_{i,1} = K_{i,1} dt - \lambda_{i,1} Y_{i,1} dt + Z_{i,11} dW_{p,i} + Z_{i,12} dW_{s,i}, \quad (5.56)$$

$$dY_{i,2} = K_{i,2} dt - \lambda_{i,2} Y_{i,2} dt + Z_{i,21} dW_{p,i} + Z_{i,22} dW_{s,i}, \quad (5.57)$$

where $\lambda_{i,j}$ are the opposite of the eigenvalues. For each component the analytic solution with constant coefficients in time can be found following the same reasoning adopted by [Peirano 2006]. We look for a solution of the form

$$Y_{i,j}(t) = H_{i,j}(t) \exp(-t\lambda_{i,j}), \quad (5.58)$$

with

$$dH_{i,j}(t) = \exp(t\lambda_{i,j}) [K_{i,j} dt + Z_{i,j1} dW_{p,i} + Z_{i,j2} dW_{s,i}]. \quad (5.59)$$

Integration between t_0 and t gives

$$\begin{aligned} Y_{i,j}(t) &= Y_{i,j}(t_0) \exp(-\Delta t \lambda_{i,j}) + \frac{K_{i,j}}{\lambda_{i,j}} [1 - \exp(-\Delta t \lambda_{i,j})] \\ &\quad + Z_{i,j1} \exp(-t\lambda_{i,j}) \int_{t_0}^t \exp(s\lambda_{i,j}) dW_{p,i} + Z_{i,j2} \exp(-t\lambda_{i,j}) \int_{t_0}^t \exp(s\lambda_{i,j}) dW_{s,i}, \end{aligned} \quad (5.60)$$

where $\lambda_{i,j}$, $K_{i,j}$, $Z_{i,jk}$ are frozen at time t_0 . The analytical solution of \mathbf{U}_p and \mathbf{U}_s can be found transforming back from \mathbf{X}_i to \mathbf{Y}_i .

Stochastic integrals appearing in the analytical solution can be discretised by using the Choleski algorithm. The resulting numerical scheme and the covariance matrices for the evaluation of the stochastic integrals are reported in the Appendix 5.A.

The uncorrelated velocity, $\delta \mathbf{v}_p$, can be treated separately from the previous ones since it has been uncoupled considering it explicitly in the \mathbf{U}_p equation. The production term

$\delta v_{p,j} \partial \langle U_{p,i} \rangle / \partial x_j$, couples the three components of $\delta \mathbf{v}_p$, thus a diagonal decomposition would be necessary to obtain three independent equations, one for each spatial component. However, analogously to how we treated it in equation (5.52) we have considered it explicitly (fixed at time step n), therefore no diagonalisation is needed. We recall that the stochastic process of the uncorrelated velocity is described by the following equation:

$$d \delta v_{p,i} = -\frac{\delta v_{p,i}}{T_\delta} dt + K_{\delta,ij} dt + B_{\delta,ij} dW_{\delta,j} + B_c dW_{c,i}, \quad (5.61)$$

with

$$\frac{1}{T_\delta} = \frac{1}{\tau_p} + \frac{(1+e)(3-e)}{4\tau_c} \quad K_{\delta,ij} = \frac{1}{\langle \alpha_p \rangle \rho_p} \frac{\partial \langle \alpha_p \rangle \rho_p \langle P_{ij} \rangle}{\partial x_j} - \delta v_{p,j} \frac{\partial \langle U_{p,i} \rangle}{\partial x_j}$$

$$B_c = \sqrt{\frac{1}{2\tau_c} (1+e)^2 \langle \Theta_p \rangle}.$$

and $[B_\delta]$ defined in equations (5.26). Equation (5.61) is formally equal to equation (5.56), therefore the same derivation is adopted, leading to the following analytical solution with constant coefficients:

$$\begin{aligned} \delta v_{p,i}(t) = & \delta v_{p,i}(t_0) \exp(-\Delta t/T_\delta) + K_{\delta,ij} T_\delta [1 - \exp(-\Delta t/T_\delta)] \\ & + B_{\delta,ij} \exp(-t/T_\delta) \int_{t_0}^t \exp(s/T_\delta) dW_{\delta,j} + B_c \exp(-t/T_\delta) \int_{t_0}^t \exp(s/T_\delta) dW_{c,i}. \end{aligned} \quad (5.62)$$

Finally the equation of the particle position (5.13) can be solved by integrating it in time and substituting the expressions of \mathbf{U}_p and $\delta \mathbf{v}_p$:

$$\mathbf{x}_p(t) = \mathbf{x}_p(t_0) + \int_{t_0}^t \mathbf{U}_p ds + \int_{t_0}^t \delta \mathbf{v}_p ds. \quad (5.63)$$

The complete expression is reported in table 5.3. Particular care must be taken in the discretisation of stochastic integrals to obtain the correct correlations between variables. The detailed form of the numerical scheme is reported in Appendix 5.A

5.6 Results

5.6.1 Test of consistency with tracer particles

The new numerical scheme proposed to solve the stochastic system of equations of the particle-phase has been validated in the dilute case, i.e. at negligible volume fraction of the particle-phase $\langle \alpha_p \rangle \rightarrow 0$. Specifically, we have tested a dilute channel with tracer particles of vanishing inertia, i.e. $\tau_p \rightarrow 0$, and we have compared our results with the ones obtained for the dilute model of Peirano *et al.* [Peirano 2006].

For this test case the shear Reynolds number is $Re_\tau = 300$ and the particle time scale $\tau_p = 10^{-6}$. All other parameters are reported in table 5.1. The values of the constants obtained from the Cluster-Induced-Turbulence (CIT) study in chapter 4 have been used and are reported in table 5.2. For a comparison with the numerical scheme for the dilute

Physical parameters		
U_b	bulk velocity	5.02 m s^{-1}
δ	channel half width	1.8 cm
$\frac{dp_f}{dz}$	pressure gradient	14.81 Pa
g	gravity magnitude	-9.81 m s^{-2}
ρ_p	particle density	2000 kg m^{-3}
ρ_f	fluid density	1 kg m^{-3}
ν_f	fluid kinematic viscosity	$1.8 \times 10^{-5} \text{ m}^2 \text{ s}^{-1}$
τ_p	particle relaxation time	$10^{-6} \quad 0.0128 \text{ s}$
dt	time step	10^{-4} s

Table 5.1: Fluid and particle parameters used in the simulations, in accordance with the Eulerian-Lagrangian DNS cases of [Capecelatro 2018]. The corresponding shear Reynolds number is $Re_\tau = 300$.

C_{0f}	C_{0p}	$C_{\varepsilon 1}$	$C_{\varepsilon 2}$	C_{3f}	C_{3p}	C_4	f_s	β
3.5	0.18	1.44	1.92	3.5	7.0	6.81	0.4	1

Table 5.2: Model constants.

model of [Peirano 2006], the same constants ($C_0, C_{\varepsilon 1}, C_{\varepsilon 2}$) have been used. A side-by-side comparison is made in figure (5.2) between the numerical scheme of [Peirano 2006] for one-way coupling (left panels) and the new numerical scheme proposed for two-way coupling (right panels), at $\varphi = 0$. From top to bottom are reported the mean velocity and the three diagonal components of the Reynolds stresses. Statistics related to particles are obtained averaging locally inside the cell. It can be seen that the two numerical schemes are fully consistent and that their solutions tend to the RA one. Indeed U_s and U_p are exactly superimposed and empty symbols corresponding to U_s are barely visible.

5.6.2 Inertial particles with two-way coupling

Some of the cases of the EL simulations of [Capecelatro 2018] have been reproduced, namely particles with Stokes number $St = 0.21$ at different mass loading, starting from zero up to $\varphi = 2$. To reach the higher values of the volume fraction we have continuously increased it starting from zero, in order to avoid numerical instabilities, and at each intermediate step we have waited for the simulation to reach a stationary state. We start by showing results at mass loading zero $\varphi = 0$ compared to the EL-DNS ones in order to show the initial bias between the two solutions. Indeed it is worth remembering that we are using a relatively simple Reynolds-stress model to describe the fluid phase and that a perfect recovery of the DNS solution cannot be expected in this case. To obtain a better agreement more complex models might be used, as for instance the non-local elliptic relaxation model [Durbin 1991], but they are out of the scope of this work. In fact here we just focus on the behaviour with the mass loading with respect to the dilute case. Figure 5.3 shows fluid-phase statistics from RANS and DNS for the average vertical velocity and Reynolds-stresses. These figures are intended to show the initial bias between the

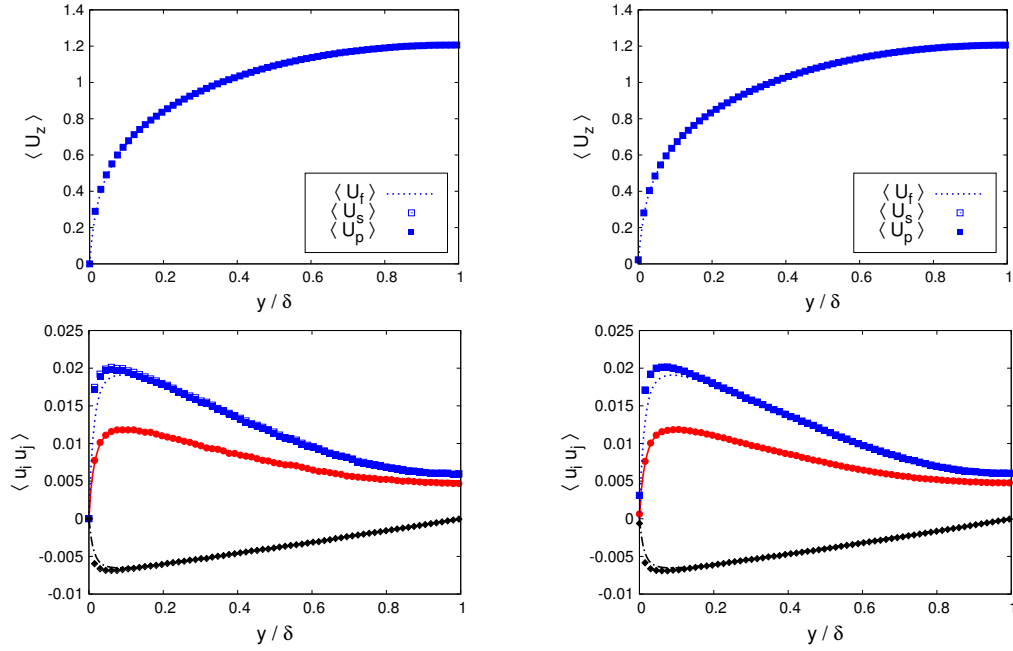


Figure 5.2: Mean velocity and Reynolds-stresses with tracer particles ($\tau_p = 10^{-6}$) in the dilute limit ($\varphi = 0$). On left panels results with the numerical scheme of [Peirano 2006], on right panels results with the new numerical scheme. All quantities are made dimensionless with the RANS bulk velocity $U_b = 3.346 m/s$. RA fluid velocity (lines), fluid velocity seen by particles (symbols), particle velocity (filled symbols). $\langle u_{f,y} u_{f,y} \rangle$ (red solid line), $\langle u_{f,z} u_{f,z} \rangle$ (blue dotted line), $\langle u_{f,y} u_{f,z} \rangle$ (black dash dotted line), $\langle u_{s,y} u_{s,y} \rangle$ (red empty circles), $\langle u_{s,z} u_{s,z} \rangle$ (blue empty squares), $\langle u_{s,y} u_{s,z} \rangle$ (black empty diamonds), $\langle u_{p,y} u_{p,y} \rangle$ (red filled circles), $\langle u_{p,z} u_{p,z} \rangle$ (blue filled squares), $\langle u_{p,y} u_{p,z} \rangle$ (black filled diamonds) .

model and the DNS and for mass loadings different from zero we will adimensionalise each quantity with the corresponding one at $\varphi = 0$.

5.6.2.1 Mean velocities

We analyze here the mean velocities of the fluid-particle flow. The average velocities of the fluid and of particles obtained with the proposed model are compared in Figures 5.4 with the respective ones of the EL-DNS of [Capecelatro 2018], at different mass loadings. In this figures we have adimensionalised the DNS and the model velocities with their respective bulk velocity, i.e. $U_b = 5.02 m/s$ for the DNS, and $U_b = 3.345 m/s$ for the model. It is evident how the model is able to capture the modulation that the particles exert on the fluid when varying the volume fraction of the particle. The particle-phase velocity exhibits a significant slip at the wall, as expected, and its prediction is good near the wall and at the channel center. However, the quantitative agreement is not completely satisfactory and the sensitivity to ϕ seems to be overestimated in the results obtained with the present model. This may be due to the fact that the model constants have not been calibrated for each case considered; conversely, the same values as for homogeneous CIT have been used.

Indeed, it is known how the drift velocity is sensitive to the model constants, see

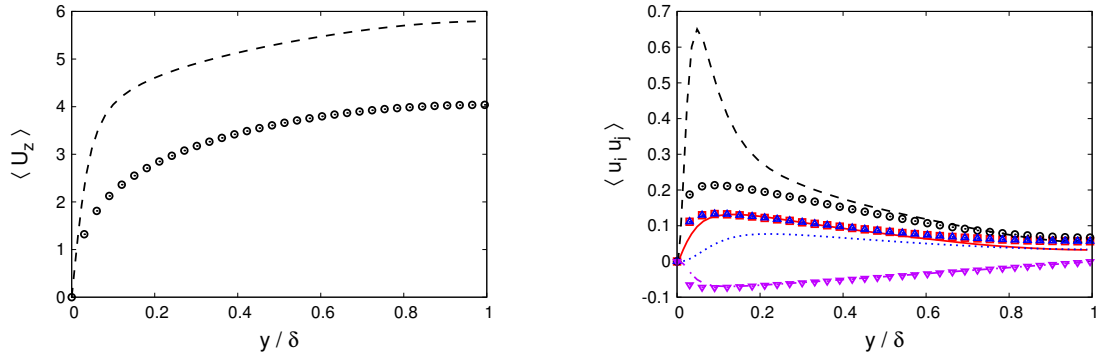


Figure 5.3: Mean velocity and Reynolds-stresses of the fluid-phase at $\varphi = 0$. Lines corresponds to EL-DNS, symbols to the model. $\langle u_{f,x} u_{f,x} \rangle$ (red solid line, squares), $\langle u_{f,y} u_{f,y} \rangle$ (blue dotted line, triangles), $\langle u_{f,z} u_{f,z} \rangle$ (black dashed line, circles), $\langle u_{f,y} u_{f,z} \rangle$ (magenta dash dotted line, downward triangles).

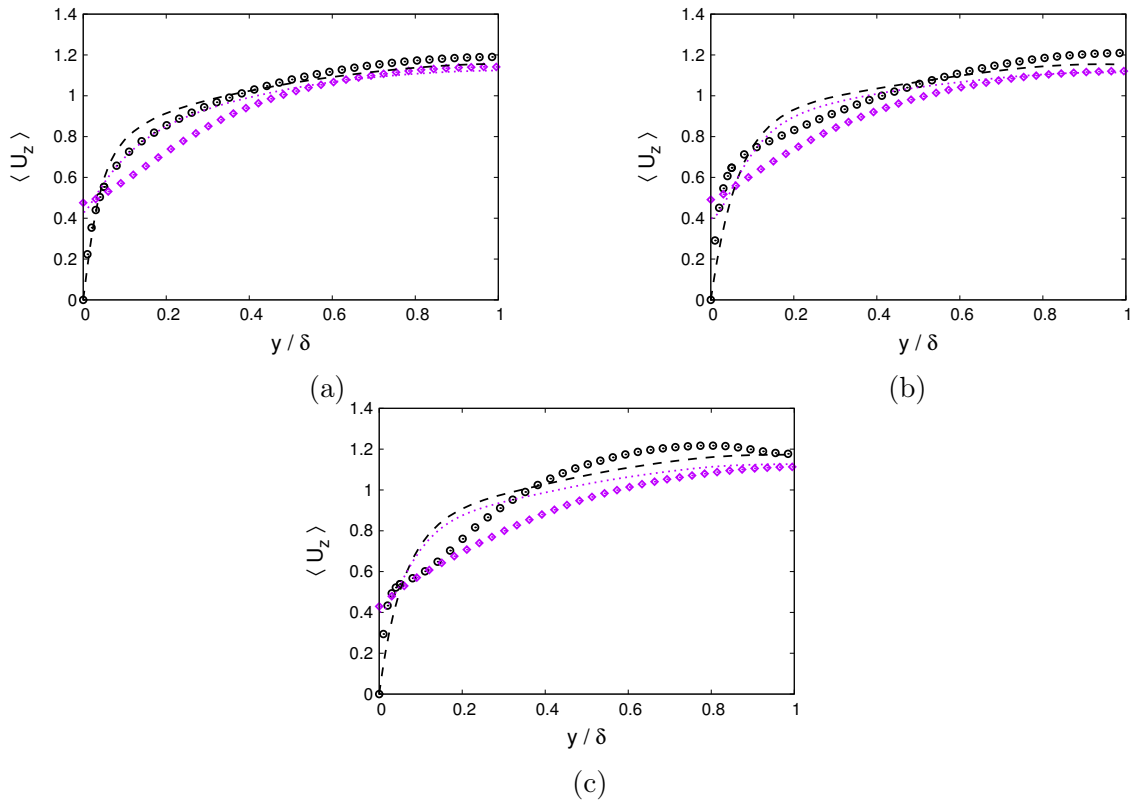


Figure 5.4: Mean velocity of the fluid and particle phase at different mass loading for $St = 0.021$ particles. Lines corresponds to EL-DNS, symbols to the model. Velocities are adimensionalised with the respective bulk velocity. $\langle U_{f,z} \rangle$ (black dashed line, circles), $\langle U_{p,z} \rangle$ (magenta dotted line, diamonds). $\varphi = 0.2$ (a), $\varphi = 1$ (b), $\varphi = 2$ (c)

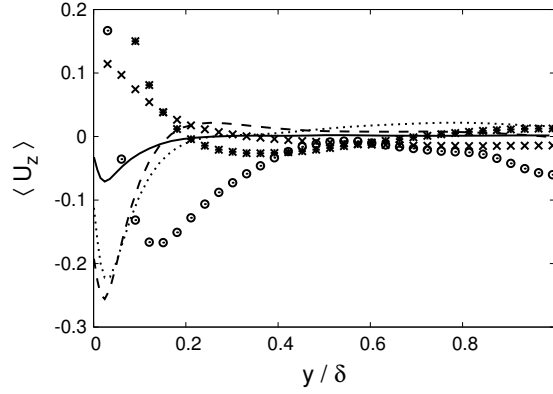


Figure 5.5: Variations of the mean fluid velocity with respect to the solution at $\varphi = 0$. Lines corresponds to EL-DNS, symbols to the model. Velocities are adimensionalised with the DNS bulk velocity. $\varphi = 0.2$ (solid line, \times), $\varphi = 1$ (dashed line, $*$). $\varphi = 2$ (dotted line, \circ).

[Capecelatro 2016b], and in particular to C_2 , which in the present case has been set to zero. In particular, as previously said, constants have been tuned on a homogeneous CIT case at $\varphi = 10$, therefore it is not surprising that at low mass loading results are not very satisfactory. It may be inferred that increasing the mass loading the used values of the constants should be more adequate and this could probably lead also to a better quantitative agreement. If we look to the relative variations with respect to the reference value at $\varphi = 0$

$$Q_r = \frac{Q(\varphi) - Q(\varphi = 0)}{Q(\varphi = 0)}, \quad (5.64)$$

the trend with mass loading holds well for further tests at higher values, as it can be seen in figure 5.5

5.6.2.2 Energy

The kinetic energies for the fluid and particle phase are compared in figure 5.6. As discussed earlier for the mean velocity a quantitative agreement is not in our expectations and a better optimization of the constant would be needed. Nevertheless it is interesting how the model is able to capture the decrease of the fluid kinetic energy when increasing the mass fraction. It has been shown [Capecelatro 2018] that there is a real transition that happens around mass loading $\varphi = 2$ and that above this value energy increases again. The reason is that after a laminarization of the flow due to the presence of particles, clusters start to become dominant, and their fluctuations induce turbulence again in the fluid phase (CIT). Therefore it is encouraging that even if the constants have been optimised on a CIT case, the model behaves qualitatively well also at low volume fraction, where the mechanism of energy transfer is qualitatively different. Concerning the particle-phase energy, we see that after an initial increase from $\varphi = 0.2$ to $\varphi = 1$, that the model describe consistently with the DNS, at $\varphi = 2$ we have a further increase instead of a reduction. This could be due to a too low dissipation of particle energy towards the granular temperature, and might be adjusted by working on the model constants in the equation of ε_p .

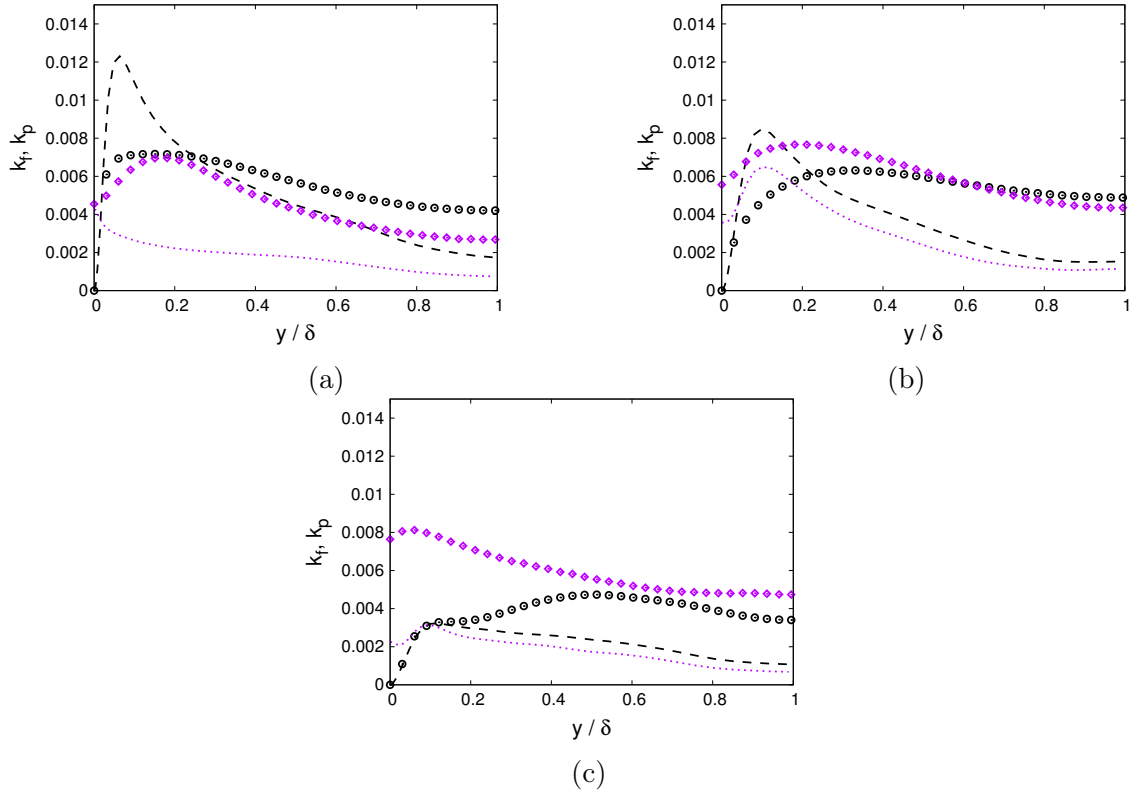


Figure 5.6: Energy of the fluid and particle phase at different mass loading. Lines corresponds to EL-DNS, symbols to the model. Energy is adimensionalised with the DNS bulk velocity. k_f (black dashed line, circles), k_p (magenta dotted line, diamonds). $\varphi = 0.2$ (a), $\varphi = 1$ (b), $\varphi = 2$ (c)

In figure 5.7 we show the trend of the average fluid turbulent kinetic energy with respect to the mass loading. As outlined above, the model predicts well the energy decrease, and apart an initial bias, the relative variations are in very good agreement with the EL-DNS.

Finally we have looked at the anisotropy of the Reynolds stresses. In homogeneous CIT the Reynolds stresses are highly anisotropic with the zz component significantly larger than the other two. In the channel case we can notice how the anisotropy becomes more and more pronounced when increasing the mass loading and thus moving towards the CIT mechanism. The agreement with the EL-DNS results is satisfactory and the zz contribution to k_f increase from an initial 50% to above 80% for $\varphi = 2$.

5.7 Conclusions

In this work we show the application of the stochastic model for dense particle-laden flows proposed in this thesis, to a turbulent channel flow. We have rephrased the model equations for this non-homogeneous application and we have proposed a new numerical scheme for the solution of the Lagrangian stochastic equations. In particular, the particle-phase equations have been solved numerically using a Monte Carlo approach. The Lagrangian equations include some new numerical difficulties due to two-way coupling compared to

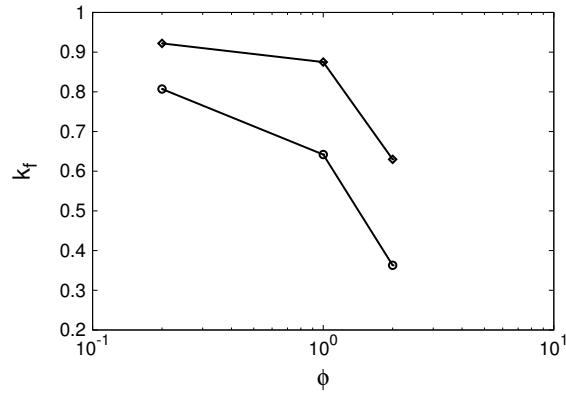


Figure 5.7: Fluid phase energy variations with respect to the mass fraction normalised by the corresponding energy at $\varphi = 0$. EL-DNS data (\circ), model (\diamond).

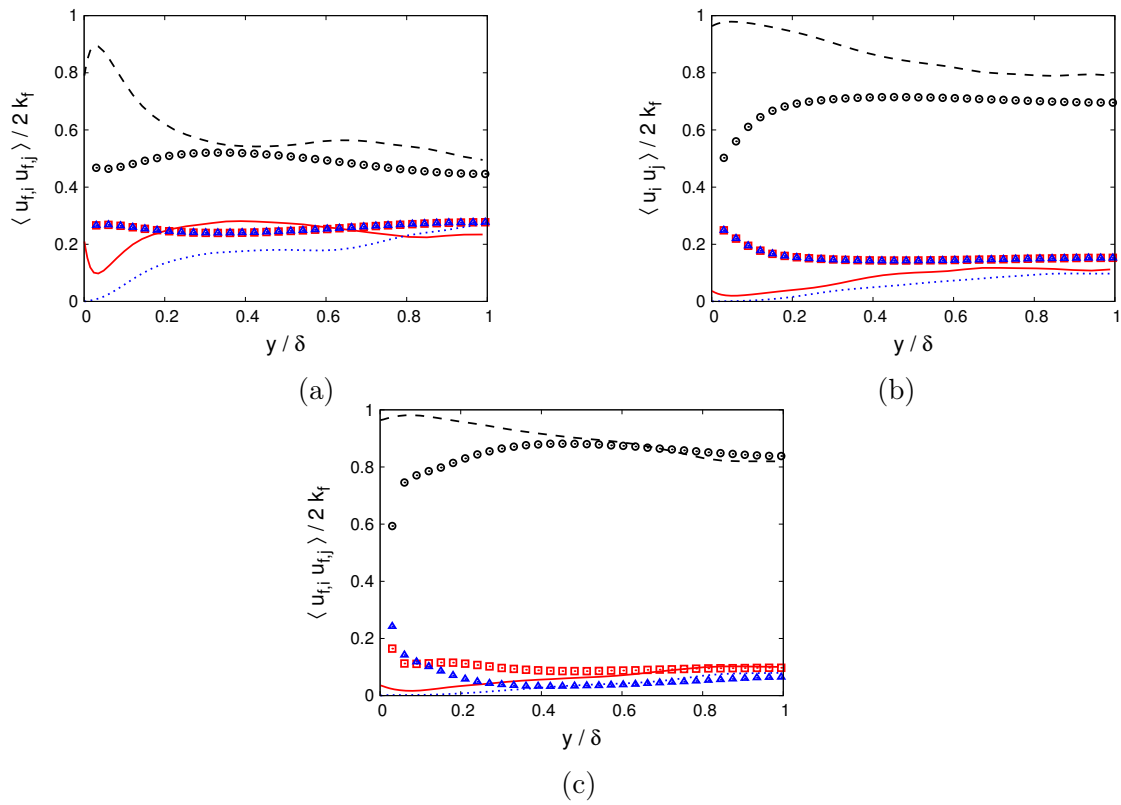


Figure 5.8: Fluid phase Reynolds stress components at different mass loading. Lines corresponds to EL-DNS, symbols to the model. $\langle u_{f,x}u_{f,x} \rangle$ (red solid line, squares), $\langle u_{f,y}u_{f,y} \rangle$ (blue dotted line, triangles), $\langle u_{f,z}u_{f,z} \rangle$ (black dashed line, circles). $\varphi = 0.2$ (a), $\varphi = 1$ (b), $\varphi = 2$ (c)

already existing models for dilute flows [Peirano 2006]. The particle and the fluid-seen velocity equations are fully coupled and therefore an initial diagonalisation of the system is needed for each statistical particle. Then, a numerical scheme can be derived based on the analytical solution that the equations admit with constant coefficients. The scheme includes also the additional terms that are present in the particle velocity equations not present in the dilute model, as well as the new equations for the uncorrelated component of the particle velocity δv_p .

A turbulent channel flow at shear Reynolds number $Re_\tau = 300$ has been simulated reproducing the same configuration of the EL-DNS of [Capecelatro 2018] that have been taken as reference to assess the model. The numerical scheme has been first validated in a test of consistency with tracer particles at negligible mass loading and the solution has been compared to that obtained by the numerical scheme for dilute flows in the same flow conditions. Direct comparison shows that the scheme reproduces exactly the same results as those of the dilute scheme and that in both cases an excellent consistency is obtained, i.e. the solution from the Lagrangian tracer particles recovers the one from the Eulerian fluid RA equations.

Then, inertial particles with Stokes number $St = 0.21$ have been simulated at different mass-loading reproducing some of the cases of the reference EL-DNS. The values of the model constants have not been changed from those obtained in the fully developed homogeneous CIT case of chapter 4, which was for high Stokes number particles at high mass loading $\varphi = 10$. Thus, the agreement with DNS results is at best qualitative, since we have tested only cases at mass loading $0 \leq \varphi \leq 2$. In fact, even with constants optimized on a case based on CIT mechanism, the model meets the good trends with respect to the mass loading. It has been discussed in [Capecelatro 2018] how different regimes are encountered when increasing the volume fraction, from weak interphase coupling ($\varphi \leq 1$) where the dominant mechanism for generating fluid-phase turbulent kinetic energy is the mean-shear production, to moderate coupling ($2 \leq \varphi \leq 4$) where the flow relaminarizes, to strong coupling ($\varphi \geq 10$) with CIT. Therefore, since different mechanisms are at play, we cannot expect to obtain a quantitative agreement for all cases by keeping the same values of the constants. Indeed we have shown that the model is able to capture some modulation of the particles on the fluid velocity, but with the present constants the variations of the mean velocity profile appear to be too sensitive to the mass fraction. However the constant reduction of turbulent kinetic energy is well captured and the repartition of energy between the different Reynolds-stress components is in good agreement with EL-DNS results. It is worth remarking that the strong anisotropy of the Reynolds-stress tensor in the homogeneous CIT is one of its key feature, therefore the trend that we have obtained up to $\varphi = 2$ is positive and bodes well for higher mass-loadings.

Albeit preliminary, overall results are very encouraging for future developments. It would be of interest to test the model at higher mass loading in the CIT range and for different particle Stokes number. Because of the low computational cost of the simulations we could also adopt techniques of uncertainty quantification to find a suitable set of constants capable of reproducing all cases with also a satisfactory quantitative accuracy in order to make the model viable for practical applications.

5.A Numerical scheme

Table 5.3: Analytical solutions to system (5.29) for time-independent coefficients.

$$\begin{aligned}
 U_{p,i}(t) = & \left\{ Y_{i,1}(t_0) \exp(-\Delta t \lambda_{i,1}) + \frac{K_{i,1}}{\lambda_{i,1}} [1 - \exp(-\Delta t \lambda_{i,1})] + \gamma_{i,p1} + \gamma_{i,s1} \right\} [T_{11}]_i \\
 & + \left\{ Y_{i,2}(t_0) \exp(-\Delta t \lambda_{i,2}) + \frac{K_{i,2}}{\lambda_{i,2}} [1 - \exp(-\Delta t \lambda_{i,2})] + \gamma_{i,p2} + \gamma_{i,s2} \right\} [T_{12}]_i,
 \end{aligned} \tag{5.65}$$

$$\begin{aligned}
 U_{s,i}(t) = & \left\{ Y_{i,1}(t_0) \exp(-\Delta t \lambda_{i,1}) + \frac{K_{i,1}}{\lambda_{i,1}} [1 - \exp(-\Delta t \lambda_{i,1})] + \gamma_{i,p1} + \gamma_{i,s1} \right\} [T_{21}]_i \\
 & + \left\{ Y_{i,2}(t_0) \exp(-\Delta t \lambda_{i,2}) + \frac{K_{i,2}}{\lambda_{i,2}} [1 - \exp(-\Delta t \lambda_{i,2})] + \gamma_{i,p2} + \gamma_{i,s2} \right\} [T_{22}]_i,
 \end{aligned} \tag{5.66}$$

$$\delta v_{p,i}(t) = \delta v_{p,i}(t_0) \exp\left(-\frac{\Delta t}{T_\delta}\right) + K_{\delta,ij} \cdot T_\delta \left[1 - \exp\left(-\frac{\Delta t}{T_\delta}\right)\right] + \sigma_{\delta,ij} + \sigma_{c,i}, \tag{5.67}$$

$$\begin{aligned}
 x_{p,i}(t) = & x_{p,i}(t_0) + \left\{ \frac{Y_{i,k}(t_0)}{\lambda_{i,k}} [1 - \exp(-\Delta t \lambda_{i,k})] + \frac{K_{i,k}}{\lambda_{i,k}} \left[\Delta t + \frac{1}{\lambda_{i,k}} (\exp(-\Delta t \lambda_{i,k}) - 1) \right] \right\} [T_{1k}]_i + \Pi_{ip} + \Pi_{is} \\
 & + \delta v_{p,i}(t_0) T_\delta [1 - \exp(-\Delta t / T_\delta)] + K_{\delta,ij} \cdot T_\delta \left[\Delta t - T_\delta \left(1 - \exp\left(-\frac{\Delta t}{T_\delta}\right)\right) \right] \\
 & + \Sigma_{\delta,ij} + \Sigma_{c,i},
 \end{aligned} \tag{5.68}$$

The stochastic integrals are given by:

$$\begin{aligned}
 \gamma_{i,p1}(t) &= Z_{i,11} \exp(-t \lambda_{i,1}) \int_{t_0}^t \exp(s \lambda_{i,1}) dW_{p,i}, & \gamma_{i,s1}(t) &= Z_{i,12} \exp(-t \lambda_{i,1}) \int_{t_0}^t \exp(s \lambda_{i,1}) dW_{s,i}, \\
 \gamma_{i,p2}(t) &= Z_{i,21} \exp(-t \lambda_{i,2}) \int_{t_0}^t \exp(s \lambda_{i,2}) dW_{p,i}, & \gamma_{i,s2}(t) &= Z_{i,22} \exp(-t \lambda_{i,2}) \int_{t_0}^t \exp(s \lambda_{i,2}) dW_{s,i}, \\
 \Gamma_{i,p1}(t) &= \int_{t_0}^t \gamma_{i,p1}(s) ds, & \Gamma_{i,s1}(t) &= \int_{t_0}^t \gamma_{i,s1}(s) ds, \\
 \Gamma_{i,p2}(t) &= \int_{t_0}^t \gamma_{i,p2}(s) ds, & \Gamma_{i,s2}(t) &= \int_{t_0}^t \gamma_{i,s2}(s) ds, \\
 \Pi_{ip}(t) &= \Gamma_{i,p1}(t) [T_{11}]_i + \Gamma_{i,p2}(t) [T_{12}]_i, & \Pi_{is}(t) &= \Gamma_{i,s1}(t) [T_{11}]_i + \Gamma_{i,s2}(t) [T_{12}]_i, \\
 \sigma_{\delta,ij}(t) &= B_{\delta,ij} \exp(-t/T_\delta) \int_{t_0}^t \exp(s/T_\delta) dW_{\delta,i}, \\
 \sigma_{c,i}(t) &= B_c \exp(-t/T_\delta) \int_{t_0}^t \exp(s/T_\delta) dW_{c,i}, \\
 \Sigma_{\delta,ij}(t) &= \int_{t_0}^t \sigma_{\delta,ij}(s) ds, & \Sigma_{c,i}(t) &= \int_{t_0}^t \sigma_{c,i}(s) ds.
 \end{aligned}$$

Table 5.4: First-order temporal discretization (Euler scheme)

Numerical integration of the system:

$$U_{p,i}^{n+1} = \left\{ Y_{i,1}^n \exp(-\Delta t \lambda_{i,1}^n) + \frac{K_{i,1}^n}{\lambda_{i,1}^n} [1 - \exp(-\Delta t \lambda_{i,1}^n)] + \gamma_{i,p1}^n + \gamma_{i,s1}^n \right\} [T_{11}]_i \\ + \left\{ Y_{i,2}^n \exp(-\Delta t \lambda_{i,2}^n) + \frac{K_{i,2}^n}{\lambda_{i,2}^n} [1 - \exp(-\Delta t \lambda_{i,2}^n)] + \gamma_{i,p2}^n + \gamma_{i,s2}^n \right\} [T_{12}]_i^n, \quad (5.69)$$

$$U_{s,i}^{n+1} = \left\{ Y_{i,1}^n \exp(-\Delta t \lambda_{i,1}^n) + \frac{K_{i,1}^n}{\lambda_{i,1}^n} [1 - \exp(-\Delta t \lambda_{i,1}^n)] + \gamma_{i,p1}^n + \gamma_{i,s1}^n \right\} [T_{21}]_i^n \\ + \left\{ Y_{i,2}^n \exp(-\Delta t \lambda_{i,2}^n) + \frac{K_{i,2}^n}{\lambda_{i,2}^n} [1 - \exp(-\Delta t \lambda_{i,2}^n)] + \gamma_{i,p2}^n + \gamma_{i,s2}^n \right\} [T_{22}]_i^n, \quad (5.70)$$

$$\delta v_{p,i}^{n+1} = \delta v_{p,i}^n \exp(-\frac{\Delta t}{T_\delta^n}) + K_{\delta,ij}^n \cdot T_\delta^n \left[1 - \exp(-\frac{\Delta t}{T_\delta^n}) \right] + \sigma_{\delta,ij}^n + \sigma_{c,i}^n, \quad (5.71)$$

$$x_{p,i}^{n+1} = x_{p,i}^n + \left\{ \frac{Y_{i,k}^n}{\lambda_{i,k}^n} [1 - \exp(-\Delta t \lambda_{i,k}^n)] + \frac{K_{i,k}^n}{\lambda_{i,k}^n} \left[\Delta t + \frac{1}{\lambda_{i,k}^n} (\exp(-\Delta t \lambda_{i,k}^n) - 1) \right] \right\} [T_{1k}]_i^n + \Pi_{ip}^n + \Pi_{is}^n \\ + \delta v_{p,i}^n T_\delta^n [1 - \exp(-\Delta t / T_\delta^n)] + K_{\delta,ij}^n \cdot T_\delta^n \left[\Delta t - T_\delta^n \left(1 - \exp(-\frac{\Delta t}{T_\delta^n}) \right) \right] \\ + \Sigma_{\delta,ij}^n + \Sigma_{c,i}^n, \quad (5.72)$$

The stochastic integrals are simulated by (analogously for $\sigma_{\delta,ij}^n$ and $\sigma_{c,i}^n$):

$$\gamma_{i,p1}^n = P_{11p}^i \mathcal{G}_{1,i}, \quad \gamma_{i,s1}^n = P_{11s}^i \mathcal{G}_{4,i} \\ \gamma_{i,p2}^n = P_{21p}^i \mathcal{G}_{1,i} + P_{22p}^i \mathcal{G}_{2,i}, \quad \gamma_{i,s2}^n = P_{21s}^i \mathcal{G}_{4,i} + P_{22s}^i \mathcal{G}_{5,i} \\ \Pi_{ip}^n = P_{31p}^i \mathcal{G}_{1,i} + P_{32p}^i \mathcal{G}_{2,i} + P_{33p}^i \mathcal{G}_{3,i}, \quad \Pi_{is}^n = P_{31s}^i \mathcal{G}_{4,i} + P_{32s}^i \mathcal{G}_{5,i} + P_{33s}^i \mathcal{G}_{6,i}$$

where $\mathcal{G}_{k,i}$ are independent $\mathcal{N}(0, 1)$ random variables.

The coefficients $P_{11p}^i, P_{21p}^i, P_{22p}^i, P_{31p}^i, P_{32p}^i, P_{33p}^i$, (analogously for P_{ijs}) are defined as:

$$P_{11p}^i = \sqrt{\langle (\gamma_{i,p1}^n)^2 \rangle}, \\ P_{21p}^i = \frac{\langle \gamma_{i,p1}^n \gamma_{i,p2}^n \rangle}{\sqrt{\langle (\gamma_{i,p1}^n)^2 \rangle}}, \quad P_{22p}^i = \sqrt{\langle (\gamma_{i,p2}^n)^2 \rangle - \frac{\langle \gamma_{i,p1}^n \gamma_{i,p2}^n \rangle^2}{\langle (\gamma_{i,p1}^n)^2 \rangle}}, \\ P_{31p}^i = \frac{\langle \gamma_{i,p1}^n \Pi_{ip}^n \rangle}{\sqrt{\langle (\gamma_{i,p1}^n)^2 \rangle}}, \quad P_{32p}^i = \frac{1}{P_{22p}^i} (\langle \gamma_{i,p2}^n \Pi_{ip}^n \rangle - P_{21p}^i P_{31p}^i), \quad P_{33p}^i = \sqrt{\langle (\Pi_{ip}^n)^2 \rangle - P_{31p}^i{}^2 - P_{32p}^i{}^2}. \quad (5.73)$$

Table 5.5: Covariance matrix

$$\begin{aligned}
\langle \gamma_{i,p1}^2 \rangle &= \frac{1}{2} \frac{Z_{i,11}^2}{\lambda_{i,1}} \left(1 - \exp(-2\Delta t \lambda_{i,1}) \right) \\
\langle \gamma_{i,p2}^2 \rangle &= \frac{1}{2} \frac{Z_{i,21}^2}{\lambda_{i,2}} \left(1 - \exp(-2\Delta t \lambda_{i,2}) \right) \\
\langle \gamma_{i,p1} \gamma_{i,p2} \rangle &= \frac{1}{2} \frac{Z_{i,11} Z_{i,21}}{(\lambda_{i,1} + \lambda_{i,2})} \left(1 - \exp(-\Delta t (\lambda_{i,1} + \lambda_{i,2})) \right) \\
\langle \gamma_{i,p1} \Pi_{ip} \rangle &= -\frac{T[1,1]_i}{2\lambda_{i,1}^2} Z_{i,11}^2 \left(1 - \exp(-2\Delta t \lambda_{i,1}) \right) - \frac{T[1,2]_i}{\lambda_{i,2}(\lambda_{i,1} + \lambda_{i,2})} Z_{i,11} Z_{i,21} \left(1 - \exp(-\Delta t (\lambda_{i,1} + \lambda_{i,2})) \right) \\
&\quad + \frac{Z_{i,11}}{\lambda_{i,1}} \left(T[1,1]_i \frac{Z_{i,11}}{\lambda_{i,1}} + T[1,2]_i \frac{Z_{i,21}}{\lambda_{i,2}} \right) \left(1 - \exp(-\Delta t \lambda_{i,1}) \right) \\
\langle \gamma_{i,p2} \Pi_{ip} \rangle &= -\frac{T[1,2]_i}{2\lambda_{i,2}^2} Z_{i,21}^2 \left(1 - \exp(-2\Delta t \lambda_{i,2}) \right) - \frac{T[1,1]_i}{\lambda_{i,1}(\lambda_{i,1} + \lambda_{i,2})} Z_{i,11} Z_{i,21} \left(1 - \exp(-\Delta t (\lambda_{i,1} + \lambda_{i,2})) \right) \\
&\quad + \frac{Z_{i,21}}{\lambda_{i,2}} \left(T[1,1]_i \frac{Z_{i,11}}{\lambda_{i,1}} + T[1,2]_i \frac{Z_{i,21}}{\lambda_{i,2}} \right) \left(1 - \exp(-\Delta t \lambda_{i,2}) \right) \\
\langle \Pi_{ip}^2 \rangle &= -\frac{T[1,1]_i^2}{2\lambda_{i,1}^3} Z_{i,11}^2 \left(1 - \exp(-2\Delta t \lambda_{i,1}) \right) + \frac{T[1,2]_i^2}{2\lambda_{i,2}^3} Z_{i,21}^2 \left(1 - \exp(-2\Delta t \lambda_{i,2}) \right) + \\
&\quad \left(\frac{T[1,1]_i Z_{i,11}}{\lambda_{i,1}} + \frac{T[1,2]_i Z_{i,21}}{\lambda_{i,2}} \right)^2 \Delta t + 2 \frac{T[1,1]_i T[1,2]_i}{\lambda_{i,1} \lambda_{i,2} (\lambda_{i,1} + \lambda_{i,2})} Z_{i,11} Z_{i,21} \left(1 - \exp(-\Delta t (\lambda_{i,1} + \lambda_{i,2})) \right) \\
&\quad - 2T[1,1]_i \frac{Z_{i,11}}{\lambda_{i,1}^2} \left(T[1,1]_i \frac{Z_{i,11}}{\lambda_{i,1}} + T[1,2]_i \frac{Z_{i,21}}{\lambda_{i,2}} \right) \left(1 - \exp(-\Delta t \lambda_{i,1}) \right) \\
&\quad - 2T[1,2]_i \frac{Z_{i,21}}{\lambda_{i,2}^2} \left(T[1,1]_i \frac{Z_{i,11}}{\lambda_{i,1}} + T[1,2]_i \frac{Z_{i,21}}{\lambda_{i,2}} \right) \left(1 - \exp(-\Delta t \lambda_{i,2}) \right)
\end{aligned}$$

Part III

Bubbly flows

Bubbly flows: phenomenology of free rise and bubble-induced turbulence at high Reynolds numbers.

In this chapter, as outlined in part I, we have analyzed a different type of multiphase flows, namely bubbly flows. In continuity with part II the objective is to study the generation of turbulence by a dispersed phase, which in the present case is represented by gas bubbles rising within a liquid. The driving motor that induces the agitation in the carrier phase is gravity, as in CIT, but resulting in the present case in a reverse direction of the velocity of the bubble that rises under the effect of buoyancy. A totally different approach and methodology have been adopted with respect to previous chapters, namely we have carried out direct numerical simulations of the bubbly flows. Indeed, turbulent bubbly flows are so complex that there is no realistic numerical experiment so far concerning the collective dynamics of many bubbles. Important experiments have been carried out in the last decades, yet a precise understanding of the mechanisms underlying the phenomenology encountered is still lacking. Hence before coming up with some models, fully resolved numerical simulations are needed in order to provide useful analysis. In particular we have investigated some physical aspects about the wake agitation that have been put forward in a recent experiment [Riboux 2010]. In the perspective of providing a systematic and consistent study, we have followed some benchmark tests available in the literature on the numerical simulation of rising bubbles to assess the accuracy of the flow solver Basilisk in this configuration. In particular we have verified the possibility of using numerical grids with an adaptive refinement, which is one of the key feature of the Basilisk code. It is evident that having a grid with an high level of refinement only where it is required (inside bubbles, in the neighborhood of the interface and in the wakes) can be a great advantage, especially if bubbles are concentrated in a restricted area of the domain as is in bubble columns. This will make more accessible also the possibility of resolving large domains where bubbles are free to evolve and interact and have sufficient space to attain fully developed wakes [Cano-Lozano 2016]. However, deciding some criterion for the grid adaptation is not trivial and one has to make sure not to under-resolve the problem if a certain degree of accuracy has to be achieved.

At this stage this part is not yet in preparation for publication, since we are waiting for some simulations to be fully accomplished for a further analysis. We present thus the results of the 2-dimensional numerical simulations concerning the bubble column configuration at a fixed volume fraction and varying the bubble diameter. A fully resolved 3-dimensional simulation with 256 bubbles is still running and results will be analysed as soon as possible.

6.1 Introduction

Multiphase flows are ubiquitous in nature and represent one of the main subject of study in fluid mechanics [Prosperetti 2009]. Among the various kind of multiphase flows, bubbly flows represent a challenging and key field of investigation, both for their fundamental dynamics and their numerous applications in engineering and environmental applications [Prosperetti 2004, Magnaudet 2000, Ern 2012].

In particular, bubble columns offer a privileged configuration to be studied. Indeed, they are conceptually simple: a gas is sparged at the bottom of a liquid-filled vessel and the bubbles rise under the effect of buoyancy. High transfer rates can then be attained owing to the increased contact area between the gas and the liquid phases, and to the liquid agitation induced by the bubble motion. On one hand, they are employed in industrial device in relation to efficient heat and mass transfer characteristics. On the other hand, this configuration appears as good benchmark to analyse the fundamental features of the bubble dynamics, as highlighted in the pioneering work of [Lance 1991]. Since a reliable prediction of bubble residence time and available interfacial area is crucial for an accurate design of industrial devices, the understanding of bubble flow dynamics is essential. In particular, due to the large density difference between gases and liquids, under the effect of buoyancy the bubbles rise with a velocity considerably different from the liquid. They thus induce velocity disturbances in the liquid that collectively generate a complex agitation. In generic flows, this bubble-induced agitation, also called pseudo-turbulence, is often coupled to a turbulent agitation inherent to the liquid phase. However, the understanding of the pure bubble-induced agitation, without a previous turbulent motion of the liquid, is key to grasp the physics of more complex flows.

For this reason, several experimental studies have been carried out to investigate this kind of problem in different configurations [Zenit 2001, Martínez-Mercado 2007, Riboux 2010]. This research has highlighted some characteristics of the bubble-induced agitation. When a single bubble is present, it has been showed that the average rise velocity is a non-monotonic function of the diameter and, more amazing, that path instability may occur producing complex oscillating trajectories [Mougin 2001, Ern 2012]. Furthermore, the bubble produces a velocity disturbance in the surrounding fluid. In particular, at large Reynolds number, a flow disturbance that decays as r^{-3} [Batchelor 2000], and a wake whose mean velocity decays with the vertical distance from the bubble z as z^{-1} in a laminar flow [Batchelor 2000] and as $z^{-2/3}$ in a turbulent one [Pope 2000]. This is an important fact, since it means that the superposition of non-interacting bubbles leads to the divergence of the variance of the liquid velocity with the number of bubbles. However, it is an experimental evidence [Risso 2002] that at moderate-to-large Reynolds numbers ($Re \gtrsim 100$) there is no such a divergence of the velocity variance because the wakes of interacting bubbles are attenuated. That shows that at large Reynolds numbers the dominant mechanism underlying liquid agitation is the nonlinear wake interaction. Therefore, the results obtained with a small amount of bubbles which interact only weakly are of a little relevance to understand large-Reynolds number flows, typical of experiments.

When many bubbles are present, the main phenomenology is the following [Risso 2018]: (i) At variance with particle-laden flows [Toschi 2009, Balachandar 2010], no significant clustering is observed, when a homogeneous swarm of spherical bubbles are considered.

(ii) The average rise velocity of the bubbles is lower than in the isolated bubble case, and the dependence on the volume fraction is still not clear. (iii) Bubble velocity fluctuations seem to present a strong asymmetry between horizontal and vertical fluctuations. (iv) The agitation of the liquid clearly increases with the bubble volume fraction. Its energy spectrum ($E(k)$) appears to display a crossover between a steeper ($E \sim k^{-3}$) slope at large scales and a milder one at small scales ($E \sim k^{-5/3}$). (v) The probability density function (pdf) of the vertical fluctuations is strongly skewed and thus non-gaussian, while the horizontal one is symmetrical and more near to a gaussian curve.

These characteristics have been revealed through important experiments which are far from being easy. For instance, it is difficult to avoid any external effects on the swarm, to impose precise homogeneous conditions and monodispersity. Furthermore, even though the measurement tools have been largely improved in the last decades, not all the above statement have the same robustness. In particular, measurements of the bubble and liquid fluctuations are very difficult and surely affected by large errors. Hence, an assessment of the above phenomenology is still important. Furthermore, some of the physical mechanisms that cause this dynamics remain to be unfold. Notably, the scale dependence of the spectrum remains unclear and the precise mechanism underlying the turbulence production is not known.

From the above consideration, it appears clear that numerical experiments, *i.e.* direct numerical simulations (DNS), of such flows are highly attractive since they permit to analyse idealised configurations and, thus, complement the experiments to understand the fundamental physics, and also they provide key guidelines in view of the development of more approximate models. For such reasons, huge efforts have been made to develop efficient numerical approaches in the last decades [Tryggvason 2011]. In particular, numerical simulations of columns of few tens of bubbles in channel flows have been carried out in many configurations at moderate Re number [Esmaeeli 1998, Esmaeeli 1999, Esmaeeli 2005], and more recently some tentative has been made to simulate homogeneous swarms at higher Reynolds number flows with very few bubbles [Roghair 2011, Roghair 2013].

However, several issues afflict DNS of bubbly flows. As it has been said before, the numerical experiments must consider a sufficiently large number of interacting bubbles to represent soundly the dynamics of realistic flows at high Reynolds numbers. Secondly, it has been clearly pointed out in a recent important work [Cano-Lozano 2016] that under-resolving the bubble dynamics, that means to use an insufficient number of mesh nodes to describe each bubble, affects dramatically the results obtained. The differences between *real* DNS of bubbly flows and under-resolved numerical simulations are unfortunately not only quantitative but also qualitative, which means that under-resolved simulations fail to capture even the régimes of the flow. Moreover, in the cited work a large campaign on numerical simulations neatly indicates that the number of points required to discretize the problem grows almost linearly with the Re number. The final drawback of DNS is that, as in general for numerical simulations of turbulent flows [Pope 2000], yet even more truly for multiphase flows, it is difficult to achieve Reynolds numbers as large as those obtained in experiments. Furthermore, we shall show in this work, that to have realistic value of the surface tension and of the density ratio between the liquid and gas phases is also necessary to avoid spurious effects. At the light of such constraints, while simulations carried out at small Re can be considered confidently, a well resolved DNS of bubble swarm at high Re

is still lacking.

Concerning the phenomenology, the issue of the dependence of the rise velocity from the bubble volume fraction has been recently addressed in the case of moderate Re and with ordered arrays, which can be simulated using a single bubble [Loisy 2017]. We will assess some of those results performing with our different numerical approach some of the numerical experiments. On the other hand, our main aim will be to focus on the statistical properties of the flow, using both two-dimensional and three-dimensional configurations. Notably, we compute the statistics in the region within the bubble swarm. Both energy distribution and velocity pdfs will be analysed.

6.2 Mathematical formulation

6.2.1 Problem statement

We investigate in this work the dynamics of a monodisperse suspension of bubbles rising under the action of buoyancy in a fluid initially at rest. The density, the viscosity and the surface tension of each fluid is considered constant during each numerical experiment. The gravity is assumed to be always aligned in the vertical direction and the possible influence of the orientation of the gravity is out of the scope of the present work. Different configurations of increasing difficulty are studied. First we consider an infinite homogeneous suspension, which is represented by the periodic repetition of cubic unit cell containing a given number of bubbles. When a single bubble is considered, we describe an ordered array of bubbles. Then we consider a more realistic configuration, in which a given number of bubbles are initially randomly distributed at the bottom of a channel and rise through it. This problem is analyzed in two dimensions varying several parameters and then is studied in three dimension at a high Reynolds number.

Many physical parameters may characterize the problem: the gas volume fraction, the number of bubbles, the diameter of the bubbles d calculated as the diameter of the sphere of equivalent volume, the gravity acceleration g , the viscosity of the two fluids μ_b , μ_l , their densities ρ_b , ρ_l , and the surface tension σ . We use the subscripts b for bubbles and l for liquid. Generally, the problem is physically described in terms of the dimensionless groups. Four dimensionless groups can be formed in addition to the number of bubbles and the volume fraction. Two are the density and viscosity ratio, $\frac{\rho_b}{\rho_l}$ and $\frac{\mu_b}{\mu_l}$. We briefly analyse the impact of the density ratio, but in almost all simulations we have fixed $\rho_b/\rho_l = 10^{-3}$ and $\mu_b = \mu_l = 10^{-2}$, which are typical values for air bubbles in water.

The other two dimensionless groups are the Galileo number

$$Ga \equiv \frac{\rho_l |\Delta\rho| g d_b^3}{\mu_l^2}, \quad (6.1)$$

where $\Delta\rho = \rho_b - \rho_l$, or equivalently the Archimedes number $Ar \equiv \sqrt{Ga}$, and the Bond (or Eotvos) number

$$Bo \equiv \frac{|\Delta\rho| g d_b^2}{\sigma} \quad (6.2)$$

These numbers indicate the importance of buoyancy and surface tension and do not include the velocity of the bubble. This allows to fix them *a priori* on the basis of the problem chosen, which is useful for numerical experiments.

When bubbles move, a typical velocity-scale has to be added among the relevant quantities. We compute at each time the velocity of each volume of fluid for both phases. From that, we can compute the average of the bubble velocity in the whole domain $\langle U_b \rangle$. Thus, it is possible to define the Reynolds number based on this velocity

$$Re \equiv \frac{\langle U_b \rangle d_b}{\nu_l}, \quad (6.3)$$

where ν_l is the kinematic viscosity of the liquid. It is also possible to use another group which compares the dynamic effects with the surface tension, the Weber number

$$We \equiv \frac{\rho_b \langle U_b \rangle^2 d_b}{\sigma} = \frac{Bo Re^2}{Ga}. \quad (6.4)$$

It is important to note that the mean bubble velocity may or may not reach a stationary state in our numerical experiments, so that in general the dynamic dimensionless numbers are dependent on time $Re = Re(t)$.

In the first part of this work, we analyse the relation $U = U(N_b, \phi, Bo, Ga)$ comparing with recent numerical studies obtained with different methods. We will measure also the impact of the density ratio, notably on the rate of coalescence. In the second part, we will study the phenomenology of some realistic configuration with the parameters fixed as in typical experiments.

6.2.2 Governing equations

Both fluids are governed by Navier-Stokes equations, which in the incompressible read

$$\nabla \cdot \mathbf{u}_i = 0 \quad (6.5)$$

$$\frac{\partial \mathbf{u}_i}{\partial t} + \nabla \cdot (\mathbf{u}_i \otimes \mathbf{u}_i) = \frac{1}{\rho_i} (-\nabla p_i + \nabla \cdot (2\mu_i \mathbf{D}_i)) + \mathbf{f}_i, \quad (6.6)$$

where $\mathbf{D}_i = [\nabla u_i + (\nabla u_i)^T]/2$ is the symmetric gradient tensor, the subscript i indicates each phase $i = b, l$, and f_i represents the acceleration due to volume forces, which in the present case are the gravity $\mathbf{f}_i = \mathbf{g}$.

In addition, the appropriate boundary conditions at the interface between the phases are to be imposed. As common for incompressible viscous flows no slip conditions are imposed at interfaces [Tryggvason 2011]. Moreover, since we do not consider any phase change, the interfacial condition for viscous fluid is simply $\mathbf{u}_b = \mathbf{u}_l$, or

$$[\mathbf{u}]_S = 0 \quad (6.7)$$

where we have used the jump notation, *i.e.* the notation $[x]_S = x_b - x_l$. When the surface tension is constant, as considered in the present work, the normal stress displays a discontinuity at the interface, whereas the shear stress is continuous. The jump at the interface is given by

$$[p] = \sigma \kappa \mathbf{n}, \quad (6.8)$$

where \mathbf{n} is the unit normal vector defined as directed outward from the bubbles, and κ is the main curvature of the interface. This set of equations are solved through the code Basilisk (<http://basilisk.fr>) with the numerical methods that have been described in section 2.5.1. We recall in the following just a few key features of the method.

6.3 Numerical method

Basilisk is an ensemble of solver-blocks written using an extension to the C programming language, called Basilisk C, useful to write discretization schemes in Cartesian grids (see <http://www.basilisk.fr/>).

Space is discretized using a Cartesian (multi-level or tree-based) grid where the variables are located at the center of each control volume (a square in 2-D, a cube in 3-D). The possibility to adapt locally the grid is key to efficiently simulate some multiphase flows [Popinet 2003]. Criteria on the velocity and on the density of each phase are used to decide the local refinement of the grid, possibly constraining it with some maximum level. In particular, in this way it is possible to have well resolved bubbles without using the same refinement far from them, where the dynamics is simpler and small scales are not present.

In our work, Navier-Stokes equations are integrated by a projection method [Chorin 1969]. Standard second-order numerical schemes for the spatial gradients are used [Popinet 2003, Popinet 2009, Lagr  e 2011]. In particular, the velocity advection term $\partial_j(u_j u_i)^{n+1/2}$ is estimated by means of the Bell-Colella-Glaz second-order unsplit upwind scheme [Popinet 2003]. In this way, the problem is reduced to the solution of a 3D Helmholtz-Poisson problem for each primitive variable and a Poisson problem for the pressure correction terms. Both the Helmholtz-Poisson and Poisson problems are solved using an efficient multilevel Poisson [Popinet 2003].

The time advancing is made through a fractional-step method using a staggered discretization in time of the velocity and the scalar fields [Popinet 2009]: one supposes the velocity field to be known at time n and the scalar fields (pressure, temperature, density) to be known at time $n - 1/2$, and one computes velocity at time $n + 1$ and scalars at time $n + 1/2$. Basilisk uses a variable time-step to ensure the following CFL condition

$$\left(\frac{u}{\Delta x} + \frac{v}{\Delta y} + \frac{w}{\Delta z} \right) \Delta t \leq \text{CFL} \quad (6.9)$$

is verified.

With regard to the interface between the fluids, it is tracked with a Volume-Of-Fluid method [Hirt 1981, Scardovelli 1999] (see section 2.5.1).

Periodic, no-slip and free-slip boundary conditions will be imposed in the different computations considered.

More details about the numerical method can be found in section 2.5.1.

6.4 Arrays of bubbles

6.4.1 Validation tests

To assess the accuracy of the numerical code for the simulation of two-phase bubbly flows, we have reproduced several literature test cases [Esmaeeli 1998, Esmaeeli 1999, Sangani 1987] which have been considered very recently with another numerical approach [Loisy 2017]. In particular we have focused on the configuration of array of rising bubbles, which, in the presence of gravity acceleration, start to rise inside a heavier fluid at rest, due to the buoyancy force. After an initial transient where bubbles accelerate, the

forces that the surrounding fluid exerts on the bubbles reach an equilibrium condition and bubbles velocity attains a steady value. Depending on bubbles size, surface tension and density, they may follow non-rectilinear paths, with periodic or chaotic lateral oscillations [Cano-Lozano 2016]. All benchmark tests consists in a regular array of bubbles, which numerically is reproduced by a single bubble in a periodic cell. Changing the cell size with respect to the bubble size, we can adjust the volume fraction of the array. It is worth remarking that since the computational domain is unbounded in all directions, an additional body force $-\langle\rho\rangle g$ must be added to avoid that the system accelerates in the vertical downward direction.

As a first validation, we reproduced the simulations of [Esmaceli 1998] of a 2-dimensional array of rising bubbles with the following non-dimensional numbers:

$$Ar = 5.6 \quad Bo = 1 \quad \rho_b/\rho_l = 0.05 \quad \mu_b/\mu_l = 0.05$$

The volume fraction is $\varphi = 0.125$. A regular grid with different level of resolutions has been tested to check the convergence of the numerical code. The details of the different grids (number of total grid points N , and number of grid points-per-bubble diameter, d_b/Δ) are reported in table 6.2. Figure 6.1 shows the rise Reynolds number $Re = (\rho_l U_b d_b)/\mu_l$ for the actual computation compared to figure 1 of [Esmaceli 1998]. The transient rise is reproduced accurately, with the rise Reynolds attaining its steady value at approximately $t = 3$. We show here also that the 64^2 grid is not fully converged as in [Esmaceli 1998], but the steady value of Re for the converged grid (the 128^2) is in excellent agreement.

N	32^2	64^2	128^2	256^2
d_b/Δ	12.5	25	50	100

Table 6.1: Grid resolutions for the 2-D array of bubbles of [Esmaceli 1998]

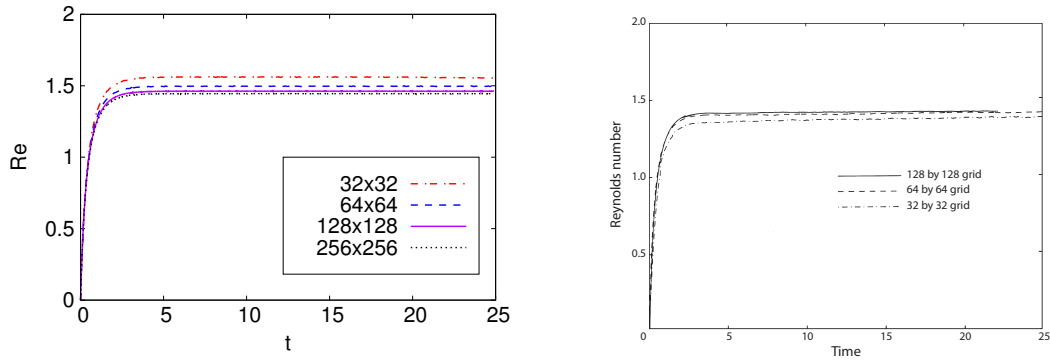


Figure 6.1: Time evolution of the Reynolds number of the rising deformable bubbles at moderate Reynolds number, for different grid resolution. Present results on the left panel, DNS by [Esmaceli 1998] on the right panel.

We have tested the numerical code also for moderate Reynolds number, reproducing the test case proposed by Esmaceli *et al.* in [Esmaceli 1999]. For this case the flow parameters are

$$Ar = 29.9 \quad Bo = 2 \quad \rho_b/\rho_l = 0.1 \quad \mu_b/\mu_l = 0.1.$$

The details of the different grids are reported in table 6.2. Results are shown in figure

N	16^3	32^3	64^3	128^3
d_b/Δ	10	20	40	80

Table 6.2: Grid resolutions for the 3-D array of bubbles of [Esmaeeli 1999]

6.2, where they are compared against both the original DNS and the more recent one [Esmaeeli 1999, Loisy 2017]. We have used a more refined grid with respect to both other DNS to test the convergence in a rigorous way. We have found, as for the 2D case, that the grid convergence is not achieved with the number of points indicated in previous works [Esmaeeli 1999, Loisy 2017], where the author indicate 30 points per diameter as sufficient. We have also compared our simulations with the theory of Sangani [Sangani 1987] for the

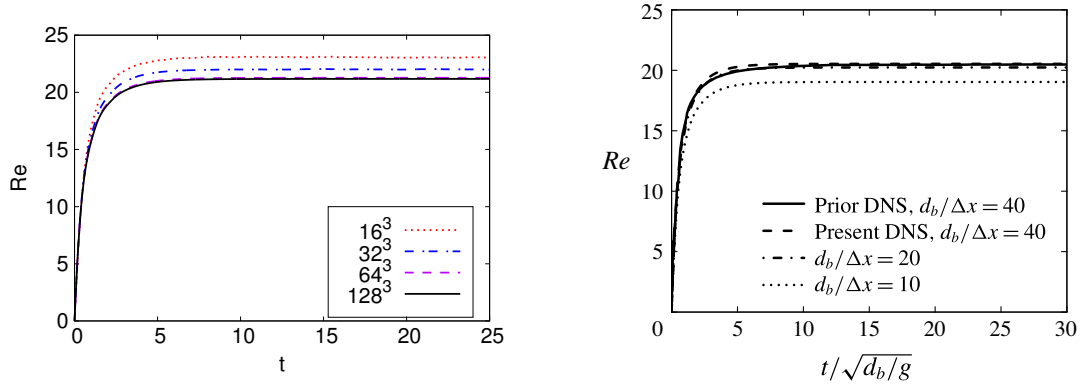


Figure 6.2: Time evolution of the rise Reynolds number for different grid resolution. Present results on the left panel, Loisy *et al.* results on the right panel. In the right panel "prior DNS" stands for Esmaeeli *et al.*, while present DNS for Loisy *et al.*

Stokes flow regime. The configuration consists in a cubic array of spherical bubbles at different volume fraction. The resolution adopted for this test case is $d_b/\Delta = 64$ and the non-dimensional numbers of the simulation are:

$$Ar = 0.15 \quad Bo = 0.38 \quad \rho_b/\rho_l = 0.1 \quad \mu_b/\mu_l = 0.1.$$

In Figure 6.3, we plot the steady state velocity of the bubble array normalized with the velocity of a single isolated bubble. The agreement between the numerical and the analytical solution $\frac{U}{U_0} = 1 - 1.1734\mu^*\phi^{1/3} + O(\phi)$, is excellent.

6.4.2 3-D oblique rise of bubbles

The last set of test cases is the oblique rise of periodic arrays of bubbles performed by [Loisy 2017], which pointed out that for certain values of the non-dimensional parameters, bubbles that in an unbounded liquid would follow a straight vertical path, can experience an oblique trajectory (not aligned with gravity) at certain volume fractions. In particular, in these regimes fluctuations enter at play and affect the bubble dynamics. Analytical considerations support the possibility of a non-trivial vertical path indicating a possible

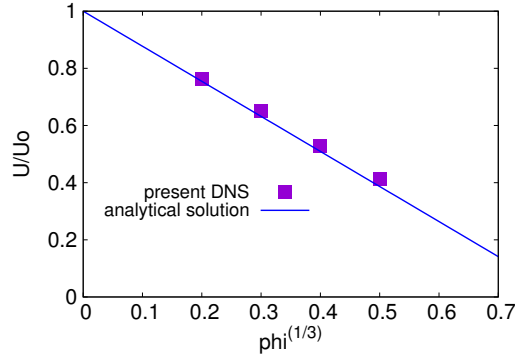


Figure 6.3: Steady state bubble velocity for an array of rising bubbles in Stokes flow conditions at different volume fraction (symbols), compared to the analytical solution of Sangani [Sangani 1987].

transition for $Ar \approx 20$. In particular three different oblique regimes have been found: (a) a steady oblique rise, (b) an oscillatory oblique rise, with a bubble motion oscillating around a straight oblique path, and (c) a chaotic oblique rise. Such a behaviour had been previously noticed numerically [Sankaranarayanan 2002], but using a diffuse interface method and a small density ratio.

In the present work we have simulated again the configurations that gave origin to the three regimes in [Loisy 2017] with a slightly increased resolution, to test if our numerical approach confirms the previous results, which were obtained with a level-set method and a diffuse interface. The parameters of the simulations are reported in table 6.3. The

Case	Ar	Bo	ϕ
<i>a</i>	29.9	2	0.008
<i>b</i>	40.7	0.38	0.13
<i>c</i>	40.7	0.38	0.038

Table 6.3: Non-dimensional parameters for the 3D-oblique test case.

density ratio and the viscosity ratio between the two phases are the same for all the cases, $\rho_b/\rho_l = 0.005$, $\mu_b/\mu_l = 0.01$. The number of points is varied with the domain size in order to get always the same resolution $d_b/\Delta = 40$ for all cases. Results are shown in figures 6.4-6.5, where for each regime we compare our results to those of previous DNS by [Loisy 2017].

The correct regime is captured in each case, while the transition may occur at a different time with respect to [Loisy 2017] since it is triggered by numerical asymmetry. The steady value of the different components of the Reynolds number is in excellent agreement for cases (a) and (b), while in case (c) where a steady regime is not reached, we can quantify the accuracy by comparing the oscillation period.

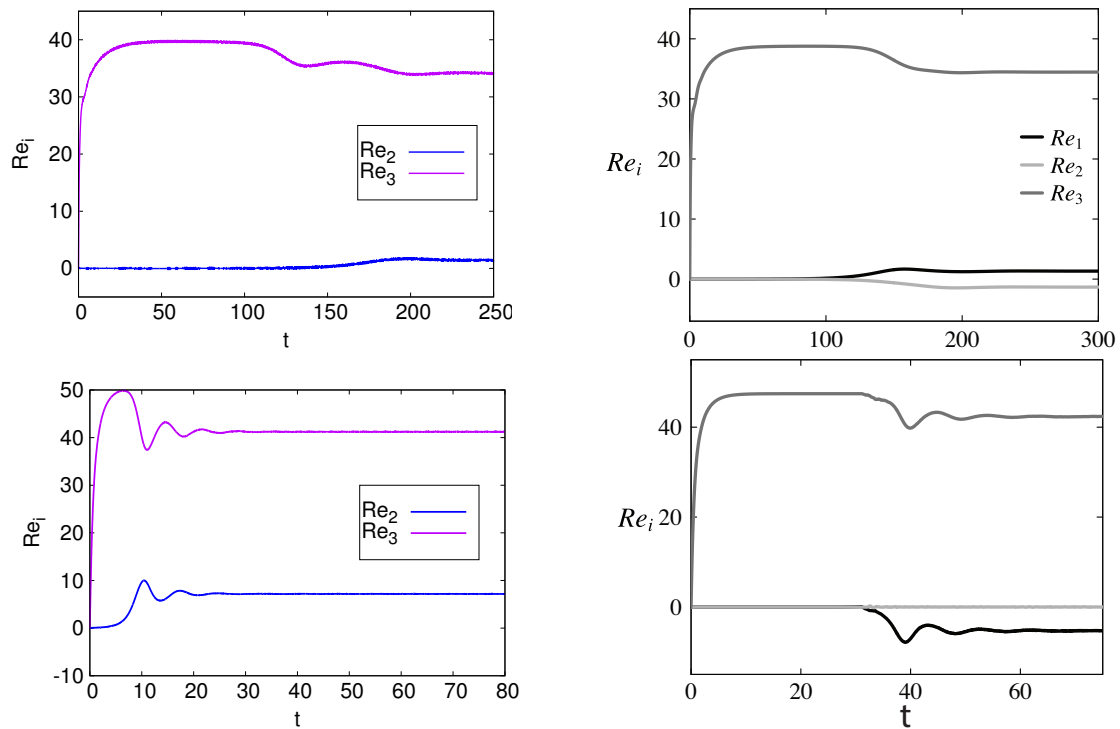


Figure 6.4: Time evolution of the three component of the rise Reynolds numbers for two different cases of steady oblique rise, regime (a). Present results on the left panel, DNS by [Loisy 2017] on the right panel.

6.5 Technical issues

In the previous section, we have analysed some cases of ordered arrays of bubbles to validate the numerical approach and compare with recent simulations carried out with a different method. In this section, we pursue the technical analysis considering some issues which are crucial from a computational point of view and may significantly alter the results of the simulations of turbulent multiphase flows. In particular, we have seen that the density ratio between the two phases is generally very high (about 1000) in realistic flows. That brings a considerable computational effort to guarantee the convergence of the method, and therefore it may be tempting to use smaller ratio in order to speed up simulations, considering the complexity of multiphase flows. In some cases, the correct physics can be correctly reproduced with a density ratio well below the realistic value [Diotallevi 2009], but that cannot be claimed in general. This is clearly a key issue for direct numerical simulations of multiphase flows.

The other issue we will analyse is the impact of the grid refinement. While convergence tests have been made for all the previous test-cases, it is yet useful to investigate this point in more complex configurations. Indeed, multiphase flows at high Reynolds number cannot be trustfully reproduced without a sufficient resolution [Cano-Lozano 2016]. This issue deserves thus particular attention.

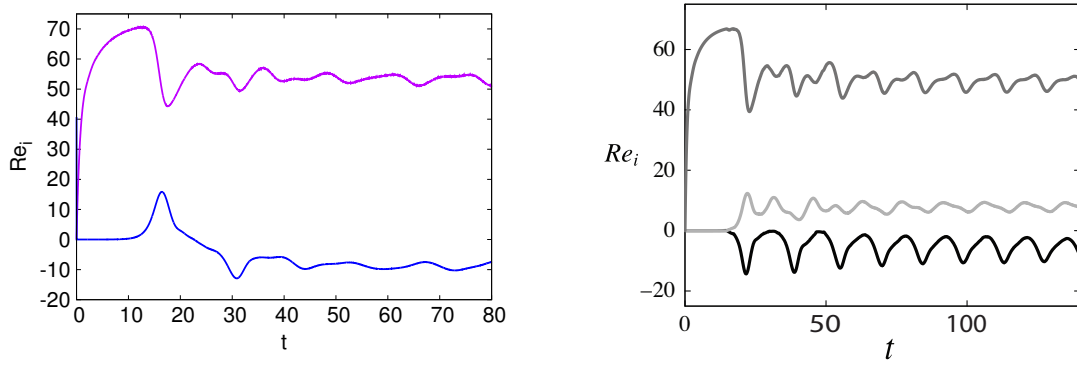


Figure 6.5: Time evolution of the three component of the rise Reynolds number for the regime (c), oscillatory oblique rise. Present results on the left panel, DNS by [Loisy 2017] on the right panel.

6.5.1 Coalescence

We study first from a qualitative point of view the coalescence of two bubbles. The study of fluid particle dynamics (coalescence and breakup) is of continuous interest because of its relevance to many industrial applications involving multiphase flow. In effect, it has been empirically shown that the dynamics of bubbly flows may be dependent from coalescence and breakage phenomena, changing the distribution of diameters and the number of bubbles. Together with breakup and mass transfer, coalescence is responsible for the evolution of drop and bubble sizes in multiphase flows. Compared to breakup, coalescence is considered more complex, since it involves not only interactions of bubbles with the surrounding liquid, but also those between bubbles themselves once they are brought together by the external flow or by body forces. This is a vast subject of research [Liao 2010] and a precise analysis of this issue is out of the scope of the present work. However, it is important to have some control on this process to avoid spurious effects and it constitutes an interesting configuration to test the influence of numerical set-up. Generally speaking, in present attempts to carry out DNS of bubbly flows there are some methods which prevent the possibility of coalescence [Tryggvason 2011, Loisy 2017]. This is convenient from a practical point of view, but it cannot be considered entirely satisfactory since in general turbulent flows in presence of buoyancy, coalescences may happen. On the contrary, VOF methods, like that used in the present work, tend to make the coalescence rate too high [Scardovelli 1999], if numerical parameters are not well controlled. In a recent work, coalescence has been observed in VOF simulations of turbulent droplet flows [Dodd 2016], but the issue of a possible spurious impact of numerics has not been considered.

Here we consider for this purpose two bubbles in a two-dimensional box of side 20 times the diameter of the bubbles with periodic boundary conditions. The physical parameters are fixed in such a way that dimensionless numbers are $Ar = 30$, $Bo = 0.1$ and $\mu_b/\mu_l = 100$. Unfortunately, due to the limited understanding of the processes underlying coalescence, it is still needed to resort to empirical correlations. To date, no satisfactory models taking into account all mechanisms and applicable to a wide range of conditions are available in literature [Jakobsen 2005]. Based on physical intuition and empirical evidence, the rate of coalescence depends on the diameters of the bubbles, their relative velocity and the

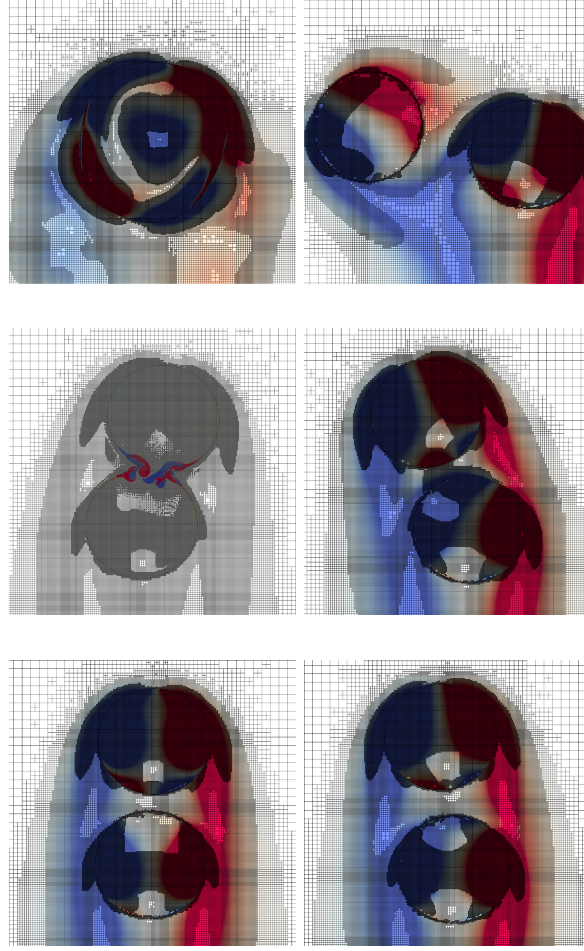


Figure 6.6: Contour plot of the vorticity at three instants of time. The grid is highlighted to show the degree of refinement and to clearly indicate the two bubbles. Right column: simulation with $\rho_l/\rho_b = 100$; Left column: simulation with $\rho_l/\rho_b = 1000$.

turbulent rate of energy dissipation, in turbulent flows. Obviously, statistically the rate of coalescence depends on the volume fraction of the bubbles. We consider two bubbles of equal diameter put initially at a distance of 1.5 diameters. The lower bubble is at 0.75 diameter from the bottom. The two bubble are initially at rest in a quiescent fluid. They start moving because of buoyancy, inducing vorticity fluctuations and creating wakes behind. From a physical point of view, those are precisely the mechanisms which bring bubbles to collide and, with a certain probability, to coalesce. With the physical parameters and initially condition chosen, the probability of coalescence is not zero but quite low, on the basis of standard empirical models [Prince 1990]. Hence we shall consider our numerical approach satisfying if coalescence is avoided in this case. In figure 6.6, we show three times of this dynamics, displaying also the vorticity field, for the first configuration studied. In this case, as highlighted in the figure, we have used a very high refinement of the grid, with a maximum refinement for the adaptive grid of 2^{13} points, which we are sure to

be at convergence. Thus, we can assess the influence of the density ratio without other possible parameters at play. In the left column of the figure we plot the results obtained considering a density ratio of $\rho_l/\rho_b = 100$, when coalescence happens. The coalescence process appears to go forward following several subprocesses, as expected by the theory: (1) the two bubbles collide, trapping a small amount of liquid between them; (2) bubbles keep in contact till the liquid film drains out to a critical thickness; (3) the film ruptures resulting in coalescence. Our simulations seem to indicate that in this particular case, dominated by buoyancy the coalescence happens following the classical drainage model [Shinnar 1960]. Indeed turbulent fluctuations and relative velocity are not sufficient to trigger a faster process. In the right column, we show the same cases obtained with a density ratio of $\rho_l/\rho_b = 1000$. In this case, the coalescence does not occur. We have investigated different density ratio in the range $\rho_l/\rho_b \in [10, 1000]$ (not shown here for the sake of clarity), and it turns out that the threshold for coalescence is about $\rho_l/\rho_b = 500$. Our results therefore point out that to can reproduce multiphase flows, a realistic density ratio is mandatory, while it possibly may be slightly less than the actual one.

Once analysed the impact of the density ratio, we focused on the grid. We have carried out the simulation of the same test-case taking the density ratio $\rho_l/\rho_b = 1000$, with different grids, coarser than the previous one that had a maximum refinement of $N_{Max} = 2^{13}$ points. We have found that convergence is attained with $N_{Max} = 2^{12}$, when the results are the same of those obtained with $N_{Max} = 2^{13}$, and shown in figure 6.6. Yet, as shown in figure 6.7, in the simulation with $N_{Max} = 2^{11}$ the coalescence occurs even with the correct density ratio. Furthermore, we can see from the figure 6.7 that both the mechanisms and the typical time-scales of the process leading to the coalescence are the same as those displayed in the left column of figure 6.6. In particular, the vorticity field at the end of the process appears to be almost identical. That means that, concerning the coalescence rate, a too coarse grid will act in a similar way to a density ratio too low. It is important to underline here that the strong impact of the grid is related to the high Ar number used in the simulations.

In some cases, it can be nevertheless relevant to avoid *a priori* coalescence, although the theoretical rate may be slightly more than zero. This can be the case, when one would like to focus on the the study of some theoretical mechanisms, through experiments, without considering a particular realistic configurations. For such cases, an algorithm has been implemented in Basilisk to completely forbid the coalescence.

6.5.2 Grid refinement effect

We have then studied in a more quantitative way the impact of the grid used.

To do that, we have replicated the results obtained by [Cano-Lozano 2016] to study the behaviour of a single bubble rising “in a large tank” i.e. far from any boundaries. We have used only the same physical parameters that we would like to use for the realistic bubble column. Namely, we fix $Ar = 185$ and $Bo = 0.28$. The acceleration of gravity is set to unity, which gives a characteristic rise velocity also of order unity, which gives a maximum time for the simulation comparable to the domain size. In this regime, it turns out that bubble trajectories are between the rectilinear and the chaotic, as found in the original paper [Cano-Lozano 2016].

As shown in figure 6.9, we have simulated the bubble rise with three different grids.

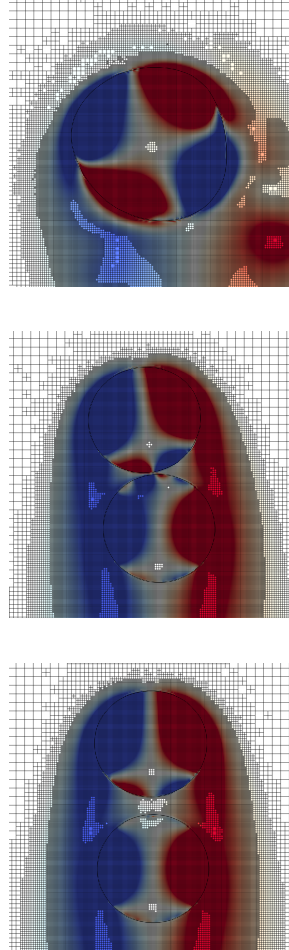


Figure 6.7: Contour plot of the vorticity at three instants of time. The grid is highlighted to show the degree of refinement and to clearly indicate the two bubbles. It is possible to see that even with the present grid which is well refined ($N_{Max} = 2^{11}$) some details of the wake and of the film surrounding the bubbles are lost with respect to the more refined simulations displayed in Fig. 6.6 right column.

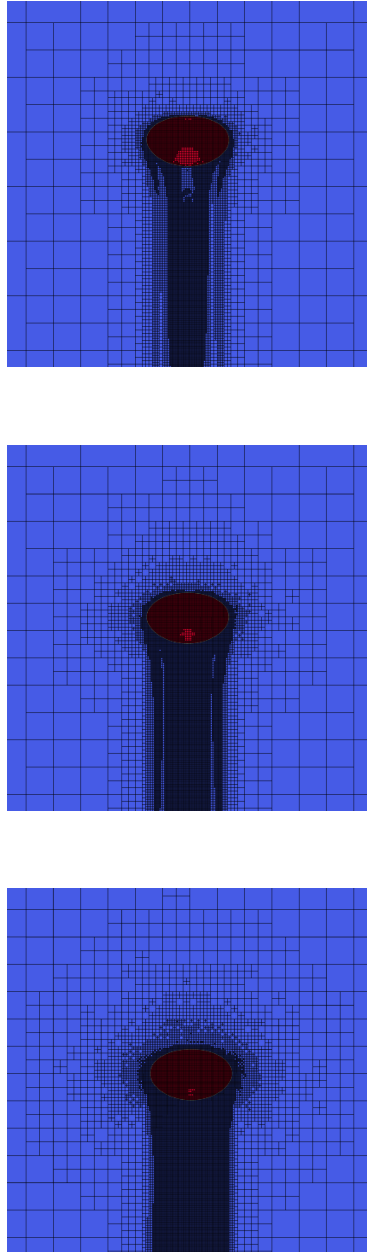


Figure 6.8: Mesh adaptation around a rising bubble with three different error threshold on the velocity: top panel $err = 0.01$, mid panel $err = 0.003$, bottom panel $err = 0.001$.

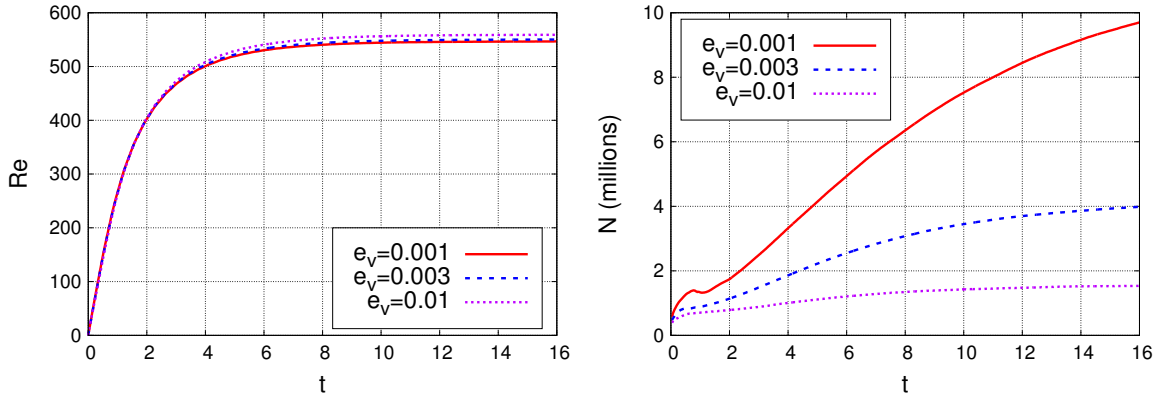


Figure 6.9: On the left panel time evolution of the bubble rising Reynolds number for the three simulations with different threshold for the grid refinement. On the right panel time evolution of the total number of cells in the domain for the same simulations.

The total maximum points allowed is always the same, $N_{Max} = 2^{12}$ such that the maximum refinement is of 82 points per diameter. However, we have performed three different simulations at varying the threshold of the error in velocity, namely fixed at $err_v = 0.001; 0.003; 0.01$, in absolute value. From figure 6.9, it is possible to see that in the coarse grid, the neighbourhoods of the wake region and the bubble are discretized with few points and most of the flow is described with very few points. On the other hand, in the grid more refined, a large portion of the flow around the bubble, including the whole wake, appears to be described with the maximum number of points allowed, indicating that with that error threshold no difference is made in this region. This inability to discriminate the presence of gradients over large scales suggest a possible over-refinement. The issue has been investigated more quantitatively looking at the dynamics of the three configurations. In Fig. 6.9a, we show the evolution of the rise velocity of the bubble, which is given by the Reynolds number in dimensionless form. It is possible to appreciate that there is no difference in practice between the results obtained with the two more refined grids (the difference is less than 1%), whereas there is a discrepancy in the final rise-velocity between these two simulations and the coarse-grid one, the error is of the order of 5%. That indicates that the three grids are sufficient to get a qualitative reproduction of the physics of the problem but that only the two more refined are at convergence. In figure 6.9b, we display the impact of the grid choice in a computational sense. Of course, the coarse grid demands much less points, yet what is interesting is the trend. From figure 6.9a, we can see that a transient is present of about $8 \div 10$ unit times. We should expect therefore that approximately after that period of time, a stabilisation in the number of grid points would be reached too. That is precisely what is observed for the intermediate grid. The coarse one, attains a *plateau* too early, and on the contrary the fine grid continues to increase the number of points monotonically. That seems to indicate again an over-refinement of the bubble, which results in an useless increasing of the number of points and thus of computational time. It is worth emphasising that there is a strong link between physical properties and numerical issues. Furthermore, it is important to stress how important is

not to overlook this kind of issue. While the simulation of a single bubble remains feasible even with the over-refined grid thanks to the adaptive mesh, it would not be possible to tackle a problem with many bubbles with the same grid. Moreover, without adaptive mesh even the single bubble case appears desperate at this large Reynolds numbers. In opposition, to use a too coarse grid may make the computation easy but it makes the simulations largely unreliable.

In the following simulations, we shall use the intermediate grid requirements, if not explicitly indicated.

6.6 Bubble column configuration

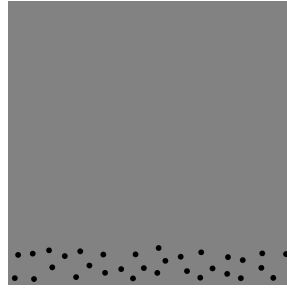


Figure 6.10: Bubble positions within the domain at $t = 0$ for simulation (a).

In this section we show the results of the 2-dimensional bubble column configuration. Namely, it consists in a square domain with the vertical direction z aligned with gravity, which acts downward. As in previous simulations we have used a non-dimensional description, therefore the dimensions are given in multiples of the bubble diameter. The tank, of size $50d \times 50d$, is filled with a liquid and 32 initially spherical bubbles are placed at the bottom, in a region confined between $z = 0$ and $z = 8d$, and are homogeneously distributed in the lateral direction y , avoiding initial bubbles overlapping, with a minimum distance between them of 1 diameter. This results in a local volume fraction in the region $0 \leq z \leq 8$ of $\alpha \simeq 7\%$. The domain is closed at the bottom by the presence of a wall (no-slip boundary condition), and an outflow boundary condition is used at the top, while on the lateral sides the domain is periodic. At $t = 0$ both the liquid and the bubbles are at rest conditions. A picture of the initial condition is shown in figure 6.10

Case	Ar	Bo	N	d_b/Δ
a	100	0.12	4096	82
b	140	0.20	8192	164
c	313	0.56	16384	328

Table 6.4: Non-dimensional parameters for the 2-dimensional bubble column. N represents the grid resolution.

The flow parameters are given with the non-dimensional groups defined in the previous sections. The viscosity and density ratios are constant in all the simulations and their

values are $\mu_l/\mu_b = 100$ and $\rho_l/\rho_b = 1000$. The other two groups are fixed by keeping constants the values of the surface tension and gravity and by varying the bubble diameter to have a more physical scaling. Specifically, the physical parameters are very close to those of air and water, having been fixed to $\sigma = 0.05 \text{ N/m}$ and $\mu_l = 7 \times 10^{-4} \text{ Pa}$. Varying the bubble diameter from $d = 0.8 \text{ mm}$ to $d = 1.7 \text{ mm}$ results in Ar numbers ranging from $Ar \simeq 100 - 300$. Three different simulations with bubbles of different diameters have been carried out, and the corresponding parameters are reported in table 6.4. In all the three cases we have used regularly spaced grids with different resolutions accordingly to the increasing bubble Reynolds number. A regular grid has been preferred to the adaptive one since in 2 dimensions the gain with adaptivity is not evident, and because a regular spacing facilitates in the evaluation of statistics, providing a constant resolution in the whole domain. In any case, the resolution requirements to get physical-sound results have been always fulfilled, as highlighted in the table 6.4.

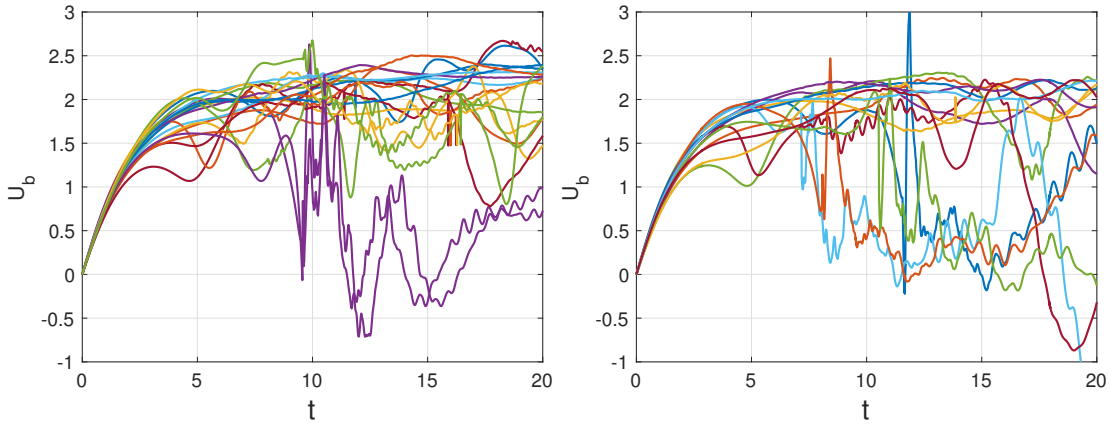


Figure 6.11: Velocities of the bubbles with respect to time. On left panel case (a), on right panel case (b).

We have started by analyzing the energy spectra of the velocity field. Since the problem is non-homogeneous and non-stationary, particular care must be taken in the definition of the interrogation window. In the experiment of [Riboux 2010], spectra are evaluated after the passage of the bubble swarm in a centered square box. In the present work we have preferred to investigate also the region where bubbles are still present, because we have observed that waiting the passage of all the bubbles may result in wakes in the decaying regime, where most of the information is lost. This is due mainly to the fact that 2D interactions are stronger and have longer range with respect to 3D, resulting in a more disturbed path of the bubbles in the wakes which can deviate significantly from the vertical motion with non-trivial downward motion at some instants. Indeed, as shown in figure 6.11, we have observed that after a short time from the beginning, the swarm spreads and is stretched in the vertical direction, and a few bubbles remain trapped in the wake region with a significantly lower vertical velocity. Moreover, coalescences are present and contribute to retarding some bubbles rise. The velocities of the bubbles for case (a) and (b), see Figure 6.11, confirms that after an initial transient, a few bubbles are involved by high levels of fluctuations with respect to the mean velocity of the front.

The spectra $S_{ii} = \langle |\hat{u}_i|^2 \rangle$, where \hat{u}_i is the Fourier transform of the velocity fluctuation in the i direction, are evaluated separately for the vertical and the horizontal components. The transform is performed in the y direction, which can reasonably be considered as homogeneous, for both the components of the velocity and is then averaged in the z direction over windows of length $5d$, which has been found to be homogeneous. In all the figures the energy is made non-dimensional with the corresponding standard deviation and on the x axis we show the reciprocal of the wavelength (λ^{-1}), which is still in non-dimensional units, yielding that $\lambda = 1$ corresponds to the bubble diameter.

In Figure 6.12 we show the spectra of the vertical velocity fluctuations for case (a) evaluated at different times, and on two different averaging windows, namely $15d \leq z \leq 20d$ and $20d \leq z \leq 25d$. It is worth remembering that time is made non-dimensional with $\sqrt{d_b/g}$. It can be seen that the spectra slope appears rather constant, without relevant changes at some characteristic scale of the flow. A slope slightly steeper than -3 is identified and it appears robust with no significance time-dependence during the passage of bubbles. It can also be seen that after all bubbles have gone out from the interrogation window, the spectrum starts to decay rapidly.

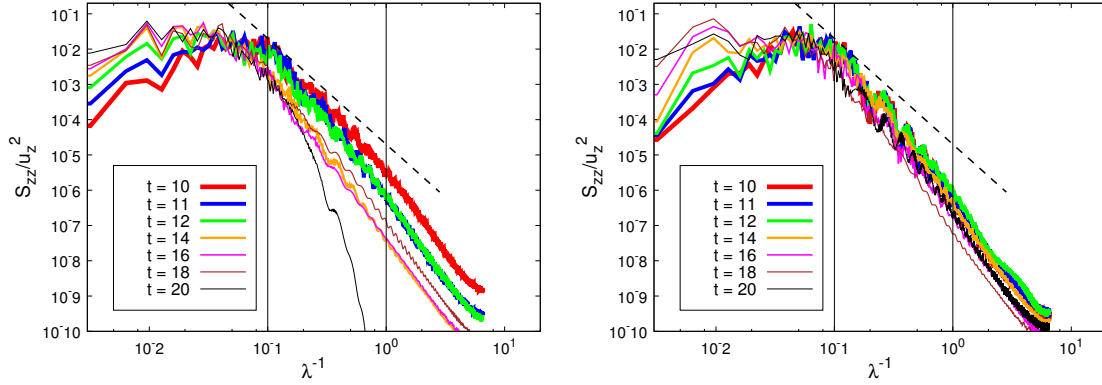


Figure 6.12: Spectra of the vertical component of the velocity for bubbles with $Ar = 100$ and $Bo = 0.1$ evaluated at different times. On the left panel the interrogation window is between 15 and 20 bubble diameters (in the vertical direction), while on the right panel is between 20 and 25. The dashed line represents the -3 slope.

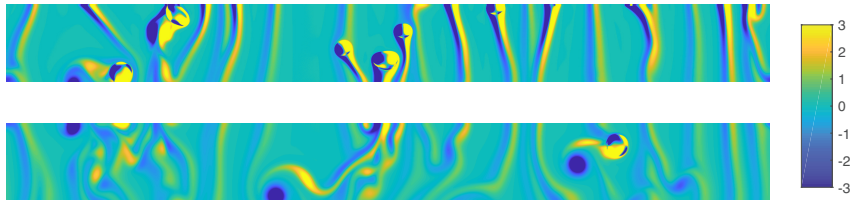


Figure 6.13: Vorticity field for bubbles with $Ar = 100$ and $Bo = 0.1$ evaluated at $t = 14$. On the top panel we show the domain between 20 and 25 bubble diameters in the vertical direction, on the bottom panel between 15 and 20.

In Figure 6.13 we show the vorticity field in the two portions of domain that have

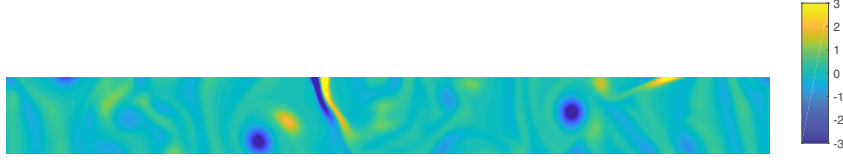


Figure 6.14: Vorticity field for bubbles with $Ar = 100$ and $Bo = 0.1$ evaluated at $t = 20$. The window is between 15 and 20 bubble diameters in the vertical direction.

been used for the evaluation of the spectra at a fixed time $t = 14$. This vorticity field shows that the spectra scaling-law that has been found has little relation to the structures of the wakes, since in the upper window no significant interaction between the wakes is present, albeit the resulting spectra are very close to those obtained in the lower window. That suggests that spectra are dominated by the coherent structures originated around the bubbles of the scale of the diameter. Smaller scales dynamics appears to be largely dominated.

Figure 6.14 shows the vorticity field at $t = 20$ in the decaying regime. In this case, the flow appears to be laminar with only some fluctuations at the largest scale.

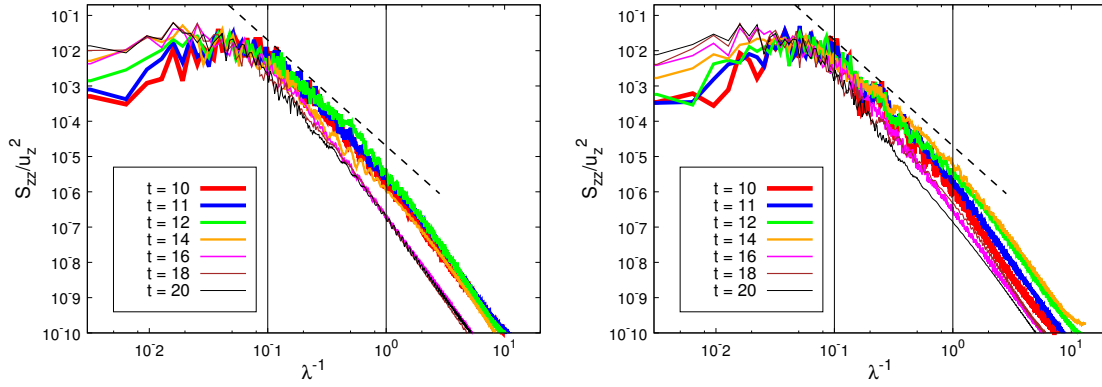


Figure 6.15: Spectra of the vertical component of the velocity for bubbles with $Ar = 140$ and $Bo = 0.2$ evaluated at different times. On the left panel the interrogation window is between 15 and 20 bubble diameters (in the vertical direction), while on the right panel is between 20 and 25. The dashed line represents the -3 slope.

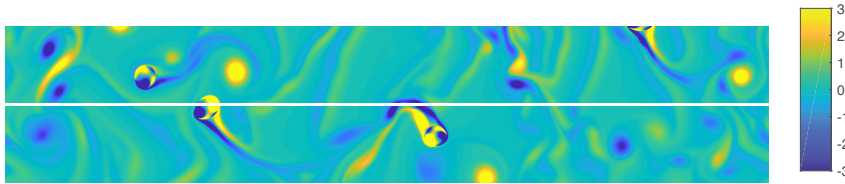


Figure 6.16: Vorticity field for bubbles with $Ar = 140$ and $Bo = 0.2$ evaluated at $t = 20$. On the top panel we show the domain between 20 and 25 bubble diameters in the vertical direction, on the bottom panel between 15 and 20.

In Figure 6.15 we show the spectra relatives to case (b). We can see a similar scaling to

case (a), but here the slope in the part at low wave numbers, i.e. for wave lengths bigger than the bubble diameter, seems closer to -3 while a slight change happen at smaller scales. Figure 6.16 shows the vorticity field for this case at $t = 20$, suggesting a stronger interaction between bubble wakes for this case.

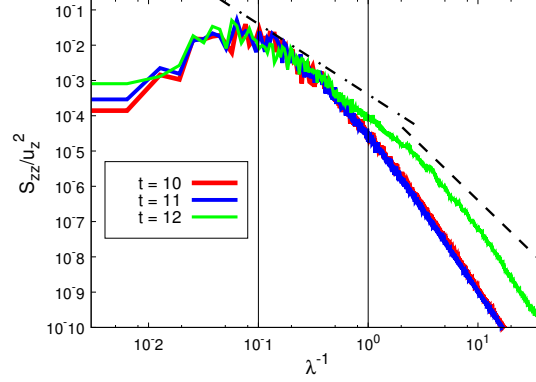


Figure 6.17: Spectra of the vertical component of the velocity for bubbles with $Ar = 313$ and $Bo = 0.56$ evaluated at different times. The interrogation window is between 15 and 20 bubble diameters (in the vertical direction). The dashed line represents the -3 slope, the dashed-dotted line the -2 slope.

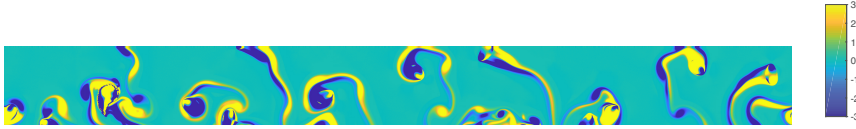


Figure 6.18: Vorticity field for bubbles with $Ar = 313$ and $Bo = 0.33$ evaluated at $t = 12$. The window is between 15 and 20 bubble diameters in the vertical direction.

Figure 6.17 shows energy spectra for case (c) at $Ar = 313$. For this case only times up to $t = 12$ are available at the moment. However, it is interesting to see how the scaling is substantially different with respect to the previous cases at least at $t = 12$. Indeed, a first part at large scales appears more flat with a slope close to -2 , while in the part at smaller scales we can see again the -3 scaling. However we think that the underlying physical mechanism at the origin of this behaviour might be rather different. While, in cases (a) and (b) the spectrum is strongly dominated by the coherent structures of the wakes, here, because of the much higher Reynolds number, some turbulent mechanism is expected to play a more important role, even if the number of bubbles is limited. The behaviour of the spectrum at the largest scales for this case could be related to the 2-d inverse cascade. Notably, bubbly dynamics leads to an injection of energy at the scale of the bubble diameter, energy is then transferred at larger scales by the inverse cascade of energy, and a corresponding $-5/3$ scaling of the spectrum is displayed. The second part of the spectrum, which reveals a -3 scaling, should be linked to a direct cascade of enstrophy present at small scales. We are pursuing this analysis, analysing the simulations available, building further data at longer times and carrying out new simulations at different volume fraction. In order to emphasize the more complex structure of the flow at high Ar number,

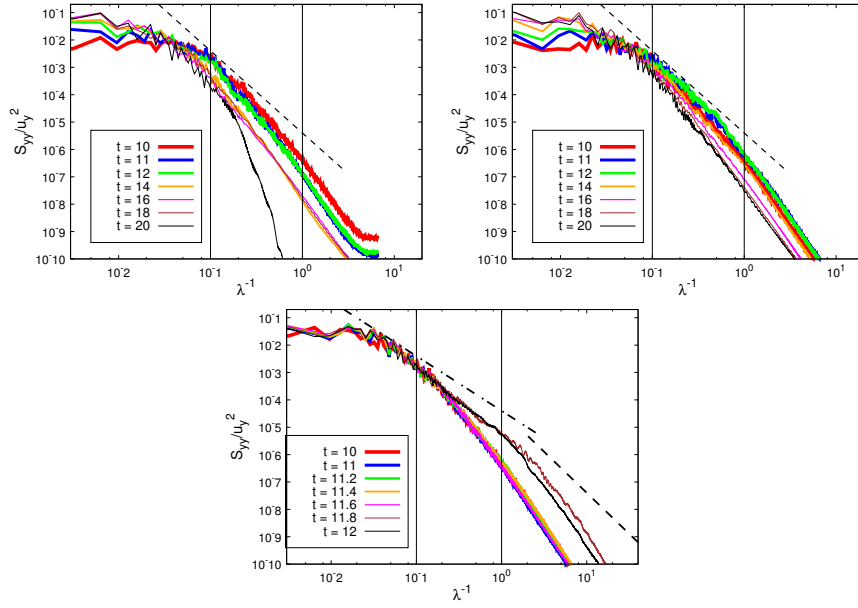


Figure 6.19: Spectra of the horizontal component of the velocity. Top left panel case (a), top right panel case (c), bottom panel case (c). The window is between 15 and 20 bubble diameters in the vertical direction. The dashed line represents the -3 slope.

the Figure 6.18 shows the vorticity field at $t = 12$. The strong interaction between wakes and the presence of dynamics at small scales is visible.

For the sake of completeness in Figure 6.19 we show the spectra of the horizontal velocity component for the three cases evaluated in the window $15 \leq z \leq 20$. It can be seen that they are qualitatively similar to those of the vertical component of the velocity.

To further investigate the spectra scalings we have used a recent method [Chen 2006, Xiao 2009] that has proved powerful, based on the filter approach, which is adopted in large-eddy simulations. We have applied this methodology to the velocity field, obtaining informations about the energy flux. The interesting advantage with respect to a spectral approach is that one can gain details also on the locality of the cascade, differentiating regions with positive or negative fluxes. We have applied a Gaussian filter to the velocity field in the same spatial windows considered above at different times. The filter is defined as:

$$G_l(\mathbf{r}) = \frac{1}{l} G\left(\frac{\mathbf{r}}{l}\right) \quad \text{with} \quad G(\mathbf{r}) = \sqrt{\frac{6}{\pi}} \exp(-6\mathbf{r}^2), \quad (6.10)$$

where l is the filter width. The application of the latter to the velocity field, yields the filtered velocity field:

$$\bar{\mathbf{u}}_l(\mathbf{x}) = \int G_l(\mathbf{r}) \mathbf{u}(\mathbf{x} + \mathbf{r}) d\mathbf{r}. \quad (6.11)$$

Numerically, the filtering is performed in spectral Fourier space, multiplying the quantity to be filtered by the Fourier transform of the filter

$$\hat{G}_l(\mathbf{k}) = \exp(-k^2 l^2 / 24), \quad (6.12)$$

and then transforming back into the physical space. The so obtained filtered field contains only the contribution from eddies larger than l and its transport equation can be obtained

applying the filter to the Navier-Stokes equations. Analogously, the equation for the large-scale kinetic energy, $\bar{e}_l = 1/2|\bar{\mathbf{u}}_l|^2$, can be obtained:

$$\frac{\partial \bar{e}_l}{\partial t} + \nabla \cdot \bar{\mathbf{q}}_l = -\Pi_l - D, \quad (6.13)$$

where $\bar{\mathbf{q}}_l$ is the transport term, D is the large scale dissipation, and

$$\Pi_l = -\bar{\mathbf{S}}_l : \boldsymbol{\tau} \quad (6.14)$$

is the local energy flux. $\bar{\mathbf{S}}_l$ and $\boldsymbol{\tau}$, are the filtered strain tensor and the subgrid scale tensor, defined as:

$$\bar{\mathbf{S}}_l = \frac{1}{2} \left(\frac{\partial \bar{u}_{l,i}}{\partial x_j} + \frac{\partial \bar{u}_{l,j}}{\partial x_i} \right), \quad \boldsymbol{\tau} = \bar{\mathbf{u}}\bar{\mathbf{u}}_l - \bar{\mathbf{u}}_l\bar{\mathbf{u}}_l. \quad (6.15)$$

The term Π_l identify the presence of a local direct (positive) or inverse (negative) energy cascade according to its sign. In Figure 6.20 we show the spatial distribution of Π_l (with $l = 0.5, 0.1d_b$) for the case with $Ar = 313$ at $t = 12$. It can be noted how the regions of higher energy transfer are in the neighbourhood of the bubbles and how positive and negative areas are present over the whole domain. In particular smaller scales transfer is effective only in the vicinity of bubbles.

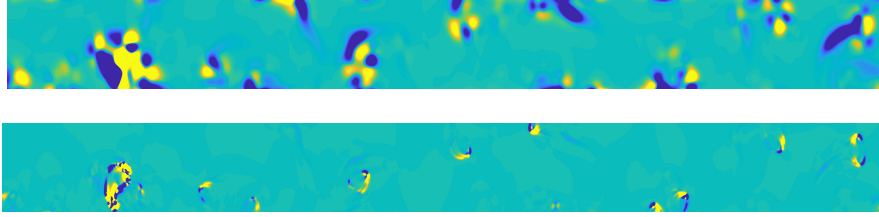


Figure 6.20: Local energy flux at $t = 12$ for case c at $Ar = 313$. In the upper panel the filter length is $l = 0.5d_b$, in the lower panel $l = 0.1d_b$. The color scale is the same in both panels.

If a spatial average is done at each different value of the filter width, one can find the average transfer of energy at each scale. Results are reported in Figure 6.21 for the three different simulations. They show that for the higher Ar number case the energy flux is negative at all scales, while in the other two cases it is mostly positive, giving a plausible explanation to the different spectra scaling found in case c . It is worth remarking that since the problem is non-stationary, this statistic can depend on time, affecting both the shape and sign of the mean fluxes. This analysis, however, has pointed out the presence of a transfer of energy, which exhibits a maximum around the bubble diameter, and the presence of instantaneous local positive and negative energy fluxes over the whole domain.

Finally we have looked at the probability density functions of the velocity fluctuations. Figures 6.22-6.23 show the PDFs of the two velocity components at various times. The first remark is that a time-dependent dynamics is clearly noticeable. Even from the qualitative point of view, the pdf display huge variations in the tails with respect to the time and to the window chosen, that is with respect to the particular region where they are calculated. Flow is clearly statistically unsteady and non-homogeneous in the vertical direction. Furthermore, fluctuations in the vertical direction are not isotropic, as it can be seen from

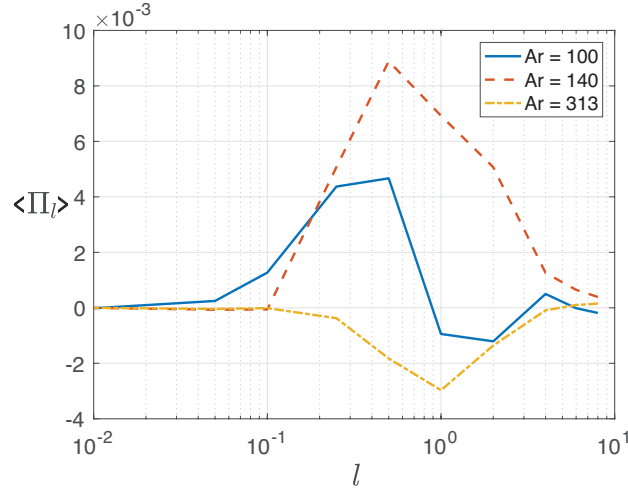


Figure 6.21: Mean energy flux with different filter length for the three simulations at $t = 10, 12, 12$ respectively. The spatial window is the same as in the computations of spectra.

the strongly asymmetric PDFs on left column. This is due to the fact that upward fluctuations are more probable because of the entrainment of the fluid in bubble wakes. The fluctuations of the horizontal component instead are more isotropic, resulting in symmetric PDFs, since bubble wakes are axisymmetric and the distribution of bubbles is uniform in the horizontal direction. These numerical results seem therefore in agreement with the results obtained in experiments. It is worth noting that fluctuations tend to a more symmetric gaussian behaviour in the decaying regime, where bubbles are absent since some time. The statistics of the velocity are thus consistent with the previous analysis based on spectra and vorticity field.

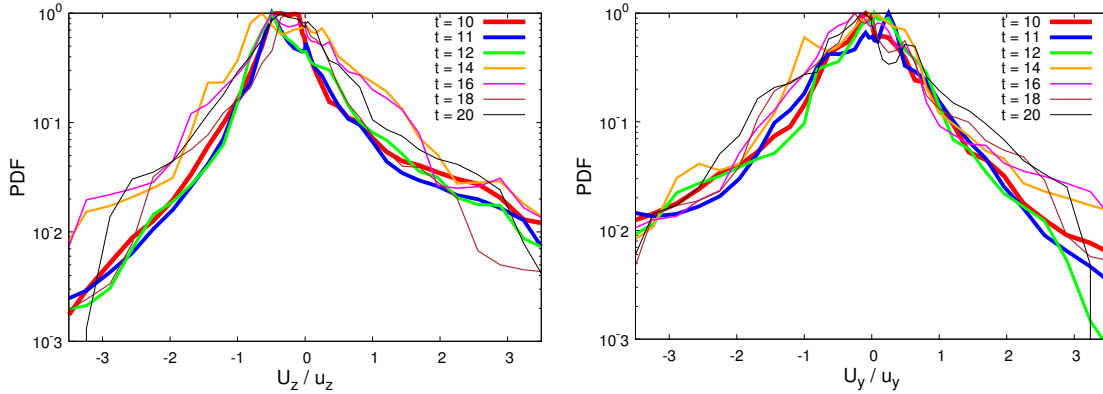


Figure 6.22: PDF of the velocity fluctuations in the vertical zz (left panel) and lateral yy (right panel) directions. Bubbles with $Ar = 100$ and $Bo = 0.1$.

As already said in the introduction, the 3-d simulation with 256 bubbles at $Ar = 180$ is running, and a complete analysis is not yet possible, being the bubbles still in a transient

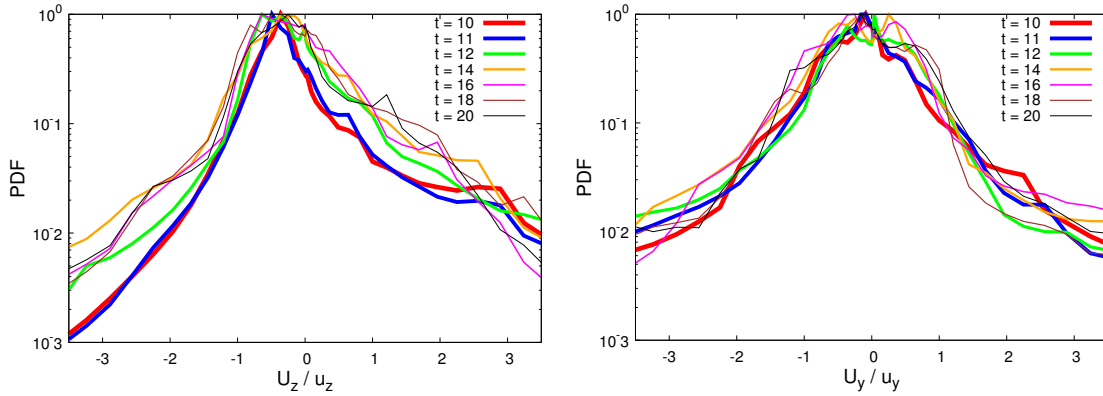


Figure 6.23: PDF of the velocity fluctuations in the vertical zz (left panel) and lateral yy (right panel) directions. Bubbles with $Ar = 140$ and $Bo = 0.2$.

phase. A snapshot at $t = 6$ of the bubbles and of the vorticity field generated by the wakes is shown in Figure 6.24.

6.7 Conclusions

In this part of the thesis we have investigated several buoyancy driven bubbly flows. A comparison with literature studies in the case of periodic arrays of rising bubbles has been done, to assess the accuracy and the performance of the numerical code that has been used. Overall we have found a very good agreement with both 2-d and 3-d literature results, where simulations were performed with different interface advection methods. Moreover, we have then studied the oblique rise of buoyant bubbles in periodic arrays, confirming the recent results of [Loisy 2017], where an oblique path of the bubble set on at certain values of the volume fraction.

Before starting simulations with many bubbles, we have studied some technical issues related to the numerics. First we have evaluated the possibility of having coalescences in 2-d simulations with two raising bubbles at an initial distance of $1.5d$. We have found that the density ratio of the two fluids plays an important role and that to avoid excessive numerical coalescences it is necessary to have realistic densities. Moreover, we have also demonstrated that the grid refinement can help, too. Indeed, in principle with an adaptive refinement of the gap between the bubbles up to high levels, it would be possible to resolve the film, recovering the correct levels of pressure that would repel the bubbles. Then we have studied more in the detail the criteria for the grid refinement, studying the 3-d rise of a single bubble to fix the parameters for the 3-d simulation with more bubbles.

Afterwards, we have performed computations of a two-dimensional bubble column at moderate and high Reynolds numbers and with a volume fraction of about 10% in the bubble layer. In this configuration, we have analyzed the velocity fluctuations in both phases finding different behaviour at different Reynolds number, even if the -3 slope of the spectra seems to be a key feature of this type of flow also in 2-d. As expected PDFs shows the strong anisotropy of the flow fluctuations in the vertical direction, while

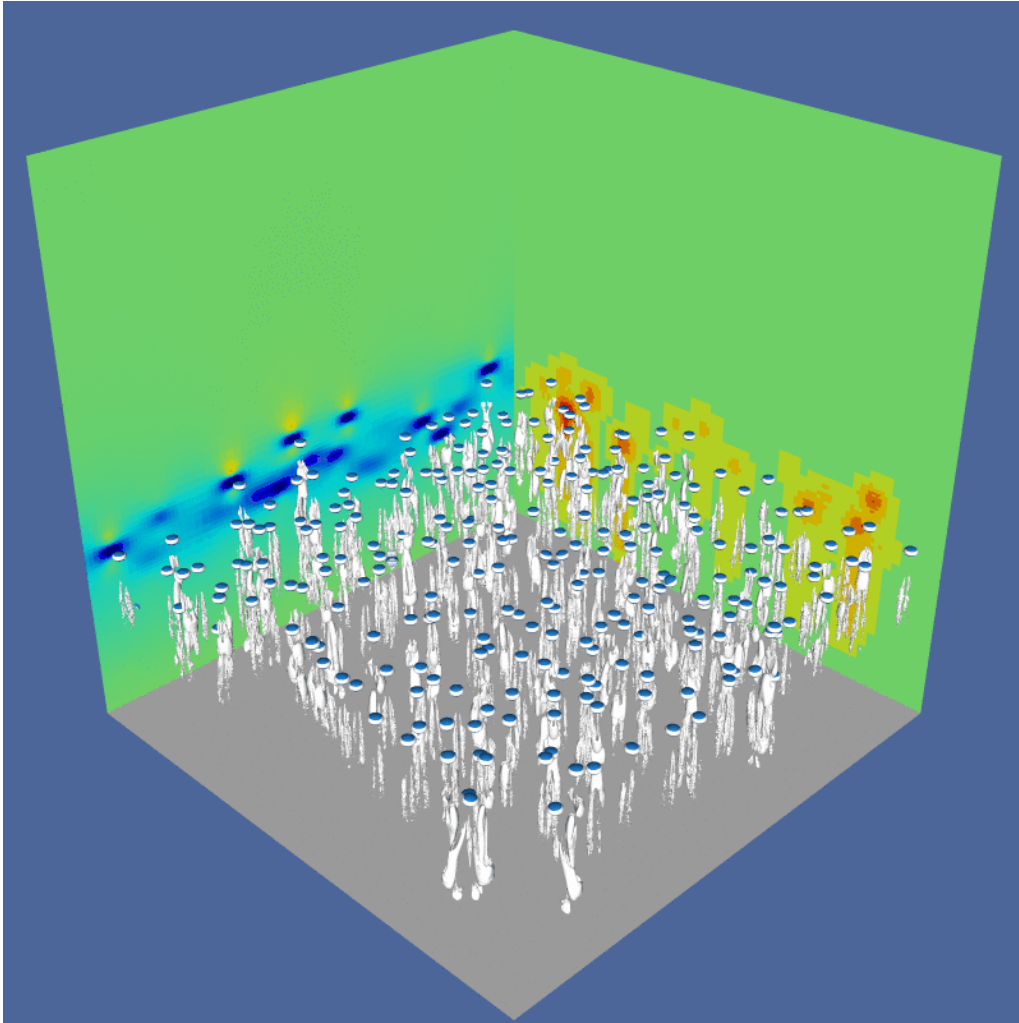


Figure 6.24: Snapshot of the 3D simulation at $t = 6$ after the release. The VOF field is showed with blue iso-surfaces and the λ_2 vorticity field is shown with grey contours. On the right wall is shown the level of mesh adaptation, while on the left panel the vertical velocity of the field.

horizontal fluctuations are symmetric. A scale-by-scale analysis of energy transfer has also shown the presence of energy fluxes at scales within two decades of the bubble diameter. We are pursuing this analysis to give a further comprehension of the scalings that have been found.

Another future development of the work would be to present and analyse the budgets of the momentum and energy equation in relation to the development of two-fluid models, that is Reynolds averaged Navier-Stokes (RANS). Indeed, the two-fluid model [Drew 1983, Drew 2006] probably represents the most widely adopted approach to describe the spatial and temporal evolution of gas-liquid flows in systems of practical relevance, due to its moderate computational cost. Unfortunately, it is known since longtime that the numerical stability of the solution obtained from the two-fluid model depends on the characteristics of the underlying equations that may be complex

[Stuhmiller 1977, Ramshaw 1978]. In such a case, the equations are not hyperbolic and the discretized equations do not allow a grid-converged solution to be achieved, and unstable modes in the solution appear, severely affecting the model prediction and its sensitivity to grid refinement. To ensure the hyperbolicity of the system and therefore stability, an ad-hoc pressure term is usually introduced by hand [Prosperetti 1987]. The shape of the term is yet controversial [Tiselj 1997] and its properties has been extensively studied [Davidson 1990, Song 2001]. While the functional dependence on the volume fraction seems to be clearly established [Panicker 2018], the multiplicative factors are unknown and may be found only from DNS or experiments. Therefore, the present DNS results could be used to analyse the momentum balance budget, and notably one should evaluate all the forces acting on the bubble in order to disentangle the contribution due to this interfacial term. Since this term is actually proportional to the gradient of the volume fraction $\nabla\alpha$, it is evident that this term is crucial when a jump in volume fraction is present, and this is precisely the case in a bubble column.

Conclusions

In this work we have presented a broad study on gravity driven dispersed multiphase flows, dealing with two different categories of problems, namely inertial solid particles in a gas, and gaseous bubbles in a liquid. We have put particular emphasis on the mechanisms of interaction between the carrier and the dispersed phase and in particular on the possibility to have large fluctuations in the carrier phase induced by the non-stationary motion of the dispersed one, leading to the generation of turbulence or pseudo-turbulence. The two class of problems that we have handled share similar features, but imply descriptions at different scales, from micrometer particles to millimeter bubbles, and therefore distinct methodologies have been required to cope with them.

In part II we have dealt with the problem of particle-laden turbulent flows in the dilute and in the dense regime, proposing, validating and testing two different models for the two regimes. For the dilute regime we have proposed a Lagrangian stochastic model based on the filtered-density-function to track point-particles in a Large-Eddy-Simulation flow field. The proposed model has been tested in a turbulent channel flow; in particular its capabilities in correctly capturing the phenomenon of particle preferential concentration have been investigated. We have shown that by reintroducing the correct amount of fluctuations that are lost because of the filtering in LES, the model prediction of the particle concentration near the wall is good if compared to Eulerian-Lagrangian DNS and a significant improvement of accuracy with respect to the case without particle sub-grid scale model is obtained. This is confirmed by an excellent estimation of the particle velocity statistics which are correlated with the fluxes of particles towards and away from the wall. Summarizing, our work indicates that a Lagrangian modelling approach for particle-laden flows is physically-sound and can be useful in those cases where Eulerian fluid models are too coarse to accurately track point-particles.

We have then investigated the dense regime at moderate particle concentration, proposing a Lagrangian stochastic model that considers two-way coupling and inter-particle collisions. The model has been derived on a rigorous formalism that shows that it is fully consistent with a Eulerian hydrodynamic description, where particle-phase mesoscale dynamics is derived from the kinetic equation. We adopted a decomposition of the particle velocity into a correlated part, related to cluster dynamics, and into a uncorrelated part, related to crossing trajectories and collisions. This made possible to identify the different relevant time scales. We were particularly interested in cluster-induced turbulence, and we have found that the particle model, coupled with a RANS model for the fluid, is able to capture the triggering of turbulence in a homogeneous flow, and to accurately predict the turbulent kinetic energy in both phases, as well as the anisotropy of the flow, if compared to Eulerian-Lagrangian two-way coupled DNS [Capecelatro 2015]. A compact, less complex, version of the model has also been proposed and tested to show that two-way coupling is sufficient to generate turbulence, but not to have a quantitative description of the energy production. In order to capture entirely the phenomenon, one should rely on the velocity decomposition.

The particle model for the dense regime, that was derived in a general form, has then been tested also in a non-homogeneous application, i.e. a turbulent channel flow. For this more complex case we have first derived a Lagrangian numerical scheme for stochastic equations in non-homogeneous problems, and in presence of two-way coupling, which has been tested and validated. Then, based on a very recent DNS study [Capecelatro 2018] that has analyzed the mechanisms of turbulence modulation by the particles in a channel flow, we have tested our model at different particle mass loadings, showing, in agreement with DNS, a decrease in the fluid turbulent kinetic energy when increasing the mass loading from zero to two, and an increase in the anisotropy of the flows. Even though these results are not conclusive and further simulations are under investigation, they show nevertheless that the stochastic model proposed for dense-collisional flows is capable to give useful insights also in non-homogeneous flows, and also in those regimes at moderate particle loadings where only some modulation of turbulence is present.

In the final part of the thesis (part III) we have investigated buoyancy-driven bubbly flows with a VOF-DNS methodology using the Basilisk code. We have repeated several literature benchmark tests for single bubbles rising at low to moderate Reynolds numbers in periodic domains, finding a comparable accuracy with front-tracking and level-set methods. We have studied some technical aspects related to the numerical code, specifically the numerical treatment of bubble coalescences and the grid refinement threshold, finding that having realistic density ratios in gas-liquid flows has a major impact on dynamics and in particular is important to avoid non-physical coalescences. Finally, we have shown results for the 2-dimensional bubble column configuration at intermediate to high Reynolds numbers, which shows several common features with the experimental results [Riboux 2010]. For all the Reynolds numbers a clear asymmetry is present in the PDF of the vertical velocity fluctuations with a strong deviation from gaussianity. For the lower Reynolds numbers, we have found at intermediate wave lengths a scaling of the spectra close to -3 , while at smaller scales a somehow steeper behaviour is present. For the highest Reynolds number case, $Ar = 313$, a different scaling is found, that could be linked to a possible inverse cascade. This scenario has yet to be confirmed by new data not available at the moment. Even if the mechanisms of energy cascades are different between 2-d and 3-d, we think that 2-d simulations have been useful to approach the problem and to give evidence of the possible similarities that are shared with the 3-dimensional case.

Summarizing, despite the extent and the complexity of the subject, in our contribution we have addressed several specific problems. As for particle-laden flows, the goal was to develop models capable of reproducing the intriguing physical mechanisms that characterize this class of flows, as e.g. particle-induced-turbulence. This has been possible thanks to the fact that the study of particles in turbulence is advanced and one can rely on a wide literature. Indeed, mechanisms like preferential concentration and particle-turbulence modulation, even though driven by a non-trivial physics, have been studied in details, providing a useful analysis for the derivation of simpler models that can grasp the key mechanisms. On the other hand, bubbly flows have required a more fundamental study, since the mechanisms of momentum and energy exchange between the phases is less clear, and features like the finite size and the deformability of the dispersed phase make the problem challenging. The rising motion of bubbles has fascinated many since a long time, and has been rather well understood, but collective dynamics of flows with

many interacting bubbles that generate strong agitations in the liquid, are still less clear. Recently, several experiments have underlined some intriguing features that can be essential for the development of models. However, numerical simulations with many rising bubbles at high Reynolds number are still in their early days, and thus we think that our work has given a contribution for a deeper understanding, even if a further analysis is still needed. It is worth remarking that thanks to different types of tackled flow problems, it has been possible during this thesis to learn and to develop different methodologies, choosing the most suitable for each case. In the context of turbulent two-phase flows, we have worked with Large-Eddy-Simulations, Reynolds-Averaged and PDF models, and two-fluids direct numerical simulations, ranging from a more theoretical approach, for the derivation of 1-D homogeneous models, to realistic numerical experiments, accomplished with large simulations.

As for future developments, in the particle dense regime, further studies for the channel flow configuration at higher mass loadings could be useful for a complete appraisal of the model, in particular to see whether after the initial decrease of the fluid kinetic energy, above a certain threshold of particle concentration, Cluster-Induced-Turbulence appears, with a new increase of turbulence. Attaining such high mass loadings is not trivial numerically in non-homogeneous applications, because the budgets of the momentum and fluid energy become dominated by the exchange terms with the particle-phase, and the Reynolds-stress fluid model does not play an important role anymore. Moreover the coupling terms coming from the stochastic model are intrinsically noisy and particular care must be taken to avoid instabilities in the Eulerian RA equations, like for instance having enough particles to have good statistics, or developing further ad-hoc numerical treatments for these terms.

On the other side, even if we have shown that the model predictions at low to intermediate mass loadings follow the good trend, we think that results in this regime could be improved by a further analysis. In this regard, it is possible to proceed on two fronts: firstly, having a more precise fluid model would be surely of help, as we have seen that the Reynolds stress model that we have used is rather inaccurate even for the single phase. An alternative could be to use elliptic-relaxation models that have been shown to give excellent results for channel flows. However, note that changing the fluid-phase model might require also some adaptation of the particle one (namely in the U_s equation) to avoid inconsistencies. Secondly, the model constants could be calibrated more specifically for this regime. Indeed, it is unlikely that the model could accurately predict all concentration regimes, by using the constant values optimized to reproduce the CIT mechanisms, as done in the present thesis. With a further analysis and with additional DNS data, a dependence of the model constants on the mass loading parameter might be found, or techniques like uncertainty quantification could be used to find a suitable set that minimizes the errors in a certain range of flow parameters. Finding more general constants would make the model best suited also for those problems where there are strong differences of particle concentration within the domain, like for instance in river sedimentation and transport [Muste 2005, Chauchat 2017].

Bubble-induced agitation leaves room for much work, too. A further analysis of the 2-d case can be useful to thoroughly explain the scaling of energy spectra, for instance by carrying out a scale-by-scale budget analysis. Moreover, further simulations at different

volume fractions would be interesting to investigate if some dependence to this parameter is present. Albeit we have shown the importance of having well resolved grids to avoid numerical coalescences, some merging still occurs, and it would be interesting to study if the change of the bubble typical size has an impact on the agitation induced in the fluid. On the modelling side, budget analysis of the averaged quantities might give a useful contribution in the development of two-fluids RA models. In particular this configuration was also chosen in order to investigate the presence of a dispersion term, proportional to the gradients of volume fraction $\nabla\alpha$, which is empirically added to two-fluids models to ensure the hyperbolicity of the system of equations. Finally 3-d simulations could also give an important contribution in this sense as well as for the comprehension of the physics. It would be interesting to do a quantitative comparison of the 3-d results with the experimental study of [Riboux 2010], since the setup is very similar, even if a limited number of bubbles have been simulated. This comparison could give additional insight, making possible a further analysis of the induced-agitation with tools that might not be used in an experimental analysis. Once this mechanisms will be completely characterized alone, it would be certainly of interest to study the interaction of the collective dynamics of bubbles with an already existing turbulent flow, to see how wakes agitation modifies classic shear-turbulence.

Collaboration

Stochastic modelling of acceleration in turbulent wall-bounded flows

Sergio Chibbaro and Alessio Innocenti

Sorbonne Université, CNRS, UMR 7190, Institut Jean Le Rond d'Alembert, F-75005 Paris, France

Nicolas Mordant and Nick Stelzenmuller

LEGI, Université Grenoble Alpes & CNRS, Grenoble, F-38058, France

I. INTRODUCTION

Stochastic processes are fundamental in the description of nonequilibrium systems[1, 2] and their use to build a theory of turbulence dates back to first works of Kraichnan[3, 4]. While they have proven to be useful for theoretical analysis of specific issues[5], they are mainly used as a tool to develop models that can be applied to general applications[6, 7]. In this framework, stochastic models describe only a coarse-grained version of the full turbulent flow, and notably they focus generally on the dynamics of the one-point and one-time probability density function (pdf) of the state-vector of the system. That is tantamount to have access to all the moments of the variables retained in the state vector, at each point and each time. These models are valuable for environmental and engineering applications, but they are also relevant to understand the phenomenology of turbulence, since they may indicate which is a minimal model giving an accurate description of the flow.

As usual, the choice of the state-vector is key to have an approximate but still accurate description of the turbulent flow considered. In particular, it is essential to retain enough variables to have a state-vector which can be described as markovian[8]. Since these models are conceived to tackle general non-homogeneous model, the state vector is usually limited to the position and velocity of the fluid particles \mathbf{x}, \mathbf{V} , and these observables are modelled as a diffusion process, that which is justified by Kolmogorov theory[9, 10]. The validity of such models may become questionable in some circumstances. The criterion used to include only fluid particle location and velocity in the state-vector is to have separation of scales $\tau_\eta \ll T_L$, where τ_η is the smallest time-scale, namely the Kolmogorov time-scale $\tau_\eta \equiv (\frac{\nu}{\epsilon})^{1/2}$, and T_L is the integral scale, typical of large-scales of the flow. This criterion is no longer met at low Reynolds numbers, with the Reynolds number defined as $Re = \frac{UL}{\nu}$ where U, L are typical velocity and length of large scales and ν is the kinematic viscosity. In this case, there is no more the separation of scale justifying the markovian description of the process \mathbf{x}, \mathbf{V} . Therefore, more variables should be added and notably the fluid particle accelerations. This can happen in two cases, in homogeneous flows with low Re , or in general non-homogeneous flows at high Re but which include walls. Indeed, near to the walls viscous friction cannot be neglected. Some proposals have been made early for the former case[11, 12], but the first experiments accessing Lagrangian fluid acceleration[13, 14] have motivated many attempts in the following with the purpose of fitting the experimental data, but without a sound link with turbulence theory[15], but in few exception[16, 17].

Yet, the latter case is more important since realistic flows are non-homogeneous and have very high Re .

The aim of this letter is to propose a first model including the acceleration of fluid particles in the general case of non-stationary and inhomogeneous turbulence, and is motivated by very recent accurate measurements of the acceleration in turbulent channel-flow at high Re -number[18]. The model developed will be general so that it can be used in all realistic flows of practical interest.

II. MODEL

The model we propose has the following form

$$dx_i = U_i dt \quad (1)$$

$$dU_i = -\frac{1}{\rho} \frac{\partial \langle P \rangle}{\partial x_i} dt + A_{ij}(U_i - \langle U_i \rangle) dt + f_i dt, \quad (2)$$

$$df_i = -\beta f_i dt + \sqrt{B} dW_i. \quad (3)$$

We use Kolmogorov theory to give an estimate of typical time-scales. Considering $\delta U_\tau = |\mathbf{U}(t + \tau) - \mathbf{U}(t)| \Rightarrow D_2^L = \langle (\delta U_\tau)^2 \rangle \sim C_0 \langle \epsilon \rangle \tau$, where C_0 is a constant. This implies for the velocity autocorrelation function that $R_L(\tau) = \frac{\langle U(t)U(t+\tau) \rangle}{u^2} \sim 1 - \frac{D_2^L(\tau)}{2u^2} \sim 1 - \frac{C_0}{2} \frac{\tau}{T}$, with T the time-scale of large scales, such that $R_L(\tau) \sim 1$ in the inertial range far from boundaries when $\tau \ll T$. We can generalise for higher-order statistics $D_n^L(\tau) = \langle \frac{d^n u}{dt^n}(t) \frac{d^n u}{dt^n}(t + \tau) \rangle$, and the same hypotheses yield $D_n^L(\tau) = \left(\frac{v_\eta}{\tau_\eta}\right)^2 \alpha(x) = \nu^{1/2-n} \langle \epsilon \rangle^{n+1/2} \alpha(x)$. Where $v_\eta \equiv (\nu \langle \epsilon \rangle)^{1/4}$, $\tau_\eta \equiv \left(\frac{\nu}{\langle \epsilon \rangle}\right)^{1/2}$, $x = \frac{\tau}{\tau_\eta}$ and $\alpha(x)$ is related to the correlation and should be an universal function. If τ is in the inertial range we can demand that the correlation is independent of the viscosity. Then, we find $D_n^L(\tau) = \langle \epsilon \rangle \tau^{1-2n} \Leftrightarrow \alpha(x) \sim x^{(1-2n)}$. Hence, for $n = 1$ we can find the acceleration correlation behaviour $R_A(\tau) = \frac{\langle A(t+\tau)A(t) \rangle}{\langle A^2 \rangle} \sim \frac{\tau_\eta}{\tau}$, and for $n = 2$ the case of derivative of acceleration $R_{\dot{A}}(\tau) \sim \left(\frac{\tau_\eta}{\tau}\right)^3$. These correlations show that the turbulent acceleration and higher derivatives of velocity depend explicitly on the fluid viscosity ν . Since for high-Reynolds number the viscosity affect only the very small-scale turbulent motion, in locally isotropic turbulence these variables are determined largely by the very small-scale motions ($l \leq \eta$). On the basis of these estimates, the fluid particle acceleration timescale β^{-1} is taken proportional to the local Kolmogorov timescale, assuming a constant of proportionality of one we get $\beta^{-1} = \tau_\eta$.

To fix the diffusion term, we demand to be consistent with the state-of-the-art Langevin model for non-homogeneous flows[10]. which has the following expression

$$\begin{aligned} dX_i &= U_i dt \\ dU_i &= -\frac{1}{\rho} \frac{\partial \langle P \rangle}{\partial x_i} dt + G_{ij} (U_i - \langle U_i \rangle) dt + \sqrt{C_0 \langle \epsilon \rangle} dW_i \end{aligned} \quad (4)$$

with $G_{ij} = -\frac{1}{T_L} \delta_{ij} + G_{ij}^a$ with $T_L = (\frac{1}{2} + \frac{3}{4} C_0)^{-1} \frac{k}{\langle \epsilon \rangle}$, and G_{ij}^a is a traceless matrix. We take $G_{ij}^a = 0$ for the sake of simplicity, which corresponds to the Rotta model for the Reynolds stress equations[6]. In the acceleration-based model equations (1)-(3), the Reynolds-stress equations are

$$\begin{aligned} \frac{\partial \langle u_i u_j \rangle}{\partial t} + \langle U_k \rangle \frac{\partial \langle u_i u_j \rangle}{\partial x_k} + \frac{\partial \langle u_i u_j u_k \rangle}{\partial x_k} &= -\langle u_i u_k \rangle \frac{\partial \langle U_j \rangle}{\partial x_k} - \langle u_j u_k \rangle \frac{\partial \langle U_i \rangle}{\partial x_k} \\ &\quad + \langle u_i a_j \rangle + \langle u_j a_i \rangle. \end{aligned} \quad (5)$$

where the correlations $\langle u_j a_i \rangle$ are solutions of transport equations, which reflect the non-zero memory effects due to the colored noise in the velocity equation. Specifically, the transport equations for the velocity-acceleration correlation are

$$\frac{\partial \langle u_i a_j \rangle}{\partial t} + \langle U_k \rangle \frac{\partial \langle u_i a_j \rangle}{\partial x_k} + \frac{\partial \langle u_i a_j u_k \rangle}{\partial x_k} = +G_{ik} \langle a_j u_k \rangle + \langle a_i a_j \rangle - \langle a_j u_k \rangle \frac{\partial \langle U_i \rangle}{\partial x_k} - \frac{\langle u_i a_j \rangle}{\tau_\eta}; \quad (6)$$

and for the variance of acceleration

$$\frac{\partial \langle a_i a_j \rangle}{\partial t} + \langle U_k \rangle \frac{\partial \langle a_i a_j \rangle}{\partial x_k} + \frac{\partial \langle a_i a_j u_k \rangle}{\partial x_k} = -2 \frac{\langle a_i a_j \rangle}{\tau_\eta} + B \delta_{ij}. \quad (7)$$

The finite value of timescale τ_η is responsible of the memory effect, thus, in the limit of $\tau_\eta \rightarrow 0$, the same source term in Reynolds-stress equations as given by the model (4) should be found. In this limit, we have $\langle a_i a_j \rangle \rightarrow \frac{B \tau_\eta}{2} \Rightarrow \langle u_i a_j \rangle = \tau_\eta (\langle a_i a_j \rangle - \frac{\langle u_i a_j \rangle}{T_L}) = \frac{B \tau_\eta^2}{2}$, therefore, in order to have the correct limit, it is necessary to impose $B = C_0 \langle \epsilon \rangle (\frac{1}{\tau_\eta^2} + \frac{1}{\tau_\eta T_L})$.

Taking the trace of Reynolds-stress equations, the equation for turbulent kinetic energy is retrieved. Considering the homogeneous case, we obtain the following relation $2 \sum_i \langle u_i a_i \rangle = -\langle \epsilon \rangle$, which defines implicitly the turbulent dissipation for our stochastic model.

III. NUMERICAL SCHEME

We study the turbulent flow in a channel between two parallel walls separated by a distance $2h$ using the same Reynolds number ($Re_\tau = \frac{u_\tau h}{\nu} \approx 1440$) in both experiments and simulations, where u_τ is the friction velocity associated to the shear stress τ_w at the wall and ν the kinematic viscosity. In the following, the superscript + indicates quantities expressed in wall units, nondimensionalized by u_τ and ν . Experiments have been recently described[18], the numerical setup is detailed in the supplemental material. Equation (3) is a stochastic differential equation of the form $d\mathbf{X} = \mathbf{A} dt + \mathbf{B} \mathbf{X} dt + \mathbf{D} d\mathbf{W}(t)$. This vector stochastic differential equation is stiff, since we have $\lim_{y \rightarrow 0} \det[\mathbf{B}] = -\infty$.

Indeed, $T_L^{-1} \sim -\frac{\epsilon}{k}$ and near to the wall this means $T_L^{-1} \sim \frac{-1}{y^2}$, which grows without bound. Moreover near the wall $U_i - \langle U_i \rangle \sim y$, for the no-slip boundary condition. Thus, the drift coefficient $[\mathbf{B}]\mathbf{U}$ scales with $1/y$ and remains unbounded for $y \rightarrow 0$. Special numerical treatment is therefore required. Furthermore, the time-scale β may be very small and instabilities may arise also far from boundaries if the time-step is bigger (typically in the inertial range) and the numerical scheme is not stable. To address these issues, we have developed a new numerical scheme unconditionally stable, following the same approach used in similar problems[19, 20]. Taking the matrix coefficients $\mathbf{A}, \mathbf{B}, \mathbf{D}$ frozen during a time-step Δt , we have obtained analytical solutions using the integrating factor $e^{-\mathbf{B}t}$. The numerical scheme is presented in the supplemental material[21]. On the other hand, the equations (3) contain several average fields, which have to be computed at each time-step. As in typical engineering calculations[6, 22], we use here a hybrid approach, computing the needed average quantities ($\langle \mathbf{U} \rangle, \langle P \rangle, \epsilon, k$) solving the Reynolds averaged Navier-Stokes (RANS) equations. In particular, to highlight the characteristics of the new model proposed for the acceleration, we use here the Rotta model, which is consistent with the model 4 when $G_{ij}^a = 0$, as considered in the present work. Since we want to analyse the behaviour near to the wall, we have added the standard Low-Re wall treatments[6]. More details can be found in the supplemental material.

IV. RESULTS

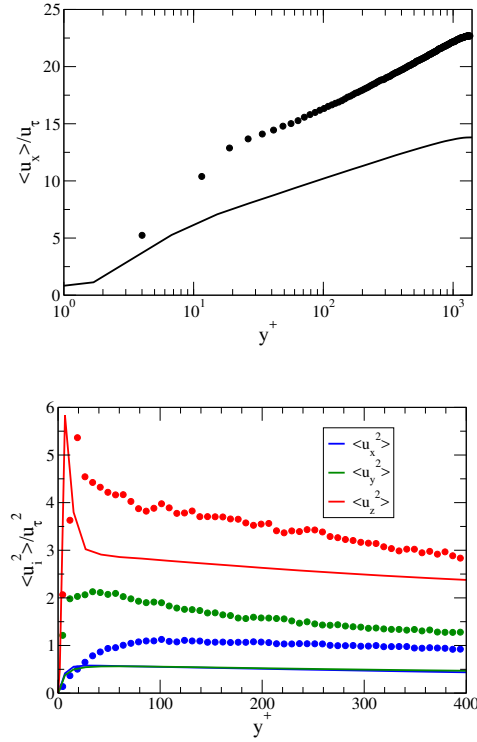


FIG. 1. Mean (a) and variance velocity profiles (b). Comparison between experiments (points) and the present model (lines). All quantities are normalized in wall units.

In Fig. 1, mean and variance velocity profiles from experiments and simulations are compared. Both experimental and numerical profiles are obtained by sampling the instantaneous velocity of particles conditioned by their wall distance y^+ . While both mean streamwise velocity profiles present a clear logarithmic behavior in the region $50 \lesssim y^+ \lesssim 1200$, an important quantitative discrepancy is displayed. This evidence is related to the RANS model used to provide $\langle \mathbf{U} \rangle$, and present results are in line with expected values[6, 19, 23]. Similar remarks can be made for wall-normal and transverse velocity variances, which are known to be underestimated in the Rotta model. Furthermore, the anisotropy is largely diminished as intrinsic in this kind of model. Instead, for the streamwise velocity variance experiments are in decent agreement with the simulations, notably for $y^+ < 50$. These variance results are in better agreement with experiments than those obtained from the RANS computations. This means that the acceleration model is able to improve the representation of the Reynolds stresses.

Figure 4 shows the mean and variance acceleration profiles obtained by our experiments and model. The agreement between experiments and simulations is fairly good, and notably the model gives correctly the negative peak of mean streamwise acceleration at $y^+ \approx 7$, which is a viscous effect. That shows that the acceleration model together with a RANS model including the boundary layer is able to describe this effect, despite the absence of ad-hoc low-Re terms in the stochastic model. Profiles of acceleration variance (Fig. 2) reveal qualitative agreement between both sets of data, although large uncertainty is seen in the experimental results near the wall. Considering also corresponding DNS results[18], larger errors in variances are found in the model with respect to the mean accelerations. In particular, a slight overestimation of the spanwise variance is present and, more pronounced, the model display all the peak around the same position, whereas experiments and DNS show some variability. Nevertheless, at their respective peaks, the standard deviation of acceleration is larger than the magnitude of the mean acceleration for all sets, indicating that the present stochastic model is already able to reproduce the acceleration fluctuations that govern the dynamics near the wall. Figures 3a-b show various components of the acceleration correlation tensor ρ_{ij} calculated at different initial wall distances y_0^+ . The agreement is globally good, showing that the stochastic model fairly reproduce both the inhomogeneity and the anisotropy of the flow, since all components are different and the decorrelation time change with the distance. A less good agreement is found in the long-time behaviour at $y^+ = 1000$, notably for ρ_{zz} . However, the model results are more similar to DNS ones, and furthermore it is worth stressing that to perform a stringent test of the approach, a coarse grid is used in the middle of the channel, as usual in RANS simulations. That causes a

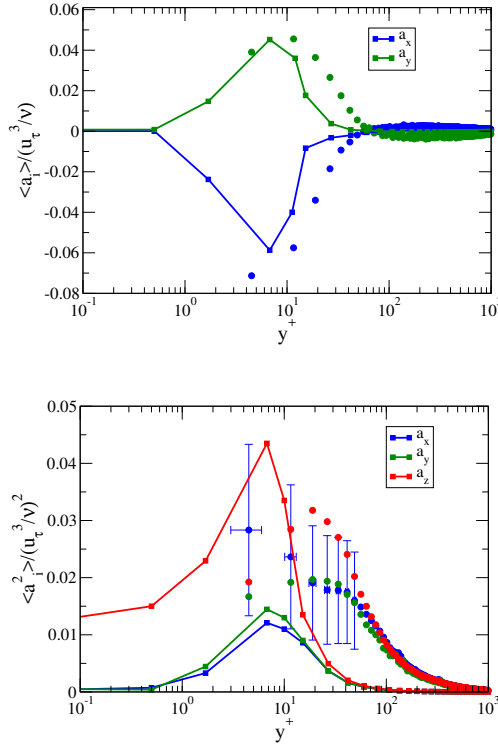


FIG. 2. Mean and variance acceleration profiles. Comparison between experiments (points) and model simulations lines.

high level of error for measurements at large y^+ . Fair convergence to DNS results is found with a fine mesh.

Fig. 13 shows the probability distribution function (PDF) of the three acceleration components obtained at different wall distances. All curves present very long tails corresponding to extremely high acceleration events associated to intermittency. Once again, good agreement is achieved between the experiments and the model, notably in the core of the PDF and for the spanwise components. The model displays a more important number of negative extreme events in the streamwise events, but this is in line with DNS results[18] and due to the fact that in numerical computations it is possible to record the events very near-to-the-wall.

V. CONCLUSIONS

In this letter, we have proposed and compared against experiments in a channel-flow a novel stochastic model, which includes the fluid particle acceleration. This model generalises both the previous propositions for the acceleration in isotropic flows and the general models for non-homogeneous flows. To deal with the fluid averages in the coefficients, In this work, we have used a hybrid RANS/PDF approach which is the one typically used in realistic computations. Furthermore, since this is the first validation of such a model and in order to carry out a stringent assessment of the stochastic model, we have chosen to not use sophisticated models for the fluid that might have improved the overall results but also blur the picture. A standard Rotta Reynolds-stress model is used, which is consistent with the standard Langevin model for the velocity[6]. For such a reason, we have put forward the simplest model which is derived using Kolmogorov theory and previous stochastic models. In particular, the use of the moment equations for the covariance of the velocity and acceleration has been found key to get a closure. Furthermore, while we have included in the RANS model some low-Re features, we have developed a stochastic model which does not take into account explicitly those effects in the velocity. However, since the inclusion of the acceleration should bring some of those effects, present results are also useful to disentangle which of those effects can be obtained in this way and which are to be introduced at the level of the velocity. However, given that average observables used in the stochastic model are far from the experimental ones, the overall behaviour of the model is remarkable showing that it captures most of the features revealed by experiments. In particular we model directly only the isotropic part of the acceleration, yet the whole model is nonlinear and is capable to model decently the anisotropy of the flow. More specifically, results show an improvement of the Reynolds stress, notably the stream-wise component is now in agreement with

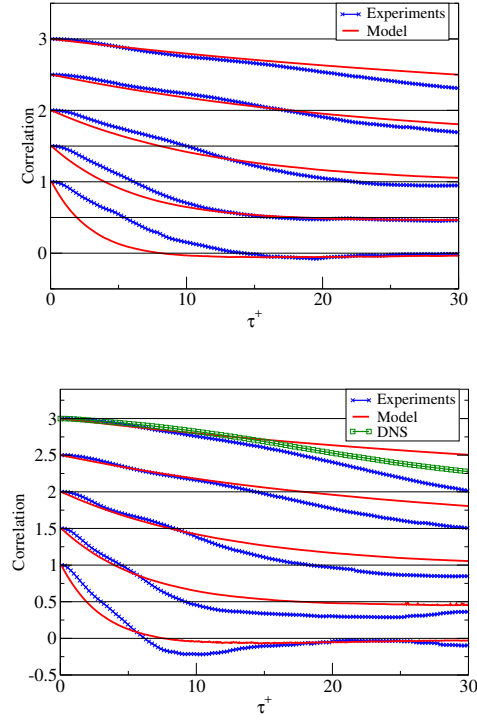


FIG. 3. From left to right, Lagrangian auto-correlations of wall-normal (ρ_{yy}) and spanwise (ρ_{zz}) particle acceleration. Correlations are computed as: $\rho_{ij}(\tau, y_0) = \frac{\langle a'_i(t_0, y_0) a'_j(t_0 + \tau, y_0) \rangle}{\langle a'^2_i(t_0, y_0) \rangle^{1/2} \langle a'^2_j(t_0 + \tau, y_0) \rangle^{1/2}}$. Experiments crossed blue lines, model red lines. Curves are shifted vertically by increments of 0.5 for clarity. From bottom to top, the curves correspond to particles located initially at $y_0^+ = 20, 60, 200, 600$ and 1000 . Horizontal grid lines show the zero-correlation level for each y_0^+ . The DNS data curve is shown for one case, for comparison.

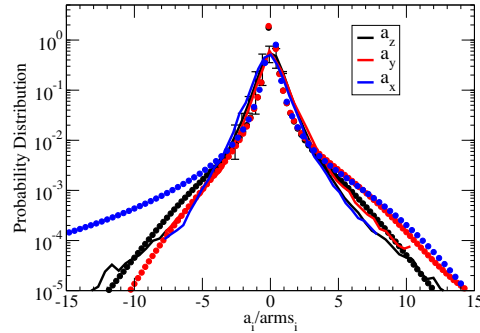


FIG. 4. PDF of streamwise, wall-normal and spanwise particle acceleration. Experiments - solid lines. Model - symbols. The PDFs are normalized by the root-mean-square value of acceleration. The PDF represent an average over the whole channel.

experiments. That emphasises that the acceleration introduces some of the near-to-the-wall effects not included in the velocity model. The acceleration is globally in line with experiments and DNS. Both first and second moments are in good agreement with experiments. The Lagrangian autocorrelation given by the model reproduces correctly the time-scale and the non-homogeneous affects. The behaviour at very short-time scale is slightly different, this is due to the introduction of a white noise at the level of the acceleration, which is therefore non-differentiable and singular at the origin. Interestingly, also the pdfs are well captured, at least at qualitative level, displaying skewness, anisotropy and far-from-gaussian tails, even without taking into account intermittency in the model. This shows that in wall flows, most of the extreme events are related to non-homogeneity. In conclusion, we believe that the present form of the stochastic model is adequate to model wall flows in realistic case. In order to improve further the performances, notably to get the correct anisotropy in Reynolds stress, improvements would be: (a) to add intermittency effects in the turbulent dissipation [6] and/or in the acceleration[17]; (b) to use a more general model for the velocity with

$G_{ij} = -\frac{1}{T_L}\delta_{ij} + G_{ij}^a$ and G^a a modelling traceless matrix. It is known that elliptic relaxation models are able to retrieve exact results for the Reynolds stress [6]. (c) Viscous effects could be added, even though they are known to have a very small impact[23].

-
- [1] S. R. De Groot and P. Mazur, *Non-equilibrium thermodynamics* (Courier Corporation, 2013).
 - [2] U. M. B. Marconi, A. Puglisi, L. Rondoni, and A. Vulpiani, *Physics reports* **461**, 111 (2008).
 - [3] R. H. Kraichnan, *Journal of Fluid Mechanics* **5**, 497 (1959).
 - [4] R. H. Kraichnan, *Journal of Mathematical Physics* **2**, 124 (1961).
 - [5] G. Falkovich, K. Gawdzki, and M. Vergassola, *Reviews of modern Physics* **73**, 913 (2001).
 - [6] S. B. Pope, *Turbulent Flows* (Cambridge University Press, 2000).
 - [7] J.-P. Minier and E. Peirano, *Phys. Rep.* **352**, 1 (2001).
 - [8] L. Onsager and S. Machlup, *Physical Review* **91**, 1505 (1953).
 - [9] A. Monin, *Statistical fluid mechanics, volume II: mechanics of turbulence*.
 - [10] S. B. Pope, *Ann. Rev. Fluid Mech.* **26**, 23 (1994).
 - [11] E. Krasnoff and R. Peskin, *Geophysical & Astrophysical Fluid Dynamics* **2**, 123 (1971).
 - [12] B. Sawford, *Physics of Fluids A: Fluid Dynamics* **3**, 1577 (1991).
 - [13] G. A. Voth, A. la Porta, A. M. Crawford, J. Alexander, and E. Bodenschatz, *Journal of Fluid Mechanics* **469**, 121 (2002).
 - [14] N. Mordant, E. L  v  que, and J.-F. Pinton, *New Journal of Physics* **6**, 116 (2004).
 - [15] T. Gotoh and R. H. Kraichnan, *Physica D: Nonlinear Phenomena* **193**, 231 (2004).
 - [16] S. B. Pope, *Physics of Fluids* **14**, 2360 (2002).
 - [17] A. Lamorgese, S. Pope, P. Yeung, and B. Sawford, *Journal of Fluid Mechanics* **582**, 423 (2007).
 - [18] N. Stelzenm  ller, J. I. Polanco, L. Vignal, I. Vinkovic, and N. Mordant, *Physical Review Fluids* **2**, 054602 (2017).
 - [19] T. D. Dreeben and S. B. Pope, *J. Fluid Mech.* **357**, 141 (1998).
 - [20] E. Peirano, S. Chibbaro, J. Pozorski, and J.-P. Minier, *Prog. Energy Combust. Sci.* **32**, 315 (2006).
 - [21] Supplemental material.
 - [22] S. B. Pope, *Prog. Energy Combust. Sci.* **11**, 119 (1985).
 - [23] T. D. Dreeben and S. B. Pope, *Phys. Fluids* **9**, 154 (1997).

Bibliography

- [Afkhami 2015] M Afkhami, A Hassanpour, M Fairweather and DO Njobuenwu. *Fully coupled LES-DEM of particle interaction and agglomeration in a turbulent channel flow*. Comput. Chem. Eng., vol. 78, no. 7, pages 248–38, 2015. (Cited on page 33.)
- [Ahmed 2000] AM Ahmed and S Elghobashi. *On the mechanisms of modifying the structure of turbulent homogeneous shear flows by dispersed particles*. Phys. Fluids (1994-present), vol. 12, no. 11, pages 2906–2930, 2000. (Cited on pages 80, 82 and 85.)
- [Alméras 2017] Elise Alméras, Varghese Mathai, Detlef Lohse and Chao Sun. *Experimental investigation of the turbulence induced by a bubble swarm rising within incident turbulence*. J. Fluid Mech., vol. 825, pages 1091–1112, 2017. (Cited on page 14.)
- [Anderson 1967] T. B. Anderson and R. Jackson. *Fluid mechanical description of fluidized beds. Equations of motion*. Ind. Engng Chem. Fundam., vol. 6, no. 4, pages 527–539, 1967. (Cited on page 107.)
- [Armenio 1999] Vincenzo Armenio, Ugo Piomelli and Virgilio Fiorotto. *Effect of the sub-grid scales on particle motion*. Phys. Fluids, vol. 11, no. 10, pages 3030–3042, 1999. (Cited on page 33.)
- [Atchley 1989] Anthony A Atchley and Andrea Prosperetti. *The crevice model of bubble nucleation*. The Journal of the Acoustical Society of America, vol. 86, no. 3, pages 1065–1084, 1989. (Cited on page 13.)
- [Aulisa 2007] Eugenio Aulisa, Sandro Manservigi, Ruben Scardovelli and Stephane Zaleski. *Interface reconstruction with least-squares fit and split advection in three-dimensional Cartesian geometry*. J. Comp. Phys., vol. 225, no. 2, pages 2301–2319, 2007. (Cited on page 27.)
- [Balachandar 2010] S. Balachandar and J. K. Eaton. *Turbulent dispersed multiphase flow*. Annu. Rev. Fluid Mech., vol. 42, pages 111–133, 2010. (Cited on pages 11, 34, 61, 63, 106 and 134.)
- [Balkovsky 2001] E. Balkovsky, G. Falkovich and A. Fouxon. *Intermittent distribution of inertial particles in turbulent flows*. Phys. Rev. Lett., vol. 86, no. 13, page 2790, 2001. (Cited on page 63.)
- [Batchelor 2000] George Keith Batchelor. *An introduction to fluid dynamics*. Cambridge university press, 2000. (Cited on page 134.)
- [Bhatnagar 1954] P. L. Bhatnagar, E. P. Gross and M. Krook. *A model for collision processes in gases. I. Small amplitude processes in charged and neutral one-component systems*. Phys. Rev., vol. 94, no. 3, page 511, 1954. (Cited on page 102.)
- [Bianco 2012] F Bianco, S Chibbaro, C Marchioli, M V Salvetti and A Soldati. *Intrinsic filtering errors of Lagrangian particle tracking in LES flow fields*. Phys. Fluids, vol. 24, no. 4, page 045103, 2012. (Cited on page 34.)

- [Blander 1975] Milton Blander and Joseph L Katz. *Bubble nucleation in liquids*. AIChE Journal, vol. 21, no. 5, pages 833–848, 1975. (Cited on page 13.)
- [Bosse 2006] T. Bosse, L. Kleiser and E. Meiburg. *Small particles in homogeneous turbulence: Settling velocity enhancement by two-way coupling*. Phys. Fluids, vol. 18, no. 2, page 027102, 2006. (Cited on page 63.)
- [Brackbill 1992] JU Brackbill, Douglas B Kothe and Charles Zemach. *A continuum method for modeling surface tension*. J. Comp. Phys., vol. 100, no. 2, pages 335–354, 1992. (Cited on page 27.)
- [Brey 1998] J. J. Brey, J. W. Dufty, C. S. Kim and A. Santos. *Hydrodynamics for granular flow at low density*. Phys. Rev. E, vol. 58, no. 4, page 4638, 1998. (Cited on pages 64 and 101.)
- [Brilliantov 2010] N. V. Brilliantov and T. Pöschel. *Kinetic theory of granular gases*. Oxford University Press, 2010. (Cited on pages 64 and 101.)
- [Burton 2005] Tristan M Burton and John K Eaton. *Fully resolved simulations of particle-turbulence interaction*. J. Fluid Mech., vol. 545, pages 67–111, 2005. (Cited on page 106.)
- [Calzavarini 2011] E. Calzavarini, A. Donini, V. Lavezzo, C. Marchioli, E. Pitton, A. Soldati and F. Toschi. *On the error estimate in the sub-grid models for particles in turbulent flows*. In V. Armenio, B.J. Geurts, J. Fröhlich and J. G. M. Kuerten, editors, *Direct and Large-Eddy Simulation 8*, Ercoftac Series. Springer, 2011. (Cited on page 33.)
- [Cano-Lozano 2016] José Carlos Cano-Lozano, Carlos Martínez-Bazán, Jacques Magnaudet and Joël Tchoufag. *Paths and wakes of deformable nearly spheroidal rising bubbles close to the transition to path instability*. Phys. Rev. Fluids, vol. 1, page 053604, Sep 2016. (Cited on pages 14, 15, 133, 135, 139, 142 and 145.)
- [Capecelatro 2014] J. Capecelatro, O. Desjardins and R. O. Fox. *Numerical study of collisional particle dynamics in cluster-induced turbulence*. J. Fluid Mech., vol. 747, page R2, 2014. (Cited on page 63.)
- [Capecelatro 2015] J. Capecelatro, O. Desjardins and R. O. Fox. *On fluid-particle dynamics in fully developed cluster-induced turbulence*. J. Fluid Mech., vol. 780, pages 578–635, 2015. (Cited on pages 2, 13, 60, 62, 63, 64, 65, 66, 75, 76, 80, 88, 90, 91, 92, 93, 94, 95, 96, 97, 106, 108, 109, 110 and 161.)
- [Capecelatro 2016a] J. Capecelatro, O. Desjardins and R. O. Fox. *Strongly coupled fluid-particle flows in vertical channels. I. Reynolds-averaged two-phase turbulence statistics*. Phys. Fluids, vol. 28, no. 3, page 033306, 2016. (Cited on pages 75 and 96.)
- [Capecelatro 2016b] J. Capecelatro, O. Desjardins and R. O. Fox. *Strongly coupled fluid-particle flows in vertical channels. II. Turbulence modeling*. Phys. Fluids, vol. 28, no. 3, page 033307, 2016. (Cited on pages 62, 66, 67, 68, 74, 90, 95, 96, 109, 110 and 123.)

- [Capecelatro 2018] Jesse Capecelatro, Olivier Desjardins and Rodney O Fox. *On the transition between turbulence regimes in particle-laden channel flows*. J. Fluid Mech., vol. 845, pages 499–519, 2018. (Cited on pages 105, 106, 114, 115, 120, 121, 123, 126 and 162.)
- [Cercignani 1988] C. Cercignani. The boltzmann equation. Springer, 1988. (Cited on page 101.)
- [Cernick 2015] Matthew J Cernick, SW Tullis and MF Lightstone. *Particle subgrid scale modelling in large-eddy simulations of particle-laden turbulence*. J. Turbul., vol. 16, no. 2, pages 101–135, 2015. (Cited on page 34.)
- [Chapman 1970] S. Chapman and T. G. Cowling. The mathematical theory of non-uniform gases: an account of the kinetic theory of viscosity, thermal conduction and diffusion in gases. Cambridge University Press, 1970. (Cited on page 101.)
- [Chauchat 2017] Julien Chauchat, Zhen Cheng, Tim Nagel, Cyrille Bonamy and Tian-Jian Hsu. *SedFoam-2.0: a 3-D two-phase flow numerical model for sediment transport*. 2017. (Cited on page 163.)
- [Chen 2006] Shiyi Chen, Robert E Ecke, Gregory L Eyink, Michael Rivera, Minping Wan and Zuoli Xiao. *Physical mechanism of the two-dimensional inverse energy cascade*. Physical review letters, vol. 96, no. 8, page 084502, 2006. (Cited on page 154.)
- [Chibbaro 2011] S. Chibbaro and J.-P. Minier. *A note on the consistency of hybrid Eulerian/Lagrangian approach to multiphase flows*. Int. J. Multiphase Flow, vol. 37, no. 3, pages 293–297, 2011. (Cited on page 74.)
- [Chibbaro 2014] Sergio Chibbaro, Cristian Marchioli, Maria Vittoria Salvetti and Alfredo Soldati. *Particle tracking in LES flow fields: conditional Lagrangian statistics of filtering error*. J. Turbul., vol. 15, no. 1, pages 22–33, 2014. (Cited on page 34.)
- [Chorin 1969] Alexandre Joel Chorin. *On the convergence of discrete approximations to the Navier-Stokes equations*. Mathematics of computation, vol. 23, no. 106, pages 341–353, 1969. (Cited on page 138.)
- [Chouippe 2015] A. Chouippe and M. Uhlmann. *Forcing homogeneous turbulence in DNS of particulate flow with interface resolution and gravity*. Phys. Fluids, vol. 27, page 123301, 2015. (Cited on page 64.)
- [Clift 1978] R. Clift, J. R. Grace and M. E. Weber. Bubbles, drops and particles. Academic Press. New York, 1978. (Cited on pages 14, 15 and 36.)
- [Colucci 1998] P. J. Colucci, F. A. Jaber, P. Givi and S. B. Pope. *The filtered density function for large-eddy simulation of turbulent reactive flows*. Phys. Fluids, vol. 10, page 499, 1998. (Cited on pages 34 and 48.)
- [Crowe 2011] C. T. Crowe, J. D. Schwarzkopf, M. Sommerfeld and Y. Tsuji. Multiphase flows with droplets and particles. CRC press, 2011. (Cited on pages 9 and 61.)

- [Daly 1970] Bart J Daly and Francis H Harlow. *Transport equations in turbulence*. Phys. Fluids, vol. 13, no. 11, pages 2634–2649, 1970. (Cited on page 21.)
- [Dasgupta 1994] S. Dasgupta, R. Jackson and S. Sundaresan. *Turbulent gas-particle flow in vertical risers*. AIChE J., vol. 40, no. 2, pages 215–228, 1994. (Cited on page 62.)
- [Davidson 1990] Malcolm R Davidson. *Numerical calculations of two-phase flow in a liquid bath with bottom gas injection: the central plume*. Applied mathematical modelling, vol. 14, no. 2, pages 67–76, 1990. (Cited on page 159.)
- [Diotallevi 2009] F Diotallevi, L Biferale, S Chibbaro, A Lamura, G Pontrelli, M Sbragaglia, S Succi and F Toschi. *Capillary filling using lattice Boltzmann equations: The case of multi-phase flows*. The European Physical Journal-Special Topics, vol. 166, no. 1, pages 111–116, 2009. (Cited on page 142.)
- [Dodd 2016] Michael S Dodd and Antonino Ferrante. *On the interaction of Taylor length scale size droplets and isotropic turbulence*. J. Fluid Mech., vol. 806, pages 356–412, 2016. (Cited on page 143.)
- [Dreeben 1998] T. D. Dreeben and S. B. Pope. *Probability density function/Monte Carlo simulation of near-wall turbulent flows*. J. Fluid Mech., vol. 357, page 141, 1998. (Cited on pages 39 and 48.)
- [Drew 1983] D.A. Drew. *Mathematical modeling of two-phase flow*. Ann. Rev. Fluid Mech., vol. 15, pages 261–291, 1983. (Cited on pages 16 and 158.)
- [Drew 2006] Donald A Drew and Stephen L Passman. *Theory of multicomponent fluids*, volume 135. Springer Science & Business Media, 2006. (Cited on page 158.)
- [Dritselis 2011] CD Dritselis and NS Vlachos. *Large eddy simulation of gas-particle turbulent channel flow with momentum exchange between the phases*. Int. J. Multiphase Flow, vol. 37, no. 7, pages 706–721, 2011. (Cited on page 33.)
- [Dritselis 2016] Chris D Dritselis. *Direct numerical simulation of particle-laden turbulent channel flows with two-and four-way coupling effects: budgets of Reynolds stress and streamwise enstrophy*. Fluid Dynamics Research, vol. 48, no. 1, page 015507, 2016. (Cited on page 106.)
- [Durbin 1991] Paul A Durbin. *Near-wall turbulence closure modeling without “damping functions”*. Theoretical and Computational Fluid Dynamics, vol. 3, no. 1, pages 1–13, 1991. (Cited on pages 20 and 120.)
- [Eaton 1994] J. K. Eaton and J. R. Fessler. *Preferential concentration of particles by turbulence*. Int. J. Multiphase Flow, vol. 20, pages 169–209, 1994. (Cited on pages 11, 63 and 106.)
- [Elghobashi 1983] S. E. Elghobashi and T. W. Abou-Arab. *A two-equation turbulence model for two-phase flows*. The Phys. Fluids, vol. 26, no. 4, pages 931–938, 1983. (Cited on page 62.)

- [Elghobashi 1992] S. Elghobashi and G. C. Truesdell. *Direct simulation of particle dispersion in a decaying isotropic turbulence*. J. Fluid Mech., vol. 242, pages 655–700, 1992. (Cited on page 61.)
- [Elghobashi 1994] S. Elghobashi. *On predicting particle-laden turbulent flows*. Applied Scientific Research, vol. 52, no. 4, pages 309–329, 1994. (Cited on pages 61, 76 and 96.)
- [Ern 2012] Patricia Ern, Frédéric Risso, David Fabre and Jacques Magnaudet. *Wake-induced oscillatory paths of bodies freely rising or falling in fluids*. Annu. Rev. Fluid Mech., vol. 44, pages 97–121, 2012. (Cited on page 134.)
- [Esmaeeli 1998] Asghar Esmaeeli and Gretar Tryggvason. *Direct numerical simulations of bubbly flows. Part 1. Low Reynolds number arrays*. J. Fluid Mech., vol. 377, pages 313–345, 1998. (Cited on pages 135, 138 and 139.)
- [Esmaeeli 1999] Asghar Esmaeeli and Gretar Tryggvason. *Direct numerical simulations of bubbly flows Part 2. Moderate Reynolds number arrays*. J. Fluid Mech., vol. 385, pages 325–358, 1999. (Cited on pages 14, 135, 138, 139 and 140.)
- [Esmaeeli 2005] Asghar Esmaeeli and Grétar Tryggvason. *A direct numerical simulation study of the buoyant rise of bubbles at $O(100)$ Reynolds number*. Phys. Fluids, vol. 17, no. 9, page 093303, 2005. (Cited on page 135.)
- [Ferrante 2003] A. Ferrante and S. Elghobashi. *On the physical mechanisms of two-way coupling in particle-laden isotropic turbulence*. Phys. Fluids, vol. 15, no. 2, pages 315–329, 2003. (Cited on page 63.)
- [Fessler 1994] John R Fessler, Jonathan D Kulick and John K Eaton. *Preferential concentration of heavy particles in a turbulent channel flow*. Phys. Fluids, vol. 6, no. 11, pages 3742–3749, 1994. (Cited on page 34.)
- [Février 2005] P. Février, O. Simonin and K. D. Squires. *Partitioning of particle velocities in gas–solid turbulent flows into a continuous field and a spatially uncorrelated random distribution: theoretical formalism and numerical study*. J. Fluid Mech., vol. 533, pages 1–46, 2005. (Cited on pages 62, 64, 76, 80, 81, 82, 83, 96 and 110.)
- [Forterre 2008] Y. Forterre and O. Pouliquen. *Flows of dense granular media*. Annu. Rev. Fluid Mech., vol. 40, pages 1–24, 2008. (Cited on page 61.)
- [Fox 2003] R. O. Fox. *Computational models for turbulent reacting flows*. Cambridge Univ Press, 2003. (Cited on pages 33, 62, 95 and 99.)
- [Fox 2012] Rodney O Fox. *Large-eddy-simulation tools for multiphase flows*. Annu. Rev. Fluid Mech., vol. 44, pages 47–76, 2012. (Cited on pages 33 and 53.)
- [Fox 2014] R. O. Fox. *On multiphase turbulence models for collisional fluid-particle flows*. J. Fluid Mech., vol. 742, pages 368–424, 2014. (Cited on pages 62, 75, 82, 83, 84, 85, 86, 87, 88, 89, 92, 95 and 112.)

- [Frisch 1995] U. Frisch. *Turbulence. The legacy of A.N Kolmogorov*. Cambridge, University press, 1995. (Cited on page 8.)
- [Garcia-Villalba 2012] Manuel Garcia-Villalba, Aman G Kidanemariam and Markus Uhlmann. *DNS of vertical plane channel flow with finite-size particles: Voronoi analysis, acceleration statistics and particle-conditioned averaging*. Int. J. Multi-phase Flow, vol. 46, pages 54–74, 2012. (Cited on page 12.)
- [Gardiner 1990] C. W. Gardiner. *Handbook of stochastic methods for physics, chemistry and the natural sciences*. Springer-Verlag, Berlin, 2nd édition, 1990. (Cited on pages 39 and 67.)
- [Garzó 2012] V. Garzó, S. Tenneti, S. Subramaniam and C. M. Hrenya. *Enskog kinetic theory for monodisperse gas–solid flows*. J. Fluid Mech., vol. 712, pages 129–168, 2012. (Cited on page 101.)
- [Gatignol 1983] R. Gatignol. *The Faxén formulae for a rigid particle in an unsteady non-uniform Stokes flow*. Journal de Mécanique Théorique et Appliquée, vol. 1, no. 2, pages 143–160, 1983. (Cited on pages 10, 64, 106 and 108.)
- [Germano 1991] Massimo Germano, Ugo Piomelli, Parviz Moin and William H Cabot. *A dynamic subgrid-scale eddy viscosity model*. Phys. Fluids A-Fluid, vol. 3, no. 7, pages 1760–1765, 1991. (Cited on pages 33 and 35.)
- [Germano 1992] M Germano. *Turbulence: the filtering approach*. J. Fluid Mech., vol. 238, pages 325–336, 1992. (Cited on pages 19, 33 and 35.)
- [Geurts 2012] BJ Geurts and JGM Kuerten. *Ideal stochastic forcing for the motion of particles in large-eddy simulation extracted from direct numerical simulation of turbulent channel flow*. Phys. Fluids, vol. 24, no. 8, page 081702, 2012. (Cited on pages 34 and 54.)
- [Gicquel 2002] Laurent YM Gicquel, P Givi, FA Jaber and SB Pope. *Velocity filtered density function for large eddy simulation of turbulent flows*. Phys. Fluids (1994-present), vol. 14, no. 3, pages 1196–1213, 2002. (Cited on pages 34, 39, 45 and 48.)
- [Glasser 1998] B. J. Glasser, S. Sundaresan and I. G. Kevrekidis. *From bubbles to clusters in fluidized beds*. Phys. Rev. Lett., vol. 81, no. 9, page 1849, 1998. (Cited on page 63.)
- [Gobert 2010] Ch Gobert. *Analytical assessment of models for large eddy simulation of particle laden flow*. J. of Turbulence, vol. 11, pages 1–25, Jan 2010. (Cited on pages 34 and 54.)
- [Gualtieri 2013] Paolo Gualtieri, Francesco Picano, Gaetano Sardina and Carlo Massimo Casciola. *Clustering and turbulence modulation in particle-laden shear flows*. J. Fluid Mech., vol. 715, pages 134–162, 2013. (Cited on page 106.)
- [Gualtieri 2017] P. Gualtieri, F. Battista and C. M. Casciola. *Turbulence modulation in heavy-load suspensions of tiny particles*. Phys. Rev. Fluids, vol. 2, page 034304, 2017. (Cited on pages 12 and 61.)

- [Guazzelli 2011] E. Guazzelli and J. F. Morris. A physical introduction to suspension dynamics, volume 45. Cambridge University Press, 2011. (Cited on page 61.)
- [Hanjalić 1972] K Hanjalić and BE Launder. *A Reynolds stress model of turbulence and its application to thin shear flows*. J. Fluid Mech., vol. 52, no. 4, pages 609–638, 1972. (Cited on page 21.)
- [Hinze 1975] J.O. Hinze. Turbulence. McGraw Hill, New-York, 2nd édition, 1975. (Cited on pages 8 and 81.)
- [Hirt 1981] Cyril W Hirt and Billy D Nichols. *Volume of fluid (VOF) method for the dynamics of free boundaries*. J. Comp. Phys., vol. 39, no. 1, pages 201–225, 1981. (Cited on page 138.)
- [Huang 1963] K. Huang. Statistical mechanics. Wiley, New York, 1963. (Cited on page 101.)
- [Innocenti 2016] A. Innocenti, C. Marchioli and S. Chibbaro. *Lagrangian filtered density function for LES-based stochastic modelling of turbulent particle-laden flows*. Phys. Fluids, vol. 28, no. 11, page 115106, 2016. (Cited on pages 65 and 106.)
- [Ishii 1987] M Ishii. *Interfacial Area Modeling*, vol. 3, 1987. (Cited on page 16.)
- [Jaberi 1999] F. A. Jaberi, P. J. Colucci, S. Givi and S. B. Pope. *Filtered mass density function for large-eddy simulation of turbulent reactive flows*. J. Fluid Mech., vol. 401, pages 85–121, 1999. (Cited on pages 34 and 48.)
- [Jakobsen 2005] Hugo A Jakobsen, Håvard Lindborg and Carlos A Dorao. *Modeling of bubble column reactors: progress and limitations*. Industrial & engineering chemistry research, vol. 44, no. 14, pages 5107–5151, 2005. (Cited on page 143.)
- [Jenkins 1983] J. T. Jenkins and S. B. Savage. *A theory for rapid flow of identical, smooth, nearly elastic, spherical particles*. J. Fluid Mech., vol. 130, pages 187–202, 1983. (Cited on pages 64, 65, 101 and 102.)
- [Jenkins 1985] J. T. Jenkins and M. W. Richman. *Grad’s 13 moment system for a dense gas of inelastic spheres*. Arch. Ratio. Mech. Anal., vol. 87, pages 355–377, 1985. (Cited on page 101.)
- [Jenny 2001] P Jenny, SB Pope, M Muradoglu and DA Caughey. *A hybrid algorithm for the joint PDF equation of turbulent reactive flows*. J. Comp. Phys., vol. 166, no. 2, pages 218–252, 2001. (Cited on page 42.)
- [Jenny 2012] P. Jenny, D. Roekaerts and N. Beishuizen. *Modeling of turbulent dilute spray combustion*. Prog. Energy Combust. Sci., vol. 38, no. 6, pages 846–887, 2012. (Cited on page 61.)
- [Jin 2015] C Jin, I Potts and MW Reeks. *A simple stochastic quadrant model for the transport and deposition of particles in turbulent boundary layers*. Phys. Fluids (1994-present), vol. 27, no. 5, page 053305, 2015. (Cited on page 34.)

- [Kloeden 1992] P.E. Kloeden and E. Platen. Numerical solution of stochastic differential equations. Springer-Verlag, Berlin, 1992. (Cited on page 100.)
- [Kolmogorov 1941a] Andrey Nikolaevich Kolmogorov. *Dissipation of energy in locally isotropic turbulence*. In Dokl. Akad. Nauk SSSR, volume 32, pages 16–18, 1941. (Cited on page 8.)
- [Kolmogorov 1941b] Andrey Nikolaevich Kolmogorov. *The local structure of turbulence in incompressible viscous fluid for very large Reynolds numbers*. In Dokl. Akad. Nauk SSSR, volume 30, pages 299–303, 1941. (Cited on page 8.)
- [Kuerten 2006] JGM Kuerten. *Subgrid modeling in particle-laden channel flow*. Phys. Fluids, vol. 18, page 025108, 2006. (Cited on page 33.)
- [Kulick 1994] Jonathan D Kulick, John R Fessler and John K Eaton. *Particle response and turbulence modification in fully developed channel flow*. J. Fluid Mech., vol. 277, pages 109–134, 1994. (Cited on page 12.)
- [Lagrée 2011] P-Y Lagrée, Lydie Staron and Stéphane Popinet. *The granular column collapse as a continuum: validity of a two-dimensional Navier–Stokes model with a μ (I)-rheology*. J. Fluid Mech., vol. 686, pages 378–408, 2011. (Cited on page 138.)
- [Lance 1991] M Lance and J Bataille. *Turbulence in the liquid phase of a uniform bubbly air–water flow*. J. Fluid Mech., vol. 222, pages 95–118, 1991. (Cited on pages 14 and 134.)
- [Launder 1975] BE Launder, G Jr Reece and W Rodi. *Progress in the development of a Reynolds-stress turbulence closure*. J. Fluid Mech., vol. 68, no. 03, pages 537–566, 1975. (Cited on pages 20, 69 and 111.)
- [Lesieur 2005] Marcel Lesieur, Olivier Métais and Pierre Comte. Large-eddy simulations of turbulence. Cambridge University Press, 2005. (Cited on page 33.)
- [Liao 2010] Yixiang Liao and Dirk Lucas. *A literature review on mechanisms and models for the coalescence process of fluid particles*. Chemical Engineering Science, vol. 65, no. 10, pages 2851–2864, 2010. (Cited on page 143.)
- [Lilly 1992] Douglas K Lilly. *A proposed modification of the Germano subgrid-scale closure method*. Phys. Fluids A-Fluid, vol. 4, no. 3, pages 633–635, 1992. (Cited on page 35.)
- [Loisy 2017] Aurore Loisy, Aurore Naso and Peter DM Spelt. *Buoyancy-driven bubbly flows: ordered and free rise at small and intermediate volume fraction*. J. Fluid Mech., vol. 816, pages 94–141, 2017. (Cited on pages 14, 136, 138, 140, 141, 142, 143 and 157.)
- [Lun 1986] C. K. K. Lun and S. B. Savage. *The effects of an impact velocity dependent coefficient of restitution on stresses developed by sheared granular materials*. Acta Mech., vol. 63, pages 15–44, 1986. (Cited on page 101.)

- [Magnaudet 2000] Jacques Magnaudet and Ian Eames. *The motion of high-Reynolds-number bubbles in inhomogeneous flows*. Annu. Rev. Fluid Mech, vol. 32, no. 1, pages 659–708, 2000. (Cited on page 134.)
- [Marchioli 2002] C. Marchioli and A. Soldati. *Mechanisms for particle transfer and segregation in a turbulent boundary layer*. J. Fluid Mech., vol. 468, no. -1, pages 283–315, 2002. (Cited on pages 18, 36, 42, 43, 45, 49, 50 and 106.)
- [Marchioli 2008a] C. Marchioli, M V Salvetti and A. Soldati. *Appraisal of energy recovering sub-grid scale models for large-eddy simulation of turbulent dispersed flows*. Acta Mech., vol. 201, pages 277–296, 2008. (Cited on pages 34, 46 and 54.)
- [Marchioli 2008b] C. Marchioli, MV Salvetti and A. Soldati. *Some issues concerning large-eddy simulation of inertial particle dispersion in turbulent bounded flows*. Phys. Fluids, vol. 20, page 040603, 2008. (Cited on pages 12, 17, 18, 33, 46 and 106.)
- [Marchioli 2008c] C. Marchioli, A. Soldati, JGM Kuerten, B. Arcen, A. Taniere, G. Goldensohn, KD Squires, MF Cargnelutti and LM Portela. *Statistics of particle dispersion in direct numerical simulations of wall-bounded turbulence: Results of an international collaborative benchmark test*. Int. J. Multiphase Flow, vol. 34, no. 9, pages 879–893, 2008. (Cited on page 42.)
- [Marconi 2008] U. M. B. Marconi, A. Puglisi, L. Rondoni and A. Vulpiani. *Fluctuation–dissipation: response theory in statistical physics*. Phys. Rep., vol. 461, no. 4-6, pages 111–195, 2008. (Cited on page 95.)
- [Martínez-Mercado 2007] Julián Martínez-Mercado, Carlos A Palacios-Morales and Roberto Zenit. *Measurement of pseudoturbulence intensity in monodispersed bubbly liquids for $10 < Re < 500$* . Phys. Fluids, vol. 19, no. 10, page 103302, 2007. (Cited on page 134.)
- [Maxey 1983] M. R. Maxey and J. J. Riley. *Equation of Motion for a Small Rigid Sphere in a Nonuniform Flow*. Phys. Fluids, vol. 26, no. 4, pages 883–889, 1983. (Cited on pages 10, 64, 106 and 108.)
- [McQuillan 1985] KW McQuillan and PB Whalley. *Flow patterns in vertical two-phase flow*. Int. J. Multiphase Flow, vol. 11, no. 2, pages 161–175, 1985. (Cited on page 9.)
- [Mehrabadi 2018] M Mehrabadi, JAK Horwitz, S Subramaniam and A Mani. *A direct comparison of particle-resolved and point-particle methods in decaying turbulence*. J. Fluid Mech., vol. 850, pages 336–369, 2018. (Cited on page 64.)
- [Michalek 2013] WR Michalek, JGM Kuerten, JCH Zeegers, Raoul Liew, J Pozorski and BJ Geurts. *A hybrid stochastic-deconvolution model for large-eddy simulation of particle-laden flow*. Phys. Fluids, vol. 25, no. 12, page 123302, 2013. (Cited on page 34.)

- [Minier 1999] J.-P. Minier and J. Pozorski. *Wall boundary conditions in the PDF method and application to a turbulent channel flow*. Phys. Fluids, vol. 11, pages 2632–2644, 1999. (Cited on page 48.)
- [Minier 2001] J.-P. Minier and E. Peirano. *The pdf approach to turbulent polydispersed two-phase flows*. Phys. Rep., vol. 352, pages 1–214, 2001. (Cited on pages 23, 24, 38, 43, 62, 69, 95, 99 and 110.)
- [Minier 2004] J.-P. Minier, E. Peirano and S. Chibbaro. *PDF model based on Langevin equation for polydispersed two-phase flows applied to a bluff body-body gas-solid flow*. Phys. Fluids, vol. 16, no. 7, page 2419, 2004. (Cited on pages 38, 69 and 79.)
- [Minier 2014] J.-P. Minier, S. Chibbaro and S. B. Pope. *Guidelines for the formulation of Lagrangian stochastic models for particle simulations of single-phase and dispersed two-phase turbulent flows*. Phys. Fluids, vol. 26, no. 11, page 113303, 2014. (Cited on pages 39, 54, 61 and 74.)
- [Minier 2015a] J.-P. Minier and C. Profeta. *Kinetic and dynamic probability-density-function descriptions of disperse turbulent two-phase flows*. Phys. Rev. E, vol. 92, no. 5, page 053020, 2015. (Cited on page 101.)
- [Minier 2015b] Jean-Pierre Minier. *On Lagrangian stochastic methods for turbulent poly-disperse two-phase reactive flows*. Prog. Energ. Combust., vol. 50, pages 1–62, 2015. (Cited on pages 34, 36, 38, 53 and 106.)
- [Moin 1982] Parviz Moin and John Kim. *Numerical investigation of turbulent channel flow*. J. Fluid Mech., vol. 118, pages 341–377, 1982. (Cited on page 35.)
- [Monchaux 2010] R. Monchaux, M. Bourgoïn and A. Cartellier. *Preferential concentration of heavy particles: a Voronoi analysis*. Phys. Fluids, vol. 22, page 103304, 2010. (Cited on pages 50 and 51.)
- [Mougin 2001] Guillaume Mougin and Jacques Magnaudet. *Path instability of a rising bubble*. Phys. Rev. L., vol. 88, no. 1, page 014502, 2001. (Cited on page 134.)
- [Muradoglu 1999] M. Muradoglu, P. Jenny and S. Pope. *A consistent hybrid finite-volume/particle method for the PDF equations of turbulent reactive flows*. J. Comp Phys., Jan 1999. (Cited on page 42.)
- [Muradoglu 2001] M. Muradoglu, S. B. Pope and D. A. Caughey. *The hybrid method for the PDF equations of turbulent reactive flows: consistency conditions and correction algorithms*. J. Comput. Phys., vol. 172, no. 2, pages 841–878, 2001. (Cited on page 74.)
- [Muste 2005] M. Muste, K. Yu, I. Fujita and R. Ettema. *Two-phase versus mixed-flow perspective on suspended sediment transport in turbulent channel flows*. Water resources research, vol. 41, no. 10, 2005. (Cited on page 163.)
- [Panicker 2018] Nithin Panicker, Alberto Passalacqua and Rodney O. Fox. *On the hyperbolicity of the two-fluid model for gas-liquid bubbly flows*. Applied Mathematical Modelling, vol. 57, pages 432–447, 2018. (Cited on page 159.)

- [Passalacqua 2011] A. Passalacqua, J. E. Galvin, P. Vedula, C. M. Hrenya and R. O. Fox. *A quadrature-based kinetic model for dilute non-isothermal granular flows*. Commun. Comput. Phys., vol. 10, no. 01, pages 216–252, 2011. (Cited on page 102.)
- [Pedley 1992] T. J. Pedley and J. O. Kessler. *Hydrodynamic phenomena in suspensions of swimming microorganisms*. Annu. Rev. Fluid Mech., vol. 24, no. 1, pages 313–358, 1992. (Cited on page 64.)
- [Peirano 2002] E. Peirano and J.-P. Minier. *Probabilistic formalism and hierarchy of models for polydispersed turbulent two-phase flows*. Phys. Rev. E, vol. 65, page 046301, 2002. (Cited on pages 70 and 73.)
- [Peirano 2006] E. Peirano, S. Chibbaro, J. Pozorski and J.-P. Minier. *Mean-field/PDF numerical approach for polydispersed turbulent two-phase flows*. Prog. En. Comb. Sci., vol. 32, no. 3, page 315, 2006. (Cited on pages 40, 41, 53, 55, 61, 69, 79, 95, 106, 116, 117, 118, 119, 120, 121 and 126.)
- [Picano 2013] F. Picano, W.-P. Breugem, D. Mitra and L. Brandt. *Shear thickening in non-Brownian suspensions: an excluded volume effect*. Phys. Rev. Lett., vol. 111, no. 9, page 098302, 2013. (Cited on page 64.)
- [Picano 2015] F. Picano, W.-P. Breugem and L. Brandt. *Modulation of isotropic turbulence by particles of Taylor length-scale size*. J. Fluid Mech., vol. 650, pages 5–55, 2015. (Cited on page 64.)
- [Picciotto 2005] M. Picciotto, C. Marchioli and A. Soldati. *Characterization of near-wall accumulation regions for inertial particles in turbulent boundary layers*. Phys. Fluids, vol. 17, page 098101, 2005. (Cited on pages 34, 36, 45 and 50.)
- [Pope 1985] S. B. Pope. *Pdf Methods for Turbulent Reactive Flows*. Prog. Energy Combust. Sci., vol. 11, pages 119–192, 1985. (Cited on page 99.)
- [Pope 1994a] S. B. Pope. *On the relationship between stochastic Lagrangian models of turbulence and second-moment closures*. Phys. Fluids, vol. 6, no. 2, pages 973–985, 1994. (Cited on pages 72 and 74.)
- [Pope 1994b] S. B. Pope. *On the Relationship between Stochastic Lagrangian Models of Turbulence and Second-Order Closures*. Phys. Fluids, vol. 6, no. 2, pages 973–985, 1994. (Cited on pages 23 and 111.)
- [Pope 2000] Stephen B. Pope. *Turbulent flows*. Cambridge University Press, Cambridge, UK, 2000. (Cited on pages 8, 9, 19, 20, 21, 23, 24, 34, 38, 48, 53, 61, 62, 67, 69, 72, 73, 74, 75, 80, 85, 95, 107, 114, 134 and 135.)
- [Pope 2013] Stephen B. Pope. *Small scales, many species and the manifold challenges of turbulent combustion*. P. Combust. Inst., vol. 34, no. 1, pages 1–31, 2013. (Cited on page 33.)
- [Popinet 2003] Stéphane Popinet. *Gerris: a tree-based adaptive solver for the incompressible Euler equations in complex geometries*. J. Comp. Phys., vol. 190, no. 2, pages 572–600, 2003. (Cited on page 138.)

- [Popinet 2009] Stéphane Popinet. *An accurate adaptive solver for surface-tension-driven interfacial flows*. J. Comp. Phys., vol. 228, no. 16, pages 5838–5866, 2009. (Cited on pages 26, 28 and 138.)
- [Post 2002] S. L. Post and J. Abraham. *Modeling the outcome of drop-drop collisions in Diesel sprays*. Int. J. Multiphase Flow, vol. 28, no. 6, pages 997–1019, 2002. (Cited on page 61.)
- [Pozorski 1998] J. Pozorski and J-P. Minier. *On the Lagrangian turbulent dispersion models based on the Langevin equation*. Int. J. Multiphase Flow, vol. 24, pages 913–945, 1998. (Cited on page 84.)
- [Pozorski 2009] J. Pozorski and S.V. Apte. *Filtered particle tracking in isotropic turbulence and stochastic modeling of subgrid-scale dispersion*. Int. J. Multiphase Flow, vol. 35, no. 2, pages 118–128, 2009. (Cited on pages 11, 12, 23, 34 and 106.)
- [Prevel 2013] M Prevel, Ivana Vinkovic, D Doppler, C Pera and M Buffat. *Direct numerical simulation of particle transport by hairpin vortices in a laminar boundary layer*. Int. J. Heat Fluid Fl., vol. 43, pages 2–14, 2013. (Cited on page 50.)
- [Prince 1990] Michael J Prince and Harvey W Blanch. *Bubble coalescence and break-up in air-sparged bubble columns*. AIChE journal, vol. 36, no. 10, pages 1485–1499, 1990. (Cited on page 144.)
- [Prosperetti 1987] A Prosperetti and AV Jones. *The linear stability of general two-phase flow models-II*. Int. J. Multiphase Flow, vol. 13, no. 2, pages 161–171, 1987. (Cited on page 159.)
- [Prosperetti 2004] A Prosperetti. *Bubbles*. Phys. Fluids, Jan 2004. (Cited on page 134.)
- [Prosperetti 2009] Andrea Prosperetti and Grétar Tryggvason. *Computational methods for multiphase flow*. Cambridge university press, 2009. (Cited on page 134.)
- [Puglisi 2014] A. Puglisi. *Transport and fluctuations in granular fluids: From boltzmann equation to hydrodynamics, diffusion and motor effects*. Springer, 2014. (Cited on page 61.)
- [Ramshaw 1978] John D Ramshaw and John A Trapp. *Characteristics, stability, and short-wavelength phenomena in two-phase flow equation systems*. Nuclear Science and Engineering, vol. 66, no. 1, pages 93–102, 1978. (Cited on page 159.)
- [Reynolds 1883] O Reynolds. *An experimental investigation of the circumstances which determine whether the motion of water shall be direct or sinuous, and of the law of resistance in parallel channels*. Philosophical Transactions of the Royal Society of London, vol. 174, pages 935–82, 1883. (Cited on page 7.)
- [Riboux 2010] Guillaume Riboux, Frédéric Risso and Dominique Legendre. *Experimental characterization of the agitation generated by bubbles rising at high Reynolds number*. J. Fluid Mech., vol. 643, pages 509–539, 2010. (Cited on pages 2, 14, 16, 133, 134, 150, 162 and 164.)

- [Richardson 1922] Lewis Fry Richardson. *Weather prediction by numerical process*. Cambridge University Press, 1922. (Cited on page 8.)
- [Risso 2002] Frédéric Risso and Kjetil Ellingsen. *Velocity fluctuations in a homogeneous dilute dispersion of high-Reynolds-number rising bubbles*. *J. Fluid Mech.*, vol. 453, pages 395–410, 2002. (Cited on page 134.)
- [Risso 2018] Frédéric Risso. *Agitation, mixing, and transfers induced by bubbles*. *Annu. Rev. Fluid Mech.*, vol. 50, pages 25–48, 2018. (Cited on page 134.)
- [Rogallo 1984] Robert S Rogallo and Parviz Moin. *Numerical simulation of turbulent flows*. *Annu. Rev. Fluid Mech.*, vol. 16, no. 1, pages 99–137, 1984. (Cited on page 33.)
- [Roghair 2011] Ivo Roghair, Julián Martínez Mercado, Martin Van Sint Annaland, Hans Kuipers, Chao Sun and Detlef Lohse. *Energy spectra and bubble velocity distributions in pseudo-turbulence: Numerical simulations vs. experiments*. *Int. J. Multiphase Flow*, vol. 37, no. 9, pages 1093–1098, 2011. (Cited on page 135.)
- [Roghair 2013] Ivo Roghair, Martin Van Sint Annaland and Hans JAM Kuipers. *Drag force and clustering in bubble swarms*. *AIChE Journal*, vol. 59, no. 5, pages 1791–1800, 2013. (Cited on page 135.)
- [Rouson 2001] D.W.I. Rouson and J.K. Eaton. *On the preferential concentration of solid particles in turbulent channel flow*. *J. Fluid Mech.*, vol. 428, no. 1, pages 149–169, 2001. (Cited on page 34.)
- [Sagaut 2006] P. Sagaut. *Large eddy simulation for incompressible flows: an introduction*. Springer Verlag, 2006. (Cited on page 33.)
- [Sangani 1987] Ashok S Sangani. *Sedimentation in ordered emulsions of drops at low Reynolds numbers*. *Zeitschrift für angewandte Mathematik und Physik ZAMP*, vol. 38, no. 4, pages 542–556, 1987. (Cited on pages 138, 140 and 141.)
- [Sankaranarayanan 2002] K Sankaranarayanan, X Shan, IG Kevrekidis and S Sundaresan. *Analysis of drag and virtual mass forces in bubbly suspensions using an implicit formulation of the lattice Boltzmann method*. *J. Fluid Mech.*, vol. 452, pages 61–96, 2002. (Cited on page 141.)
- [Scardovelli 1999] Ruben Scardovelli and Stéphane Zaleski. *Direct numerical simulation of free-surface and interfacial flow*. *Annu. Rev. Fluid Mech.*, vol. 31, no. 1, pages 567–603, 1999. (Cited on pages 26, 138 and 143.)
- [Sheikhi 2003] M Sheikhi, T Drozda, P Givi and S Pope. *Velocity-scalar filtered density function for large eddy simulation of turbulent flows*. *Phys. Fluids*, Jan 2003. (Cited on pages 34 and 48.)
- [Sheikhi 2007] M Sheikhi, P Givi and S Pope. *Velocity-scalar filtered mass density function for large eddy simulation of turbulent reacting flows*. *Phys. Fluids*, vol. 19, no. 9, page 095106, 2007. (Cited on pages 34 and 48.)

- [Sheikhi 2009] M Sheikhi, P Givi and S Pope. *Frequency-velocity-scalar filtered mass density function for large eddy simulation of turbulent flows*. Phys. Fluids, Jan 2009. (Cited on pages 34 and 48.)
- [Shinnar 1960] Reuel Shinnar and James M Church. *Statistical theories of turbulence in predicting particle size in agitated dispersions*. Industrial & Engineering Chemistry, vol. 52, no. 3, pages 253–256, 1960. (Cited on page 145.)
- [Shotorban 2005] B. Shotorban and F. Mashayek. *Modeling subgrid-scale effects on particles by approximate deconvolution*. Phys. Fluids, vol. 17, page 081701, 2005. (Cited on page 34.)
- [Smagorinsky 1963] Joseph Smagorinsky. *General circulation experiments with the primitive equations: I. The basic experiment*. Monthly weather review, vol. 91, no. 3, pages 99–164, 1963. (Cited on pages 19, 33 and 35.)
- [Soldati 2009] A. Soldati and C. Marchioli. *Physics and modelling of turbulent particle deposition and entrainment: Review of a systematic study*. Int. J. Multiphase Flow, vol. 35, no. 9, pages 827–839, 2009. (Cited on pages 34, 36, 42, 43, 49 and 50.)
- [Soldati 2012] A. Soldati and C. Marchioli. *Sediment transport in steady turbulent boundary layers: Potentials, limitations, and perspectives for Lagrangian tracking in DNS and LES*. Adv. Water Resour., vol. 48, no. 9, pages 18–30, 2012. (Cited on page 34.)
- [Song 2001] JinHo Song and Mamoru Ishii. *The one-dimensional two-fluid model with momentum flux parameters*. Nuclear Engineering and Design, vol. 205, no. 1-2, pages 145–158, 2001. (Cited on page 159.)
- [Spelt 1997] PDM Spelt and A Biesheuvel. *On the motion of gas bubbles in homogeneous isotropic turbulence*. J. Fluid Mech., vol. 336, pages 221–244, 1997. (Cited on page 13.)
- [Stickel 2005] J. J. Stickel and R. L. Powell. *Fluid mechanics and rheology of dense suspensions*. Annu. Rev. Fluid Mech., vol. 37, pages 129–149, 2005. (Cited on page 61.)
- [Stuhmiller 1977] JH Stuhmiller. *The influence of interfacial pressure forces on the character of two-phase flow model equations*. Int. J. Multiphase Flow, vol. 3, no. 6, pages 551–560, 1977. (Cited on page 159.)
- [Sundaram 1999] S. Sundaram and L. R. Collins. *A numerical study of the modulation of isotropic turbulence by suspended particles*. J. Fluid Mech., vol. 379, pages 105–143, 1999. (Cited on pages 12, 76, 80, 82, 85, 86, 87 and 96.)
- [Tagawa 2012] Yoshiyuki Tagawa, Julián Martínez Mercado, Vivek N Prakash, Enrico Calzavarini, Chao Sun and Detlef Lohse. *Three-dimensional Lagrangian Voronoï analysis for clustering of particles and bubbles in turbulence*. J. Fluid Mech., vol. 693, pages 201–215, 2012. (Cited on page 13.)
- [Tanaka 2017] M. Tanaka. *Effect of gravity on the development of homogeneous shear turbulence laden with finite-size particles*. J. Turb., vol. 18, no. 12, pages 1144–1179, 2017. (Cited on page 64.)

- [Tchen 1947] C.M. Tchen. *Mean value and correlation functions connected with the motion of small particles suspended in a turbulent fluid*. PhD Thesis, Delft, 1947. (Cited on page 81.)
- [Ten Cate 2004] A. Ten Cate, J. J. Derksen, L. M. Portela and H. E. A. Van Den Akker. *Fully resolved simulations of colliding monodisperse spheres in forced isotropic turbulence*. J. Fluid Mech, vol. 519, pages 233–271, 2004. (Cited on page 64.)
- [Tiselj 1997] Iztok Tiselj and Stojan Petelin. *Modelling of two-phase flow with second-order accurate scheme*. J. Comp. Phys., vol. 136, no. 2, pages 503–521, 1997. (Cited on page 159.)
- [Toschi 2009] F Toschi and E Bodenschatz. *Lagrangian properties of particles in turbulence*. Annu. Rev. Fluid Mech, vol. 41, pages 375–404, 2009. (Cited on page 134.)
- [Tryggvason 2011] Grétar Tryggvason, Scardovelli Ruben and Zaleski Stéphane. *Direct numerical simulations of gas - liquid multiphase flows*. Cambridge Univ Press, 2011. (Cited on pages 13, 27, 135, 137 and 143.)
- [Uhlmann 2008] Markus Uhlmann. *Interface-resolved direct numerical simulation of vertical particulate channel flow in the turbulent regime*. Phys. Fluids, vol. 20, no. 5, page 053305, 2008. (Cited on page 106.)
- [Van Noije 1998] T. P. C. Van Noije and M. H. Ernst. *Velocity distributions in homogeneous granular fluids: the free and the heated case*. Granul. Matter, vol. 1, no. 2, pages 57–64, 1998. (Cited on page 101.)
- [Vance 2006] MW Vance, KD Squires and O Simonin. *Properties of the particle velocity field in gas-solid turbulent channel flow*. Phys. Fluids, vol. 18, no. 6, page 063302, 2006. (Cited on page 33.)
- [Viollet 1994] P. L. Viollet and O. Simonin. *Modelling dispersed two-phase flows: closure, validation and software development*. Appl. Mech. Rev, vol. 47, no. 6, pages S80–S84, 1994. (Cited on page 62.)
- [Vreman 2009] Bert Vreman, Bernard J Geurts, NG Deen, JAM Kuipers and Johannes GM Kuerten. *Two-and four-way coupled Euler–Lagrangian large-eddy simulation of turbulent particle-laden channel flow*. Flow, turbulence and combustion, vol. 82, no. 1, pages 47–71, 2009. (Cited on page 12.)
- [Wacławczyk 2004] M Wacławczyk, J Pozorski and JP Minier. *Probability density function computation of turbulent flows with a new near-wall model*. Phys. Fluids, vol. 16, page 1410, 2004. (Cited on pages 39 and 48.)
- [Wang 1993a] L. P. Wang and D. E. Stock. *Dispersion of heavy particles by turbulent motion*. J. Atm. Sc., vol. 50, no. 13, pages 1897–1913, 1993. (Cited on pages 38 and 70.)
- [Wang 1993b] L.P. Wang and M.R. Maxey. *Settling velocity and concentration distribution of heavy particles in homogeneous isotropic turbulence*. J. Fluid Mech., vol. 256, no. -1, pages 27–68, 1993. (Cited on pages 34 and 106.)

- [Xiao 2009] Z Xiao, M Wan, S Chen and GL Eyink. *Physical mechanism of the inverse energy cascade of two-dimensional turbulence: a numerical investigation*. Journal of Fluid Mechanics, vol. 619, pages 1–44, 2009. (Cited on page [154](#).)
- [Yamamoto 2001] Y Yamamoto, M Potthoff, T Tanaka, T Kajishima and Y Tsuji. *Large eddy simulation of turbulent gas-particle flow in a vertical channel: Effect of considering inter-particle collisions*. J. Fluid Mech., vol. 442, no. 9, pages 303–334, 2001. (Cited on page [33](#).)
- [Zamansky 2013] Rémi Zamansky, Ivana Vinkovic and Mikhael Gorokhovski. *Acceleration in turbulent channel flow: universalities in statistics, subgrid stochastic models and an application*. J. Fluid Mech., vol. 721, pages 627–668, 2013. (Cited on page [33](#).)
- [Zenit 2001] Roberto Zenit, Donald L Koch and Ashok S Sangani. *Measurements of the average properties of a suspension of bubbles rising in a vertical channel*. J. Fluid Mech., vol. 429, pages 307–342, 2001. (Cited on page [134](#).)
- [Zhang 1994] DZ Zhang and A Prosperetti. *Averaged equations for inviscid disperse two-phase flow*. J. Fluid Mech., vol. 267, pages 185–219, 1994. (Cited on page [16](#).)
- [Zhao 2012] LH Zhao, C Marchioli and HI Andersson. *Stokes number effects on particle slip velocity in wall-bounded turbulence and implications for dispersion models*. Phys. Fluids, vol. 24, no. 2, page 021705, 2012. (Cited on page [48](#).)